EFFECTS OF ACID GAS INTERACTIONS ON THE ADSORPTION AND SEPARATION PROPERTIES OF ZEOLITIC IMIDAZOLATE FRAMEWORK (ZIF) MATERIALS

A Dissertation
Presented to
The Academic Faculty

by

Souryadeep Bhattacharyya

In Partial Fulfillment
of the Requirements for the Degree
Doctor of Philosophy in the
School of Chemical & Biomolecular Engineering

Georgia Institute of Technology
December 2018

EFFECTS OF ACID GAS INTERACTIONS ON THE ADSORPTION AND SEPARATION PROPERTIES OF ZEOLITIC IMIDAZOLATE FRAMEWORK (ZIF) MATERIALS

Approved by:

Dr. Sankar Nair, Advisor
School of Chemical &
Biomolecular Engineering
Georgia Institute of Technology

Dr. Yoshiaki Kawajiri,
School of Chemical &
Biomolecular Engineering
Georgia Institute of Technology

Dr. David S. Sholl, Co-Advisor
School of Chemical &
Biomolecular Engineering
Georgia Institute of Technology

Dr. Thomas M. Orlando,
School of Chemistry and
Biochemistry
Georgia Institute of Technology

Dr. Krista S. Walton,
School of Chemical &
Biomolecular Engineering
Georgia Institute of Technology

Date Approved: September 10th, 2018

Dedicated to my supportive parents Mala and Jagadish Bhattacharyya

ACKNOWLEDGEMENTS

This thesis is the product of many personal trials and tribulations that can be traced back to the year 2012. Leaving my home country and family in India to come to the U.S for a Ph.D. in 2012 was difficult, and became considerably harder when, in the spring of 2014, I had to change my thesis adviser, and research area due to external factors beyond my control. Without any doubt, through those "dark" days of 2014 to the "sunnier" present, my thesis advisors Prof. Sankar Nair and Prof. David Sholl have supported me greatly and I owe them a world of gratitude. Getting the opportunity to work with such world-renowned researchers has been a transformative experience, and I thank them deeply for their belief in my abilities and persistence.

Gratitude is also due to the members of my thesis committee Prof. Krista Walton, Prof. Thomas Orlando, and Prof. Yoshiaki Kawajiri for their support and guidance through the 4 years of my Ph.D. I would also like to express my sincere appreciation to all my colleagues in the Nair and Sholl research group, whose insight and support have been instrumental to my success. Special thanks are due to all my wonderful collaborators: Jason Bentley, Ke Zhang, Jason A. Gee, Krishna C. Jayachandrababu, William Mounfield, Michael R. Dutzer, Wun-Gwi Kim, Yang Jiao, Simon Pang, Guanghui Zhu, Yadong Chiang (Leo), Yang Liu, Rebecca Han, Yi Huang, Chu Han, Julian T. Hungerford, Jayraj N. Joshi, Mayank Agrawal, Alexander C. Elder, and Chen Ma.

I especially want to thank Krishna and Chen, who synthesized a number of ZIF materials for my work, Leo, for measuring a number of water adsorption isotherms, Michael and Julian, for carrying out dry SO_2 isotherm measurements, Simon, for his

assistance in aqueous SO_2 exposures, Guanghui and Jay for their help with dry NO_2 experiments, and Rebecca, for carrying out all the computational work that I have mentioned in this thesis. This thesis would not have been possible without all of your direct support.

I would also like to thank my M.S. thesis advisor Dr. Pamela Peralta-Yahya at Georgia Tech, for giving me the opportunity to work in the field of synthetic biology and metabolic engineering, which considerably widened my breadth of knowledge. My M.Tech. thesis advisor at IIT Kanpur Prof. Ashutosh Sharma is an inspiration in my scientific journey, from whom I got the real first taste of cutting edge research. I am also deeply indebted to Prof. Sri Sivakumar for his invaluable guidance during my M.Tech. research at IIT Kanpur. All these remarkable individuals and their unique styles of advising have left an indelible mark on me as a researcher and an individual.

I would like to thank all my inspirational teachers from Jadavpur University and South Point School, especially Prof. Chandan Guha and Prof. Chiranjib Bhattacharjee, who were instrumental in shaping my thinking. Special credit is due to my favorite teacher Dr. Debasis Barman, and Rabi Da (Prof. Rabibrata Mukherjee) of IIT Kharagpur, who inspired me to take up Chemical Engineering as my major during my undergraduate studies. Friends are an essential ingredient to a happy life and I would like to thank all my close friends from school and college who have been there for me when I needed them the most. The India Club was truly a home away from home and my extended family here at Georgia Tech, and I would like to thank all the wonderful people at the Club I have grown close to, who have worked tirelessly towards making the experience of the larger Indian community at Georgia Tech better. I would also like to thank my colleagues at the Georgia Tech

Student Government Association who toil selflessly to improve the lives of their fellow graduate students on campus. Serving with you all was a pleasure.

My identity as a person is incomplete without music and my guruji Pt. Alok Lahiri has been an inspiration for me through his teaching and mentorship. I will be indebted to him, Guruma Kajol Lahiri, Gurudada Abhisek Lahiri for their love and affection. My deep gratitude is also to my first music guru, the late Sri Jayanta Roy Chowdury, who passed away last year. His love and affection for me knew no bounds. Whenever I came home from the U.S, we would meet and spend hours playing music. I will miss you dearly "Mastermashai".

Finally, no person can succeed in life without a supportive family, and I would like to thank every member of my extended family for their continuing support and belief in me. I would like to thank my loving wife Mandovi for her extensive support in the thesis writing and editing process, and for proofreading this document. My sister Aishee is also an inspiration who has overcome many personal challenges in her life and also successfully defeated me to the title of "Doctor" (a real one) in the present generation of our extended family! Without doubt, parents are one's pillars of support. My mother Dr. Mala Bhattacharyya and my father Jagadish Bhattacharyya are people I adore and look up to for inspiration. Their belief in me, and their unconditional affection have guided me through difficult times. I owe my limited success in life to their unconditional love and many sacrifices.

TABLE OF CONTENTS

LIST OF TABLES

LIST OF FIGURES

LIST OF SYMBOLS AND ABBREVIATIONS

ORNL	Oak Ridge National Laboratory
MOF	Metal-organic framework
SBU	Secondary building unit
ZIF	Zeolitic Imidazolate Framework
PIM	Polymers of intrinsic microporosity
WFGD	Wet flue gas desulfurization
DSI	Dry sorbent injection
SCR	Selective catalytic reduction
SNCR	Selective non-catalytic reduction
HSAB	Hard and soft acids and bases
PXRD	Powder X-ray diffraction
R.H.	Relative humidity
GCMC	Grand canonical Monte Carlo
XPS	X-ray photoelectron spectroscopy
NP	Nitrogen physisorption
BET	Brunauer–Emmett–Teller
SEM	Scanning electron microscopy
FTIR	Fourier Transform Infrared Spectroscopy
EDX	Energy dispersive X-Ray spectroscopy
NMR	Nuclear magnetic resonance
ABE	Acetone-butanol-ethanol
DMF	N,N-dimethylformamide

DI	Deionized
VLE	vapor-liquid equilibrium
DBST	Dortmund Databank Software and Separation Technology
NIST	National Institute of Standards and Technology
2-mim	2-methylimidazole
DFT	Density functional theory
P	Membrane Permeability
J	Membrane Flux
Δp	Transmembrane Pressure Difference
l	Membrane Thickness
D_i	Diffusion Coefficient of component i
$\alpha_{i/j}$	Membrane Selectivity/Separation Factor of component i with respect to j
q	Adsorbed amount
u	volumetric flow rate
C_i	Concentration of component i
m_{ads}	MOF loaded in packed column
t	time

SUMMARY

Separation technology is central to industrial chemical processes, and accounts for ~15% of the world's energy consumption. Large energy reduction opportunities exist if traditional separation technologies such as distillation can be replaced or augmented by materials-based, energy efficient processes such as adsorption or membrane separation. The efficacy of such technologies depends on the performance of the materials used as separation agents, which interact at a molecular level with the targeted components of the feed stream in order to accomplish their separation.

Among various classes of materials, nanoporous Zeolitic Imidazolate Frameworks (ZIFs), a subclass of Metal Organic Frameworks (MOFs), have been shown to have tremendous potential for applications in chemical separations. This can be attributed to their diverse capabilities for selective separation of molecules, relative thermal and chemical stability among MOFs, and the possibility of fine control over their pore dimensions and functionality through judicious selection of linkers and synthesis conditions. However, the successful translation of these materials in industrial separations not only depends on their selectivity and throughput in a particular separation process, but also on their stability under realistic process conditions. A number of practical applications involve complex mixtures of molecules including acid gas species (e.g., CO_2, SO_x, NO_x, H_2S), whose presence can lead to irreversible structural changes in ZIFs and have a detrimental effect on the separation performance. The overall goal of this thesis is to systematically investigate the effects of various acid gases (CO_2, SO_2, and NO_2) on the

stability of ZIF materials under different conditions of interest, leading to a more quantitative and generalized mechanistic understanding of ZIF-acid gas interactions.

Three objectives are defined to achieve this goal: **i)** establish a general framework for systematic investigation of acid gas stability of ZIFs, with particular focus on the underlying mechanistic routes of ZIF degradation, specific to each acid gas, **ii)** create an extensive information database on the stability of different ZIF materials to acid gas species for their immediate selection and application in separation processes, and **iii)** develop a quantitative approach to the ZIF degradation process from fundamental knowledge, allowing predictions of material stability in acid gas environments

This first objective led to the establishment of a general set of characterization tools, to probe the bulk stability of all ZIF materials to different acid gases and the associated reaction mechanisms. This toolkit was first applied to study the effects of the acid gas CO_2 on ZIF stability in Chapter 2, which motivated further investigations on interactions of ZIFs with stronger acid gases SO_2 and NO_2 in Chapters 3-6. The general investigative framework was applied successfully to 16 ZIF materials and all three acid gases studied in the thesis, revealing striking differences in reaction pathways specific to the properties of individual ZIFs and the acid gas.

The second objective led to a large expansion of the (previously very limited) knowledge base on the acid gas stability of ZIF materials, through documentation of individual observations for a library of more than 15 different ZIFs with varying functionalities and crystal structures, towards humid air, water, dry and humid CO_2 and SO_2 gases. The stability chart in Chapter 4 summarizes these observations, allowing rapid

selection of stable ZIF materials towards practical separation applications. Three characteristic ZIFs were then selected to study ZIF-NO_2 stability in Chapter 5 providing valuable insights on the action of this acid gas which is different from CO_2 or SO_2.

The third objective led to the emergence of a quantitative approach to the stability of ZIF materials on acid gas exposure. The rate of humid SO_2 induced degradation reactions were measured for different ZIFs and statistically correlated with multiple characteristic material properties. The surprising results of this approach provided new insights on material stability in acid gases and are presented in Chapter 4. The relation between the degradation rate and relative humidity is explored in Chapter 6, leading to the development of the first predictive model of the durability of a ZIF material towards an acid gas over long time scales.

CHAPTER 1. INTRODUCTION

1.1 Materials research: key to energy efficient chemical production

Energy produced from different primary sources is utilized to meet the demands of our modern society, such as comfort and heating (27%) (residential and commercial), convenient transportation (38.5%), and manufacture of desired products by industry (34.5%).[1-2] Industrial separations, central to product purification in chemical engineering and a fundamental part of almost all chemical processes, account for 45-55% of the total industrial energy demand.[3-4] The chemical engineering industry is therefore uniquely positioned to direct changes and realize efficiency improvements necessary to limit the increase in global energy demand and CO_2 emissions. At present, 84% of the total separation energy is consumed by just 12 chemical processes such as petroleum refining, paper production etc. which employ well-established thermally driven technologies of distillation, evaporation and drying.[3-4] The energy intensiveness of such technologies results from the requirement of phase change to enable the separation of one or more components, with the energy input applied to the entire feed mixture instead of the target component(s). As an example, the well-established Linde process of cryogenic distillation to separate gas mixtures in the chemical industry, operates *via* liquefaction of the entire gas mixture followed by distillation at cryogenic temperatures.

In contrast, non-thermal based separation technologies such as adsorption, membrane separation and pervaporation operate at near-ambient conditions and selectively target the component of interest consuming about an order of magnitude less energy (**Figure 1.1**).[5] Consequently, large energy reduction opportunities exist if high energy

consuming separation technologies such as distillation can be replaced or augmented by energy efficient separation systems. The effectiveness, and therefore the economic viability, of these low energy alternatives depend on the efficacy of separation agents (sorbents, membranes, molecular sieves, ion-exchange resins etc.) that interact physically/chemically at a molecular level with the target component(s) in the separation mixture. Therefore the possibility of replacing or augmenting energy intensive separation technologies in industry hinge on the development of new and advanced materials suitable for use as separation agents.

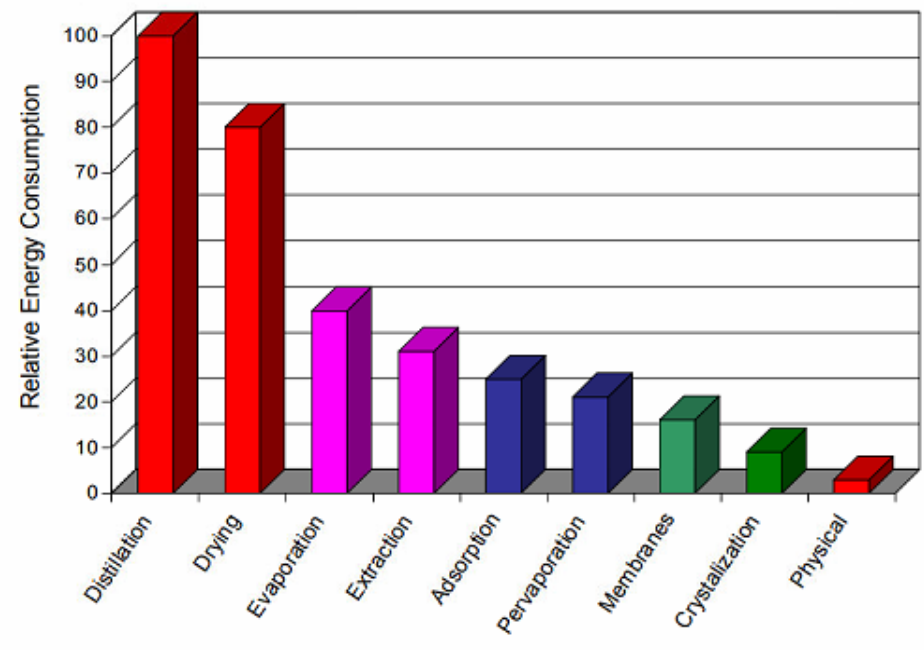

Figure 1.1. Relative energy use by different separation technologies. Source: Materials for Separation Technologies: Energy and Emission Reduction Opportunities, ORNL.[3]

1.1.1 Performance metrics for separation agents

Different separation technologies such as extraction, absorption, adsorption, pervaporation and other membrane based separations utilize materials as separation agents.

A number of performance thresholds need to be met to enable widespread use of materials as effective separation agents in such applications. These include:

1. High material selectivity, *i.e.* affinity towards the target component relative to the other mixture components, that enables achievement of desired purity levels;
2. High throughput (loading capacity, flux etc.) of the desired component enabling achievement of reasonable system economics;
3. High material durability (maintenance of desired performance) under harsh industrial environments (pressure, temperature, corrosiveness) with no or simple fouling prevention or cleaning protocols, enabling long term material use, and
4. Cheap and scalable material synthesis and material packaging equipment enabling process cost reductions through economies of scale.

1.1.2 Energy efficient separation technologies

Of the different separation technologies, significant research attention has been focused on low energy intensive separation technologies such as adsorption, pervaporation and other membrane based separations. Compared to traditional thermal separation processes such as distillation, these alternatives can be up to 90% more energy efficient.[4]

1.1.2.1 Adsorption

Unlike absorption, which is distinguished by mass transfer of the desired component(s) into the bulk of a solid/liquid (absorbent), adsorption is concerned with the selective collection of desired components (adsorbates) on the surface of a material (adsorbent), typically a microporous solid. At a fundamental level, adsorption results from

intermolecular interactions between the adsorbate and the adsorbent, leading to spatial localization of the adsorbate within an adsorbed phase on the adsorbent surface. This results in a decrease in the molar entropy, which must be offset by a comparable decrease in the molar enthalpy to render the process thermodynamically favorable. Adsorption is thus an exothermic process, and depending on the strength of the adsorbate-adsorbent intermolecular interaction, may be classified into two kinds: physisorption and chemisorption. Physisorptive processes have low adsorption enthalpies (<40 kJ/mol) resulting from weak van der Waals intermolecular forces and are characterized by reversible, non-specific interactions that may allow formation of adsorbate multilayers. Chemisorptive processes in contrast have high adsorption enthalpies (>100 kJ/mol) due to the formation of highly specific adsorbate-adsorbent chemical bonds. The high enthalpy of adsorption makes chemisorptive processes practically irreversible, with formation of adsorbate monolayers resulting from the specificity of adsorbate-adsorbent interactions. The equilibrium relationship of the adsorbate uptake (expressed as a function of the adsorbate partial pressure or concentration) by the adsorbent at a fixed temperature is termed an adsorption isotherm. Favorable molecular interactions between the desired adsorbate and the adsorbent lead to high selectivities while the overall saturation capacity is determined by the total number of available adsorption sites for the adsorbate on the adsorbent surface.

Adsorption technology functions by rapid cycles of adsorption and desorption (adsorbent regeneration by release of the captured adsorbate), with energy expended (by raising temperature, reducing pressure etc.) to remove the adsorbed component during desorption. Therefore, adsorbent materials with high surface area per unit weight and low

adsorption enthalpy for the separation are preferred in industrial processes to facilitate high adsorbate loading during the adsorption cycle and easy desorption during adsorbent regeneration. Adsorption technology is industrially applied to remove low adsorbate concentrations from an incoming process feed such as in air dehumidification, decolorization of petroleum products etc.[3]

1.1.2.2 Membrane separations

A membrane is essentially an engineered thin selective barrier separating two phases by controlling the transport of matter between them. An influent feed stream is separated by a membrane into two effluent streams: one containing the feed components that can pass through the membrane (permeate), and a second containing the feed components that are rejected by the membrane (retentate). In pervaporation, vacuum is applied to the permeate side of the membrane, generating a pressure gradient, and the resulting permeate vapor stream is then condensed. Components are transported from one phase to another across a membrane by the application of a driving force (pressure, concentration etc.) and the absence of a phase change (except in pervaporation) makes this separation process highly energy efficient. Membranes have the potential to be a continuous separation process unlike adsorption, which requires cycling between adsorptive and desorptive states.

Transport mechanisms for molecular separations using membranes are different from simple filtration, which primarily occurs *via* size exclusion or hydrodynamic sieving.[6] Unless the size differential between mixture components is considerable (~ several Å), molecular scale discrimination between similarly sized molecules by membranes occurs

via a sorption-diffusion mechanism, i.e. both by thermodynamic partitioning (sorption coefficients) and kinetic mobility (diffusion coefficients). Membrane permeability (P) for a component i is defined as the flux of that component through the membrane (J) normalized by the transmembrane partial pressure difference (Δp) and the selective membrane thickness (l) (Equation 1). For a coupled sorption-diffusion process, the component permeability (P_i) is the product of its sorption (S_i) and diffusion (D_i) coefficients in the membrane. The intrinsic membrane selectivity towards two components of a feed mixture ($\alpha_{i/j}$) is a ratio of their permeabilities through the membrane, and by extension, a product of their sorption selectivity (S_i/S_j) and diffusion selectivity (D_i/D_j) (Equation 2).

$$P_i = \frac{J_i}{\frac{\Delta p_i}{l}} = S_i . D_i \tag{1}$$

$$\alpha_{i/j} = \frac{P_i}{P_j} = (S_i/S_j).(D_i/D_j) \tag{2}$$

Thus, the chemical nature and morphology of the membrane material can be tuned to tailor complementary diffusion and sorption selectivities, while maintaining reasonably high fluxes for economic viability of the separation process.

It is evident that the effectiveness of a material as an adsorbent or a membrane towards a separation process depends on its interactions with the components of that particular bulk mixture. Therefore, the selection and/or development of high performance materials for separations is intrinsically process-specific. However, scientific knowledge generated during materials development for a particular application can accelerate advancement in other application areas. Materials development, geared towards ensuring

availability of appropriate materials that can weather the severe performance demands of industrial operations, is therefore critical to achieve major improvements in separation technology, and in turn reduce the carbon footprint of chemical industries.

1.2 Next generation separation materials

Two of the desirable material properties for their use in a particular separation application are high selectivity and high throughput. Unfortunately, there is often a trade-off between these two important performance metrics: between selectivity and adsorption capacity (adsorption based separation systems) or between permeability and selectivity (membrane based systems). For example, highly selective membranes often have poor permeability and *vice versa*. This intrinsic trade-off is referred to as the Robeson's 'upper bound', a concept developed in the context of (glassy) polymeric materials, which dominate the present membrane materials market.[7-8] Efforts to surpass this performance limit have fueled research interest in i) composite systems, where additives are introduced to incrementally enhance performance, and ii) in the development of next generation high performance porous materials for separations. Among the several high performance materials that are being actively developed and considered for industrial applications, metal-organic frameworks (MOFs) have a number of distinct advantages which make them well-suited to be the premier material of choice in a variety of challenging adsorptive and membrane separation applications.[6, 9-12]

1.2.1 Metal Organic Frameworks (MOFs)

Metal–organic frameworks (MOFs) are a class of hybrid organic–inorganic porous crystalline materials comprised of two key components: inorganic nodes comprised of metal ion or metal ion clusters (termed secondary building unit (SBU)), connected by an organic unit called the linker, to from a regular repeating structure. Large variety of available building blocks (SBUs and organic linkers) allows for synthesis of diverse MOFs from these simple components, each with its unique adsorption properties and textural characteristics.[10-11] The internal surface area of some synthesized MOFs can reach ~7000 m^2/g and combinations of different SBUs and linkers have been predicted to form 137,953 hypothetical MOF structures.[13-14]

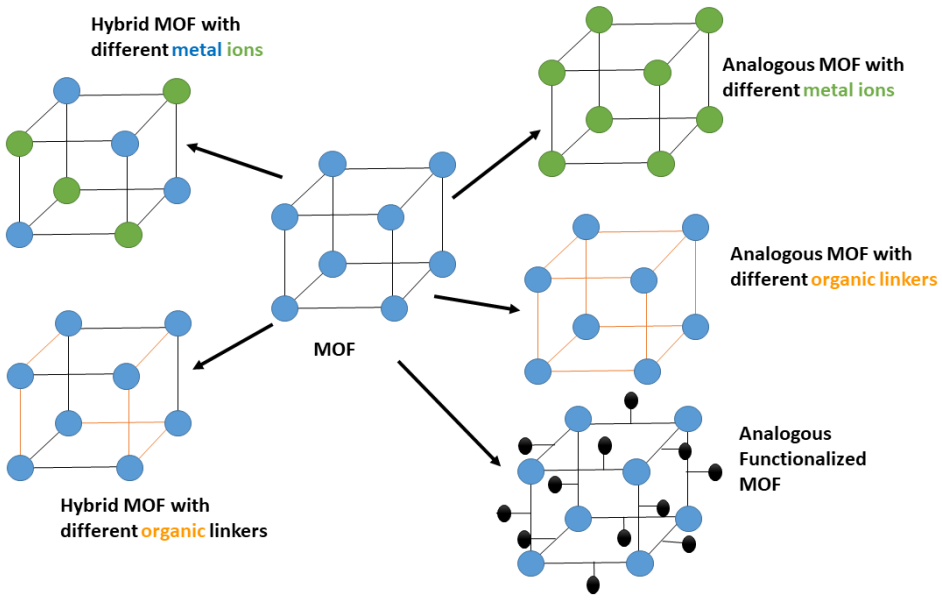

Figure 1.2. Schematic representation of analogous and hybrid MOFs.

Analogous MOFs can be synthesized on combining (a) identical linkers with different SBUs, (b) identical SBUs with different linkers, and (c) SBUs with functionalized

MOF linkers, while combining one or more SBUs/linkers within the same MOF structure gives rise to hybrid MOFs (**Figure 1.2**).[15] Facile tunability of pore sizes and shapes from the microporous to the mesoporous scale *via* judicious selection of the SBUs and bridging linkers allows tailoring of the MOF pore environment towards specific separation applications. Composite mixed matrix systems consist of a primary polymer phase and a secondary dispersed phase (zeolites/MOFs etc.) with the aim to synergize the advantages of both the constituent phases, such as the ease of processability and permeability of the polymer phase with the high selectivity of the secondary dispersed phase.[16] The organic-inorganic hybrid nature of MOF materials promotes the formation of a close interface with the organic polymer phase, critical to preventing non-selective interstitial space creation within the composite.[16] Thus, the rich diversity in MOF structure and its tunable functionality, coupled with ease of synthesis (coordination chemistry) confers MOFs advantages over other inorganic and organic materials used in separations, such as zeolites and polymers. A comparison of the important properties of zeolites, MOFs and microporous polymers (eg. PIMs) critical to separation processes is shown in **Figure 1.3**.[10] This thesis focuses on a subclass of MOF materials known as Zeolitic Imidazolate Frameworks (ZIFs) which are of particular interest to separation applications because of their advantageous properties among MOF materials.

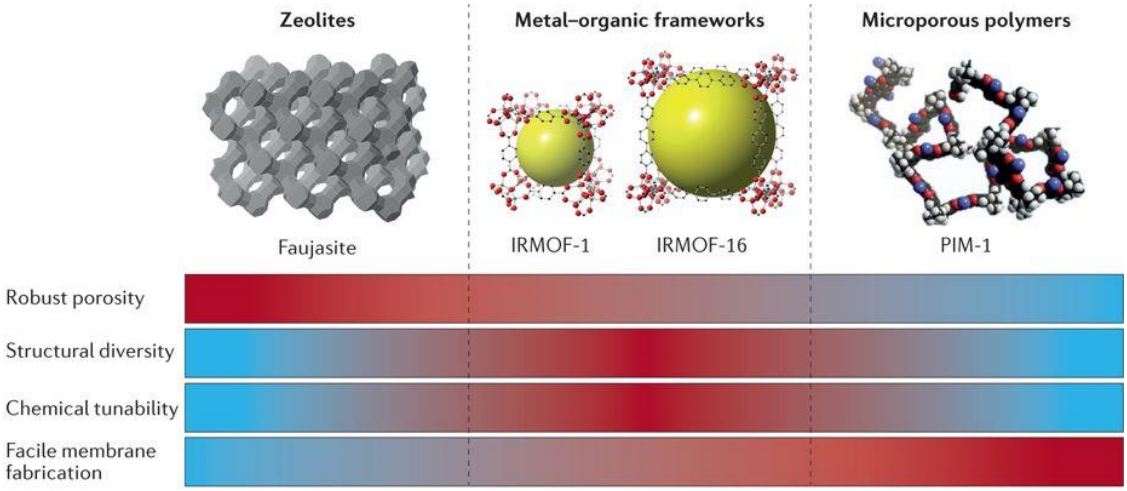

Figure 1.3. Comparison of properties of different microporous materials.[10]

1.2.1.1 Zeolitic Imidazolate Frameworks (ZIFs)

ZIFs, an important subclass of MOFs, have been reported to possess remarkable thermal and chemical stability among MOF materials which make them well-suited for potential industrial applications under harsh process conditions.[17-18] Like MOFs, these materials also allow the possibility of fine control over pore aperture, framework chemistry, surface area, and pore volume by judicious selection of appropriate linkers and synthesis conditions.[5, 19] Crucially, pore apertures of many ZIFs are similar to the dimensions of molecules relevant to many industrial separation processes (~5 Å), positioning them among MOFs as prime candidates for applications such as gas separations.[4-5, 19-23]

ZIFs consist of Zn or Co metal centers tetrahedrally coordinated to imidazole-derived organic linkers, with a metal-imidazole-metal bond angle similar to the Si-O-Si bond angle in zeolites.[19] These porous materials possess an inherently hydrophobic framework in the absence of hydrophilic functionalities with over 150 different synthesized ZIF structures reported (**Figure 1.4**).[5]

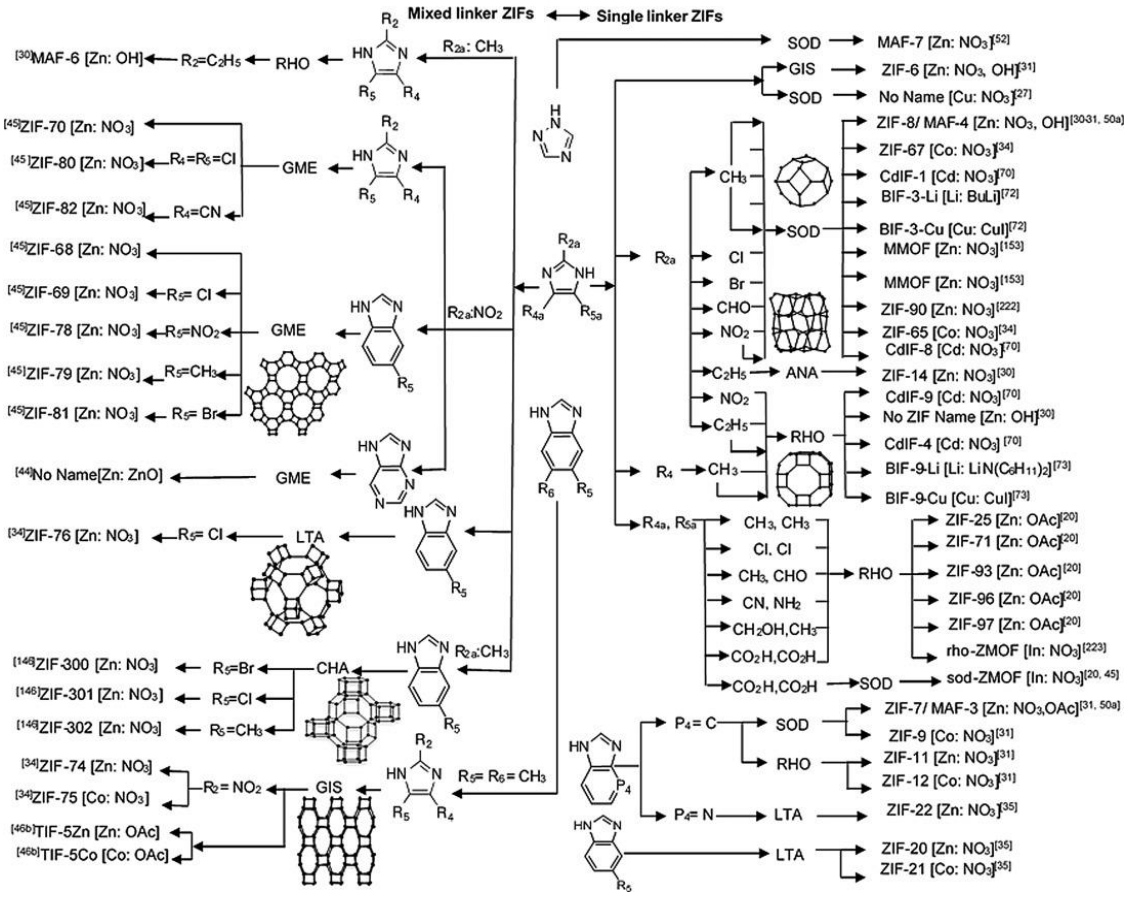

Figure 1.4. A summary of common single-linker and mixed-linker ZIFs classified based on their topology. References in the figure correspond to the numbering in the original publication.[5]

A distinguishing feature of many ZIF structures is their framework flexibility, where interaction between the ZIF framework and different adsorbates can induce molecular rearrangements, such as rotation of the imidazolate linkers, which lead to a crystallographic transition increasing the accessible pore size and volume, and therefore the adsorbate uptake.[24-26] This flexible nature of ZIFs implies that molecular sieving effects of the material are less effective than those of rigid zeolites, and is an important consideration for realistic adsorption and membrane applications. For example, ZIF-8 contains 2-methylimidazole linkers and has a 3.4 Å crystallographic pore aperture, but the effective pore aperture has been shown to be much larger, making it accessible to much larger molecules such as xylenes.[24, 26]

1.2.2 Applications of ZIFs in separation processes

Several studies have demonstrated the performance of ZIF materials as adsorbents or membranes in separation processes. Gas adsorption in coordinately saturated ZIF materials exhibit a weak dependence on metal-adsorbate interactions, attributed to steric effects due to insufficient space around the metal center.[27-28] A number of ZIFs have been studied as adsorbents for CO_2 capture from dry gas mixtures containing CO_2/N_2[29-31 32-35], CO_2/O_2[35], CO_2/CH_4[29-30, 35-37], and CO_2/CO[38-40]. Computational and experimental studies have demonstrated stronger interactions between the quadrupolar CO_2 molecule and polar linkers of ZIFs due to increased electrostatic forces.[29-30, 32, 35, 41] For chemically identical ZIFs, SOD topology materials with narrower pore apertures (close to the CO_2 kinetic diameter) interact with CO_2 more strongly at low adsorbate partial pressures than their structurally more open RHO topology counterparts.[33-34] Post-synthetic modification of ZIFs with amine containing groups can be an effective route to increasing adsorbent

affinity towards CO_2.[31] Accounting for dry flue gas conditions (14:86 composition of CO_2:N_2 at 1 bar) ZIFs can reach CO_2/N_2 selectivities of ~30, although the effect of competitive adsorption and material stability under high humidity and contaminants present in flue gases such as SO_2/NO_2 are not known.[5] Water adsorption isotherms of ZIF materials demonstrate their inherent framework hydrophobicity in the absence of polar functional groups, implying that a number of ZIFs are promising for separations involving water molecules.[21, 42-43] Hydrophobic ZIF-8 and ZIF-71 and hydrophilic ZIF-90 have been evaluated for separation of C1-C4 alcohols from aqueous solutions, and promising adsorptive selectivity for biobutanol separation was predicted for ZIF-8 and ZIF-71 from single component adsorption isotherms.[20-21, 44] ZIF-8 and ZIF-7 have been investigated as adsorbents for C2 and C3 olefin/paraffin separations for different hydrocarbon pairs and exhibit a small selectivity towards the saturated hydrocarbons over olefins, attributed to lack of open metal centers and charged surface groups.[45-47] However, slight differences in the sizes of C3 olefins and paraffins in ZIF-8 lead to significant differences in diffusivity of the two species, allowing for kinetic membrane based separations.[48-50] In addition, ZIFs have been evaluated as adsorbents for separation of C6 isomers[51-52], where they adsorb both the linear and mono-branched alkanes, and for xylene isomer separations[53], exhibiting a small para xylene selectivity.

A number of applications of ZIFs in membrane based separations have also been reported in literature. ZIF-8 can be effectively used in the separation of olefins from paraffins such as propylene/propane separation, both as an inorganic membrane material[50, 54-56] and as a mixed matrix membrane filler[57-58], on account of its strong diffusive selectivity towards the olefin. Propylene/propane selectivities >100 have been reported[50],

though membrane performance varies significantly depending on different synthesis protocols. ZIF-8 is less effective for diffusion selective ethylene/ethane separations as these smaller molecules are less hindered by the ZIF-8 pores in comparison with propylene or propane.[59-60] ZIF-8 has been utilized for H_2 purification from H_2/CO_2[61-64], H_2/N_2[61, 65] and H_2/CH_4[61-62, 65-66] mixtures, and have been reported to exceed the polymeric upper bound for these separations in a number of cases. Polymer-ZIF mixed matrix membranes have also been utilized for bioalcohol separations *via* pervaporation.[67-68] Mixed matrix membranes containing ZIF-8 as filler have also been evaluated for natural gas sweetening[58, 62, 65, 69] (CO_2/CH_4), and CO_2 capture from flue gases[70-72], reaching CO_2/N_2 selectivities ~20-30.[5] Apart from ZIF-8, other ZIFs such as ZIF-7, ZIF-90, and ZIF-69 have been evaluated for CO_2/CH_4 and CO_2/N_2 separations with promising results obtained for the smaller pore ZIF-7 material.[73-76]

ZIF materials constitute the majority among various MOFs investigated for gas separation membranes and the above non-exhaustive summary of the applications of ZIF materials in a variety of important separation processes gives a clear idea about their potential for large scale industrial implementation.[16] The next section of the thesis summarizes some of the major challenges that impede applications of MOF/ZIF materials in industrial separations.[6, 9, 11-12, 16]

1.2.3 Challenges of MOFs/ZIFs in separation processes

The large diversity of MOFs makes it challenging to identify materials among them best suited towards a specific separation process by experimental methods alone. In addition, the inherent flexibility of some MOFs/ZIFs requires determination of their

practical pore diameter cut-offs, which are different from the crystallographic pore diameter.[26] High throughput computational screening methods that accurately incorporate such varied material properties specific to each MOF/ZIF and predict their separation performance is critical to augment experimental research.[77-79]

Scaling up the solvothermal laboratory scale syntheses of MOFs/ZIFs to produce large volumes of high quality material is necessary to meet the requirements for their deployment in industry while lowering material production costs. Long reaction times (hours or days), prohibitive cost of linkers, high solvent consumption, and lower material quality on scale up are a few challenges associated with the large scale synthesis of MOFs/ZIFs. Efficient heating methods (microwave/ultrasonic radiation)[80] that reduce the reaction time, or continuous flow systems that can deliver high production yields[81-82] could mitigate such issues.

Formation of macroscopic or microscopic cracks on MOF/ZIF membranes can be induced by thermal stresses during cooling or drying of these brittle materials, severely affecting membrane performance.[10-11, 16] Improving the processability of these materials for membrane fabrication by ensuring good compatibility with support materials and minimizing inter-crystalline defect formation through innovative methods[49-50, 83-86] are essential to take these materials from the laboratory scale to commercialization.

Performance predictions for MOFs/ZIFs in separations are often inferred from single component adsorption/permeation tests which cannot capture the inherent complexities in real systems such as, competitive or cooperative effect of various components, including process impurities, on the separation performance. This leads to

poor estimates of material performance under realistic process conditions.[4] Industry-academia collaboration to establish proxy mixtures containing common components and trace impurities for specific separations are essential to address this concern.[87]

Finally, the industrial applicability of MOF/ZIF materials hinge on their long term stability under process conditions. Elevated process temperatures, exposure to humidity/water, as well as other impurities, even in trace concentrations, can have a detrimental effect on the material performance and restrict prolonged use. Many reports on separation applications utilizing adsorbents/membrane materials focus on performance metrics such as selectivity and capacity/permeability, but do not address this important issue of stability.[4, 88-91] For example, none of the reports on applications of ZIF materials as adsorbents or membranes for CO_2 capture from flue gases (CO_2/N_2) or natural gas sweetening (CO_2/CH_4) summarized in the previous section, evaluated the effects of high humidity, or the contaminants such as SO_2, NO_2 and H_2S that are present in such process streams.[5] Stability affects the material's functional lifetime and replacement costs associated with technology implementation and must be factored into the economic analysis of these technologies.

There will be little incentive to replace the capital intensive but highly reliable traditional separation units in operation today in the chemical industry, unless the above challenges and perceived risks associated with MOF/ZIF materials are addressed. In this thesis, I will focus on addressing the key issue of stability of ZIF materials towards acid gas species (specifically SO_2, NO_2, and CO_2) present in many chemical process streams, which are likely to have deleterious effects on the separation performance of these materials.[92-94]

1.3 Acid Gases

The term acid gas has often been used in the context of natural gas purification to refer specifically to the contaminants H_2S and CO_2.[95-96] However, the definition of an acid gas spans much wider and encompasses any gas or gaseous mixture which forms an acidic solution in the presence of water.[97-98] Some examples of acid gases commonly encountered in the chemical industry include CO_2, H_2S, NO_2, NO, and SO_2. Acid gases, often present in process streams containing water or humidity are highly corrosive, causing severe damage to process equipment and are often highly toxic, leading to significant health hazards. These considerations have led to regulations limiting their concentration in a marketed product or in atmospheric emissions from industries. For example, CO_2 content in crude natural gas has to be reduced at least to pipeline specifications (< 2% v/v)[99] for safe delivery at an acceptable heating value, while toxic H_2S content in the final treated natural gas must be limited to 4 ppm.[99] In this thesis, I will mainly focus on two major acid gases present in a variety of industrial process streams: SO_2 and NO_2.

The U.S. Environmental Protection Agency (EPA) is required by the Clean Air Act of the U.S. Government to set National Ambient Air Quality Standards (NAAQS) for 6 criteria air pollutants that have severe negative effects on human health, property and the environment: ground level ozone (O_3), particulate matter (PM), carbon monoxide (CO), lead (Pb), sulfur dioxide (SO_2) and nitrogen dioxide (NO_2).[100] Of these 6 criteria air pollutants, the acid gases SO_2 and NO_2 are considered particularly harmful as apart from their direct detrimental effects, these also lead to formation of the other criteria air pollutants through secondary reactions in the atmosphere.[92, 94] For example, atmospheric chemical reactions of SO_2 and NO_2 lead to the formation of PM, a complex mixture of

minute solid particles and liquid droplets in air, which can cause severe health hazards on inhalation.[94, 101] NO_2 reacts with different volatile organic compounds (VOCs) in the atmosphere in presence of sunlight to form ground level ozone, which is the main component of smog in urban areas around the world.[94, 102] In the next section, relevant properties of the two acid gases SO_2 and NO_2 along with their many negative effects on human health and environment are discussed.

1.3.1 Sulfur Dioxide

The sharp smelling colorless gas sulfur dioxide (SO_2) is the main constituent of the general class of pollutants termed sulfur oxides (SO_x). It is used industrially in the manufacture of sulfuric acid, as a food preservative due to its antimicrobial action, and in winemaking.[23] Anthropogenic SO_2 emissions account for ~99% of the SO_2 in the Earth's atmosphere while natural sources of SO_2 include volcanoes and hot springs.[103] Burning of fossil fuels for power generation in industrial facilities is the single largest source of SO_2 in air accounting for 87% of the SO_2 emissions in the U.S.[92, 94] Other industrial point sources of SO_2 emission include metal extraction from ores, cement manufacturing, thermal incineration, and petroleum refining. Mobile sources of SO_2 emissions such as burning of high S content fuel in the heavy transportation sector also contribute to anthropogenic SO_2 emissions.[104] SO_2 inhalation affects the human respiratory system causing coughing, wheezing, and shortness of breath apart from its indirect detrimental effects *via* formation of sulfate based PM.[103-104] SO_2 undergoes chemical transformations in humid atmosphere forming sulfuric acid (H_2SO_4), which gets deposited in the form of acid rain causing damage to foliage, sensitive ecosystems and building materials.[105-106] These toxic effects of SO_2 on human health have been recognized by the government and

resulted in regulations limiting SO_2 exposure in the workplace. The National Institute of Occupational Safety and Health (NIOSH) has defined the immediately dangerous to life or health (IDLH) limit of SO_2 exposure as 100 ppm while the Occupational Safety and Health Administration (OSHA) of the U.S. government has defined a 8 hour time-weighted average (TWA) value of 5 ppm as the permissible exposure limit (PEL) for SO_2 exposure in the workplace.[107] The recommended exposure limit (REL) by NIOSH is lower (~2 ppm average over 10 hours) with a maximum 15 minute short term exposure (ST) limit of 5 ppm.[107]

1.3.2 Nitrogen Dioxide

Nitrogen dioxide (NO_2) is a reddish-brown toxic gas with a sharp odor. Along with nitric oxide (NO), it forms the general class of pollutants termed as nitrogen oxides (NO_x). NO_2 is a free radical with an unpaired valence electron in its molecular structure, which makes it more reactive in comparison to SO_2. NO_2 is present in equilibrium with its dimer N_2O_4 in the gas phase with the equilibrium towards NO_2 favored at high temperatures or low concentrations with an equilibrium constant (K_p) of 0.143 atm at 298 K.[108-109] It is used industrially in nitric acid manufacturing, and as a nitrating and nitrosating agent. Natural sources of NO_2 production in the atmosphere include lightning and nitrification/denitrification processes by some plants and microbes.[110] However the majority of NO_2 emissions is anthropogenic, with burning of fossil fuels for power generation in industrial facilities responsible for 67% of NO_x emissions. Any combustion process generating sufficient heat can lead to the chemical combination of N_2 and O_2 to form NO_x.[111] Emissions from mobile transportation sources with internal combustion engines account for ~80% of NO_2 emissions in urban centers while other sources of NO_2

emissions include cement kilns, petroleum refining, thermal incinerators, process heaters, glass furnaces, municipal and hazardous solid waste combustion units etc.[110, 112] Direct NO_2 inhalation irritates the human respiratory system and aggravates ailments such as asthma, cough, flu, wheezing and bronchitis while its indirect effects include formation of other criteria air pollutants such as ground-level ozone and PM through secondary atmospheric reactions.[110, 112] In humid atmosphere, NO_2 transforms to nitric acid (HNO_3) and gets deposited as acid rain, causing damage to sensitive ecosystems.[106] These toxic effects of NO_2 on human health have resulted in regulations limiting workplace NO_2 exposure. OSHA has defined a 8 hour time-weighted average (TWA) ceiling value of 5 ppm as the permissible exposure limit (PEL) for NO_2 exposure in the workplace.[107] The recommended maximum 15 minute short term exposure (ST) limit for NO_2 by NIOSH is 1 ppm while its IDLH limit has been set at 20 ppm.[107]

1.3.3 Comparison with Carbon Dioxide

It is useful to compare the properties of the two acid gases SO_2 and NO_2 with CO_2, another common acid gas that is the focus of many separation processes (**Table 1.1**) such as natural gas sweetening and post-combustion CO_2 capture. While CO_2 is a linear non-polar molecule (no dipole moment), both SO_2 and NO_2 are v-shaped bent structures with permanent dipole moment.[113] SO_2 has the highest dipole moment and polarizability among these three acid gases and is also the most water soluble. The solubility of the NO_2 molecule in water is the smallest, but it has been reported that dissolution of NO_2 in water occurs through its dimer N_2O_4 which is more soluble than SO_2.[114] Additionally, it is evident from the permissible exposure limits set by OSHA that both NO_2 and SO_2 are significantly more toxic than CO_2.[115] In summary, polar SO_2 and NO_2 molecules are expected to interact more

strongly with ZIFs than CO_2 resulting in a higher susceptibility of ZIF degradation on exposure to these two acid gases.[12]

Table 1.1. Comparison of the properties of SO_2, NO_2, and CO_2

Property	**SO_2**	**NO_2**	**CO_2**
Molecular Weight	64.1	46	44
Bond Length (Å)[113]	1.432	1.193	1.162
Bond Angle (°)[113]	119.5	134.1	180
Boiling Point (K)	263	294	sublimes
PEL (ppm)[107]	5	5	5000
REL (ppm)[107]	2	1	5000
IDLH (ppm)[115]	100	20	40000
Dipole Moment (Debye)[114]	1.63	0.316	0
Polarizability($Å^3$)[114]	3.882	2.91	2.507
Henry's Constant[113] ($mol.kg^{-1}.bar^{-1}$)#	1.25	0.0225	0.034

Henry's coefficients for aqueous solutions averaged over all NIST data

1.3.4 Present Industrial Technologies for Acid Gas Capture

Stringent regulations limit atmospheric emissions of corrosive, toxic acid gases SO_2 and NO_2 from electric power plants, which are major point sources of their generation. The established technology for removal of SO_2 in industry is wet flue gas desulfurization

(WFGD) which utilizes a calcium or sodium based alkaline reagent (usually lime or limestone) to oxidize SO_2 into either calcium or sodium sulfate at temperatures of 150-370 °C.[92, 116] Despite high conversion efficiency, the WFGD process suffers from disadvantages such as high capital cost, equipment complexity, large water consumption and space requirement, scaling and deposition of the wet reaction products that may result in a visible plume. SO_2 removal may also be accomplished by the less efficient Dry Sorbent Injection (DSI) process which injects powdered sorbent directly into the furnace at high temperatures (950-1000° C).[92, 116] These SO_2 removal technologies have been applied to stationary coal and oil fired combustion units, municipal and medical waste incinerators, cement and lime kilns, metal smelters, petroleum refineries, glass furnaces and sulfuric acid manufacturing.[116]

Removal of high concentration NO_x is usually carried out in industry by the selective catalytic reduction process (SCR), in which NO_x is chemically reduced to nitrogen and water using a reducing agent such as ammonia or urea over a selective catalyst (usually V_2O_5) at temperatures ranging from 250-430 °C.[92, 94, 117-118] This established NO_x removal process is energy intensive and has a high cost of operation due to the large volume of catalyst and reagent (usually NH_3) required. Deactivation of catalyst can occur through poisoning or high temperature sintering while unreacted NH_3 (ammonia slip) can result in downstream equipment corrosion and ash contamination.[92, 119] Industrial NO_x removal can also accomplished by the lower efficiency selective non-catalytic reduction (SNCR) process in which the above chemical reduction to nitrogen occurs without using the catalyst at elevated temperatures (800-1100 °C).[92, 120] These NO_x removal technologies have been applied to stationary fossil fuel combustion units such as electrical utility boilers and

industrial boilers, process heaters, gas turbines, reciprocating internal combustion engines, nitric acid manufacturing plants, thermal incinerators, municipal and hazardous solid waste combustion units, cement kilns and glass furnaces.[120-121]

In addition, high efficiency for CO_2 removal from gas streams has been demonstrated through absorption technologies utilizing aqueous amine solutions (monoethanolamine, diethanolamine etc.).[122] This technology also has significant drawbacks resulting from the corrosive property of liquid amines, loss of amines during the absorption and a high energy penalty to regenerate the amines due to the chemisorptive amine-CO_2 interactions.[122] These three acid gases (SO_2, NO_2, and CO_2) are often present together in industrial process streams generated from combustion of carbonaceous fuels. For example, flue gas from a typical coal fired power plant contains around 13-15% CO_2, along with tens to hundreds of ppm SO_2 and NO_2 saturated with water vapor and excess oxygen.[123]

For material based separations to be effective competitors to one or more of these established technologies for acid gas removal (*eg*. post combustion CO_2 capture) or function efficiently towards a different separation target in the presence of acid gases (*eg.* biobutanol separations), their long-term stability to acid gases must be demonstrated under realistic process conditions.

1.4 Stability of MOFs

It is important to first define the stability of a crystalline porous MOF in the context of separation applications. The stability of such a material can be defined in terms of the extent to which it retains (1) its porous crystal structure, (2) internal surface area, and (3)

the target separation function upon exposure to the species under investigation at the exposure conditions of interest (temperature, humidity, concentration). A 'more stable' material will be able to retain these characteristics for longer exposure times and/or higher exposure levels in comparison to a 'less stable' one.

1.4.1 Factors affecting MOF stability

The chemical stability of a MOF towards a specific attacking species can arise from either thermodynamic or kinetic considerations. A number of factors have been linked to MOF/ZIF stability in literature, mostly in the context of water exposure.[88, 91, 124-128] These stability indicators can be expected to be applicable for comparing the chemical stability of different ZIFs to acid gases and are summarized below.

1.4.1.1 Thermodynamic Factors

Coordination bonds between the inorganic nodes and the organic linkers are key to the rich variety and tunability of MOF structures and distinguish it from other porous materials such as zeolites and activated carbons. Unfortunately, these relatively labile coordination bonds are believed to be the major factor contributing to the challenges associated with MOF stability.[88, 125-126] The strength of a MOF's coordination bond therefore determines its thermodynamic stability under different operating environments and various stability indicators have been used as predictors of this bond strength in literature.

MOFs form by association of cations and negatively charged (deprotonated) linkers. Hence, a higher basicity of the deprotonated linker (*i.e.* its ability to donate

electrons and form coordination bonds) is an indicator of a more stable MOF. According to the Lewis acid-base coordination theory, the conjugated base of a weaker acid (*i.e.*, a protonated MOF linker with a lower K_a) has a higher basicity than the conjugated base of a stronger acid. Therefore, linker pK_a (i.e., its relative ease of protonation) can be an effective indicator of the MOF coordination bond strength, and a higher value is correlated with greater thermodynamic stability.[88, 127, 129] In this thesis, linker pK_a is expected to be particularly insightful in the context of the relative stability of ZIFs, as the inorganic nodes (Zn^{2+}) across these materials are identical. In addition to linker pK_a, a higher electron density (more negative charge) on the coordinating atom of the MOF linker has also been correlated with a more stable coordination bond.[127]

Properties of the metal centers constituting the inorganic node of MOF materials have also been correlated with their thermodynamic stability. Higher charge density on the metal cation has been associated with a higher strength of the coordination bond. Therefore high-valent metal ions (such as group IV metals) with high oxidation states have been correlated with strong coordination bonds and stable MOFs.[88, 125, 128, 130-131] Since in this thesis, all the ZIFs investigated have the same Zn^{2+} metal center, this factor will have no effect on any observed relative stability differences.

Lewis acids and bases can be classified as hard or soft on the basis of their polarizabilities (ratio of the induced dipole moment to the externally applied electric field).[132] According to Pearson's hard/soft acid/base (HSAB) principle[126, 132], hard and soft acids bind strongly to hard and soft bases respectively. In the case of MOFs, similar polarizability of the linker and the metal center has been associated with a stronger binding coordination complex.[88, 126, 132] Therefore, coordination between hard acids (eg. high-valent

metal ions) and hard bases (eg. carboxylates) or, soft acids (eg. low-valent metal ions) and soft bases (eg. imidazolates) has been associated with greater MOF stability (**Figure 1.5**).[126] ZIFs, constituted by coordination between soft acids and bases, can be classified as stable MOFs according to the HSAB principle.

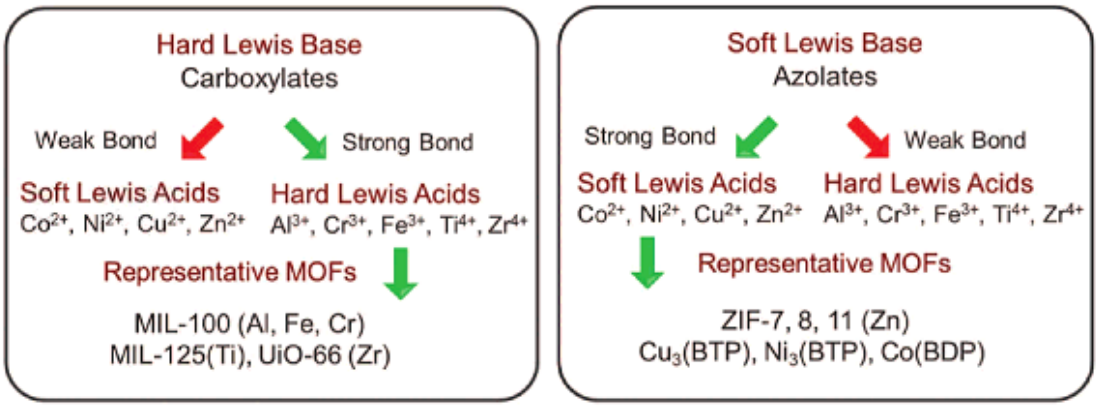

Figure 1.5. Stable MOF construction strategy based on HSAB principle.[126]

1.4.1.2 Kinetic Factors

In addition to the coordination bond strength which determines the thermodynamic stability of MOFs, kinetic factors also influence its overall stability. For any degradation reaction to proceed, regardless of the reaction thermodynamics, the attacking species must first be able to come sufficiently close to, and interact with, the MOF's metal center.

A high connectivity of the inorganic nodes (higher metal coordination number) has been correlated with increased MOF stability.[88, 91, 124-128] A highly coordinated MOF leads to a dense, rigid structure with a high activation energy barrier for its dissociation reaction. This is attributed to steric effects that prevent easy approach of attacking molecules towards

the metal center. In addition, a high metal coordination number is associated with a greater structural tolerance of the MOF towards the attacking species before complete lattice collapse.[88, 133]

The organic linker can also alter the activation energy barrier for MOF degradation through its rigidity. The robustness of a MOF framework has been correlated with a short linker length and high linker rigidity.[134] Coordinated organic linkers are required to be bent in transition states of the MOF degradation/substitution reaction and their rigidity can raise the activation energy barrier for this process.[126, 133]

Hydrophobicity of the linker has been correlated with MOF stability under humidity or water exposure.[88, 124-126] Hydrophobic linkers prevent access of the water molecules to the reaction sites inside MOF pores by limiting the water adsorbed by the MOF and/or by shielding the MOF metal center from any adsorbed water. However, while ZIFs cannot be expected to be stable to acid gases under dry conditions due to linker hydrophobicity alone, it could play a significant role under humid acid gas attack if the degradation reaction is aided by water co-adsorption or dissolution within the ZIF pores. Additionally, if specific ZIF linkers minimize the adsorption of the acid gas into the porous structure (analogous to a hydrophobic linker's water adsorption capacity), the concentration of the attacking species could be contained, substantially reducing the reaction rate. This however, will not be useful if the aim of the separation process is to maximize the acid gas adsorption using a stable ZIF.

1.4.2 Stability of ZIFs to acid gases

Given the worldwide efforts to develop new membranes, adsorbents, and catalysts based upon nanoporous materials, their stability in acid gas environments is an increasingly important issue. A number of ZIFs have been reported to be resistant to steam for hours and for a week in boiling water based upon powder X-ray diffraction (PXRD) patterns.[17, 24, 128, 135] ZIFs have also exhibited high thermodynamic stability among MOFs; for example, ZIF-8 can withstand temperatures of 300 °C under inert atmosphere for over 24 hours.[18] A number of practical applications (*e.g.*, CO_2 capture from flue gas, landfill gas separation, natural gas sweetening, biobutanol recovery, hydrocarbon separations) involve complex mixtures of molecules including acid gas species (*e.g.*, CO_2, SO_x, NO_x, H_2S) which can lead to irreversible structural changes in ZIFs and have a detrimental effect on their separation performance. The limited literature on ZIF stability to acid gases prior to this thesis work is summarized in this section. Recent computational work on ZIF stability by my collaborators, whose results are consistent with the conclusions of this thesis, has been summarized in Chapter 7.

Mottillo *et al.* reported the degradation of ZIF-8 based upon changes in PXRD patterns in a CO_2 environment under 100% relative humidity (R.H.) at 45 °C after 12 days of exposure.[136] This degradation did not take place under air or an inert environment, thus suggesting the importance of the combined role of CO_2 (a weak acid gas) and water. A study of ZIF-8 stability under acidic and basic aqueous environments has recently been reported.[137] It was shown that ZIF-8 was stable for 3 days in strongly basic (*p*H 12) and weakly acidic (*p*H 4) solutions at room temperature, but not in a strongly acidic (*p*H 0) solution. However, after continued exposure for 2 months, changes in the PXRD patterns

and loss of surface areas are observed even at *p*H 12 and *p*H 4. A study of ZIF-8 stability in aqueous acids has also been reported where, the material was reported to maintain its pore volume and bulk crystal structure on mild aqueous SO_2 exposure, although its surface was seen to etch away preferentially along the (110) facet.[138] Water insertion into the Zn-imidazole bond was hypothesized as the reaction mechanism. The effect of humidity, and the combined effect of SO_2 and NO_2 exposure on the adsorption properties of ZIF-8, ZIF-7 and ZIF-90 along with other MOFs was investigated recently.[139] Exposure to 15 ppm of SO_2 was followed by a 10 ppm NO_2 exposure for 2 days, each at 80% R.H. before characterization, so the detrimental impact of the two acid gases could not be individually distinguished. The combined acid gas exposure reduced the CO_2 and N_2 uptake for all adsorbents with significant changes observed in the PXRD pattern of ZIF-90 post the combined acid gas exposure.[139] This remains the only experimental study on the stability of ZIFs with SO_2 and NO_2 gases to the best of my knowledge. Grand canonical Monte Carlo (GCMC) simulations of SO_2 and CO_2 adsorption in ZIFs revealed a cooperative effect on the adsorption of these two molecules under dry conditions.[140] A significant decrease in CO_2 capacity was observed only in hydrophilic ZIFs in the presence of water in this study. However equilibrium adsorption simulations of SO_2 in presence of water *via* GCMC methods cannot account for the effects of any reactive species that may form during the exposure by the synergistic action of humidity and SO_2.

1.4.3 Stability of MOFs towards SO_2 and NO_2

Given the paucity of published literature on ZIF stability to the acid gases SO_2 and NO_2, I have also summarized the present literature on the stability of MOF materials to the acid gases SO_2 and NO_2 in this following section.[22-23, 92] This section does not contain

recent work by my collaborators on MOF stability conducted during the time frame of this thesis, which I have summarized in Chapter 7.

1.4.3.1 Literature review on MOF Stability to SO_2

A limited number of experimental and computational investigations have been carried out to probe the interactions of the acid gas SO_2 on MOF materials.[22-23, 92, 94, 140-145] Binding enthalpy of SO_2 has been reported to be higher than H_2O and CO_2 in different M-MOF-74s (M=metal site) using DFT simulations[141] and the coordinately unsaturated MOFs Cu-BTC and Mg-MOF-74 were reported to be most efficient for SO_x and NO_x removal from dry flue gases in an independent computational study using GCMC simulations.[94] However, Cu-BTC and Mg-MOF-74 are both unstable in the presence of humidity which hinders their practical applications in acid gas capture.[146-147] In a computational investigation of MOF stability to flue gas contaminants using DFT, hydrates of SO_2 (formed under humid conditions) and to a lesser extent, dry SO_2, SO_3 and hydrates of NO_x were reported to irreversibly chemisorb on MOFs with open metal sites such as Mg-MOF-74 and MIL-101(Cr).[142] Strong chemisorptive interactions by acid gas species, including those formed *in situ* by the action of SO_x/NO_x with humidity, can result in irreversible damage to the MOF structure on reactivation.

In multiple experimental studies on MOF materials (MFM-300 (In/Al), M(bdc))ted)$^{0.5}$,[M=Zn, Ni]), dry SO_2 gas has been reported to weakly interact with O atoms in the MOFs *via* its S atom and form hydrogen bonds with aromatic and aliphatic C-H and O-H groups of the MOFs at ambient temperature, with regeneration of the porous MOF structures reported on reactivation.[148-150] Crystal structure retention post exposure to dry SO_2 up to 2 bar is also observed in fluorinated FMOF-2 at room temperature, consistent

with physisorptive interactions.[151] Experimental investigations on different variants of the MOF-74 series reveal high SO_2 removal capacity under dry conditions at 298 K which decrease in presence of humidity (80% R.H.), but their structural stability pre and post exposure to SO_2 was not reported.[152-153] Experimental breakthrough studies have reported insignificant SO_2 removal capacity of Cu-BTC at 293 K while Cu-BTC impregnated with barium salts react with dry SO_2 at elevated temperatures (473 K) forming sulfates.[154-155]

1.4.3.2 Literature review on MOF Stability to NO_2

Few reports exist on the stability of MOFs in general to dry or humid NO_2 gas.[22-23] Cu-BTC was reported to be the best performing MOF based on selectivity and working capacity for NO_x removal from dry flue gases in a simulation based screening study of potential MOFs.[94] Mg-MOF-74 was reported to be the most promising MOF for the simultaneous removal of CO_2, NO_x and SO_2 from the dry flue gas mixture in the same study with electrostatic interactions between polar acid gases and partial positive charges on these open metal site MOF atoms leading to preferred adsorption.[156] However, both Cu-BTC and Mg-MOF-74 are unstable under humid conditions and these MOFs cannot be implemented in real world applications of acid gas capture and storage.[146-147] In fact, NO_2 adsorption under both dry and humid conditions (70% R.H.) led to significant degradation of Cu-BTC and Cu-BTC/Graphite Oxide composites.[119, 157] Formation of nitrates bound to Cu and the release of NO on the reactive adsorption of NO_2 on Cu was proposed as the reaction mechanism for this degradation under dry conditions. The coordinately saturated MOF UiO-66 has also been investigated for its NO_2 adsorption and removal performance by several researchers.[158-161] UiO-66 was reported to retain its surface area on humid NO_2 exposure (71% R.H. and 1000 ppm NO_2) but degraded on dry NO_2 exposure while the

more hydrophilic UiO-67 degraded both under dry and moist conditions.[160] Incorporation of urea and melamine into UiO-66 or UiO-67 to create amine groups resulted in higher NO_2 adsorption but the porous materials were severely degraded under both dry and moist NO_2 exposures.[159] Incorporation of oxalic acid groups to create UiO-66 with missing linkers doubled its dry NO_2 adsorption capacity but PXRD patterns post exposure showed significant changes indicating framework degradation.[158] More recently, UiO-66-NH_2 was evaluated for NO_2 adsorption under dry and moist conditions (80% R.H.) and was reported to have a higher adsorption capacity than activated carbon.[161] X-ray photoelectron spectroscopy (XPS) patterns indicated nitrate formation under both exposure conditions with a marginal decrease in the surface area.

A number of studies conducted on the adsorption performance of MOFs to these acid gases do not report the stability of these materials towards the adsorbates.[152-153] Defining stability of porous materials in a practical quantitative manner that is applicable to all and establishing a protocol by consensus to investigate this important performance metric is crucial to the practical applicability of MOFs and ZIFs in separation processes.

1.5 Assessing ZIF Stability

In this thesis, I have used the following criteria and methods to determine the structural and functional stability of ZIF materials along with mechanistic details of their acid gas interaction:

1.5.1 Structural Stability

1) The effect of acid gas interaction on material crystallinity was investigated using **powder X-ray diffraction** (**PXRD**). PXRD patterns of crystalline ZIF materials

were measured pre and post exposure to acid gas species under dry and/or humid conditions and compared for changes in peak intensities and appearance of new peaks. For better visualization of subtle changes, PXRD patterns were normalized with respect to the highest intensity peak.

2) MOFs with unchanged PXRD patterns can exhibit significant losses in their surface area and porosity.[88, 147] The Brunauer-Emmett-Teller (BET) surface area and pore volume of porous ZIFs were measured and compared pre and post exposure using **nitrogen physisorption (NP)** at 77 K. For ZIFs with narrow pores impermeable to N_2 (*eg.* ZIF-7), CO_2 was used as the probe molecule to investigate ZIF porosity by comparing its adsorption isotherms measured at 273 K. A ZIF was defined to exhibit "bulk stability" in this thesis if it maintained its PXRD pattern and retained its pore volume on acid gas exposure to at least 90% of the initial value.
3) Visualization of ZIF crystal surfaces pre and post exposure to acid gases was carried out in select cases *via* **scanning electron microscopy (SEM)** to compare effects of the exposure on the crystal morphology. Surface cracks or fractures may form locally on exposure, or in some cases, materials can undergo phase transformations on exposure to attacking species, with visible changes in morphology.

1.5.2 Functional Stability

1) The functional stability of a ZIF is the extent to which its performance towards a target separation function is retained post acid gas exposure. This can be achieved by comparing the target process selectivity or the adsorption capacity/permeability of a relevant probe molecule before and after acid gas exposure.[139] For example,

with the biobutanol separation process as a target application, **butanol adsorption isotherms** in selected ZIFs were measured pre and post acid gas exposure in this thesis in Chapter 2. The effect of the acid gas (CO_2) on the functional stability of selected ZIFs was quantified through the change in the **butanol saturation loading** of those materials.

It is important to note that while the above criteria are useful to define and determine stability, they provide no mechanistic information about interactions of the ZIF with acid gases that lead to such structural and functional changes. For mechanistic investigations, additional characterizations were done as follows:

1.5.3 Stability Mechanisms

1) *Ex situ* **Fourier Transform Infrared Spectroscopy (FTIR)** was utilized as an important tool to provide information on the vibrational modes corresponding to bond formation or breakage in ZIFs on acid gas exposure. Peak assignments in the FTIR spectra after acid gas exposure were guided by reported literature. *In situ* IR spectroscopy was also utilized in this thesis, to visualize temporal changes in the FTIR pattern on ZIF exposure to the acid gas NO_2 in Chapter 5. The temporal evolution of new peaks in this method was visualized in the form of a difference spectra, obtained by subtracting the spectra at each time from the initial spectrum.
2) **Energy dispersive X-Ray spectroscopy (EDX)** can be utilized to probe the elemental composition of ZIFs pre and post acid gas exposure. Since pristine ZIFs contain no S atoms, this characterization tool was especially useful to probe ZIF degradation mediated by the acid gas SO_2 in this thesis. Residual S detected by EDX

in a partially degraded ZIF on SO_2 exposure can be directly correlated to defect site creation, allowing a detailed study of the acid gas reaction kinetics.

3) **X-ray photoelectron spectroscopy (XPS)** can give important information about the chemical bonding environment near the surface (~10 nm depth) of a material. This characterization tool was utilized in select cases in this thesis to probe reaction mechanisms of ZIFs with acid gases.

In conclusion, PXRD and BET surface area measurements are mandatory characterization tests to evaluate a crystalline porous ZIF's "bulk stability". These characterization methods must be combined with FTIR, EDX etc. to gain more insight on the mechanisms of the acid gas attack process.

1.6 Thesis Objectives

Applicability of ZIF materials as adsorbents and membranes in chemical separation processes hinges on a better fundamental understanding of their stability under process conditions. Acid gases are present in many process streams where the potential use of ZIF materials are envisioned, but little or no information exists on their effect on the stability of these materials, impeding practical applications. The overall goal of this thesis is therefore to systematically investigate the effects of various acid gases (CO_2, SO_2, and NO_2) on the stability of ZIF materials under different conditions of interest and aid in their practical applications in separation processes.

The observations and findings of this thesis are relevant to all separation processes containing one or more of the acid gases CO_2, SO_2 and NO_2 in which the use of ZIF materials are being considered. The fundamental knowledge generated in this thesis will

help create a better understanding of the behavior of ZIFs towards acid gases and aid in the design of robust and functional materials for chemical separations. The objectives of my research presented in this thesis are as follows:

Objective 1: Establish a general framework for systematic investigation of acid gas stability of ZIFs, with particular focus on the underlying mechanistic routes of ZIF degradation, specific to each acid gas

This thesis establishes a general set of characterization tools, to probe the bulk stability of all ZIF materials to different acid gases, which have been summarized in Section 1.7 of this Chapter. Successful applicability of this toolkit, towards probing ZIF stability is demonstrated across Chapters 2-6. ZIF materials may be destabilized by their interactions with dry acid gases alone or due to the synergistic action of acid gases and water in the presence of humidity. Such reactions may proceed *via* different homogeneous or heterogeneous routes depending on the specific acid gas and the ZIF material. This thesis places particular importance on evaluating mechanistic insights into ZIF-acid gas interactions, aided by present literature on specific acid gas reaction pathways in the presence or absence of water. In each Chapter of this thesis, I explain the likely reaction pathway(s) of ZIF materials with specific acid gases which not only expands the overall knowledge base on ZIF-acid gas interactions but also provides valuable insights into the intelligent design of robust ZIF materials in future.

Objective 2: Create an extensive information database on the stability of different ZIF materials to acid gas species for their immediate selection and application in separation processes

A major hurdle to widespread applicability of ZIF materials in industrial separations is limited knowledge about their stability under different process conditions. A major aim of this thesis is to augment available information on ZIF stability towards dry and humid acid gases (SO_2, and CO_2), along with liquid water and humid air by documenting observations for a library of 16 different ZIF materials with varied functionalities and topologies. An important feature of this thesis is therefore the stability chart (Chapter 4), which will allow researchers to choose ZIF materials that are robust under their particular application process condition for further investigation. Characteristic ZIFs from this chart were further selected to probe stability towards the acid gas NO_2 in Chapter 5. The large dataset of diverse materials investigated allows applicability of the observations of this thesis to a broader class of porous materials.

Objective 3: Develop a quantitative approach to the ZIF degradation process from fundamental knowledge, allowing predictions of material stability in acid gas environments

A focus of this thesis is to go beyond reporting of ZIF stability observations with respect to various acid gases, by comparing quantitatively the relative stability of different ZIF materials on acid gas exposure. This is accomplished in this thesis by measuring the reaction kinetics for the acid gas (SO_2) induced degradation process for various ZIF materials (Chapter 4). Deducing the degradation reaction rate constants for each ZIF allows statistical correlations of the observed rate with multiple characteristic material properties revealing exciting new information about the factors affecting the acid gas stability of ZIFs (Chapter 4). The influence of this degradation rate constant on external factors such as

relative humidity is also explored in Chapter 6, leading to the development of the first predictive model of the durability of any ZIF material towards an acid gas over long time scales.

REFERENCES

1. Department of Energy, U. S., Energy Flow Charts. Laboratory, L. L. N., Ed. https://flowcharts.llnl.gov/content/assets/images/charts/Energy/Energy_2017_United-States.png, 2018.

2. Energy Information Adminitration, U. S., Annual Energy Outlook 2018. https://www.eia.gov/outlooks/aeo/pdf/AEO2018.pdf, 2018.

3. Laboratory, O. R. N., Materials for Separation Technologies: Energy and Emission Reduction Opportunities https://www1.eere.energy.gov/manufacturing/industries_technologies/imf/pdfs/separationsreport.pdf, 2005.

4. Sholl, D. S.; Lively, R. P., Seven chemical separations to change the world. *Nature* **2016,** *532* (7600), 435-437.

5. Pimentel, B. R.; Parulkar, A.; Zhou, E.-k.; Brunelli, N. A.; Lively, R. P., Zeolitic Imidazolate Frameworks: Next-Generation Materials for Energy-Efficient Gas Separations. *Chemsuschem* **2014,** *7* (12), 3202-3240.

6. Koros, W. J.; Zhang, C., Materials for next-generation molecularly selective synthetic membranes. *Nat. Mater.* **2017,** *16*, 289.

7. Robeson, L. M., Correlation of separation factor versus permeability for polymeric membranes. *J. Membr. Sci.* **1991,** *62* (2), 165-185.

8. Robeson, L. M., The upper bound revisited. *J. Membr. Sci.* **2008,** *320* (1), 390-400.

9. Adatoz, E.; Avci, A. K.; Keskin, S., Opportunities and challenges of MOF-based membranes in gas separations. *Sep. Purif. Technol.* **2015,** *152*, 207-237.

10. Denny, M. S.; Moreton, J. C.; Benz, L.; Cohen, S. M., Metal-organic frameworks for membrane-based separations. *Nat. Rev. Mater.* **2016,** *1* (12), 17.

11. Duan, J. G.; Pan, Y. C.; Liu, G. P.; Jin, W. Q., Metal-organic framework adsorbents and membranes for separation applications. *Curr. Opin. Chem. Eng.* **2018,** *20*, 122-131.

12. Hendon, C. H.; Rieth, A. J.; Korzynski, M. D.; Dinca, M., Grand Challenges and Future Opportunities for Metal-Organic Frameworks. *ACS Central Sci.* **2017,** *3* (6), 554-563.

13. Farha, O. K.; Eryazici, I.; Jeong, N. C.; Hauser, B. G.; Wilmer, C. E.; Sarjeant, A. A.; Snurr, R. Q.; Nguyen, S. T.; Yazaydın, A. Ö.; Hupp, J. T., Metal–Organic Framework Materials with Ultrahigh Surface Areas: Is the Sky the Limit? *J.Am.Chem.Soc.* **2012,** *134* (36), 15016-15021.

14. Wilmer, C. E.; Leaf, M.; Lee, C. Y.; Farha, O. K.; Hauser, B. G.; Hupp, J. T.; Snurr, R. Q., Large-scale screening of hypothetical metal–organic frameworks. *Nat. Chem.* **2011,** *4*, 83.

15. Jhung, S. H.; Khan, N. A.; Hasan, Z., Analogous porous metal–organic frameworks: synthesis, stability and application in adsorption. *Crystengcomm* **2012,** *14* (21), 7099-7109.

16. Shah, M.; McCarthy, M. C.; Sachdeva, S.; Lee, A. K.; Jeong, H. K., Current Status of Metal-Organic Framework Membranes for Gas Separations: Promises and Challenges. *Ind. Eng. Chem. Res.* **2012,** *51* (5), 2179-2199.

17. Park, K. S.; Ni, Z.; Cote, A. P.; Choi, J. Y.; Huang, R. D.; Uribe-Romo, F. J.; Chae, H. K.; O'Keeffe, M.; Yaghi, O. M., Exceptional chemical and thermal stability of zeolitic imidazolate frameworks. *Proc. Natl. Acad. Sci. U. S. A.* **2006,** *103* (27), 10186-10191.

18. Yin, H.; Kim, H.; Choi, J.; Yip, A. C. K., Thermal stability of ZIF-8 under oxidative and inert environments: A practical perspective on using ZIF-8 as a catalyst support. *Chem. Eng. J.* **2015,** *278*, 293-300.

19. Phan, A.; Doonan, C. J.; Uribe-Romo, F. J.; Knobler, C. B.; O'Keeffe, M.; Yaghi, O. M., Synthesis, Structure, and Carbon Dioxide Capture Properties of Zeolitic Imidazolate Frameworks. *Acc. Chem. Res.* **2010,** *43* (1), 58-67.

20. Gee, J. A.; Chung, J.; Nair, S.; Sholl, D. S., Adsorption and Diffusion of Small Alcohols in Zeolitic Imidazolate Frameworks ZIF-8 and ZIF-90. *J. Phys. Chem. C* **2013,** *117* (6), 3169-3176.

21. Zhang, K.; Lively, R. P.; Dose, M. E.; Brown, A. J.; Zhang, C.; Chung, J.; Nair, S.; Koros, W. J.; Chance, R. R., Alcohol and water adsorption in zeolitic imidazolate frameworks. *Chem. Commun.* **2013,** *49* (31), 3245-3247.

22. Bobbitt, N. S.; Mendonca, M. L.; Howarth, A. J.; Islamoglu, T.; Hupp, J. T.; Farha, O. K.; Snurr, R. Q., Metal-organic frameworks for the removal of toxic industrial chemicals and chemical warfare agents. *Chem. Soc. Rev.* **2017,** *46* (11), 3357-3385.

23. DeCoste, J. B.; Peterson, G. W., Metal–Organic Frameworks for Air Purification of Toxic Chemicals. *Chem. Rev.* **2014,** *114* (11), 5695-5727.

24. Zhang, K.; Lively, R. P.; Zhang, C.; Chance, R. R.; Koros, W. J.; Sholl, D. S.; Nair, S., Exploring the Framework Hydrophobicity and Flexibility of ZIF-8: From Biofuel Recovery to Hydrocarbon Separations. *J.Phys.Chem.Lett.* **2013,** *4* (21), 3618-3622.

25. Zhao, P.; Lampronti, G. I.; Lloyd, G. O.; Wharmby, M. T.; Facq, S.; Cheetham, A. K.; Redfern, S. A. T., Phase Transitions in Zeolitic Imidazolate Framework 7: The Importance of Framework Flexibility and Guest-Induced Instability. *Chem. Mater.* **2014,** *26* (5), 1767-1769.

26. Zhang, C.; Lively, R. P.; Zhang, K.; Johnson, J. R.; Karvan, O.; Koros, W. J., Unexpected Molecular Sieving Properties of Zeolitic Imidazolate Framework-8. *J.Phys.Chem.Lett.* **2012,** *3* (16), 2130-2134.

27. Peralta, D.; Chaplais, G.; Simon-Masseron, A.; Barthelet, K.; Pirngruber, G. D., Synthesis and adsorption properties of ZIF-76 isomorphs. *Microporous Mesoporous Mater.* **2012,** *153*, 1-7.

28. Zhou, M.; Wang, Q.; Zhang, L.; Liu, Y.-C.; Kang, Y., Adsorption Sites of Hydrogen in Zeolitic Imidazolate Frameworks. *J. Phys. Chem. B* **2009,** *113* (32), 11049-11053.

29. Amrouche, H.; Aguado, S.; Pérez-Pellitero, J.; Chizallet, C.; Siperstein, F.; Farrusseng, D.; Bats, N.; Nieto-Draghi, C., Experimental and Computational Study of Functionality Impact on Sodalite–Zeolitic Imidazolate Frameworks for CO_2 Separation. *J. Phys. Chem. C* **2011,** *115* (33), 16425-16432.

30. Liu, B.; Smit, B., Molecular Simulation Studies of Separation of CO_2/N_2, CO_2/CH_4, and CH_4/N_2 by ZIFs. *J. Phys. Chem. C* **2010,** *114* (18), 8515-8522.

31. Thompson, J. A.; Brunelli, N. A.; Lively, R. P.; Johnson, J. R.; Jones, C. W.; Nair, S., Tunable CO_2 Adsorbents by Mixed-Linker Synthesis and Postsynthetic Modification of Zeolitic Imidazolate Frameworks. *J. Phys. Chem. C* **2013,** *117* (16), 8198-8207.

32. Morris, W.; Leung, B.; Furukawa, H.; Yaghi, O. K.; He, N.; Hayashi, H.; Houndonougbo, Y.; Asta, M.; Laird, B. B.; Yaghi, O. M., A Combined Experimental-Computational Investigation of Carbon Dioxide Capture in a Series of Isoreticular Zeolitic Imidazolate Frameworks. *J.Am.Chem.Soc.* **2010,** *132* (32), 11006-11008.

33. Morris, W.; He, N.; Ray, K. G.; Klonowski, P.; Furukawa, H.; Daniels, I. N.; Houndonougbo, Y. A.; Asta, M.; Yaghi, O. M.; Laird, B. B., A Combined Experimental-Computational Study on the Effect of Topology on Carbon Dioxide Adsorption in Zeolitic Imidazolate Frameworks. *J. Phys. Chem. C* **2012,** *116* (45), 24084-24090.

34. Chen, C.; Kim, J.; Yang, D.-A.; Ahn, W.-S., Carbon dioxide adsorption over zeolite-like metal organic frameworks (ZMOFs) having a sod topology: Structure and ion-exchange effect. *Chem. Eng. J.* **2011,** *168* (3), 1134-1139.

35. Banerjee, R.; Furukawa, H.; Britt, D.; Knobler, C.; O'Keeffe, M.; Yaghi, O. M., Control of Pore Size and Functionality in Isoreticular Zeolitic Imidazolate Frameworks and their Carbon Dioxide Selective Capture Properties. *J.Am.Chem.Soc.* **2009,** *131* (11), 3875-3877.

36. Houndonougbo, Y.; Signer, C.; He, N.; Morris, W.; Furukawa, H.; Ray, K. G.; Olmsted, D. L.; Asta, M.; Laird, B. B.; Yaghi, O. M., A Combined Experimental–Computational Investigation of Methane Adsorption and Selectivity in a Series of Isoreticular Zeolitic Imidazolate Frameworks. *J. Phys. Chem. C* **2013,** *117* (20), 10326-10335.

37. Liu, J.; Keskin, S.; Sholl, D. S.; Johnson, J. K., Molecular Simulations and Theoretical Predictions for Adsorption and Diffusion of CH_4/H_2 and CO_2/CH_4 Mixtures in ZIFs. *J. Phys. Chem. C* **2011,** *115* (25), 12560-12566.

38. Banerjee, R.; Phan, A.; Wang, B.; Knobler, C.; Furukawa, H.; O'Keeffe, M.; Yaghi, O. M., High-throughput synthesis of zeolitic imidazolate frameworks and application to CO_2 capture. *Science* **2008,** *319* (5865), 939-943.

39. Sirjoosingh, A.; Alavi, S.; Woo, T. K., Grand-Canonical Monte Carlo and Molecular-Dynamics Simulations of Carbon-Dioxide and Carbon-Monoxide Adsorption in Zeolitic Imidazolate Framework Materials. *J. Phys. Chem. C* **2010,** *114* (5), 2171-2178.

40. Huang, H.; Zhang, W.; Liu, D.; Liu, B.; Chen, G.; Zhong, C., Effect of temperature on gas adsorption and separation in ZIF-8: A combined experimental and molecular simulation study. *Chem. Eng. Sci.* **2011,** *66* (23), 6297-6305.

41. Liu, Y.; Liu, J.; Chang, M.; Zheng, C., Effect of Functionalized Linker on CO_2 Binding in Zeolitic Imidazolate Frameworks: Density Functional Theory Study. *J. Phys. Chem. C* **2012,** *116* (32), 16985-16991.

42. Canivet, J.; Fateeva, A.; Guo, Y.; Coasne, B.; Farrusseng, D., Water adsorption in MOFs: fundamentals and applications. *Chem. Soc. Rev.* **2014,** *43* (16), 5594-5617.

43. Nalaparaju, A.; Zhao, X. S.; Jiang, J. W., Molecular Understanding for the Adsorption of Water and Alcohols in Hydrophilic and Hydrophobic Zeolitic Metal−Organic Frameworks. *J. Phys. Chem. C* **2010,** *114* (26), 11542-11550.

44. Lively, R. P.; Dose, M. E.; Thompson, J. A.; McCool, B. A.; Chance, R. R.; Koros, W. J., Ethanol and water adsorption in methanol-derived ZIF-71. *Chem. Commun.* **2011,** *47* (30), 8667-8669.

45. Böhme, U.; Barth, B.; Paula, C.; Kuhnt, A.; Schwieger, W.; Mundstock, A.; Caro, J.; Hartmann, M., Ethene/Ethane and Propene/Propane Separation via the Olefin and Paraffin Selective Metal–Organic Framework Adsorbents CPO-27 and ZIF-8. *Langmuir* **2013,** *29* (27), 8592-8600.

46. Bux, H.; Chmelik, C.; Krishna, R.; Caro, J., Ethene/ethane separation by the MOF membrane ZIF-8: Molecular correlation of permeation, adsorption, diffusion. *J. Membr. Sci.* **2011,** *369* (1), 284-289.

47. Gücüyener, C.; van den Bergh, J.; Gascon, J.; Kapteijn, F., Ethane/Ethene Separation Turned on Its Head: Selective Ethane Adsorption on the Metal−Organic Framework ZIF-7 through a Gate-Opening Mechanism. *J.Am.Chem.Soc.* **2010,** *132* (50), 17704-17706.

48. Li, K.; Olson, D. H.; Seidel, J.; Emge, T. J.; Gong, H.; Zeng, H.; Li, J., Zeolitic Imidazolate Frameworks for Kinetic Separation of Propane and Propene. *J.Am.Chem.Soc.* **2009,** *131* (30), 10368-10369.

49. Brown, A. J.; Brunelli, N. A.; Eum, K.; Rashidi, F.; Johnson, J. R.; Koros, W. J.; Jones, C. W.; Nair, S., Interfacial microfluidic processing of metal-organic framework hollow fiber membranes. *Science* **2014,** *345* (6192), 72-75.

50. Eum, K.; Ma, C.; Rownaghi, A.; Jones, C. W.; Nair, S., ZIF-8 Membranes via Interfacial Microfluidic Processing in Polymeric Hollow Fibers: Efficient Propylene Separation at Elevated Pressures. *ACS Appl. Mater. Interfaces* **2016,** *8* (38), 25337-25342.

51. Ferreira, A. F. P.; Mittelmeijer-Hazeleger, M. C.; Granato, M. A.; Martins, V. F. D.; Rodrigues, A. E.; Rothenberg, G., Sieving di-branched from mono-branched and linear alkanes using ZIF-8: experimental proof and theoretical explanation. *Phys. Chem. Chem. Phys.* **2013,** *15* (22), 8795-8804.

52. Peralta, D.; Chaplais, G.; Simon-Masseron, A.; Barthelet, K.; Pirngruber, G. D., Separation of C6 Paraffins Using Zeolitic Imidazolate Frameworks: Comparison with Zeolite 5A. *Ind. Eng. Chem. Res.* **2012,** *51* (12), 4692-4702.

53. Peralta, D.; Chaplais, G.; Paillaud, J.-L.; Simon-Masseron, A.; Barthelet, K.; Pirngruber, G. D., The separation of xylene isomers by ZIF-8: A demonstration of the extraordinary flexibility of the ZIF-8 framework. *Microporous Mesoporous Mater.* **2013,** *173*, 1-5.

54. Kwon, H. T.; Jeong, H.-K., In Situ Synthesis of Thin Zeolitic–Imidazolate Framework ZIF-8 Membranes Exhibiting Exceptionally High Propylene/Propane Separation. *J.Am.Chem.Soc.* **2013,** *135* (29), 10763-10768.

55. Pan, Y.; Li, T.; Lestari, G.; Lai, Z., Effective separation of propylene/propane binary mixtures by ZIF-8 membranes. *J. Membr. Sci.* **2012,** *390-391*, 93-98.

56. Kwon, H. T.; Jeong, H.-K., Highly propylene-selective supported zeolite-imidazolate framework (ZIF-8) membranes synthesized by rapid microwave-assisted seeding and secondary growth. *Chem. Commun.* **2013,** *49* (37), 3854-3856.

57. Zhang, C.; Dai, Y.; Johnson, J. R.; Karvan, O.; Koros, W. J., High performance ZIF-8/6FDA-DAM mixed matrix membrane for propylene/propane separations. *J. Membr. Sci.* **2012,** *389*, 34-42.

58. Askari, M.; Chung, T.-S., Natural gas purification and olefin/paraffin separation using thermal cross-linkable co-polyimide/ZIF-8 mixed matrix membranes. *J. Membr. Sci.* **2013,** *444*, 173-183.

59. James, J. B.; Wang, J.; Meng, L.; Lin, Y. S., ZIF-8 Membrane Ethylene/Ethane Transport Characteristics in Single and Binary Gas Mixtures. *Ind. Eng. Chem. Res.* **2017,** *56* (26), 7567-7575.

60. Chmelik, C.; Freude, D.; Bux, H.; Haase, J., Ethene/ethane mixture diffusion in the MOF sieve ZIF-8 studied by MAS PFG NMR diffusometry. *Microporous Mesoporous Mater.* **2012,** *147* (1), 135-141.

61. Tao, K.; Kong, C.; Chen, L., High performance ZIF-8 molecular sieve membrane on hollow ceramic fiber via crystallizing-rubbing seed deposition. *Chem. Eng. J.* **2013,** *220*, 1-5.

62. Ordoñez, M. J. C.; Balkus, K. J.; Ferraris, J. P.; Musselman, I. H., Molecular sieving realized with ZIF-8/Matrimid® mixed-matrix membranes. *J. Membr. Sci.* **2010,** *361* (1), 28-37.

63. Yang, T.; Shi, G. M.; Chung, T.-S., Symmetric and Asymmetric Zeolitic Imidazolate Frameworks (ZIFs)/Polybenzimidazole (PBI) Nanocomposite Membranes for Hydrogen Purification at High Temperatures. *Adv. Energy Mater.* **2012,** *2* (11), 1358-1367.

64. Yang, T.; Chung, T.-S., High performance ZIF-8/PBI nano-composite membranes for high temperature hydrogen separation consisting of carbon monoxide and water vapor. *Int. J. Hydrogen Energy* **2013,** *38* (1), 229-239.

65. Bushell, A. F.; Attfield, M. P.; Mason, C. R.; Budd, P. M.; Yampolskii, Y.; Starannikova, L.; Rebrov, A.; Bazzarelli, F.; Bernardo, P.; Carolus Jansen, J.; Lanč, M.; Friess, K.; Shantarovich, V.; Gustov, V.; Isaeva, V., Gas permeation parameters of mixed matrix membranes based on the polymer of intrinsic microporosity PIM-1 and the zeolitic imidazolate framework ZIF-8. *J. Membr. Sci.* **2013,** *427*, 48-62.

66. Bux, H.; Liang, F.; Li, Y.; Cravillon, J.; Wiebcke, M.; Caro, J., Zeolitic Imidazolate Framework Membrane with Molecular Sieving Properties by Microwave-Assisted Solvothermal Synthesis. *J.Am.Chem.Soc.* **2009,** *131* (44), 16000-16001.

67. Liu, X.-L.; Li, Y.-S.; Zhu, G.-Q.; Ban, Y.-J.; Xu, L.-Y.; Yang, W.-S., An Organophilic Pervaporation Membrane Derived from Metal–Organic Framework Nanoparticles for Efficient Recovery of Bio-Alcohols. *Angew. Chem., Int. Ed.* **2011,** *50* (45), 10636-10639.

68. Liu, S.; Liu, G.; Zhao, X.; Jin, W., Hydrophobic-ZIF-71 filled PEBA mixed matrix membranes for recovery of biobutanol via pervaporation. *J. Membr. Sci.* **2013,** *446*, 181-188.

69. Song, Q.; Nataraj, S. K.; Roussenova, M. V.; Tan, J. C.; Hughes, D. J.; Li, W.; Bourgoin, P.; Alam, M. A.; Cheetham, A. K.; Al-Muhtaseb, S. A.; Sivaniah, E., Zeolitic imidazolate framework (ZIF-8) based polymer nanocomposite membranes for gas separation. *Energy Environ. Sci.* **2012,** *5* (8), 8359-8369.

70. Dai, Y.; Johnson, J. R.; Karvan, O.; Sholl, D. S.; Koros, W. J., Ultem®/ZIF-8 mixed matrix hollow fiber membranes for CO_2/N_2 separations. *J. Membr. Sci.* **2012,** *401-402*, 76-82.

71. Lively, R. P.; Dose, M. E.; Xu, L. R.; Vaughn, J. T.; Johnson, J. R.; Thompson, J. A.; Zhang, K.; Lydon, M. E.; Lee, J. S.; Liu, L.; Hu, Z. S.; Karvan, O.; Realff, M. J.; Koros, W. J., A high-flux polyimide hollow fiber membrane to minimize footprint and energy penalty for CO_2 recovery from flue gas. *J. Membr. Sci.* **2012,** *423*, 302-313.

72. Basu, S.; Cano-Odena, A.; Vankelecom, I. F. J., MOF-containing mixed-matrix membranes for CO_2/CH_4 and CO_2/N_2 binary gas mixture separations. *Sep. Purif. Technol.* **2011,** *81* (1), 31-40.

73. Li, T.; Pan, Y.; Peinemann, K.-V.; Lai, Z., Carbon dioxide selective mixed matrix composite membrane containing ZIF-7 nano-fillers. *J. Membr. Sci.* **2013,** *425-426*, 235-242.

74. Liu, Y.; Zeng, G.; Pan, Y.; Lai, Z., Synthesis of highly c-oriented ZIF-69 membranes by secondary growth and their gas permeation properties. *J. Membr. Sci.* **2011,** *379* (1), 46-51.

75. Brown, A. J.; Johnson, J. R.; Lydon, M. E.; Koros, W. J.; Jones, C. W.; Nair, S., Continuous Polycrystalline Zeolitic Imidazolate Framework-90 Membranes on Polymeric Hollow Fibers. *Angew. Chem., Int. Ed.* **2012,** *51* (42), 10615-10618.

76. Bae, T.-H.; Lee, J. S.; Qiu, W.; Koros, W. J.; Jones, C. W.; Nair, S., A High-Performance Gas-Separation Membrane Containing Submicrometer-Sized Metal–Organic Framework Crystals. *Angew. Chem., Int. Ed.* **2010,** *49* (51), 9863-9866.

77. Kulkarni, A. R.; Sholl, D. S., Screening of Copper Open Metal Site MOFs for Olefin/Paraffin Separations Using DFT-Derived Force Fields. *J. Phys. Chem. C* **2016,** *120* (40), 23044-23054.

78. Chung, Y. G.; Camp, J.; Haranczyk, M.; Sikora, B. J.; Bury, W.; Krungleviciute, V.; Yildirim, T.; Farha, O. K.; Sholl, D. S.; Snurr, R. Q., Computation-Ready, Experimental Metal–Organic Frameworks: A Tool To Enable High-Throughput Screening of Nanoporous Crystals. *Chem. Mater.* **2014,** *26* (21), 6185-6192.

79. Watanabe, T.; Sholl, D. S., Accelerating Applications of Metal–Organic Frameworks for Gas Adsorption and Separation by Computational Screening of Materials. *Langmuir* **2012,** *28* (40), 14114-14128.

80. Chalati, T.; Horcajada, P.; Gref, R.; Couvreur, P.; Serre, C., Optimisation of the synthesis of MOF nanoparticles made of flexible porous iron fumarate MIL-88A. *J. Mater. Chem.* **2011,** *21* (7), 2220-2227.

81. Batten, M. P.; Rubio-Martinez, M.; Hadley, T.; Carey, K.-C.; Lim, K.-S.; Polyzos, A.; Hill, M. R., Continuous flow production of metal-organic frameworks. *Curr. Opin. Chem. Eng.* **2015,** *8*, 55-59.

82. Rubio-Martinez, M.; Hadley, T. D.; Batten, M. P.; Constanti-Carey, K.; Barton, T.; Marley, D.; Mönch, A.; Lim, K.-S.; Hill, M. R., Scalability of Continuous Flow Production of Metal–Organic Frameworks. *ChemSusChem* **2016,** *9* (9), 938-941.

83. Eum, K.; Ma, C.; Koh, D.-Y.; Rashidi, F.; Li, Z.; Jones, C. W.; Lively, R. P.; Nair, S., Zeolitic Imidazolate Framework Membranes Supported on Macroporous Carbon

Hollow Fibers by Fluidic Processing Techniques. *Adv. Mater. Interfaces* **2017,** *4* (12), 1700080.

84. Sheng, L.; Wang, C.; Yang, F.; Xiang, L.; Huang, X.; Yu, J.; Zhang, L.; Pan, Y.; Li, Y., Enhanced C_3H_6/C_3H_8 separation performance on MOF membranes through blocking defects and hindering framework flexibility by silicone rubber coating. *Chem. Commun.* **2017,** *53* (55), 7760-7763.

85. Hu, Y.; Wei, J.; Liang, Y.; Zhang, H.; Zhang, X.; Shen, W.; Wang, H., Zeolitic Imidazolate Framework/Graphene Oxide Hybrid Nanosheets as Seeds for the Growth of Ultrathin Molecular Sieving Membranes. *Angew. Chem., Int. Ed.* **2016,** *55* (6), 2048-2052.

86. Dong, X.; Huang, K.; Liu, S.; Ren, R.; Jin, W.; Lin, Y. S., Synthesis of zeolitic imidazolate framework-78 molecular-sieve membrane: defect formation and elimination. *J. Mater. Chem.* **2012,** *22* (36), 19222-19227.

87. Walton, K. S.; Sholl, D. S., Research Challenges in Avoiding "Showstoppers" in Developing Materials for Large-Scale Energy Applications. *Joule* **2017,** *1* (2), 208-211.

88. Burtch, N. C.; Jasuja, H.; Walton, K. S., Water Stability and Adsorption in Metal-Organic Frameworks. *Chem. Rev.* **2014,** *114* (20), 10575-10612.

89. Sholl, D. S.; Lively, R. P., Defects in Metal-Organic Frameworks: Challenge or Opportunity? *J.Phys.Chem.Lett.* **2015,** *6* (17), 3437-3444.

90. Keskin, S.; van Heest, T. M.; Sholl, D. S., Can Metal-Organic Framework Materials Play a Useful Role in Large-Scale Carbon Dioxide Separations? *Chemsuschem* **2010,** *3* (8), 879-891.

91. Duan, J.; Jin, W.; Kitagawa, S., Water-resistant porous coordination polymers for gas separation. *Coord. Chem. Rev.* **2017,** *332*, 48-74.

92. Rezaei, F.; Rownaghi, A. A.; Monjezi, S.; Lively, R. P.; Jones, C. W., SO_x/NO_x Removal from Flue Gas Streams by Solid Adsorbents: A Review of Current Challenges and Future Directions. *Energy Fuels* **2015,** *29* (9), 5467-5486.

93. Sanz-Perez, E. S.; Murdock, C. R.; Didas, S. A.; Jones, C. W., Direct Capture of CO_2 from Ambient Air. *Chem. Rev.* **2016,** *116* (19), 11840-11876.

94. Sun, W.; Lin, L.-C.; Peng, X.; Smit, B., Computational screening of porous metal-organic frameworks and zeolites for the removal of SO_2 and NO_x from flue gases. *AIChE J.* **2014,** *60* (6), 2314-2323.

95. Alcheikhhamdon, Y.; Hoorfar, M., Natural gas purification from acid gases using membranes: A review of the history, features, techno-commercial challenges, and process intensification of commercial membranes. *Chem. Eng. Process.* **2017,** *120*, 105-113.

96. Alcheikhhamdon, Y.; Hoorfar, M., Natural gas quality enhancement: A review of the conventional treatment processes, and the industrial challenges facing emerging technologies. *J. Nat. Gas Sci. Eng.* **2016,** *34*, 689-701.

97. Mokhatab, S.; Poe, W. A.; Speight, J. G., Chapter 7 - Acid gas treating. In *Handbook of Natural Gas Transmission and Processing*, Mokhatab, S.; Poe, W. A.; Speight, J. G., Eds. Gulf Professional Publishing: Burlington, 2006; pp 261-294.

98. Control, T. A. P., Acid Gases. http://tapc.com.au/acid-gases/, 2018; Vol. 2018.

99. Baker, R. W.; Lokhandwala, K., Natural gas processing with membranes: An overview. *Ind. Eng. Chem. Res.* **2008,** *47* (7), 2109-2121.

100. U.S.E.P.A., Criteria Air Pollutants. https://www.epa.gov/criteria-air-pollutants, 2018; Vol. 2018.

101. U.S.E.P.A., Particulate Matter Basics. https://www.epa.gov/pm-pollution/particulate-matter-pm-basics#PM, 2018; Vol. 2018.

102. U.S.E.P.A., Basic Information about ozone. https://www.epa.gov/ozone-pollution/basic-information-about-ozone#what%20where%20how, 2018.

103. Department of the Environment and Energy, A. G., SO_2 Factsheet. http://www.environment.gov.au/protection/publications/factsheet-sulfur-dioxide-so2, 2005.

104. U.S.E.P.A., Sulfur Dioxide Basics. https://www.epa.gov/so2-pollution/sulfur-dioxide-basics#what%20is%20so2, 2018.

105. Eatough, D. J.; Caka, F. M.; Farber, R. J., The conversion of SO_2 to sulfate in the atmosphere. *Isr. J. Chem.* **1994,** *34* (3-4), 301-314.

106. U.S.E.P.A., Acid Rain. https://www.epa.gov/acidrain/what-acid-rain, 2018.

107. Labor, U. S. D. o., Permissible Exposure Limits. OSHA, Ed. https://www.osha.gov/dsg/annotated-pels/tablez-1.html#niosh_rel, 2018.

108. Gray, P.; Yoffe, A. D., The Reactivity And Structure Of Nitrogen Dioxide. *Chem. Rev.* **1955,** *55* (6), 1069-1154.

109. Altshuller, A. P., Thermodynamic Considerations in the Interactions of Nitrogen Oxides and Oxy-Acids in the Atmosphere. *J. Air Pollut. Control Assoc.* **1956,** *6* (2), 97-100.

110. Department of the Environment and Energy, A. G., NO_2 Factsheet. http://www.environment.gov.au/protection/publications/factsheet-nitrogen-dioxide-no2, 2005.

111. J.O.Nriagu, M. S. S., *Environmental Oxidants*. John Wiley & Sons, Inc.: 1994; Vol. 28.

112. U.S.E.P.A., Basic Information about NO_2. https://www.epa.gov/no2-pollution/basic-information-about-no2#What%20is%20NO2, 2018.

113. NIST, NIST Chemistry Webbook. https://webbook.nist.gov/chemistry/name-ser/, 2018.

114. NIST, Computational Chemistry Comparison and Benchmark DataBase. https://cccbdb.nist.gov/alldata1x.asp, 2018.

115. NIOSH, NIOSH pocket guide to chemical hazards. https://www.cdc.gov/niosh/npg/search.html, 2018.

116. U.S.E.P.A., Air Pollution Control Technology Fact Sheet: Flue Gas Desulfurization. https://www3.epa.gov/ttncatc1/dir1/ffdg.pdf, 2018.

117. E.I.A., U. S., Monthly Energy Review. 2017.

118. Sumida, K.; Rogow, D. L.; Mason, J. A.; McDonald, T. M.; Bloch, E. D.; Herm, Z. R.; Bae, T.-H.; Long, J. R., Carbon Dioxide Capture in Metal–Organic Frameworks. *Chem. Rev.* **2012,** *112* (2), 724-781.

119. Levasseur, B.; Petit, C.; Bandosz, T. J., Reactive Adsorption of NO_2 on Copper-Based Metal-Organic Framework and Graphite Oxide/Metal-Organic Framework Composites. *ACS Appl. Mater. Interfaces* **2010,** *2* (12), 3606-3613.

120. U.S.E.P.A., Air Pollution Control Technology Fact Sheet: Selective Non-Catalytic Reduction. https://www3.epa.gov/ttncatc1/dir1/fsncr.pdf, 2018.

121. U.S.E.P.A., Air Pollution Control Technology Fact Sheet: Selective Catalytic Reduction. https://www3.epa.gov/ttncatc1/dir1/fscr.pdf, 2018.

122. Sanz-Pérez, E. S.; Murdock, C. R.; Didas, S. A.; Jones, C. W., Direct Capture of CO_2 from Ambient Air. *Chem. Rev.* **2016,** *116* (19), 11840-11876.

123. N.E.T.L, Carbon Capture 2020 Workshop summary. http://www.netl.doe.gov/publications/proceedings/09/CC2020/pdfs/Richards_Summary.pdf, 2009.

124. Bosch, M.; Zhang, M.; Zhou, H.-C., Increasing the Stability of Metal-Organic Frameworks. *Adv. Chem.* **2014,** *2014*, 8.

125. Howarth, A. J.; Liu, Y.; Li, P.; Li, Z.; Wang, T. C.; Hupp, J. T.; Farha, O. K., Chemical, thermal and mechanical stabilities of metal–organic frameworks. *Nat. Rev. Mater.* **2016,** *1*, 15018.

126. Yuan, S.; Feng, L.; Wang, K.; Pang, J.; Bosch, M.; Lollar, C.; Sun, Y.; Qin, J.; Yang, X.; Zhang, P.; Wang, Q.; Zou, L.; Zhang, Y.; Zhang, L.; Fang, Y.; Li, J.; Zhou, H. C., Stable Metal-Organic Frameworks: Design, Synthesis, and Applications. *Adv Mater* **2018,** *0* (0), 1704303.

127. Lu, P.; Wu, Y.; Kang, H.; Wei, H.; Liu, H.; Fang, M., What can pKa and NBO charges of the ligands tell us about the water and thermal stability of metal organic frameworks? *J. Mater. Chem. A* **2014,** *2* (38), 16250-16267.

128. Low, J. J.; Benin, A. I.; Jakubczak, P.; Abrahamian, J. F.; Faheem, S. A.; Willis, R. R., Virtual High Throughput Screening Confirmed Experimentally: Porous Coordination Polymer Hydration. *J.Am.Chem.Soc.* **2009,** *131* (43), 15834-15842.

129. Colombo, V.; Galli, S.; Choi, H. J.; Han, G. D.; Maspero, A.; Palmisano, G.; Masciocchi, N.; Long, J. R., High thermal and chemical stability in pyrazolate-bridged metal–organic frameworks with exposed metal sites. *Chem. Sci.* **2011,** *2* (7), 1311-1319.

130. Yuan, S.; Qin, J.-S.; Lollar, C. T.; Zhou, H.-C., Stable Metal–Organic Frameworks with Group 4 Metals: Current Status and Trends. *ACS Central Sci.* **2018,** *4* (4), 440-450.

131. Devic, T.; Serre, C., High valence 3p and transition metal based MOFs. *Chem. Soc. Rev.* **2014,** *43* (16), 6097-6115.

132. Pearson, R. G., Hard and Soft Acids and Bases. *J.Am.Chem.Soc.* **1963,** *85* (22), 3533-3539.

133. Wang, K.; Lv, X.-L.; Feng, D.; Li, J.; Chen, S.; Sun, J.; Song, L.; Xie, Y.; Li, J.-R.; Zhou, H.-C., Pyrazolate-Based Porphyrinic Metal–Organic Framework with Extraordinary Base-Resistance. *J.Am.Chem.Soc.* **2016,** *138* (3), 914-919.

134. DeCoste, J. B.; Peterson, G. W.; Jasuja, H.; Glover, T. G.; Huang, Y.-g.; Walton, K. S., Stability and degradation mechanisms of metal–organic frameworks containing the $Zr_6O_4(OH)_4$ secondary building unit. *J. Mater. Chem. A* **2013,** *1* (18), 5642-5650.

135. Kuesgens, P.; Rose, M.; Senkovska, I.; Froede, H.; Henschel, A.; Siegle, S.; Kaskel, S., Characterization of metal-organic frameworks by water adsorption. *Microporous Mesoporous Mater.* **2009,** *120* (3), 325-330.

136. Mottillo, C.; Friscic, T., Carbon Dioxide Sensitivity of Zeolitic Imidazolate Frameworks. *Angew. Chem., Int. Ed.* **2014,** *53* (29), 7471-7474.

137. Leus, K.; Bogaerts, T.; De Decker, J.; Depauw, H.; Hendrickx, K.; Vrielinck, H.; Van Speybroeck, V.; Van Der Voort, P., Systematic study of the chemical and hydrothermal stability of selected "stable" Metal Organic Frameworks. *Microporous Mesoporous Mater.* **2016,** *226*, 110-116.

138. Pang, S. H.; Han, C.; Sholl, D. S.; Jones, C. W.; Lively, R. P., Facet-Specific Stability of ZIF-8 in the Presence of Acid Gases Dissolved in Aqueous Solutions. *Chem. Mater.* **2016,** *28* (19), 6960-6967.

139. Han, S.; Huang, Y.; Watanabe, T.; Dai, Y.; Walton, K. S.; Nair, S.; Sholl, D. S.; Meredith, J. C., High-Throughput Screening of Metal-Organic Frameworks for CO_2 Separation. *ACS Comb. Sci.* **2012,** *14* (4), 263-267.

140. Ding, L. F.; Yazaydin, A. O., The effect of SO_2 on CO_2 capture in zeolitic imidazolate frameworks. *Phys. Chem. Chem. Phys.* **2013,** *15* (28), 11856-11861.

141. Lee, K.; Howe, J. D.; Lin, L. C.; Smit, B.; Neaton, J. B., Small-Molecule Adsorption in Open-Site Metal-Organic Frameworks: A Systematic Density Functional Theory Study for Rational Design. *Chem. Mater.* **2015,** *27* (3), 668-678.

142. Yu, K.; Kiesling, K.; Schmidt, J. R., Trace Flue Gas Contaminants Poison Coordinatively Unsaturated Metal-Organic Frameworks: Implications for CO_2 Adsorption and Separation. *J. Phys. Chem. C* **2012,** *116* (38), 20480-20488.

143. Ding, L.; Yazaydin, A. Ö., How Well Do Metal–Organic Frameworks Tolerate Flue Gas Impurities? *J. Phys. Chem. C* **2012,** *116* (43), 22987-22991.

144. Tan, K.; Zuluaga, S.; Gong, Q.; Gao, Y.; Nijem, N.; Li, J.; Thonhauser, T.; Chabal, Y. J., Competitive Coadsorption of CO_2 with H_2O, NH_3, SO_2, NO, NO_2, N_2, O_2, and CH_4 in M-MOF-74 (M = Mg, Co, Ni): The Role of Hydrogen Bonding. *Chem. Mater.* **2015,** *27* (6), 2203-2217.

145. Fioretos, K. A.; Psofogiannakis, G. M.; Froudakis, G. E., Ab-Initio Study of the Adsorption and Separation of NO_x and SO_x Gases in Functionalized IRMOF Ligands. *J. Phys. Chem. C* **2011,** *115* (50), 24906-24914.

146. DeCoste, J. B.; Peterson, G. W.; Schindler, B. J.; Killops, K. L.; Browe, M. A.; Mahle, J. J., The effect of water adsorption on the structure of the carboxylate containing metal-organic frameworks Cu-BTC, Mg-MOF-74, and UiO-66. *J. Mater. Chem. A* **2013,** *1* (38), 11922-11932.

147. Schoenecker, P. M.; Carson, C. G.; Jasuja, H.; Flemming, C. J. J.; Walton, K. S., Effect of Water Adsorption on Retention of Structure and Surface Area of Metal–Organic Frameworks. *Ind. Eng. Chem. Res.* **2012,** *51* (18), 6513-6519.

148. Yang, S.; Sun, J.; Ramirez-Cuesta, A. J.; Callear, S. K.; DavidWilliam, I. F.; Anderson, D. P.; Newby, R.; Blake, A. J.; Parker, J. E.; Tang, C. C.; Schröder, M., Selectivity and direct visualization of carbon dioxide and sulfur dioxide in a decorated porous host. *Nat Chem* **2012,** *4* (11), 887-894.

149. Savage, M.; Cheng, Y.; Easun, T. L.; Eyley, J. E.; Argent, S. P.; Warren, M. R.; Lewis, W.; Murray, C.; Tang, C. C.; Frogley, M. D.; Cinque, G.; Sun, J.; Rudić, S.; Murden, R. T.; Benham, M. J.; Fitch, A. N.; Blake, A. J.; Ramirez-Cuesta, A. J.; Yang, S.;

Schröder, M., Selective Adsorption of Sulfur Dioxide in a Robust Metal–Organic Framework Material. *Adv. Mater.* **2016,** *28* (39), 8705-8711.

150. Tan, K.; Canepa, P.; Gong, Q.; Liu, J.; Johnson, D. H.; Dyevoich, A.; Thallapally, P. K.; Thonhauser, T.; Li, J.; Chabal, Y. J., Mechanism of Preferential Adsorption of SO_2 into Two Microporous Paddle Wheel Frameworks M(bdc)(ted)$_{0.5}$. *Chem. Mater.* **2013,** *25* (23), 4653-4662.

151. Fernandez, C. A.; Thallapally, P. K.; Motkuri, R. K.; Nune, S. K.; Sumrak, J. C.; Tian, J.; Liu, J., Gas-Induced Expansion and Contraction of a Fluorinated Metal−Organic Framework. *Crystal Growth & Design* **2010,** *10* (3), 1037-1039.

152. Britt, D.; Tranchemontagne, D.; Yaghi, O. M., Metal-organic frameworks with high capacity and selectivity for harmful gases. *Proc. Natl. Acad. Sci.* **2008,** *105* (33), 11623-11627.

153. Glover, T. G.; Peterson, G. W.; Schindler, B. J.; Britt, D.; Yaghi, O., MOF-74 building unit has a direct impact on toxic gas adsorption. *Chem. Eng. Sci.* **2011,** *66* (2), 163-170.

154. Peterson, G. W.; Rossin, J. A.; DeCoste, J. B.; Killops, K. L.; Browe, M.; Valdes, E.; Jones, P., Zirconium Hydroxide–Metal–Organic Framework Composites for Toxic Chemical Removal. *Ind. Eng. Chem. Res.* **2013,** *52* (15), 5462-5469.

155. Dathe, H.; Peringer, E.; Roberts, V.; Jentys, A.; Lercher, J. A., Metal organic frameworks based on Cu^{2+} and benzene-1,3,5-tricarboxylate as host for SO_2 trapping agents. *C. R. Chim.* **2005,** *8* (3), 753-763.

156. Karra, J. R.; Walton, K. S., Effect of Open Metal Sites on Adsorption of Polar and Nonpolar Molecules in Metal−Organic Framework Cu-BTC. *Langmuir* **2008,** *24* (16), 8620-8626.

157. Petit, C.; Levasseur, B.; Mendoza, B.; Bandosz, T. J., Reactive adsorption of acidic gases on MOF/graphite oxide composites. *Microporous Mesoporous Mater.* **2012,** *154*, 107-112.

158. DeCoste, J. B.; Demasky, T. J.; Katz, M. J.; Farha, O. K.; Hupp, J. T., A UiO-66 analogue with uncoordinated carboxylic acids for the broad-spectrum removal of toxic chemicals. *New J. Chem.* **2015,** *39* (4), 2396-2399.

159. Ebrahim, A. M.; Bandosz, T. J., Effect of amine modification on the properties of zirconium–carboxylic acid based materials and their applications as NO_2 adsorbents at ambient conditions. *Microporous Mesoporous Mater*. **2014,** *188* (Supplement C), 149-162.

160. Ebrahim, A. M.; Levasseur, B.; Bandosz, T. J., Interactions of NO_2 with Zr-Based MOF: Effects of the Size of Organic Linkers on NO_2 Adsorption at Ambient Conditions. *Langmuir* **2013,** *29* (1), 168-174.

161. Peterson, G. W.; Mahle, J. J.; DeCoste, J. B.; Gordon, W. O.; Rossin, J. A., Extraordinary NO_2 Removal by the Metal–Organic Framework UiO-66-NH_2. *Angew. Chem., Int. Ed.* **2016,** *55* (21), 6235-6238.

CHAPTER 2. BUTANOL SEPARATION FROM HUMID CO_2-CONTAINING MULTICOMPONENT VAPOR MIXTURES BY ZEOLITIC IMIDAZOLATE FRAMEWORKS

2.1 Introduction*

In this Chapter, I present a detailed investigation of butanol separation from realistic multicomponent mixtures using ZIF adsorbents. This work highlights the practical importance of obtaining insight into the acid gas stability of MOF/ZIF materials in realistic applications. In addition to thoroughly evaluating a promising technological application for a ZIF adsorbent, the findings of this Chapter provide considerable motivation for the extensive investigation of acid gas stability of ZIFs that is presented in the following Chapters of this work. The application of interest is the recovery of butanol from butanol-water vapor feed mixtures, as well as the acetone-butanol-ethanol (ABE) mixture (3:6:1 weight ratio of acetone: butanol : ethanol), with and without the presence of CO_2.[1] The ABE mixture is typical of biobutanol fermenters in which acetone and ethanol are generated as byproducts. CO_2 is present in substantial amounts in the headspace of the fermenter, and the presence of humid CO_2 (an acid gas) can affect the separation performance and long-term stability of ZIF adsorbents.

* Work in this Chapter has been published previously in **S. Bhattacharyya**, K.C. Jayachandrababu, Y. Chiang, D. S. Sholl, S. Nair, "Butanol Separation from Humid CO_2-Containing Multicomponent Vapor Mixtures by Zeolitic Imidazolate Frameworks". *ACS Sustainanble Chem. Eng.* **2017,** *5* (10), 9467-9476

I first introduce the practical importance and challenges associated with biobutanol separations, followed by an evaluation of the separation performance of ZIF-8, ZIF-90, and ZIF-71, and mixed-linker ZIF-8_x-71_{100-x} and ZIF-8_x-90_{100-x} ($0 < x < 100$) adsorbents. The effective pore size, hydrophobicity and organophilicity of ZIFs can be continuously tuned using mixed-linker ZIFs, making them a more generalized materials platform for molecular separations.[2] I therefore also investigate the tunability of separation performance parameters like adsorption selectivity and adsorbed amounts across the hybrid ZIFs in this work. To my knowledge, this is the first investigation on MOF adsorbents for vapor-phase biobutanol separations in combination with gas stripping.

2.1.1 Importance and challenges of biobutanol separations

A number of well-known economic and environmental factors have led to increasing interest in biomass-derived fuels and chemicals.[1, 3] Among the candidate molecules being investigated for replacing gasoline, 1-butanol (henceforth referred to as butanol) has many advantages. It has a 30% higher energy density than ethanol, good compatibility with pipeline infrastructure (due to its low vapor pressure, high flash point, and low hygroscopicity), fewer groundwater contamination issues (due to its low solubility in water), better gasoline miscibility than ethanol, and high compatibility with existing automobile engine design. Butanol also has wide-ranging industrial applications as a precursor to paints, polymers, latex surface coatings, enamels and lacquers, as diluents for brake fluid formulations, and as a solvent in antibiotics, vitamins and hormone production.[4-5] Today, butanol is synthesized mainly from petroleum sources (petrobutanol), but it can also be produced *via* biological routes (biobutanol) by fermentation of sugars and

starches.[1] In fact, production of biobutanol by fermentation historically precedes petrobutanol synthesis.[3-4]

Despite renewed interest in biobutanol production,[3, 5-6] several challenges remain in making biobutanol production prevalent in the biofuels market, which is estimated to be worth ~$250 billion by 2020.[1] Presently, the butanol concentration in the aqueous ABE fermentation broth is low (~ 20 g/L), and hence a major challenge is to find an energy-efficient and cost-effective separation process to recover butanol from the dilute aqueous solution.[1, 3-5] The low butanol concentration and its high boiling point (390 K) make conventional distillation energy intensive and industrially unattractive.[7-9] Stripping the fermentation broth by sparging with inert gas or the fermentation off-gas (CO_2/H_2 mixture) offers a simple approach to concentrate the ABE components[1, 3, 10-14] while leaving non-volatile components like biomass, organic acids, and nutrients in the broth.[8, 15] Detailed analyses of separation methods to recover butanol from the ABE mixture have been carried out previously, and indicate that adsorption and membrane pervaporation are most promising.[7, 9] Adsorptive separation of butanol from aqueous ABE solution requires adsorbents that reject water molecules and still have high affinity towards alcohols (which are also quite polar).[16-17] Adsorbents such as silicas and zeolites have been considered for liquid-phase separation directly from clarified broths, but there are drawbacks of fouling problems caused by microbial biofilm formation and poisoning by impurities such as organic acids.[18-24] Advantages and challenges of various separation methods evaluated for butanol recovery from the ABE mixture are summarized in **Table A.1** in Appendix A.[7, 9, 25-26]

2.1.2 The Hybrid Separation Approach

Combining individual separation methods can result in effective butanol separation from the ABE mixture due to synergistic effects[12, 27-30] For example, separation of butanol from the stripped humid ABE vapor can potentially alleviate the concerns with liquid phase adsorption while resulting in higher butanol selectivities than gas stripping alone. However, few literature reports exist regarding this approach.[8, 15, 31-33] In general, for adsorbents to be effective in this vapor-phase butanol separation, the prerequisites are favorable butanol uptakes at low activities and unfavorable water uptakes throughout the entire activity range, including at high activities.[17] Recently, a system of two complementary adsorption columns in series was proposed for vapor phase butanol separation from ABE mixtures using zeolites Si-LTA and Si-CHA.[15] Under high relative humidity conditions, a butanol to ethanol selectivity of 7 was reported for the Si-LTA column which was used to adsorb butanol from the ABE vapors. However, though hydrophobic zeolites like high-silica MFI, CHA, or LTA can yield good butanol-over-water selectivity and adsorption capacity[15, 31] these characteristics – especially at low butanol activities – are very sensitive to the concentration of hydrophilic defects in the zeolite, and the synthesis of zeolites in defect-free, high-silica form is often difficult.[34]

As mentioned in Chapter 1 of this thesis, Zeolitic imidazolate frameworks (ZIFs) form a large and interesting class of adsorbent materials in which metal centers (usually Zn^{2+}) are connected by organic imidazolate (Im) linkers through Zn-N coordinate bonds.[35-38] They can also be synthesized with inherently more hydrophobic frameworks than zeolites, and therefore could be potential adsorbents for this challenging separation.[36, 38-39] ZIF-8 and ZIF-71 are well-known hydrophobic ZIFs with 2-methylimidazole linkers and

4,5-dichloroimidazole linkers respectively. Crystallographic pore aperture diameters for ZIF-8 and ZIF-71 are 3.4 Å and 4.2 Å respectively, but it has been shown that the pores are dynamically flexible and are accessible even to larger molecules.[37, 39-41] In contrast, ZIF-90 with the imidazole-2-carboxaldehyde linker has a hydrophilic character.[2, 39] These three materials can be considered to be well representative of the hydrophilic and hydrophobic properties that can be obtained in ZIF frameworks. For this reason, single-component butanol and water isotherms for these ZIFs were measured in previous work at Georgia Tech, and it was hypothesized that the hydrophobic ZIF-8 and ZIF-71 might be effective adsorbents for butanol separation, especially in the presence of humidified CO_2 in the feed mixture.[39] This Chapter examines the above hypothesis through a systematic investigation of biobutanol separation by ZIFs using a hybrid separation approach combining gas stripping and vapor phase adsorption. In doing so, the importance of developing a more generalized insight into the acid gas stability of ZIF materials is clearly highlighted.

2.2 Experimental Methods

2.2.1 Materials

Zinc(II) nitrate hexahydrate (99%), imidazole-2-carboxaldehyde (97%) and 1-butanol (99%) were purchased from Alfa Aesar. 2-methylimidazole (99%), 4,5-dichloroimidazole (98%) and sodium formate (99 %) were obtained from Sigma-Aldrich while methanol (99.8%) and N,N-dimethylformamide (DMF) (99.8%) were obtained from BDH. All chemicals were used as received without further purification. Ultra high purity N_2 gas, N_2/He (90:10 by volume) gas mixture and N_2:CO_2:He (12:12:76) gas mixture were

purchased from Airgas. Deionized (DI) water was obtained with an EMD Millipore water purification system.

2.2.2 Synthesis of ZIF adsorbents

ZIF-8 and ZIF-90 were synthesized by modifying the procedure reported by Gee et al.[42] 0.972 g 2-methylimidazole and 1.614 g sodium formate were dissolved in 120 cc methanol and sonicated to dissolve completely. 1.764 g zinc (II) nitrate was dissolved in 120 cc methanol added to the first solution. The combined solution was then heated in a glass jar to 363 K for 24 hours. The crystals were collected and washed with fresh methanol thrice and then air dried at 333 K. ZIF-90 was synthesized by dissolving 11.904 g zinc (II) nitrate and 15.368 g imidazole-2-carboxaldehyde in 400 cc DMF. The solution was then heated to 393 K in an oil bath for 10 minutes and then cooled to ambient temperature. The crystals obtained were washed with methanol thrice and then air dried at 333 K.

ZIF-71 was synthesized using the procedure followed by Zhang et al.[17] 297 mg zinc (II) acetate and 876 mg 4,5-dichloroimidazole were separately dissolved in 60 cc methanol. The zinc acetate solution was then added to the 4,5-dichloroimidazole solution and kept at room temperature without stirring for 24 hours. The crystals obtained were washed with methanol thrice and then air dried at 333 K.

SOD topology ZIF-71 was synthesized using the recent procedure reported by Wiebcke et al.[43] $Zn(NO_3)_2.6H_2O$ (0.796 g) was dissolved in 100 cc 1-propanol. 4,5-dichloroimidazole (1.466 g) and 1-methylimidazole (0.88 g) were dissolved in 100 cc 1-propanol. The first solution was poured into the second solution and stirred for 48 hours at

room temperature. Crystals were collected by centrifugation at 8500 rpm for 10 minutes, followed by washing with fresh methanol thrice. Crystals were air dried at 333 K.

Hybrid ZIF-8_{55}-71_{45} was synthesized using the following procedure. 1.192 g $Zn(NO_3)_2.6H_2O$ was dissolved in 50 cc 1-propanol. 0.986 g 2-methylimidazole, 0.548 g 4,5-dichloroimidazole, and 0.164 g 1-methylimidazole were dissolved in 50 cc DMF. Both solutions were mixed together in a glass jar and sealed. The jar was immersed in an oil bath at 373 K for 48 hours. The crystals were collected by centrifugation at 8500 rpm for 5 min followed by washing with fresh methanol thrice. The crystals were air dried at 333 K.

Mixed-linker (hybrid) ZIF-8_x-90_{100-x} materials were synthesized using the procedure reported by Thompson *et al* and Eum *et al*.[2, 44-45] 2-methylimidazole, imidazole-2-carboxaldehyde and sodium formate were dissolved in methanol by heating to 323 K under stirring and then cooled down to ambient temperature. Zinc (II) nitrate was dissolved in water. Both solutions were mixed together under stirring. The solution was kept stirred for 24 hours. The crystals were then separated by centrifugation and washed with methanol thrice and then air dried at 333 K. The compositions used for mixed-linker ZIF syntheses are given in **Table A.2** (Appendix A). All crystals were activated by degassing at 453 K in vacuum for 24 hours.

2.2.3 Characterization

Activated ZIF samples were characterized with powder X-ray diffraction (PXRD), nitrogen physisorption (NP), fourier transform infrared spectroscopy (FTIR), solution ^1H NMR and scanning electron microscopy (SEM). PXRD measurements were conducted on an X'Pert Pro PANalytical X-ray diffractometer in reflection (Bragg-Brentano) geometry

operating with a Cu anode at 45 kV and 40 mA. PXRD patterns were collected with a step size of 0.02° 2θ and scan time of 10 s/step. Surface area and pore volume analysis was conducted by NP at 77 K using a BET surface area analyzer (Tristar, Micromeritics). BET surface areas were calculated in individually determined pressure ranges.[46] FTIR spectra were recorded by a Thermo Scientific Nicolet iS50 FT-IR equipped with an iS50 ATR module. Spectra were obtained in the 550-4000 cm^{-1} range with 96 scans at a resolution of 2 cm^{-1}. Solution ^{1}H NMR measurements were performed with a Bruker 400 MHz spectrometer after digesting the ZIF crystals in d_4-acetic acid (CD_3CO_2D). To determine the fraction of each imidazole linker in the ZIF material, the integrated peak area of the methyl protons of 2-methylimidazole (chemical shift 2.65 ppm) was normalized to that of the aldehyde proton of imidazole-2-carboxaldehyde (9.84 ppm) for the ZIF-8_x-90_{100-x} hybrids and to the proton on the 2-carbon atom of the 4,5-dichloroimidazole linker (8.04 ppm) for the ZIF-8_x-71_{100-x} hybrids. The chemical shifts of both imidazole linkers were referenced to the chemical shift (2.30 ppm) of d_4-acetic acid. SEM imaging was carried out with Zeiss LEO 1530 scanning electron microscopes operating at 15 kV. Samples were first sputtered with gold under vacuum for 60 seconds.

2.2.4 Adsorption Isotherms and Breakthrough Experiments

Single-component adsorption measurements were conducted using a VTI-SA vapor sorption analyzer at 308 K. Each experiment was preceded by *in situ* activation of the adsorbent under nitrogen at 383 K for 12 hours. Adsorption data was collected at adsorbate relative pressures (P/P_0, where P_0 is the saturation vapor pressure) ranging from 0.05 – 0.95. Each data point was collected with sufficient time (2-24 hours) for reaching equilibration (based on visual inspection of the real-time weight change plot). A simplified

schematic of the vapor breakthrough apparatus is shown in **Figure A.1** in Appendix A. The apparatus has two gas inlets (*a*) for N_2 and a multi-gas mixture of either N_2/He (90:10) or N_2/CO_2/He (12:12:76). After flowing through a mass flow controller (MFC) (*b*) the multi-gas mixture is passed through a sparger (*d*) containing the desired liquid mixture kept inside the insulated column oven. When the control valves (*c*) are switched on towards the breakthrough column, the inlet streams merge (*e*) and continue through the packed column (*f*). After exiting the packed column the mixture goes to the Mass Spectrometer (MS) (*g*) for analysis. In this work, N_2 was used as the desorbent and He as the tracer. For each experimental run, 100 mg of adsorbent was loaded into the column. Prior to the breakthrough runs, the pre-activated adsorbent underwent *in situ* reactivation under N_2 flow at 453 K for 3 hours. The aqueous solution, either 1 (mole) % butanol in water or the model ABE solution containing 1% butanol, 0.6 mole % acetone, and 0.25 mole % ethanol in water, was bubbled with the multi-gas mixture for equilibration at a flowrate of 22 cc/min for 15 hours. The entire apparatus was maintained in a constant-temperature chamber at 308 K. The vapor-liquid equilibrium (VLE) data for the butanol/water system were determined using the Mixture Property Predictor of the Dortmund Databank Software and Separation Technology (DDBST)[47] and also independently verified using an online vapor-liquid equilibrium calculation toolbox at vle-calc.com[48] and supporting experimental data at 298 K.[49] The Mixture Property Predictor of the DDBST was also used for the ABE system VLE with the UNIFAC method. Details of the equilibrium compositions, component properties, and activity coefficients are given in **Tables A.3-A.5**. The mass spectrum (electron ionization) signals being used for detection of the individual molecules by the mass spectrometer were selected carefully to prevent overlap. Breakthrough runs

were carried out at 308 K. The dilute liquid solution was renewed after every 3 days. The adsorbed amounts q (mol/g) were first calculated for each species by integration of the breakthrough curves:

$$q = \frac{1}{m_{ads}} \times \int_0^t u(C_{in} - C_{out})dt \quad (1)$$

Here u is the volumetric flow rate of the feed (cc/min), C_{in} and C_{out} are the concentrations of the molecule at the column inlet and outlet respectively (mol/cc), t is the time (min) and m_{ads} is the loading of the MOF in the column (g). Separation factors $\alpha_{i,j}$ were calculated as

$$\alpha_{ij} = \frac{q_i}{q_j} \times \frac{C_j}{C_i} \quad (2)$$

Here q_i and q_j are the amounts of species i and j adsorbed per unit mass of MOF (mol/g), and C_i and C_j are the concentrations (mol/cc) of the species i and j in the external vapor phase at the column inlet.

2.2.5 Humid CO_2 Exposure

Activated samples were exposed to a 12% CO_2/12% N_2/76% He stream humidified at a relative humidity of 90% for 3 days at 298 K. The dry gas mixture was bubbled at 60 cc/min through deionized water and the humid stream generated entered the exposure chamber (a Secador mini-desiccator). The relative humidity was continuously monitored by a sensor (Ambient Weather). All samples were re-activated at 453 K in vacuum for 24 hours after exposure and prior to characterization.

2.3 Results and Discussion

Figure 2.1 and **Figure A.2** show the PXRD patterns of activated ZIF adsorbents used in this work. The patterns for ZIF-8, ZIF-90 and ZIF-8_x-90_{100-x} hybrids are normalized with respect to the most intense Bragg peak at 7.33° 2θ corresponding to the (011) planes.[50-52] There is no qualitatively significant difference in the patterns of ZIF-8, ZIF-90 and the ZIF-8_x-90_{100-x} hybrids because all these adsorbents have the framework topology (SOD) and near-identical electron density distributions.[2] The patterns of the ZIF-71 adsorbents are normalized with respect to the most intense Bragg peak at 4.35° 2θ. The pattern of the hybrid ZIF-8_{55}-71_{45}, which has been synthesized for the first time in this work, is very different from the RHO topology of ZIF-71, and has the SOD framework topology of ZIF-8. BET surface areas and pore volumes of these adsorbents were calculated from NP at 77 K and are tabulated in **Table A.6**. It is noteworthy (as discussed later in this Chapter) that the surface area and pore volume for the ZIF-8_{45}-71_{55} material are lower than those of the two 'parent' materials (ZIF-8 and ZIF-71). While the structural reasons for this behavior are not known presently, I speculate that the accommodation of the bulky 4,5-dichloroimidazole linkers in the SOD ZIF-8 framework may consume a large amount of pore volume.

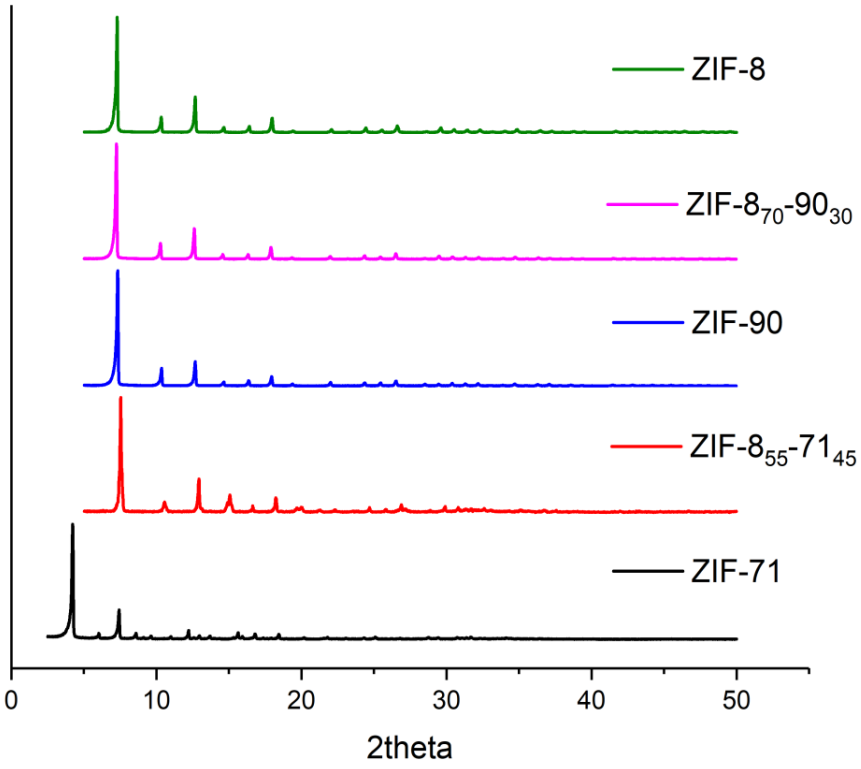

Figure 2.1. PXRD patterns of selected ZIFs used in this study. Corresponding patterns for ZIF-8$_{50}$-90$_{50}$ and ZIF-8$_{30}$-90$_{70}$ can be found in Figure A.2.

The adsorption characteristics of seven adsorbents (ZIF-8, ZIF-8$_{70}$-90$_{30}$, ZIF-8$_{50}$-90$_{50}$, ZIF-8$_{30}$-90$_{70}$, ZIF-90, ZIF-71 and ZIF-8$_{55}$-71$_{45}$) for the vapor-phase separation of butanol from dilute aqueous mixtures are investigated next. First, I consider the separation of butanol from dilute butanol/water mixtures using nitrogen as the carrier gas, using packed bed vapor breakthrough experiments. The vapor feed is generated from a 1 mole%

aqueous butanol solution at 308 K at atmospheric pressure. **Figure 2.2** compares the breakthrough characteristics in terms of normalized mole fraction of water and butanol at the column outlet for ZIF-8, ZIF-8_{50}-90_{50}, ZIF-8_{55}-71_{45}, and ZIF-71. The corresponding data for ZIF-8_{70}-90_{30}, ZIF-8_{30}-90_{70} and ZIF-90 are shown in **Figure A.3**. Water breaks through before butanol in all cases, indicating that all the adsorbents investigated are butanol-selective irrespective of their hydrophobic or hydrophilic character. For all the materials except ZIF-8, a rise (or even a roll-up effect) in the water concentration at the outlet is observed at the onset of butanol breakthrough, indicating that some water adsorbs at the beginning of the breakthrough run but is later displaced by the stronger adsorbing butanol molecules. The adsorbed amounts of water and butanol were calculated for each adsorbent from the breakthrough data and compared with predictions from the ideal adsorbed solution theory (IAST), which is often used to predict mixture adsorption loadings from single-component adsorption isotherms.[53-54] IAST assumes the equal availability of the adsorbent surface area towards all the adsorbates and that in the adsorbed phase the different species mix ideally. Single-component isotherm data used for the IAST predictions for ZIF-8, ZIF-90 and ZIF-8_x-90_{100-x} hybrids were taken from previous work[2] and are reproduced in **Figure A.4**, along with new single-component isotherm data collected in this work for ZIF-71 and the ZIF-8_{55}-71_{45} hybrid.

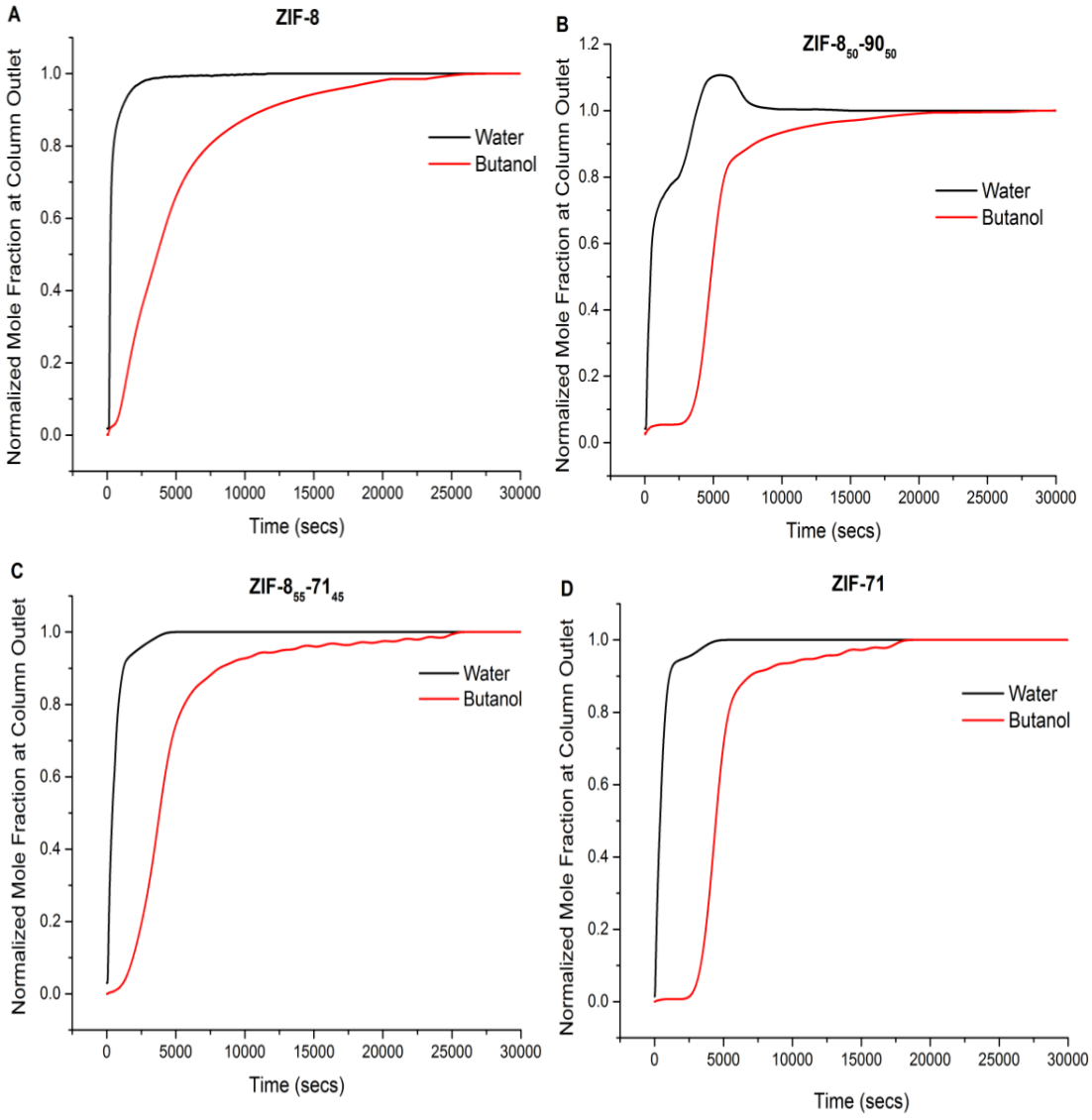

Figure 2.2. Breakthrough curves showing the normalized vapor-phase mole fractions of water and butanol at the outlet of the packed bed adsorber with a step input of the equilibrated vapor phase from a 1 mol% butanol/water solution at a total pressure of 1 atm, temperature of 308 K, and flowrate of 22 cc/min. The four adsorbents shown are: A) ZIF-8, B) ZIF-8_{50}-90_{50}, C) ZIF-8_{55}-71_{45}, and D) ZIF-71.

Figure 2.3 shows the comparison of butanol and water loadings for a 11:89 butanol/water feed vapor mixture at 1 atm and 308 K, obtained from experimental

breakthrough data and IAST predictions. The numerical values are shown in **Table A.7**.The experimentally observed butanol loadings are lowest in ZIF-90, which is also the most hydrophilic adsorbent. As the ZIF-8 linker is introduced in greater amounts *via* the hybrid ZIF-8_x-90_{100-x} series (all in the SOD topology), the water loadings drop substantially whereas the butanol loadings steadily increase and go through a maximum at the ZIF-8_{70}-90_{30} hybrid. In contrast, variation of the linker composition between ZIF-8 and ZIF-71 leads to a minimum in the butanol loading at the ZIF-8_{55}-71_{45} hybrid. This is consistent with the lower BET surface area and pore volume (**Table A.6**) of the SOD-topology ZIF-8_{55}-71_{45} material in relation to both ZIF-8 (SOD) and ZIF-71 (RHO). IAST predictions for butanol loading are in reasonable agreement with the experimental observations, and are able to reproduce the experimentally observed maximum and minimum in the ZIF-8_{70}-90_{30} and ZIF-8_{55}-71_{45} materials respectively. The water adsorption predictions from IAST follow the same trend as the experimental data, but deviate substantially in quantitative terms, especially for the more hydrophobic adsorbents. While IAST predicts close to zero water loading for the hydrophobic materials ZIF-8, ZIF-71, ZIF-8_{55}-71_{45} and ZIF-8_{70}-90_{30}, experimental binary breakthrough data show significantly higher water adsorption. This clearly indicates the role of water co-adsorption *via* hydrogen-bonding to the adsorbing butanol molecules[55-56], an effect that cannot be predicted by IAST.

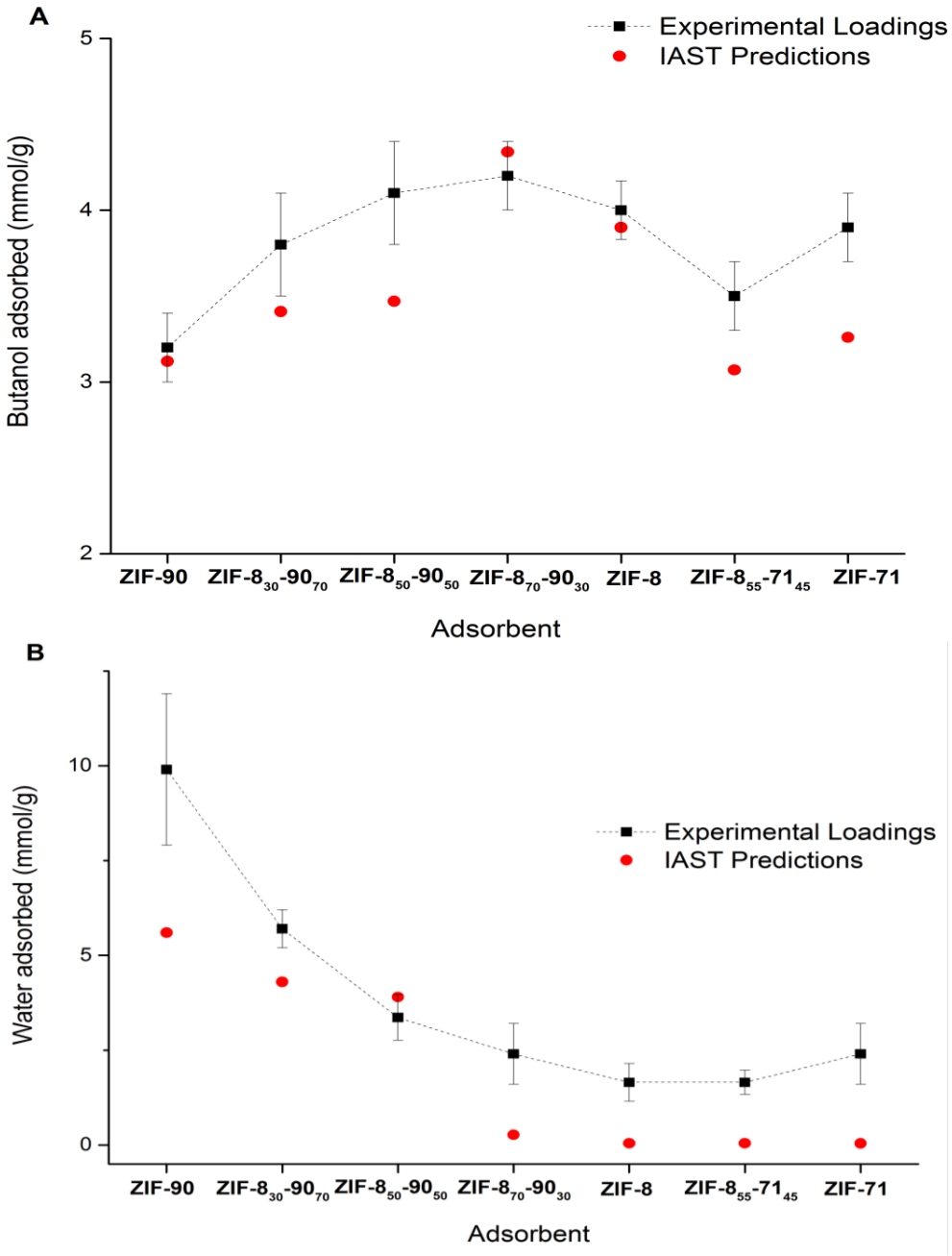

Figure 2.3. A) Butanol and B) water loadings in seven ZIF adsorbents obtained from breakthrough experiments using an 11:89 butanol/water vapor mixture generated from a 1:99 butanol/water solution, at a total pressure of 1 atm at 308 K. IAST predictions are shown for comparison.

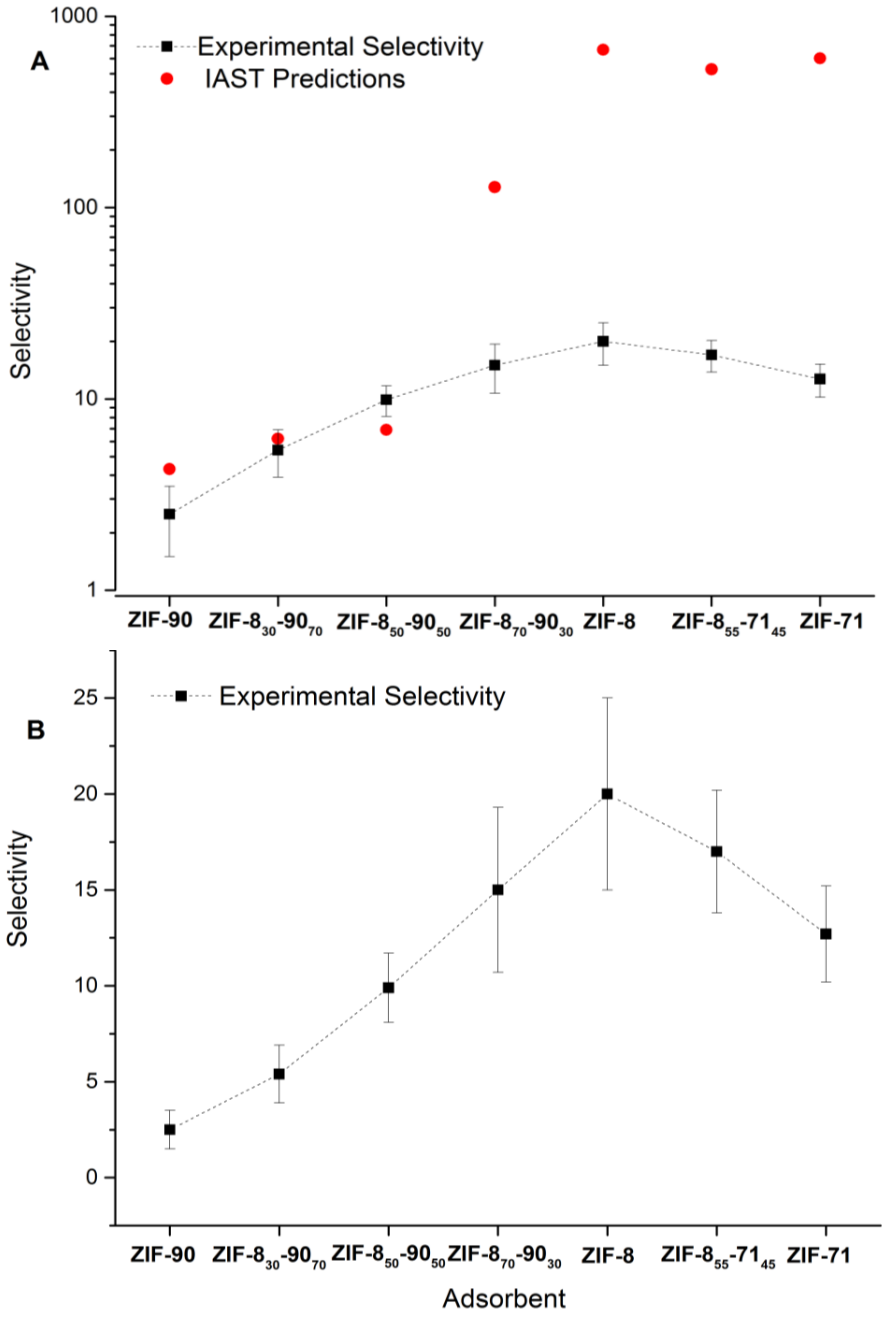

Figure 2.4. Comparison of butanol/water adsorption selectivities obtained from the data shown in Figure 2.3: A) experimental values and IAST predictions on a logarithmic scale, and B) experimental values only plotted on a linear scale.

Figure 2.4 shows the comparison of butanol/water adsorption selectivities from experimental results and IAST predictions, and the numerical values are shown in **Table A.7**. The selectivity increases from ZIF-90 to ZIF-8 among the ZIF-8_x-90_{100-x} hybrids, and ZIF-8 has the highest selectivity (~20) among all seven adsorbents. The ZIF-8_{55}-71_{45} hybrid has comparable selectivity to ZIF-8 (~17) while the next most selective adsorbents are ZIF-71 and the ZIF-8_{70}-90_{30} hybrid. In general, the more hydrophobic adsorbents display higher butanol selectivities. The IAST predictions are close to the experimentally observed selectivities for the more hydrophilic adsorbents ZIF-90, ZIF-8_{30}-90_{70} and ZIF-8_{50}-90_{50}, but greatly overestimate the selectivities for the more hydrophobic adsorbents (**Figure 2.4A**) since IAST cannot predict effects of water co-adsorption. ZIF-8 has the highest butanol selectivity, and hybridization of ZIF-8 in both the ZIF-90 and ZIF-71 directions leads to a decrease in selectivity (**Figure 2.4B**). At this stage, I can therefore identify ZIF-8 and ZIF-71 as the more viable adsorbents for butanol recovery among those studied in this work.

Butanol production by anaerobic fermentation also leads to acetone and ethanol as liquid-phase byproducts, along with evolution of CO_2 and H_2.[1, 3, 57] These fermentation off-gases accumulate in the headspace of the fermenter, and could be used to sparge the fermentation broth instead of using an external inert gas (N_2) stream. Sparging with a gas mixture containing 10% CO_2 and 10% H_2 along with N_2 has been observed to lead to higher butanol yields and a higher butanol/acetone ratio than sparging with N_2 alone.[57] However, if CO_2 (an acid gas under humid conditions) is used for sparging, its effect on the long-term separation performance and stability of any proposed ZIF adsorbents must be evaluated. The presence of acid gases can lead to irreversible structural changes in some

adsorbents and have a detrimental effect on their separation performance.[58-61] The presence of humidity has been shown to be crucial in the acid-gas induced degradation of ZIF-8.[58, 62] PXRD patterns of ZIF-8 have been observed to change in a CO_2 environment under 100% relative humidity (R.H.) at 45 °C after 12 days of exposure.[62] However, no data on the changes in textural or functional properties of ZIF-8 during this process are available. To my knowledge, there are no reports on butanol separation under humid CO_2 conditions using ZIFs. PXRD patterns of ZIF-8 and ZIF-71 adsorbents before and after exposure to humid air and dry CO_2 are shown in **Figure A.5**, and no changes are observed. **Figures 2.5 A-B** show the PXRD patterns of ZIF-8 and ZIF-71 before and after humid CO_2 exposure, while **Figures 2.5 C-D** show the corresponding FTIR spectra. Details of the exposure conditions, and the resulting observed BET surface areas and pore volumes of ZIF-8 and ZIF-71, are tabulated in **Table 2.1**. PXRD patterns and FTIR spectra for all the other adsorbents before and after humid CO_2 exposure are shown in **Figures A.6-A.7** in Appendix A. Under humid CO_2 exposure conditions, considerable changes in the PXRD patterns are observed for ZIF-8, with the appearance of several new peaks, along with a reduction in intensity of the most intense Bragg peak at 7.33° 2θ. These new peaks are similar to those reported in an earlier study on prolonged (12 days) exposure of ZIF-8 under 100% R.H. under a CO_2 atmosphere.[62] The new PXRD peaks can be attributed to the formation of complex carbonate species, which is further corroborated by the FTIR spectra showing new peaks corresponding to carbonate formation at 1330 cm^{-1}.[62] **Figures A.6-A.7** show that complex carbonate formation under humid CO_2 exposure is not limited to ZIF-8 but also occurs in all ZIF-8_x-90_{100-x} hybrids, ZIF-90, and the ZIF-8_{55}-71_{45} hybrid, even though all of these adsorbents are stable under dry CO_2 exposures (data not shown).

The instability of the ZIF-8_x-90_{100-x} hybrids under humid CO_2 is understandable, given that both the parent materials ZIF-8 and ZIF-90 are unstable under the same exposure conditions. Among the materials studied, only the ZIF-71 PXRD patterns and FTIR spectra remain unchanged after humid CO_2 exposure (**Figures 2.5 B, D**) indicating its higher structural stability towards humid CO_2 acid gas attack. The SOD analog of ZIF-71 was also synthesized according to recent literature and I found that it undergoes a partial phase transition even under humid air into a nonporous phase (data not shown).[43] The hybrid ZIF-8_{55}-71_{45} (SOD topology) is stable under humid air but not under humid CO_2 exposure. It appears that ZIF-8 linkers are able to impart phase stability to SOD ZIF-71 under humid air, but the presence of ZIF-8 linkers also allows humid CO_2 attack of the hybrid. It is difficult to ascertain the precise mechanisms associated with the high stability of RHO ZIF-71 at present. The steric effect of 4,5-dichloroimidazole linkers and the electron withdrawing effects of the chlorine atoms could stabilize the Zn-N coordination bond, but the RHO topology also clearly plays a role because of the lack of stability observed in the analogous SOD material.

The textural characteristics shown in **Table 2.1** and **Figure A.8** are consistent with the above observations. All four hydrophobic adsorbents maintain BET surface areas and pore volumes under humid air and dry CO_2. ZIF-71 remains stable after humid CO_2 exposure of more than 10^5 ppm-days, but the other adsorbents lose 25-50% of their surface area and pore volume under these conditions. Clear differences due to the effects of humid CO_2 are observed in the pre and post-exposure SEM images of ZIF-8 in **Figure A.9** while ZIF-71 maintains its morphology and texture before and after humid CO_2 exposure. **Figure**

2.6 shows single-component butanol adsorption isotherms before and after humid CO_2 exposure. ZIF-71 completely maintains its butanol adsorption capacity, whereas the other materials show large decreases. Because of the advantages of using the CO_2-rich headspace off-gas for fermenter sparging to generate the vapor product stream, I conclude that ZIF-71 is a promising adsorbent for use under realistic operational conditions for biobutanol separation.

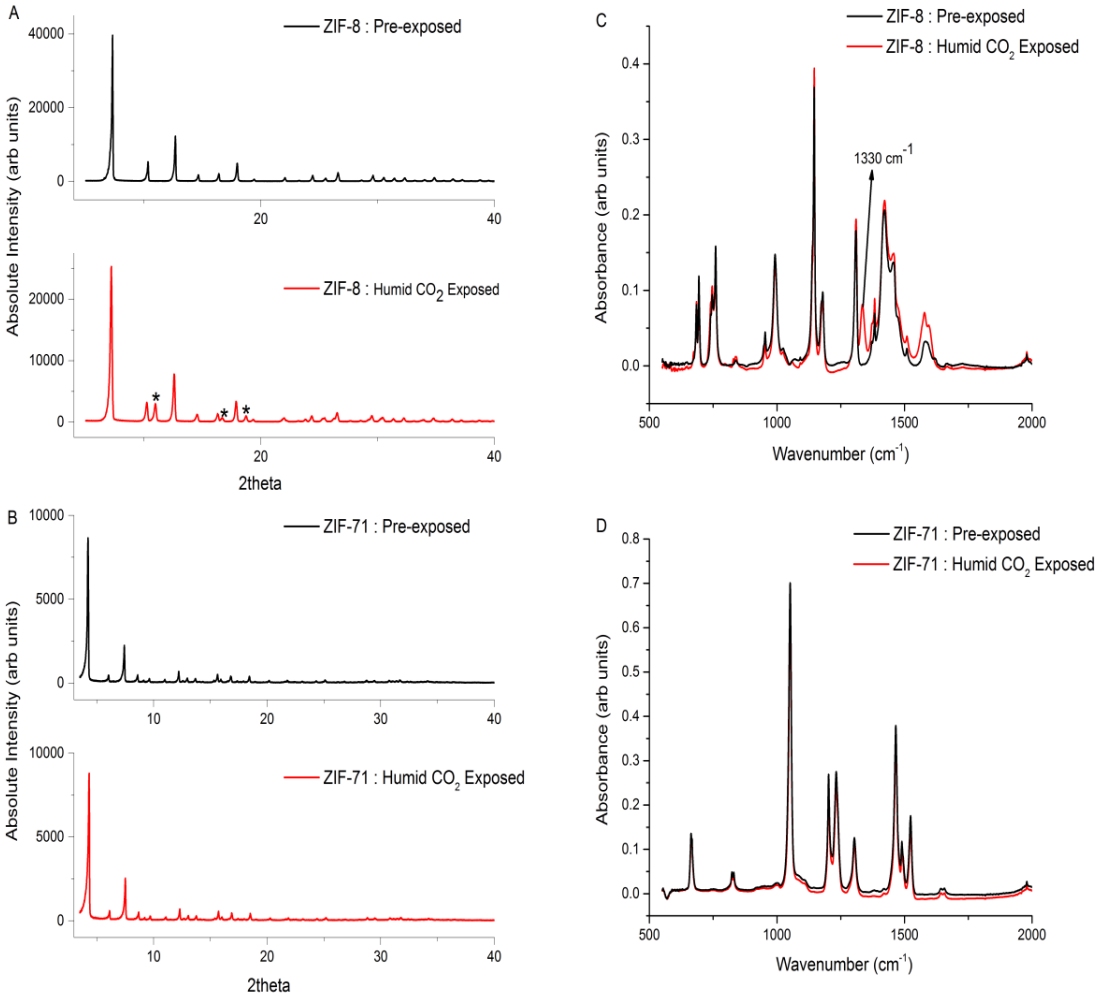

Figure 2.5. PXRD patterns and FTIR spectra of ZIF-8 (A,C) and ZIF-71 (B,D) before and after exposure to humid CO_2. Important PXRD peaks arising after exposure are marked (*).

Table 2.1. Textural characteristics of ZIF-8 and ZIF-71 before and after exposure experiments. The BET surface area is reported as a percentage relative to the pre-exposure value (Table A.5).

Exposure Condition	Exposed Time (days)	CO_2 Conc.	Relative Humidity (%)	Overall Exposure (ppm-days)	Relative BET S.A.		Pore Vol. (cc/g)	
					ZIF-8	ZIF-71	ZIF-8	ZIF-71
Pre-exposure	NA	NA	NA	NA	100	100	0.61	0.34
Humid Air	5	0	90%	0	99	99	0.62	0.34
Dry CO_2	3	12%	0%	3.6×10^5	99	98	0.61	0.33
Humid CO_2	3	12%	90%	3.6×10^5	66	99	0.45	0.34

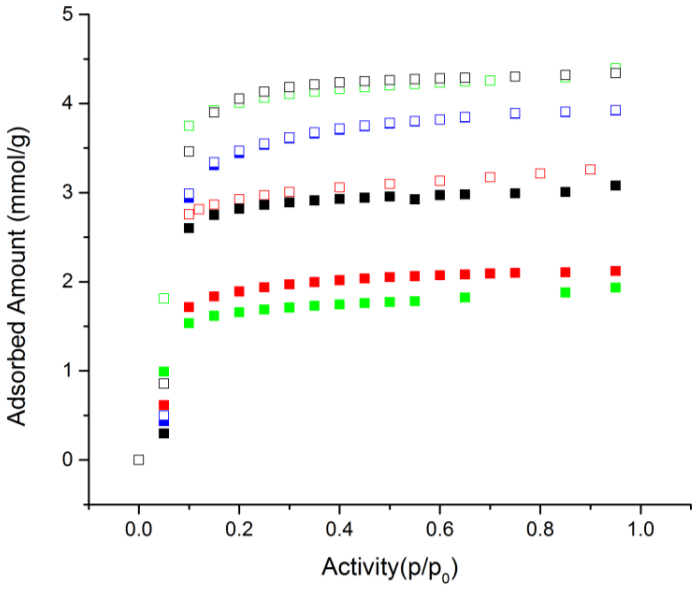

Figure 2.6. Butanol adsorption isotherms of ZIF-8 (black), ZIF-8_{70}-90_{30} (green), ZIF-71 (blue) and ZIF-8_{55}-71_{45} (red). Open symbols correspond to the pristine materials and closed symbols to the materials after humid CO_2 exposure.

Having selected ZIF-71 as the adsorbent of choice for butanol separation from humid CO_2-containing mixtures, its characteristics are now evaluated in more detail. I first consider the case where a 1 mol% butanol-in-water solution is sparged with a 12% CO_2 /12% N_2/76% He gas mixture. Since CO_2 solubility in water is much lower than that of butanol, the vapor compositions in **Table A.3** remain valid. **Figure 2.7A** shows the breakthrough profiles of butanol and water. A rise in outlet water concentration is observed concurrent to butanol breakthrough (as in **Figure 2.2D)**, indicating displacement of water from the adsorbent by the stronger-adsorbing butanol. **Table A.8** summarizes the performance characteristics. The butanol loading and the butanol/water selectivity of 8±2 are comparable to, but lower than, the case where CO_2 is not present (**Table A.7**). The difference is due to increased water adsorption in ZIF-71 in the presence of CO_2. Water and CO_2 form intermolecular hydrogen bonds with each other and this is the likely cause of cooperative adsorption.[63] Finally, I consider the case where a model aqueous ABE solution (total organics content of 1.85 mol%, and 0.6:1:0.25 molar ratio of acetone: butanol: ethanol)[1] is sparged with the same CO_2-enriched gas mixture. The vapor-phase composition remains as given in **Table A.5**. The breakthrough profiles in **Figure 2.7B** show that ZIF-71 remains selective to butanol (**Table A.8**) even in the presence of ethanol, water and acetone with an overall butanol selectivity of 6 (with respect to all the three components taken together). A significant roll up effect is observed for acetone with the onset of butanol breakthrough, and the complex shapes of the breakthrough profiles indicate the effects of competitive and cooperative adsorption in ZIF-71 by the different adsorbates. The butanol capacity remains high (3.1 mmol/g). The higher hydrocarbon content of butanol over acetone and ethanol allows its selective adsorption in ZIF-71. The

ZIF-71 adsorbent was found to retain its entire BET surface area and pore volume on reactivation after the breakthrough run with the ABE model solution with a BET surface area of 830 m^2/g and pore volume of 0.33 cc/g.

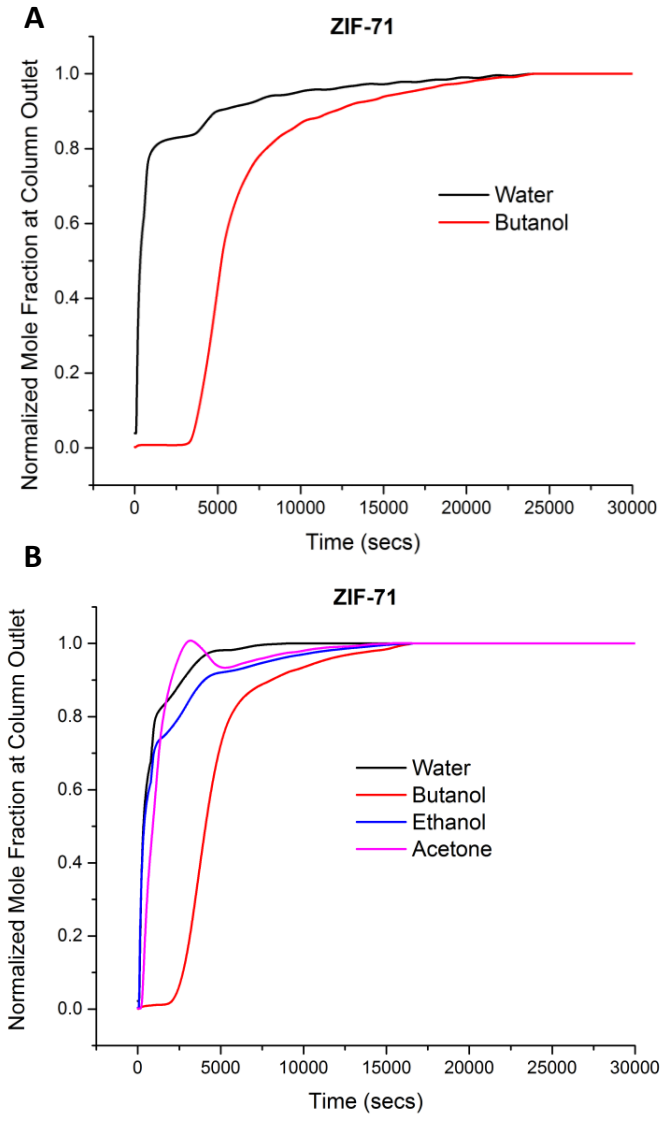

Figure 2.7. Breakthrough profiles showing the normalized mole fractions at the outlet of the packed bed adsorber for two cases: (A) sparged vapor-gas mixture from a 1 mol% butanol in water solution and (B) sparged vapor-gas mixture from a model ABE solution (0.6:1:0.25 molar ratio of acetone : butanol : ethanol) containing 1.85 mol% organics in water. The sparging gas is 12% CO_2 at 1 atm, 308 K, and flowrate of 20 cc/min.

I have also analyzed the desorption of the adsorbed butanol-rich phase in ZIF-71, to determine the ease of product removal from the adsorption column (**Figure A.10**). Analysis of the sequential desorption runs carried out at 308 K and 453 K showed that 90% of the adsorbed butanol and 70% of the adsorbed ethanol was desorbed at 453 K (with the remainder being already removed at 308 K), while more than 75% of the water and acetone were already desorbed at 308 K. These observations are consistent with the stronger adsorption of alcohols in ZIF-71 compared to acetone or water. The high adsorption selectivity for butanol relative to all the other components seen in ZIF-71 (~6), coupled with the vapor-phase butanol enrichment factor (~7.5) due to gas stripping of the ABE solution (**Table A.5**), leads to an overall butanol selectivity ~45.[64] This, combined with the good butanol loading capacity (> 3 mmol/g gravimetric capacity, or equivalently 3.5 mmol/cm^3 ZIF-71 volumetric capacity) and acid gas stability, makes ZIF-71 an attractive option for effective butanol recovery from dilute ABE mixtures. For example, the main desorption product obtained at 453 K (**Figure A.10**) is substantially enriched in butanol with a molar composition of 65%. The residual acetone and ethanol can be easily removed (*e.g.*, in a flash tank) due to their large relative volatilities with respect to butanol, whereas residual water would be removed by well-known approaches such as a hydrophilic zeolite/silica adsorbent or a hydrophilic pervaporation membrane.[1, 65-66]

2.4 Conclusions

In this work I have investigated the separation performance of several representative ZIF adsorbents for 1-butanol separation from dilute aqueous solutions *via* vapor-phase breakthrough experiments combined with gas stripping. When inert gases (N_2 and He) were used for gas stripping from a 1 mol% butanol-water solution, ZIF-8 followed

by ZIF-8_{55}-71_{45}, ZIF-8_{70}-90_{30} and ZIF-71 were found to be most butanol selective, with ZIF-8_{70}-90_{30} showing the maximum butanol capacity of ~4.25 mmol/g. The existence of adsorption maxima and minima in the hybrid ZIF-8-90 and ZIF-8-71 materials points to the potential for further tunability of separation behavior in materials of this kind. Adsorption selectivity predictions using Ideal Adsorbed Solution Theory (IAST) are reasonable for the hydrophilic adsorbents ZIF-90, ZIF-8_{30}-90_{70} and ZIF-8_{50}-90_{50} but are not reliable for the more hydrophobic adsorbents due to the cooperative adsorption of butanol and water. The effect of using CO_2 in the stripping gas was evaluated through humid CO_2 exposure of the ZIF adsorbents. Except for ZIF-71, all the other adsorbents form complex carbonates along with a decrease in butanol uptakes and porosity. This means that ZIF-71, rather than ZIF-8, is the more promising adsorbent under realistic conditions. In general, this finding highlights the importance of determining the performance of ZIF/MOF adsorbents under realistic multicomponent conditions to obtain reliable structure-property relationships that may be quite different from those estimated under idealized or single-component/binary mixture conditions. The importance of acid gas stability in the potential technological applications of ZIFs/MOFs is also illustrated by the present findings. I then extended the study to a model ABE aqueous solution (0.6:1:0.25 mole ratio of acetone, butanol, and ethanol), and found that ZIF-71 was highly butanol-selective even in the presence of multiple other adsorbing components. Sequential desorption was shown to remove butanol at higher temperatures, which is useful in its selective recovery. To my knowledge, this is the first investigation on MOFs being evaluated as adsorbents for vapor-phase biobutanol separations under realistic conditions.

This Chapter explores a practical application of ZIF materials that are stable to acid gases (humid CO_2) and establishes the importance of stability as a metric while choosing materials for an application. Without stability considerations, ZIF-8 has the best performance towards biobutanol separations, but its instability to humid CO_2 makes ZIF-71 the material of choice for this separation application. The results of this Chapter raise a number of fundamental and open questions concerning the stability of ZIFs to stronger acid gases such as SO_2, and NO_2 in the presence of high humidity as well as under dry conditions. It may be possible to impart stability to an incoming humid process stream containing a mixture of different acid gases by removing or reducing the water content to an appropriate level if ZIFs are demonstrated to be stable to other dry acid gases as well. The following Chapters of this thesis are entirely concerned with addressing these questions in a generalized and fundamental manner.

REFERENCES

1. Huang, H. J.; Ramaswamy, S.; Liu, Y. Y., Separation and purification of biobutanol during bioconversion of biomass. *Sep. Purif. Technol.* **2014,** *132*, 513-540.

2. Eum, K.; Jayachandrababu, K. C.; Rashidi, F.; Zhang, K.; Leisen, J.; Graham, S.; Lively, R. P.; Chance, R. R.; Sholl, D. S.; Jones, C. W.; Nair, S., Highly Tunable Molecular Sieving and Adsorption Properties of Mixed-Linker Zeolitic Imidazolate Frameworks. *J.Am.Chem.Soc.* **2015,** *137* (12), 4191-4197.

3. Ranjan, A.; Moholkar, V. S., Biobutanol: science, engineering, and economics. *Int. J. Energy Res.* **2012,** *36* (3), 277-323.

4. Dürre, P., Biobutanol: An attractive biofuel. *Biotechnol. J.* **2007,** *2* (12), 1525-1534.

5. Green, E. M., Fermentative production of butanol - the industrial perspective. *Curr. Opin. Biotechnol.* **2011,** *22* (3), 337-343.

6. Kumar, M.; Gayen, K., Developments in biobutanol production: New insights. *Appl. Energy* **2011,** *88* (6), 1999-2012.

7. Oudshoorn, A.; van der Wielen, L. A. M.; Straathof, A. J. J., Assessment of Options for Selective 1-Butanol Recovery from Aqueous Solution. *Ind. Eng. Chem. Res.* **2009,** *48* (15), 7325-7336.

8. Abdehagh, N.; Dai, B.; Thibault, J.; Tezel, F. H., Biobutanol separation from ABE model solutions and fermentation broths using a combined adsorption - gas stripping process. *J. Chem. Technol. Biotechnol.* **2017,** *92* (1), 245-251.

9. Qureshi, N.; Hughes, S.; Maddox, I. S.; Cotta, M. A., Energy-efficient recovery of butanol from model solutions and fermentation broth by adsorption. *Bioprocess Biosyst. Eng.* **2005,** *27* (4), 215-222.

10. Qureshi, N.; Blaschek, H. P., Recovery of butanol from fermentation broth by gas stripping. *Renewable Energy* **2001,** *22* (4), 557-564.

11. Ennis, B. M.; Marshall, C. T.; Maddox, I. S.; Paterson, A. H. J., Continuous product recovery by in-situ gas stripping/condensation during solvent production from whey permeate using *Clostridium acetobutylicum*. *Biotechnol. Lett.* **1986,** *8* (10), 725-730.

12. Xue, C.; Liu, F. F.; Xu, M. M.; Zhao, J. B.; Chen, L. J.; Ren, J. A.; Bai, F. W.; Yang, S. T., A novel in situ gas stripping-pervaporation process integrated with acetone-butanol-ethanol fermentation for hyper n-butanol production. *Biotechnol. Bioeng.* **2016,** *113* (1), 120-129.

13. Xue, C.; Liu, M.; Guo, X. W.; Hudson, E. P.; Chen, L. J.; Bai, F. W.; Liu, F. F.; Yang, S. T., Bridging chemical- and bio-catalysis: high-value liquid transportation fuel production from renewable agricultural residues. *Green Chem.* **2017,** *19* (3), 660-669.

14. Xue, C.; Zhao, J. B.; Lu, C. C.; Yang, S. T.; Bai, F. W.; Tang, I. C., High-titer n-butanol production by clostridium acetobutylicum JB200 in fed-batch fermentation with intermittent gas stripping. *Biotechnol. Bioeng.* **2012,** *109* (11), 2746-2756.

15. Van der Perre, S.; Gelin, P.; Claessens, B.; Martin-Calvo, A.; Cousin Saint Remi, J.; Duerinck, T.; Baron, G. V.; Palomino, M.; Sánchez, L. Y.; Valencia, S.; Shang, J.; Singh, R.; Webley, P. A.; Rey, F.; Denayer, J. F. M., Intensified Biobutanol Recovery by using Zeolites with Complementary Selectivity. *ChemSusChem* **2017,** *10* (14), 2968-2977.

16. Saint Remi, J. C.; Baron, G.; Denayer, J., Adsorptive separations for the recovery and purification of biobutanol. *Adsorption-Journal of the International Adsorption Society* **2012,** *18* (5-6), 367-373.

17. Zhang, K.; Lively, R. P.; Dose, M. E.; Brown, A. J.; Zhang, C.; Chung, J.; Nair, S.; Koros, W. J.; Chance, R. R., Alcohol and water adsorption in zeolitic imidazolate frameworks. *Chem. Commun.* **2013,** *49* (31), 3245-3247.

18. Cousin Saint Remi, J.; Baron, G.; Denayer, J., Adsorptive separations for the recovery and purification of biobutanol. *Adsorption* **2012,** *18* (5-6), 367-373.

19. Maddox, I. S., Use of silicalite for the adsorption of nomal-butanol from fermentation liquors. *Biotechnol. Lett.* **1982,** *4* (11), 759-760.

20. Nielsen, L.; Larsson, M.; Holst, O.; Mattiasson, B., Adsorbents for extractive bioconversion applied to the acetone-butanol fermentation. *Appl. Microbiol. Biotechnol.* **1988,** *28* (4-5), 335-339.

21. Regdon, I.; Kiraly, Z.; Dekany, I.; Lagaly, G., Adsorption of 1-butanol from water on modified silicate surfaces. *Colloid Polym. Sci.* **1994,** *272* (9), 1129-1135.

22. Remy, T.; Saint Remi, J. C.; Singh, R.; Webley, P. A.; Baron, G. V.; Denayer, J. F. M., Adsorption and Separation of C1-C8 Alcohols on SAPO-34. *J. Phys. Chem. C* **2011,** *115* (16), 8117-8125.

23. Saint Remi, J. C.; Remy, T.; Van Hunskerken, V.; van de Perre, S.; Duerinck, T.; Maes, M.; De Vos, D.; Gobechiya, E.; Kirschhock, C. E. A.; Baron, G. V.; Denayer, J. F. M., Biobutanol Separation with the Metal-Organic Framework ZIF-8. *Chemsuschem* **2011,** *4* (8), 1074-1077.

24. Saravanan, V.; Waijers, D. A.; Ziari, M.; Noordermeer, M. A., Recovery of 1-butanol from aqueous solutions using zeolite ZSM-5 with a high Si/Al ratio; suitability of a column process for industrial applications. *Biochem. Eng. J.* **2010,** *49* (1), 33-39.

25. Xue, C.; Zhao, J. B.; Chen, L. J.; Bai, F. W.; Yang, S. T.; Sun, J. X., Integrated butanol recovery for an advanced biofuel: current state and prospects. *Appl. Microbiol. Biotechnol.* **2014,** *98* (8), 3463-3474.

26. Xue, C.; Zhao, J. B.; Chen, L. J.; Yang, S. T.; Bai, F. W., Recent advances and state-of-the-art strategies in strain and process engineering for biobutanol production by Clostridium acetobutylicum. *Biotechnol. Adv.* **2017,** *35* (2), 310-322.

27. Vane, L. M.; Alvarez, F. R., Hybrid vapor stripping-vapor permeation process for recovery and dehydration of 1-butanol and acetone/butanol/ethanol from dilute aqueous solutions. Part 1. Process Simulations. *J. Chem. Technol. Biotechnol.* **2013,** *88* (8), 1436-1447.

28. Vane, L. M.; Alvarez, F. R.; Rosenblum, L.; Govindaswamy, S., Hybrid vapor stripping-vapor permeation process for recovery and dehydration of 1-butanol and acetone/butanol/ethanol from dilute aqueous solutions. Part 2. Experimental validation with simple mixtures and actual fermentation broth. *J. Chem. Technol. Biotechnol.* **2013,** *88* (8), 1448-1458.

29. Xue, C.; Wang, Z. X.; Wang, S. D.; Zhang, X. T.; Chen, L. J.; Mu, Y.; Bai, F. W., The vital role of citrate buffer in acetone-butanol-ethanol (ABE) fermentation using corn stover and high-efficient product recovery by vapor stripping-vapor permeation (VSVP) process. *Biotechnol. Biofuels* **2016,** *9*, 1-9.

30. Xue, C.; Zhao, J. B.; Liu, F. F.; Lu, C. C.; Yang, S. T.; Bai, F. W., Two-stage in situ gas stripping for enhanced butanol fermentation and energy-saving product recovery. *Bioresour. Technol.* **2013,** *135*, 396-402.

31. Farzaneh, A.; Zhou, M.; Potapova, E.; Bacsik, Z.; Ohlin, L.; Holmgren, A.; Hedlund, J.; Grahn, M., Adsorption of Water and Butanol in Silicalite-1 Film Studied with in Situ Attenuated Total Reflectance-Fourier Transform Infrared Spectroscopy. *Langmuir* **2015,** *31* (17), 4887-4894.

32. Cao, Y. H.; Wang, K. L.; Wang, X. M.; Gu, Z. R.; Gibbons, W.; Vu, H., Butanol vapor adsorption behavior on active carbons and zeolite crystal. *Appl. Surf. Sci.* **2015,** *349*, 1-7.

33. Cao, Y. H.; Wang, K. L.; Wanga, X. M.; Gu, Z. R.; Gibbons, W.; Vu, H., Adsorption of butanol vapor on active carbons with nitric acid hydrothermal modification. *Bioresour. Technol.* **2015,** *196*, 525-532.

34. Farzaneh, A.; DeJaco, R. F.; Ohlin, L.; Holmgren, A.; Siepmann, J. I.; Grahn, M., Comparative Study of the Effect of Defects on Selective Adsorption of Butanol from Butanol/Water Binary Vapor Mixtures in Silicalite-1 Films. *Langmuir* **2017,** *33* (34), 8420-8427.

35. Banerjee, R.; Phan, A.; Wang, B.; Knobler, C.; Furukawa, H.; O'Keeffe, M.; Yaghi, O. M., High-throughput synthesis of zeolitic imidazolate frameworks and application to CO_2 capture. *Science* **2008,** *319* (5865), 939-943.

36. Park, K. S.; Ni, Z.; Cote, A. P.; Choi, J. Y.; Huang, R. D.; Uribe-Romo, F. J.; Chae, H. K.; O'Keeffe, M.; Yaghi, O. M., Exceptional chemical and thermal stability of zeolitic imidazolate frameworks. *Proc. Natl. Acad. Sci. U. S. A.* **2006,** *103* (27), 10186-10191.

37. Phan, A.; Doonan, C. J.; Uribe-Romo, F. J.; Knobler, C. B.; O'Keeffe, M.; Yaghi, O. M., Synthesis, Structure, and Carbon Dioxide Capture Properties of Zeolitic Imidazolate Frameworks. *Acc. Chem. Res.* **2010,** *43* (1), 58-67.

38. Pimentel, B. R.; Parulkar, A.; Zhou, E.-k.; Brunelli, N. A.; Lively, R. P., Zeolitic Imidazolate Frameworks: Next-Generation Materials for Energy-Efficient Gas Separations. *Chemsuschem* **2014,** *7* (12), 3202-3240.

39. Zhang, K.; Lively, R. P.; Zhang, C.; Chance, R. R.; Koros, W. J.; Sholl, D. S.; Nair, S., Exploring the Framework Hydrophobicity and Flexibility of ZIF-8: From Biofuel Recovery to Hydrocarbon Separations. *J.Phys.Chem.Lett.* **2013,** *4* (21), 3618-3622.

40. Zhang, C.; Lively, R. P.; Zhang, K.; Johnson, J. R.; Karvan, O.; Koros, W. J., Unexpected Molecular Sieving Properties of Zeolitic Imidazolate Framework-8. *J.Phys.Chem.Lett.* **2012,** *3* (16), 2130-2134.

41. Zhang, K.; Lively, R. P.; Zhang, C.; Koros, W. J.; Chance, R. R., Investigating the Intrinsic Ethanol/Water Separation Capability of ZIF-8: An Adsorption and Diffusion Study. *J. Phys. Chem. C* **2013,** *117* (14), 7214-7225.

42. Gee, J. A.; Chung, J.; Nair, S.; Sholl, D. S., Adsorption and Diffusion of Small Alcohols in Zeolitic Imidazolate Frameworks ZIF-8 and ZIF-90. *J. Phys. Chem. C* **2013,** *117* (6), 3169-3176.

43. Schweinefuss, M. E.; Springer, S.; Baburin, I. A.; Hikov, T.; Huber, K.; Leoni, S.; Wiebcke, M., Zeolitic imidazolate framework-71 nanocrystals and a novel SOD-type polymorph: solution mediated phase transformations, phase selection via coordination modulation and a density functional theory derived energy landscape. *Dalton Trans.* **2014,** *43* (9), 3528-3536.

44. Thompson, J. A.; Blad, C. R.; Brunelli, N. A.; Lydon, M. E.; Lively, R. P.; Jones, C. W.; Nair, S., Hybrid Zeolitic Imidazolate Frameworks: Controlling Framework Porosity and Functionality by Mixed-Linker Synthesis. *Chem. Mater.* **2012,** *24* (10), 1930-1936.

45. Thompson, J. A.; Brunelli, N. A.; Lively, R. P.; Johnson, J. R.; Jones, C. W.; Nair, S., Tunable CO_2 Adsorbents by Mixed-Linker Synthesis and Postsynthetic Modification of Zeolitic Imidazolate Frameworks. *J. Phys. Chem. C* **2013,** *117* (16), 8198-8207.

46. Walton, K. S.; Snurr, R. Q., Applicability of the BET method for determining surface areas of microporous metal-organic frameworks. *J.Am.Chem.Soc.* **2007,** *129* (27), 8552-8556.

47. Dortmund Data Bank. 2017 ed.; http://www.ddbst.com/, 2017.

48. VLE-calc. 2017 ed.; http://vle-calc.com/index.html, 2017.

49. Butler, J. A. V.; Thomson, D. W.; Maclennan, W. H., The free energy of the normal aliphatic alcohols in aqueous solution - Part I The partial vapour pressures of aqueous solutions of methyl, n-propyl, and n-butyl alcohols - Part II The solubilities of some normal aliphatic alcohols in water - Part III The theory of binary solutions, and its application to aqueous-alcoholic solutions. *J.Chem.Soc.* **1933**, 674-686.

50. Venna, S. R.; Jasinski, J. B.; Carreon, M. A., Structural Evolution of Zeolitic Imidazolate Framework-8. *J.Am.Chem.Soc.* **2010,** *132* (51), 18030-18033.

51. Yen, C. I.; Liu, S. M.; Lo, W. S.; Wu, J. W.; Liu, Y. H.; Chein, R. J.; Yang, R. Q.; Wu, K. C. W.; Hwu, J. R.; Ma, N. H.; Shieh, F. K., Cytotoxicity of Postmodified Zeolitic Imidazolate Framework-90 (ZIF-90) Nanocrystals: Correlation between Functionality and Toxicity. *Chem. - Eur. J.* **2016,** *22* (9), 2925-2929.

52. Jian, M.; Liu, B.; Liu, R.; Qu, J.; Wang, H.; Zhang, X., Water-based synthesis of zeolitic imidazolate framework-8 with high morphology level at room temperature. *RSC Adv.* **2015,** *5* (60), 48433-48441.

53. Myers, A. L.; Prausnitz, J. M., Thermodynamics of mixed-gas adsorption. *AIChE J.* **1965,** *11* (1), 121-127.

54. Walton, K. S.; Sholl, D. S., Predicting multicomponent adsorption: 50 years of the ideal adsorbed solution theory. *AIChE J.* **2015,** *61* (9), 2757-2762.

55. Fouad, W. A.; Wang, L.; Haghmoradi, A.; Asthagiri, D.; Chapman, W. G., Understanding the Thermodynamics of Hydrogen Bonding in Alcohol-Containing Mixtures: Cross-Association. *J. Phys. Chem. B* **2016,** *120* (13), 3388-3402.

56. Nalaparaju, A.; Zhao, X. S.; Jiang, J. W., Molecular Understanding for the Adsorption of Water and Alcohols in Hydrophilic and Hydrophobic Zeolitic Metal-Organic Frameworks. *J. Phys. Chem. C* **2010,** *114* (26), 11542-11550.

57. Mollah, A. H.; Stuckey, D. C., The influence of H_2, CO_2 and dilution rate on the continuous fermentation of acetone-butanol. *Appl. Microbiol. Biotechnol.* **1992,** *37* (5), 533-538.

58. Bhattacharyya, S.; Pang, S. H.; Dutzer, M. R.; Lively, R. P.; Walton, K. S.; Sholl, D. S.; Nair, S., Interactions of SO_2-Containing Acid Gases with ZIF-8: Structural Changes and Mechanistic Investigations. *J. Phys. Chem. C* **2016,** *120* (48), 27221-27229.

59. Pang, S. H.; Han, C.; Sholl, D. S.; Jones, C. W.; Lively, R. P., Facet-Specific Stability of ZIF-8 in the Presence of Acid Gases Dissolved in Aqueous Solutions. *Chem. Mater.* **2016,** *28* (19), 6960-6967.

60. Mounfield, W. P.; Han, C.; Pang, S. H.; Tumuluri, U.; Jiao, Y.; Bhattacharyya, S.; Dutzer, M. R.; Nair, S.; Wu, Z.; Lively, R. P.; Sholl, D. S.; Walton, K. S., Synergistic Effects of Water and SO_2 on Degradation of MIL-125 in the Presence of Acid Gases. *J. Phys. Chem. C* **2016,** *120* (48), 27230-27240.

61. Zhu, G. H.; Hoffman, C. D.; Liu, Y.; Bhattacharyya, S.; Tumuluri, U.; Jue, M. L.; Wu, Z. L.; Sholl, D. S.; Nair, S.; Jones, C. W.; Lively, R. P., Engineering Porous Organic Cage Crystals with Increased Acid Gas Resistance. *Chem. - Eur. J.* **2016,** *22* (31), 10743-10747.

62. Mottillo, C.; Friscic, T., Carbon Dioxide Sensitivity of Zeolitic Imidazolate Frameworks. *Angew. Chem., Int. Ed.* **2014,** *53* (29), 7471-7474.

63. Kumar, P. P.; Kalinichev, A. G.; Kirkpatrick, R. J., Hydrogen-Bonding Structure and Dynamics of Aqueous Carbonate Species from Car-Parrinello Molecular Dynamics Simulations. *J. Phys. Chem. B* **2009,** *113* (3), 794-802.

64. Hu, S.; Guan, Y.; Cai, D.; Li, S. F.; Qin, P. Y.; Karim, M. N.; Tan, T. W., A novel method for furfural recovery via gas stripping assisted vapor permeation by a polydimethylsiloxane membrane. *Sci. Rep.* **2015,** *5*, 1-9.

65. Vane, L. M., Separation technologies for the recovery and dehydration of alcohols from fermentation broths. *Biofuels, Bioprod. Biorefin.* **2008,** *2* (6), 553-588.

66. Luyben, W. L., Control of the Heterogeneous Azeotropic n-Butanol/Water Distillation System. *Energy Fuels* **2008,** *22* (6), 4249-4258.

CHAPTER 3. INTERACTIONS OF SO_2-CONTAINING ACID GASES WITH ZIF-8

3.1 Introduction*

As mentioned in Chapter 1, the well-known ZIF-8 provides a useful starting point for developing a generalized understanding of the stability of ZIFs in acid gas environments. In this Chapter, I have investigated the stability of a well-known ZIF (ZIF-8) on exposure to the acid gas SO_2 in dry, humid and aqueous environments. Stability of ZIF-8 in the context of this thesis is defined in terms of the extent to which it retains its porous crystal structure and internal surface area upon exposure under the particular conditions, as in similar earlier characterization of MOF stability upon water exposure.[1] I have first characterized in quantitative detail the effects of acid gas exposure on the structure and textural properties of ZIF-8. Then, I have investigated the mechanistic aspects of the degradation characteristics of ZIF-8, and presented a molecular-level mechanism that is consistent with the experimental observations.

* Work in this Chapter has been published previously in **S. Bhattacharyya**, **S**. H. Pang, M. R. Dutzer, R. P. Lively, K. S. Walton, D. S. Sholl, S. Nair, "Interactions of SO_2-Containing Acid Gases with ZIF-8: Structural Changes and Mechanistic Investigations". *J.Phys.Chem.C* **2016,** *120* (48), 27221-27229

3.2 Experimental Methods

3.2.1 ZIF-8 Synthesis

Zinc(II) nitrate hexahydrate (Alfa Aesar), 2-methylimidazole (Sigma-Aldrich), sodium formate (Sigma-Aldrich) and methanol (BDH, HPLC grade) were used as received without further purification. ZIF-8 was synthesized by modifying the procedure reported by Gee et al.[2] 0.972 g 2-methylimidazole and 1.614 g sodium formate were dissolved in 120 mL methanol and sonicated to dissolve completely. 1.764 g zinc (II) nitrate was dissolved in 120 mL methanol added to the first solution. The combined solution was then heated in a glass jar to 90 °C for 24 hours. The crystals were collected and washed with fresh methanol three times and then air dried at 60 °C. All crystals were activated at 180 °C in vacuum for 24 hours prior to exposure experiments.

3.2.2 Humid SO_2 Exposure

Activated samples were exposed to varying concentrations (ppm) of SO_2 in air with relative humidity of 85% for different time intervals (5 days and 10 days) at room temperature (298 K). The acid gas mixture was prepared according to previous literature reports, with slight modifications.[3] The SO_2 gas was generated from a 400 mL aqueous solution of 0.5 mg/mL $NaHSO_3$ at a *p*H of 3.7 at 318 K. The temperature of the solution was maintained with a water bath (VWR). Air at 60 mL/min was bubbled through the solution and carried humid SO_2 gas stream to the exposure unit (Secador mini-desiccator). Gas concentration inside the transparent exposure unit was continuously monitored with the portable PAC 7000 SO_2 detector purchased from Dräger. Data from the detector was transferred to a computer after the exposure run was finished. The relative humidity was

continuously monitored by a commercial available humidity sensor (Ambient Weather). A second SO_2 sensor was kept running outside the exposure unit for leak detection. Steady state levels of SO_2 and relative humidity were achieved within a few hours. The $NaHSO_3$ solution was refilled to maintain SO_2 level after every 2 days. The water bath, acid gas generator unit and exposure unit were all placed inside a fume hood with high exhaust rates and handled with caution at all times. All samples were re-activated at 453 K in vacuum for 24 hours after exposure experiments prior to characterization. For energy dispersive X-ray spectroscopy (EDX) and Fourier transform infrared spectroscopy (FTIR) measurements, samples were characterized both before and after reactivation following acid gas exposure.

3.2.3 Aqueous SO_2 Exposure

Dilute aqueous solutions of SO_2 were prepared by diluting a stock solution of aqueous SO_2 (6.2%, Sigma Aldrich). The SO_2 concentration of 2.5×10^{-5} mol/kg was determined based on the concentration in equilibrium with 20 ppm SO_2 in the vapor phase, according to Henry's law ($K_{H,\ SO2}$ = 1.25 mol/kg·bar). A solution at the desired concentration was introduced into a 60 mL glass vial with approximately 200 mg of ZIF-8 and sealed. The vials were briefly sonicated to ensure good dispersions of the particles within the solutions. After 5 days at room temperature, the resulting solids were filtered or centrifuged and washed copiously with DI water and methanol to remove weakly bound ions and decomposed linkers. All samples were re-activated at 453 K in vacuum for 24 hours after exposure experiments prior to characterization.

3.2.4 Dry SO_2 Adsorption

Sulfur dioxide (Airgas, anhydrous, 99.98% purity) adsorption isotherms were measured at 298 K for pressures ranging from 0 to approximately 2.5 bar using a lab-built volumetric system. Each sample (30-50 mg) was outgassed under dynamic vacuum at 453 K for 5 hours. SO_2 adsorption loading was determined by measuring the pressure drop in the sample cell, and this pressure drop was converted to moles using the Peng-Robinson equation of state.

3.2.5 Characterization

Activated ZIF-8 samples before and after exposure to acid gases were characterized with powder X-ray diffraction (PXRD), nitrogen physisorption (NP) at 77 K, scanning electron microscopy (SEM), energy dispersive X-ray spectroscopy (EDX), Fourier transform infrared spectroscopy (FTIR) and X-ray photoelectron spectroscopy (XPS). PXRD measurements were conducted on an X'Pert Pro PANalytical Xray Diffractometer in reflection Bragg-Brentano geometry operating with a Cu anode at 45 kV and 40 mA. PXRD patterns were collected with a step size of 0.02 degrees 2θ and scan time of 10 s/step over 4-50 degrees 2θ using an X'celerator detector. The peak intensities were normalized with respect to the highest intensity peak (indexed as (011)) in ZIF-8. The surface area and pore volume analysis was conducted by NP (p/p_o = 0.05 to 0.3) at 77 K using a BET surface area analyzer (Tristar, Micromeritics). SEM imaging and EDX measurements were carried out with Zeiss LEO 1530 and 1550 scanning electron microscopes. Samples were first coated with gold by sputtering under vacuum for 60 seconds. Images were taken at 15 kV accelerating voltage, and EDX analysis was also done at 15 kV. FTIR spectroscopy was

recorded by a Thermo Scientific Nicolet iS50 FT-IR equipped with an iS50 ATR module. Samples were analyzed in powder form from 550-4000 cm^{-1} with 96 scans with a resolution of 2 cm^{-1}. X-ray photoelectron spectra were acquired on a Thermo K-Alpha XPS with Al Kα radiation. High-resolution spectra for the S2p binding region were acquired from 157-175 eV in 0.1 eV steps over 8 scans.

3.3 Results and Discussion

The crystalline structure of the activated ZIF-8 samples before and after exposure to humid air, aqueous SO_2, dry SO_2 and humid SO_2 is characterized by PXRD (**Figure 3.1**). The PXRD intensities are shown on a log scale to highlight subtle changes. The PXRD patterns of ZIF-8 exposed to humid air at 85% R.H. for 5 days, 100 ppm-days of aqueous SO_2, and to dry SO_2 do not change significantly from that of the pre-exposure ZIF-8. This indicates structural stability and retention of long-range order. However, at 200 ppm-days humid SO_2 exposure, the PXRD pattern shows considerable changes (**Figure 3.1**) especially at $2\theta > 20°$. The PXRD patterns after humid SO_2 exposure over 100 or 200 ppm-days show a progressive decrease in the peak intensities and increase in the background signal, indicating structural degradation and increasing amorphous character. For display purposes, the patterns in **Figure 3.1** are normalized with respect to the most intense Bragg peak at 7.33° 2θ corresponding to (011) planes[4], and are plotted without any vertical offsets. Integrated areal intensity (**Figure 3.2**) of the non-normalized (011) Bragg peak is used to estimate the relative crystallinity. **Figure 3.2** shows a sharp decrease in the (011) Bragg intensity upon 100 ppm-days of humid SO_2 exposure. Exposure to humid air, dry SO_2 or aqueous SO_2 does not lead to any significant loss in (011) peak intensity. The

greatest relative crystallinity loss (82%) is observed for the ZIF-8 sample exposed to 200 ppm-days of humid SO_2.

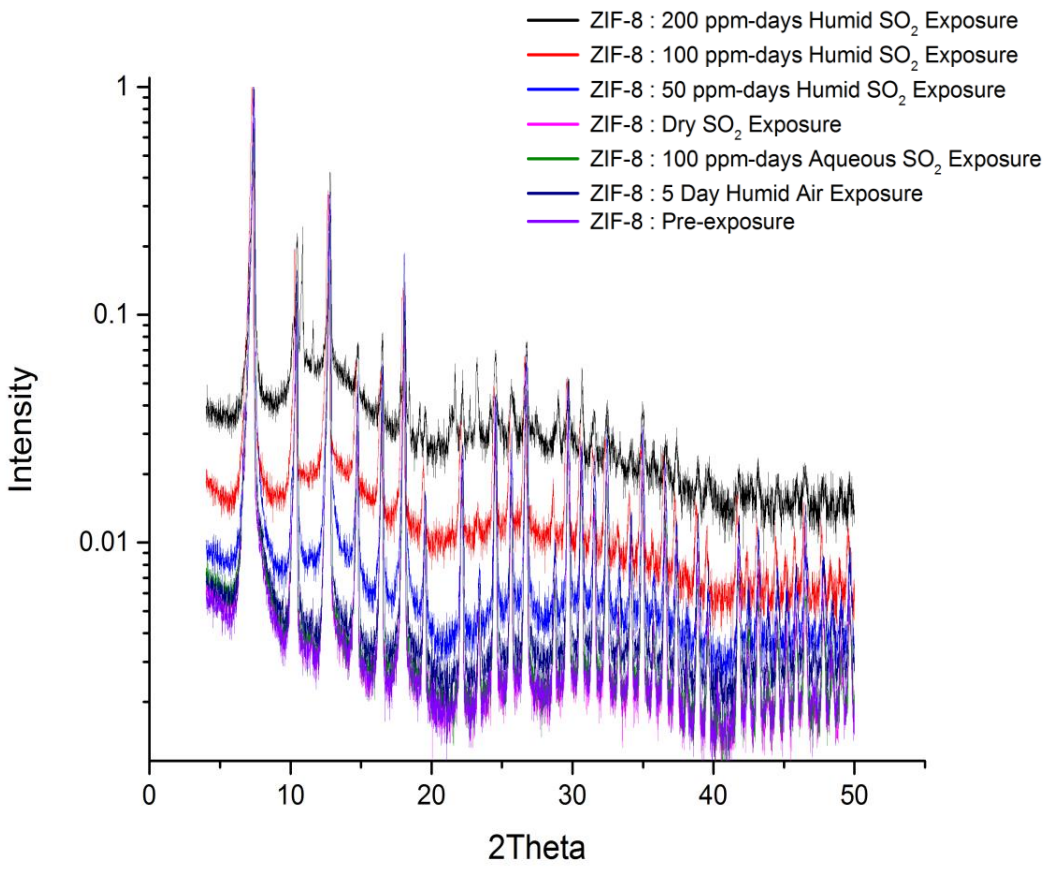

Figure 3.1. PXRD patterns of ZIF-8 under different exposure conditions.

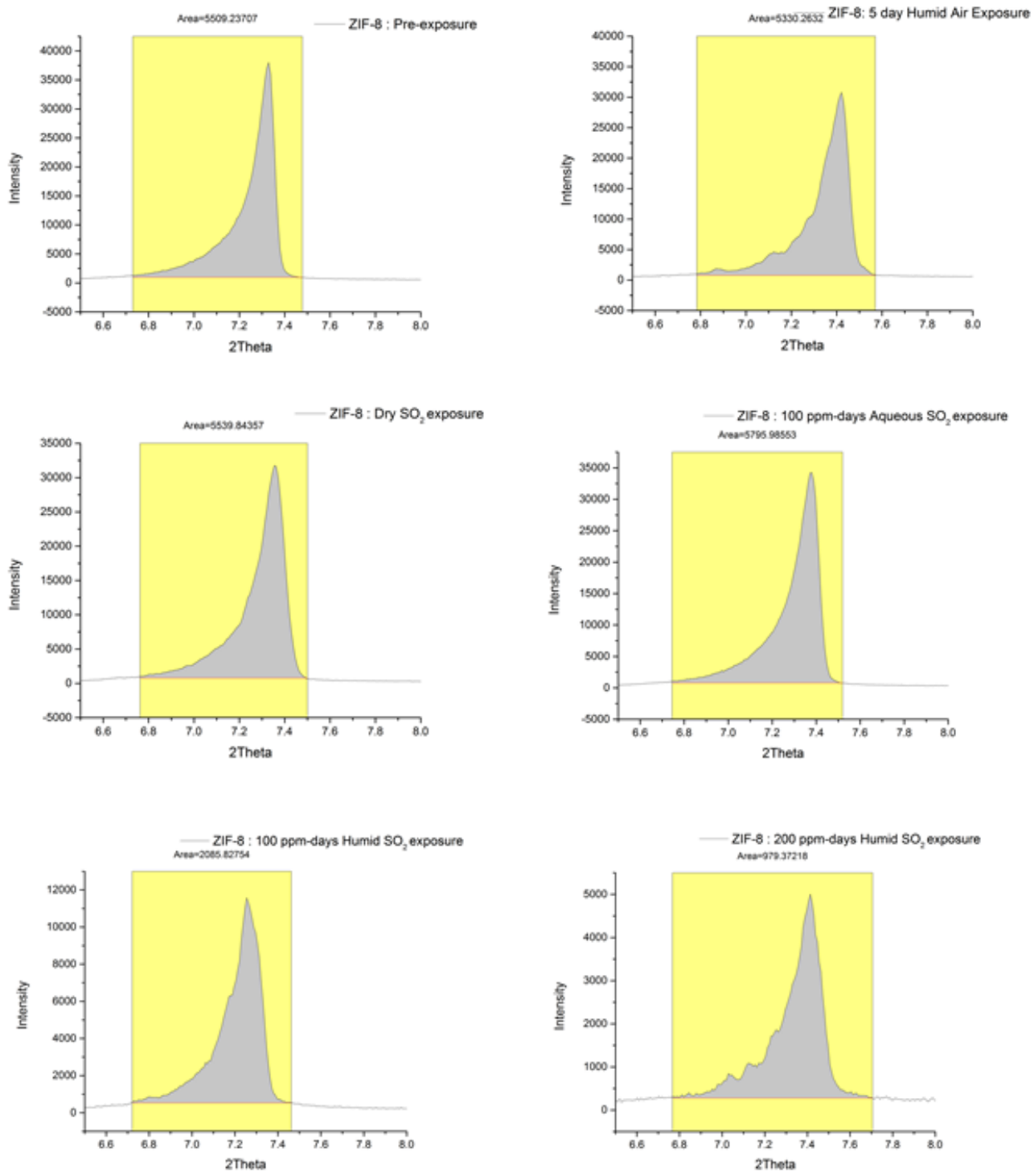

Figure 3.2. Integration of the areal intensity of the ZIF-8 (011) peak. The ratio of this integrated area with respect to that of the pre-exposed ZIF-8 sample was used to determine the relative crystallinity of the sample under different exposure conditions.

Figure 3.3 shows the NP isotherms at 77 K after various exposures to SO_2. The calculated Brunauer–Emmett–Teller (BET) surface areas and the measured pore volumes are shown in **Table 3.1**. Adsorbed N_2 amounts remain essentially unchanged after exposure to dry SO_2, aqueous SO_2, and humid air. Upon humid SO_2 exposure, ZIF-8 shows a decrease of BET surface area by 11%, 32% and 70% after 50 ppm-days, 100 ppm-days and 200 ppm-days of exposure, respectively. The pore volumes also decrease from ~0.61 cc/g for pre-exposed ZIF-8 to 0.54, 0.42 and 0.19 cc/g, respectively, for progressive humid SO_2 exposures. The information in **Table 3.1** and **Figures 3.1-3.3** conclusively establish that the combined attack by SO_2 and water vapor greatly increases the rate of ZIF-8 degradation in relation to other exposure modes.

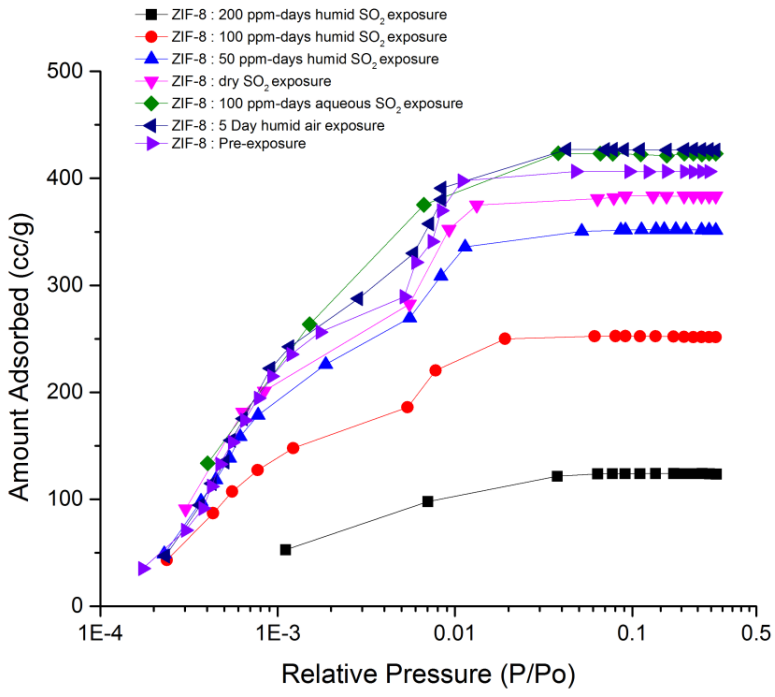

Figure 3.3. N_2 physisorption at 77 K in pre-exposed ZIF-8 and reactivated ZIF-8 after different exposure protocols.

Table 3.1. Textural characteristics of ZIF-8 after different exposure experiments. BET surface area is reported as a percentage relative to pre-exposed ZIF-8.
* Based upon the average SO_2 concentration during the dry SO_2 isotherm measurements.

Exposure Condition	Exposed Time (days)	SO_2 Conc.	Overall Exposure (ppm-days)	Relative BET SA	Pore Vol. (cc/g)
Pre-exposed	NA	NA	NA	100	0.61
Humid air	5	0	0	99	0.62
Aq. SO_2	5	20 ppm	100	102	0.62
Dry SO_2	0.15	99.98%	$*1.8 \times 10^5$	96	0.61
Humid SO_2	5	10 ppm	50	88	0.54
Humid SO_2	5	20 ppm	100	68	0.42
Humid SO_2	10	20 ppm	200	30	0.19

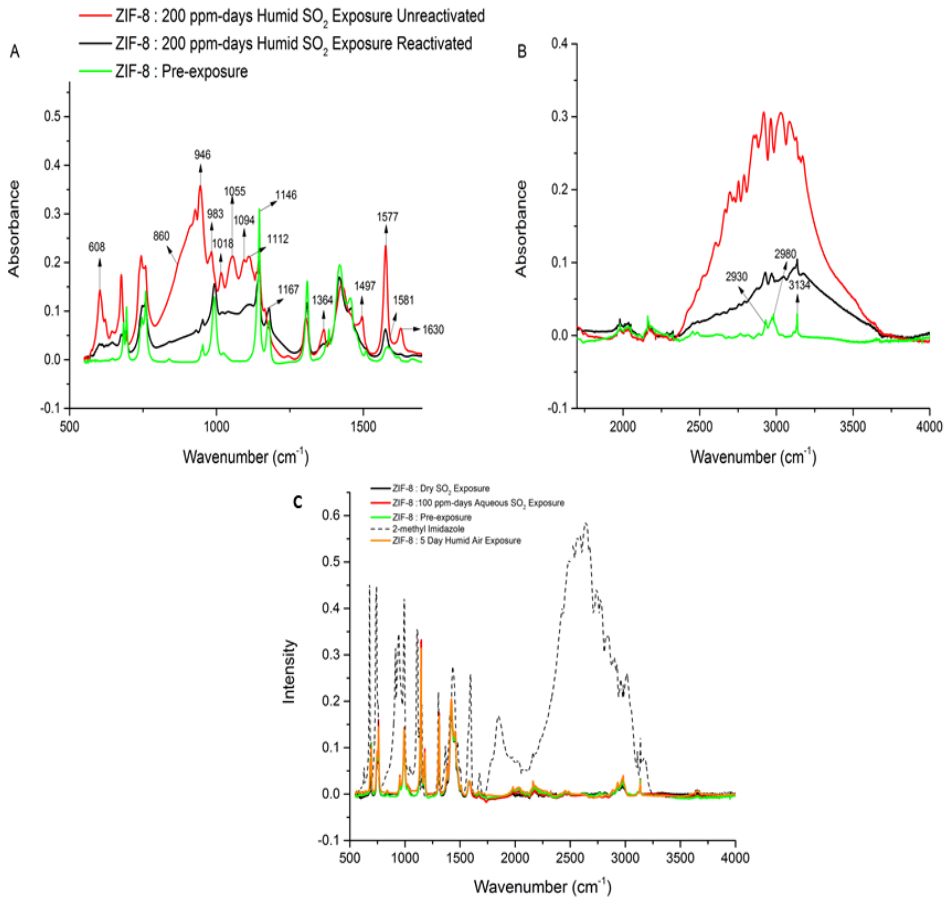

Figure 3.4. FTIR spectra in two different wavenumber ranges (A-B) for pre-exposed ZIF-8 (green), ZIF-8 exposed to 200 ppm-days humid SO_2 before reactivation (red) and ZIF-8 exposed to 200 ppm-days humid SO_2 after reactivation (black). (C) FTIR spectra of ZIF-8 exposed to SO_2 under dry, humid and aqueous conditions compared to pre-exposed ZIF-8 and the protonated 2-mim linker.

I have used FTIR spectroscopy to examine the changes in the chemical bonding environments in ZIF-8 before and after humid SO_2 exposure. **Figures 3.4 A-B** show the pre-exposed ZIF-8 and the 200 ppm-days humid SO_2 exposed ZIF-8 FTIR spectra before and after reactivation with specific peaks discussed below marked. The FTIR spectrum of the protonated ZIF-8 linker 2-methylimidazole (2-mIm) is shown in **Figure 3.4 C**. The

spectrum obtained from the ZIF-8 sample before exposure is in good agreement with the literature.[5-7] The peaks in the range of 900-1350 cm^{-1} are assigned to the in-plane bending of the imidazole ring, while peaks below 800 cm^{-1} are caused by out-of-plane bending of the ring.[5, 7] Specifically, the peak at 1146 cm^{-1} can be assigned to =C-H bending[6], the peak at 1581 cm^{-1} is due to C=N stretching, and bands observed between 1350 and 1500 cm^{-1} are associated with the vibration of the ring.[5, 7] The peak at 2930 cm^{-1} is due to the C-H symmetric stretch of the methyl group[6] whereas the asymmetric stretch is at 2980 cm^{-1}. The =C-H stretch for the aromatic ring is observed at 3134 cm^{-1} as in previous literature reports.[6-7] Due to the wavenumber range limitation of the FTIR instrument, the Zn–N stretch mode at ~420 cm^{-1} could not be observed.[5] A comparison of the FTIR spectra of pre-exposed ZIF-8 versus that of the 2-mIm linker reveals some major differences. The protonated linker in ZIF-8 has a broad absorption band around 3200–2200 cm^{-1} due to the N-H stretch region, specifically the hydrogen bond formed between the -NH group of a 2-mIm molecule and a neighboring nitrogen on a different 2-mIm molecule.[5, 8] The broad shape of the N-H stretch region and its shift to lower frequencies from the theoretical value confirms the presence of the hydrogen bond.[8-9] The peak at 1845 cm^{-1} in the 2-mIm spectrum can be attributed to the resonance between the out-of-plane N-H---N bending and the N-H stretching vibrations.[8] Both of these bands are absent in the ZIF-8 samples pre-exposure, confirming the deprotonation of 2-mIm and the separation of individual 2-mIm molecules by the Zn^{2+} centers in the ZIF-8 crystal structure.

Figure 3.4 A-B also reveals a number of changes in the humid SO_2 exposed ZIF-8 materials versus the pre-exposed material, while there are no significant changes observed in ZIF-8 exposed to humid air, dry SO_2 or aqueous SO_2 (**Figure 3.4 C**). For the humid SO_2

exposed ZIF-8 materials before reactivation (**Figures 3.4 A-B**), several new peaks are observed upon 200 ppm-days of exposure. The broad absorption region centered around 860 cm^{-1} and the peaks at 946 cm^{-1} , 1018 cm^{-1} , 1167 cm^{-1} and 1094 cm^{-1} are characteristic of the presence of (bi)sulfite groups as observed in the FTIR spectrum of zinc sulfite dihydrate.[10] A similar broad absorption region between 700-990 cm^{-1} was attributed to the formation of sulfite groups during zinc sulfide oxidation.[11-12] Peaks at 1364 cm^{-1} and 1497 cm^{-1} can be attributed to adsorbed SO_2 while the peak at 1577 cm^{-1} can be attributed to water adsorption.[11-12] The peaks at 608 cm^{-1}, 983 cm^{-1}, 1055 cm^{-1} and 1112 cm^{-1} are attributed to the vibrations of the (bi)sulfate group which are similar to those observed in the FTIR spectrum of zinc sulfate heptahydrate crystals.[13-15]

A broad absorption region from 2300-3600 cm^{-1} is observed in ZIF-8 exposed to humid SO_2. A comparison with the spectrum of 2-mIm suggests the region is comprised of the hydrogen-bonded NH stretch region along with an OH stretch region from ~3200 cm^{-1} onwards.[16] This indicates the protonation of the nitrogen in 2-mIm and resulting cleavage of the Zn-N coordination bond of ZIF-8 during humid SO_2 exposure. Further similarities with the 2-mIm linker spectra are observed, namely the 2-mIm peaks at 676, 944 and 1112 cm^{-1}, the last two of which overlap with the peaks for the (bi)sulfite and (bi)sulfate groups respectively. The peak at 1112 cm^{-1} in 2-mIm corresponds to C-H bending, which is shifted to 1146 cm^{-1} in ZIF-8.[5] The peak observed at 1626 cm^{-1} can be attributed to the bending vibrations of adsorbed water.[17-18] After reactivation of the above humid SO_2 exposed sample, the peak intensities decrease substantially in the broad (bi)sulfite stretch region centered around 860 cm^{-1}. The peaks corresponding to the (bi)sulfate groups and adsorbed SO_2 also decrease in intensity. The water bending peak at 1626 cm^{-1} disappears, whereas

the intensities of the NH stretch and OH stretch region decrease. However, the overall FTIR spectrum of the reactivated ZIF-8 after humid SO_2 exposure is still significantly different from the pre-exposed ZIF-8, and complete removal of sulfur-containing species from ZIF-8 is not achieved upon reactivation.

Figure 3.5 shows the results of XPS measurements of reactivated ZIF-8 after 100 ppm-days exposure humid SO_2 compared to pre-exposed ZIF-8. The XPS results are all normalized to the Zn*2p* peak to account for any variations in sample mass in the irradiation area. The C*1s* spectrum of ZIF-8 consists of two components, the C atoms in the C-C bond (284.5 eV) and the C-N bond (285.5 eV).[19] A decrease in the C*1s* intensity is observed upon humid SO_2 exposure, possibly due to the detachment of 2-mIm linkers from the surface layers. The N*1s* peak is observed at 399.5 eV for both the pre-exposed and exposed materials. This peak also agrees with the previously reported XPS characteristics of ZIF-8.[20] Like the C*1s* peak, a decrease in the N*1s* peak intensity is observable after 5-day humid SO_2 exposure. The O*1s* peak of pre-exposed ZIF-8 at 532.4 eV can be ascribed to oxygen atoms in hydroxyl groups.[21] This peak increases in intensity on humid SO_2 exposure and indicates -OH group insertion into the ZIF-8 surface. The S*2p* peak of XPS is seen at 169 eV after humid SO_2 exposure. According to the National Institute of Standards and Technology (NIST) database, the expected peak for sulfites is expected to be between 166.6-167.6 eV and between 168.9-169.2 eV for sulfates.[22] Hence the S*2p* peak in the XPS for reactivated ZIF-8 after a 100 ppm-day humid SO_2 exposure can be attributed to the presence of sulfate (or bisulfate) species.[22] XPS measurements of samples before reactivation were not experimentally feasible, since desorption from the sample made it difficult to obtain the required ultra-low vacuum conditions in a reasonable time.

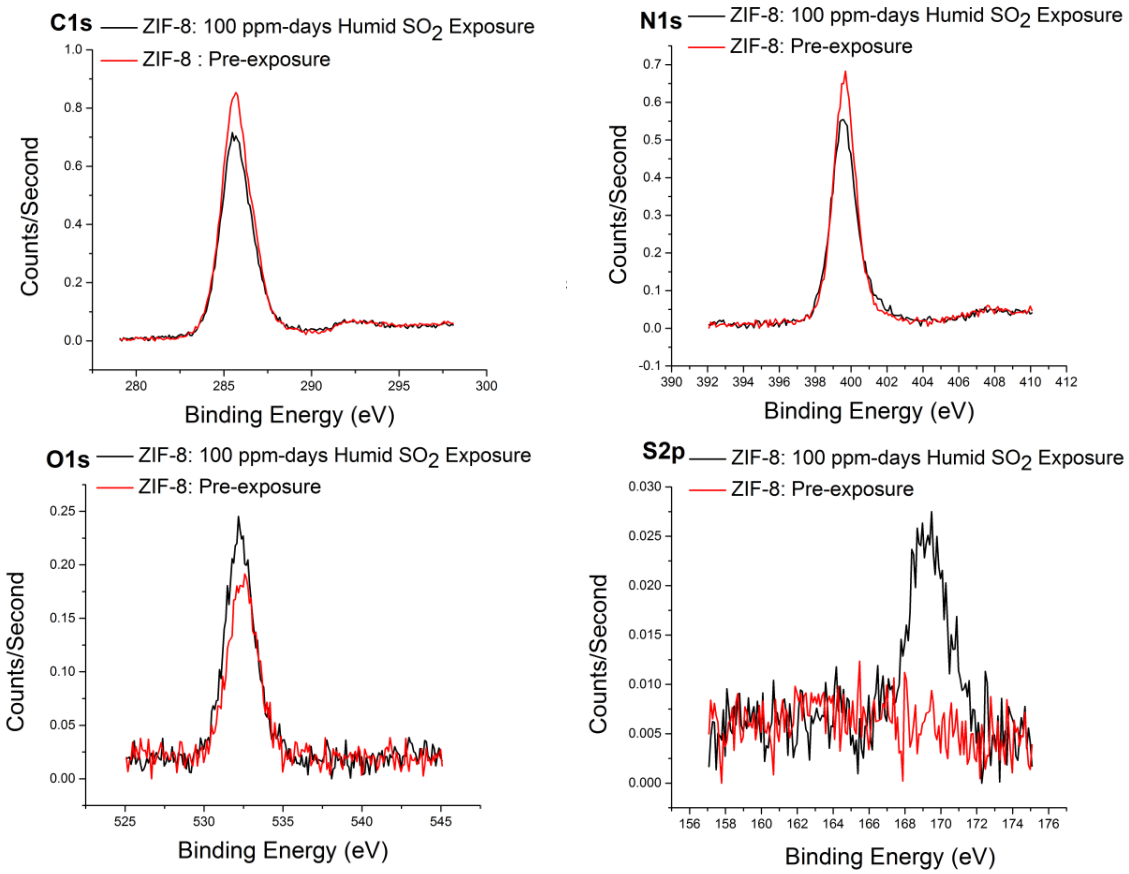

Figure 3.5. X-ray photoelectron spectra of ZIF-8 exposed to 100 ppm-days humid SO_2. The counts/second are normalized to that of the *Zn2p* peak.

The change in morphology of ZIF-8 on exposure to humid SO_2 is observed by SEM (**Figure 3.6 A-B**). In pre-exposed ZIF-8, the crystal shapes, facets, and edges are clearly visible After 200 ppm-days humid SO_2 exposure, there are significant morphological changes; the crystal edges become rounded and they lose their well-defined shape. ZIF-8 particles are observed under various degrees of degradation, often with large cracks. A number of smaller irregularly-shaped fragments are also observed after humid SO_2

exposure. The color of the humid SO_2 exposed ZIF-8 powder samples also changes from white to yellowish-black (**Figure 3.6 C**).

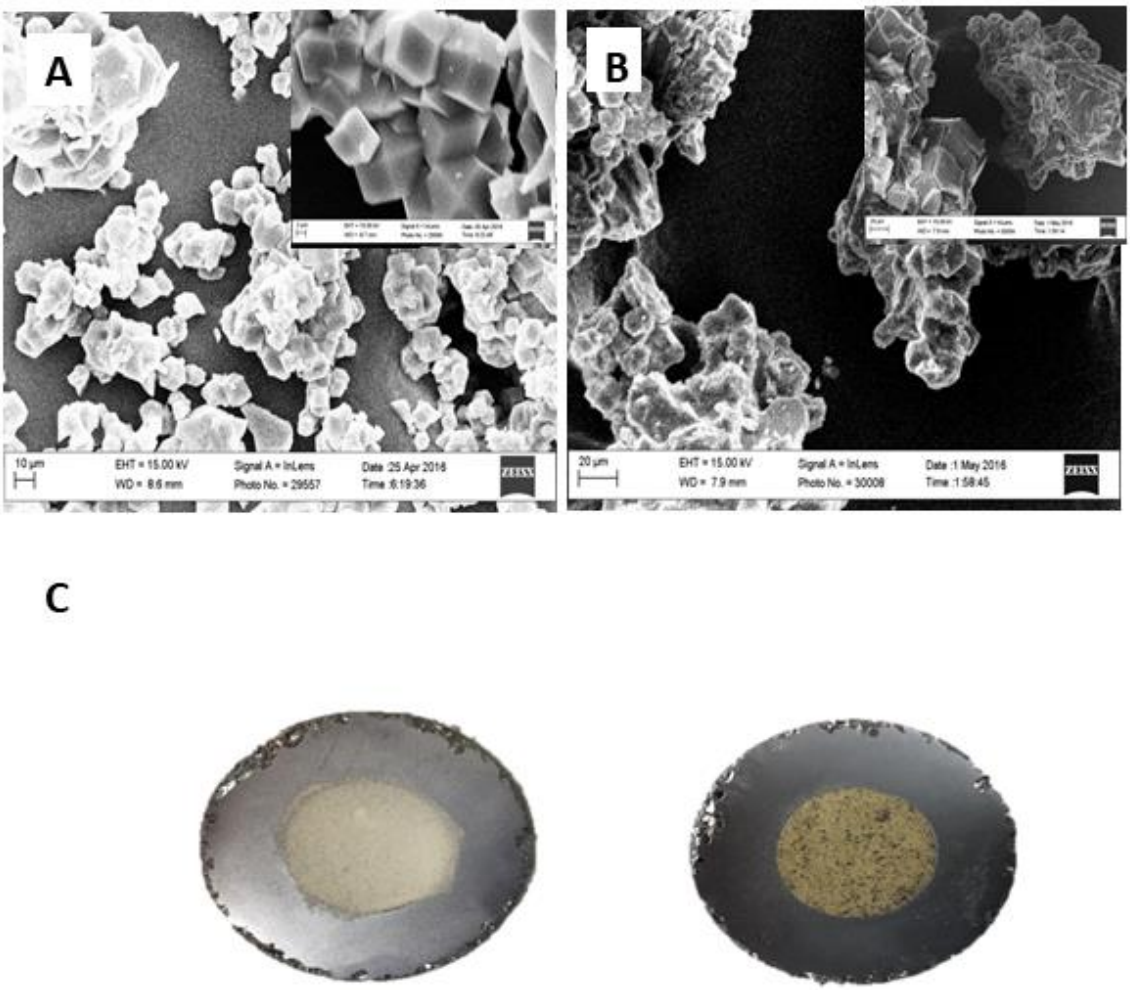

Figure 3.6. SEM images of (A) pre-exposed ZIF-8 and (B) 200 ppm-days humid SO_2 exposed and reactivated ZIF-8, and (C) sample color of pristine activated ZIF-8 (left), and after 100 ppm-days humid SO_2 exposure followed by reactivation (right).

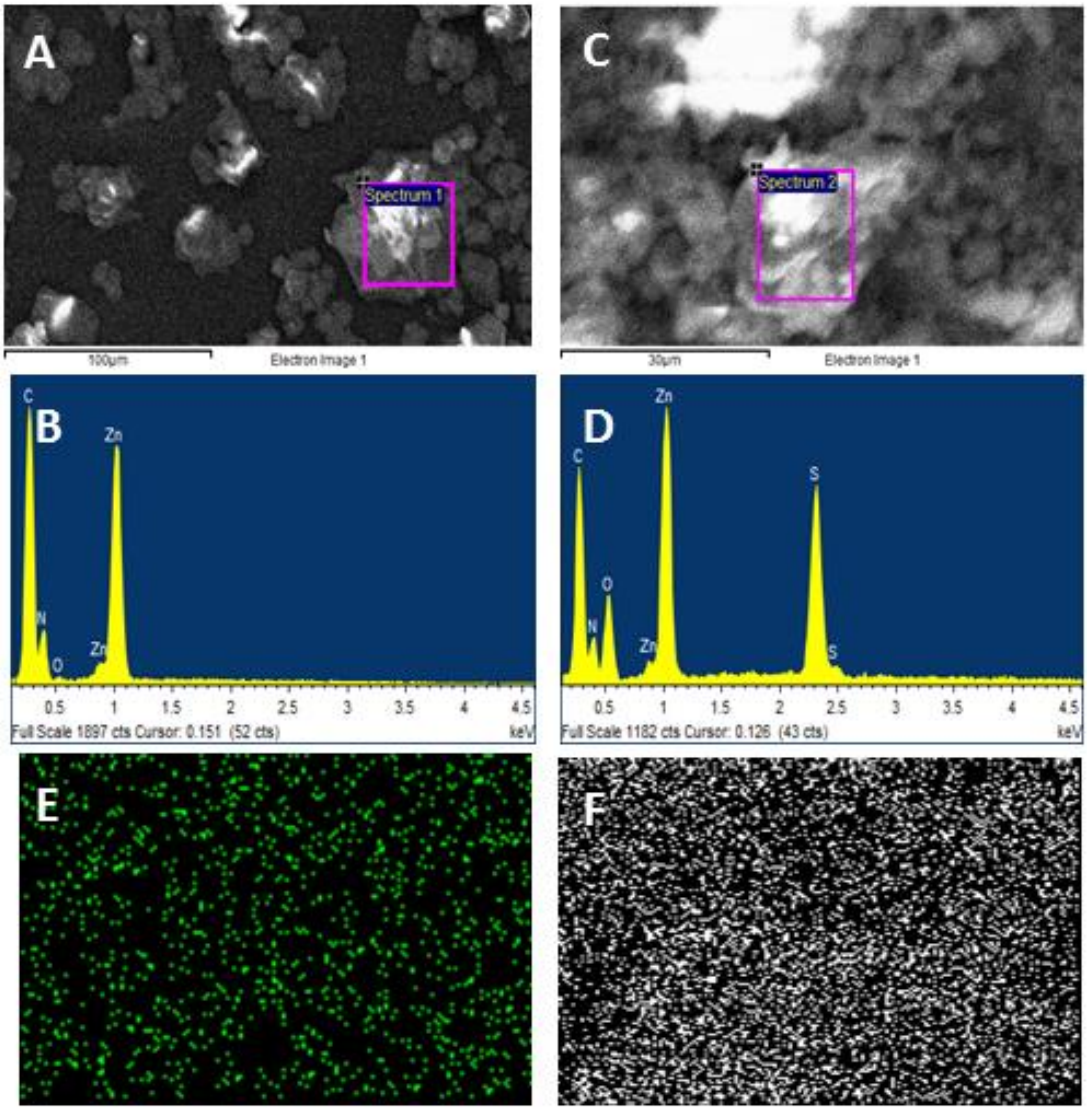

Figure 3.7. SEM images of (A) pre-exposed ZIF-8 and (C) reactivated ZIF-8 after 200 ppm-days of humid SO_2 exposure; (B) and (D): corresponding EDX spectra from inset areas of the SEM images; elemental distributions of (E) oxygen and (F) sulfur in the exposed ZIF-8 sample corresponding to the inset area shown in (C). The inset area is magnified and rotated by 90° in the elemental distribution images to match the rectangular area of the other images in the figure.

The results of elemental analysis conducted by EDX are illustrated in **Figure 3.7**. Whereas XPS probes only the near-surface (< 10 nm) regions of the ZIF-8 particles, EDX also probes their interior (~ 1 μm). **Figures 3.7 A**, **C** are SEM images of the pre-exposed and exposed (200 ppm-days humid SO_2, then reactivated) samples showing the areas (inset) selected for EDX analysis. **Figures 3.7 B, D** are the corresponding EDX spectra. The SEM images of the EDX samples have lower visual clarity than those in **Figure 3.6**, because no gold coating was sputtered on these samples. Trace amounts of oxygen (~2 atom %), but no sulfur, are observed in the pre-exposed ZIF-8 sample, in agreement with the XPS results (**Figure 3.5**). Significant increase in the amounts of oxygen and sulfur are observed on humid SO_2 exposure. An average of thirty spatially unique elemental distribution scans of the 200 ppm-days humid SO_2 exposed ZIF-8 sample indicates an increasing presence of sulfur (~2.5 atom%) and oxygen (21 atom%) before reactivation that decreases to 1.5 atom% and 17 atom% respectively after reactivation. This indicates partial desorption of the sulfur containing species such as adsorbed SO_2, (bi)sulfite and (bi)sulfate on reactivation. The O and S content is found to be homogeneously distributed across the entire region being probed (**Figures 3.7 E** and **F**). This finding is consistent with the FTIR measurements on the exposed reactivated materials. The Zn:S atomic ratio is obtained as 0.9:1 in the humid SO_2 exposed sample before reactivation and changes to 2:1 after reactivation, and is discussed later in this Chapter.

Figure 3.8 shows the dry SO_2 adsorption isotherm of ZIF-8 at 298 K up to a SO_2 pressure of 2.5 bar. ZIF-8 readily adsorbs dry SO_2 gas with a saturation value of about 8.1 mmol/g at 2.5 bar. After reactivation following the dry SO_2 adsorption measurements, the PXRD pattern, FTIR spectra, and NP characteristics are found to be essentially identical (**Figures 3.1, 3.3,** and **Table 3.1**) to pre-exposed ZIF-8. This confirms the stability of ZIF-8 even at very high concentrations of dry SO_2. As already described earlier in this Chapter, ZIF-8 is also found to be stable under at high R.H. water vapor exposure. These control measurements further corroborate the combined role of SO_2 and water vapor in degradation of the material.

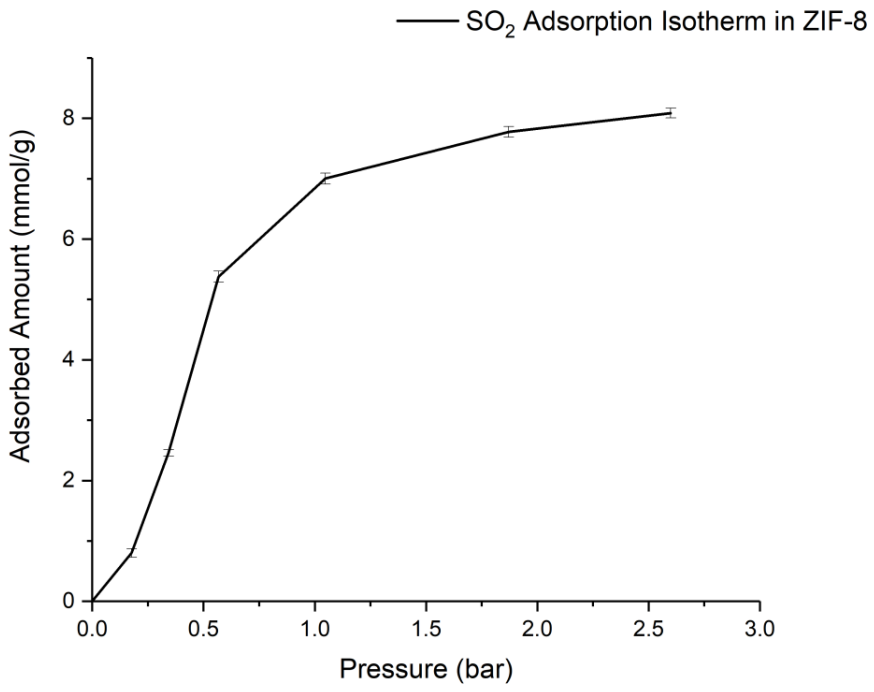

Figure 3.8. Dry SO_2 adsorption isotherm in ZIF-8 at 298 K.

I now consider all the foregoing information and discuss the mechanism of ZIF-8 degradation upon exposure to SO_2. XPS and EDX clearly reveal residual sulfur (S) present in humid SO_2 exposed ZIF-8 both before and after its reactivation, thereby indicating the formation of new chemical bonds involving S. FTIR clearly shows a combination of adsorbed SO_2, (bi)sulfites and (bi)sulfates to be present before reactivation, and a decrease in all these species upon reactivation. The decreasing atomic percentage of S measured by EDX before and after reactivation of the 200 ppm-days humid SO_2 exposed ZIF-8 sample further corroborates the partial desorption of adsorbed SO_2, (bi)sulfites and (bi)sulfates during the reactivation procedure. The FTIR results clearly indicate cleavage of some of the Zn-N coordination bonds and protonation of the linker upon humid SO_2 exposure, although the overall ZIF-8 crystal topology remains the same (PXRD). In pre-exposed ZIF-8, each Zn atom forms four Zn-N coordination bonds, and each 2-mIm linker is attached to two Zn atoms via its two N atoms. Assuming that each acidic species (*e.g.*, HSO_4^- or H_2SO_4) can respectively cleave one or two Zn-N bonds and simultaneously protonate one or two N atoms, then in a theoretical case of complete degradation of ZIF-8 one can expect a Zn:S ratio in the range of 1:4 - 1:2. From EDX, the Zn:S ratio before reactivation of the most strongly exposed sample (200 ppm-days humid SO_2) is 0.9:1 which changes to is 2:1 after reactivation due to partial desorption of S containing species. Thus one can estimate that only 13-25% of the Zn-N bonds are permanently disrupted. Clearly, this is insufficient to collapse the entire ZIF-8 structure (as also confirmed by PXRD) but it is sufficient to bring about significant degradation in its crystallinity, pore volume, and internal surface area. A recent computational study on the characterization of possible point defects in ZIF-8 suggested that linker vacancies and ‘dangling linker’ defects (due to Zn-N bond cleavage

and 2-mIm protonation by an acid species) are the most thermodynamically favored defects.[23] Since the percentage of cleaved Zn-N bonds is low under the present conditions, one can calculate that there is a low statistical probability (2-6%) that two protonated linkers are found adjacent to each other and can thereby form an N-H---N hydrogen bond, assuming the degradation events are spatially uncorrelated. As a result, the peak at 1845 cm^{-1} in the pure 2-mIm linker FTIR spectrum (which is due to the resonance between the out-of-plane N-H---N bending and the N-H stretching vibrations) is absent/very weak in humid SO_2 exposed ZIF-8. While humid SO_2 exposure leads to substantial bulk degradation of ZIF-8, a similar exposure in aqueous SO_2 shows different results. Similar to dry SO_2 and humid air exposure, the aqueous SO_2 exposed ZIF-8 retains its bulk crystallinity, porosity and vibrational characteristics (**Figures 3.1, 3.3** and **3.4**). However a closer inspection of the surfaces of ZIF-8 exposed to aqueous SO_2 by SEM indicates that though the overall crystal shapes and edges are maintained, increased surface roughness can be observed (**Figure 3.9**). The effects of aqueous SO_2 exposure at different concentrations on the surface of ZIF-8 particles have been investigated in detail in another recent work.[24]

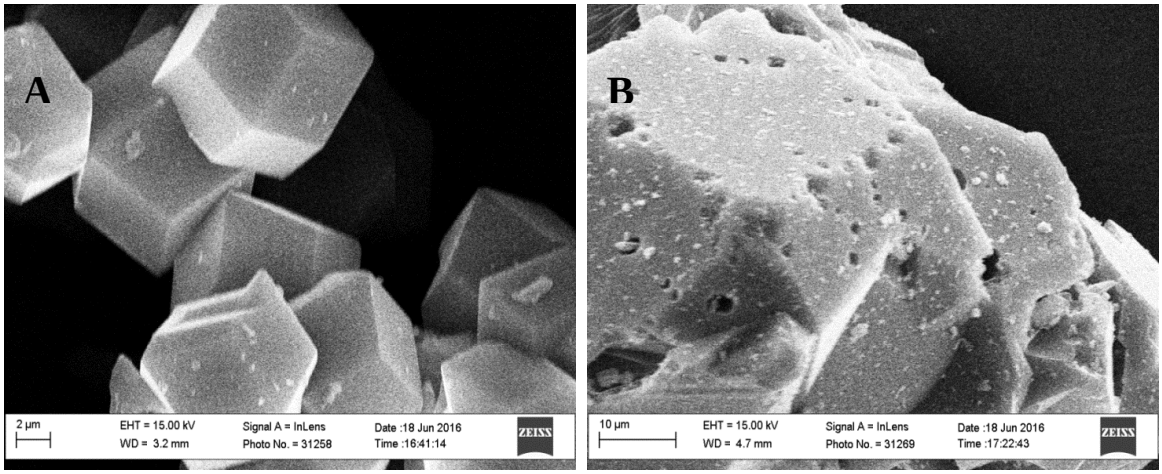

Figure 3.9. SEM images of (A) pre-exposed ZIF-8 and (B) 100 ppm-days aqueous SO_2 exposed and reactivated ZIF-8.

Next, it is important to comment on the nature of the attacking species responsible for the degradation of ZIF-8. The solubility of SO_2 in the aqueous phase strongly increases with increasing *p*H.[25-27] The following reactions occur in the aqueous phase:

$$SO_2\,(g) \leftrightarrow SO_2\,(l) \quad (1a)$$

$$SO_2\,(l) + H_2O \leftrightarrow H_2SO_3 \leftrightarrow H^+ + HSO_3^- \quad (1b)$$

$$HSO_3^- \leftrightarrow H^+ + SO_3^{2-} \quad (1c)$$

The *p*H of the solution determines how the dissolved SO_2 (*l*) species will form bisulfite (Equation 1b) or sulfite (Equation 1c) species. At the weakly acidic *p*H (~4) of the aqueous SO_2 solutions used in this work, almost the entire dissolved SO_2 will form bisulfite ions.[26] In the vapor phase, there are multiple routes for conversion of SO_2. In air, the oxidation of SO_2 to SO_3 and its subsequent hydration to H_2SO_4 is one route.[28] Other mechanisms of homogenous and heterogeneous oxidation of SO_2 to H_2SO_4 are also possible in the vapor

phase catalyzed by different oxidative groups.[25, 29] But even under dark exposure conditions (with no external irradiation) at 90% relative humidity and 45°C, up to 20% of SO_2 was shown to be oxidized to sulfuric acid in a synthetic air mixture even with short residence times.[30] Clustering of SO_2 with water molecules has been proposed to facilitate its oxidation and nucleation to form H_2SO_4 aerosols.[30] Another possible route of SO_2 oxidation is heterogeneous reaction on surfaces such as transition metals. The H_2SO_4 product has a very low vapor pressure and is quickly converted to a condensed species which can act as a heterogeneous nucleation site for further oxidation of SO_2.[25, 30] Under the exposure conditions used in this work (laboratory light) and the average residence time of SO_2 in the exposure chamber (~3 hours), it is likely that conversion of SO_2 to H_2SO_4 takes place by one or more reaction routes inside the exposure chamber. On the other hand, direct hydration of SO_2 to sulfurous acid (H_2SO_3) through Equation (1b) is stated to be kinetically and thermodynamically unfavorable in the gas/vapor phase under standard conditions at 1 bar pressure.[31-32] The presence of water molecules in the gas/vapor phase decreases the high energy barrier for the direct hydrolysis of SO_2, but the resulting hydrated sulfurous acid (H_2SO_3-$(H_2O)_{n-1}$ complex is still thermodynamically unstable with respect to the reactant complex SO_2-$(H_2O)_n$.[32-33] However, in the presence of sulfuric acid in the gas phase, the hydrolysis reaction of SO_2 and water is thermodynamically favorable forming complex products such as H_2SO_4-H_2SO_3 , H_2SO_4-H_2SO_3-H_2O or $(H_2SO_4)_2$-H_2SO_3.[32]

In the aqueous phase, oxidation of dissolved SO_2 is mainly carried out by strong oxidizing agents such as hydrogen peroxide (H_2O_2) or ozone (O_3).[25-27] Oxidation of the bisulfite species by dissolved oxygen in the aqueous phase is known to be negligible.[34]

Since the present aqueous SO_2 exposure experiments were carried out in a closed vessel in dark conditions, negligible oxidation of the bisulfite species is expected to take place. Thus the aqueous-phase species interacting with the ZIF-8 structure would be H_2O and HSO_3^-, whereas in the vapor phase one would have H_2O, SO_2,, H_2SO_4, and sulfuric-sulfurous complexes such as such as H_2SO_4-H_2SO_3 , H_2SO_4-H_2SO_3-H_2O or $(H_2SO_4)_2$-H_2SO_3. My control experiments confirm that neither H_2O nor SO_2 on their own react appreciably with ZIF-8. The above considerations are based upon my analysis of data obtained in this study and in previous studies. However, additional speculations are also possible. For example, some SO_2 may also dissolve in a hypothetical aqueous adsorbed film formed on the external surfaces of individual ZIF-8 particles at high humidity in the vapor phase, leading to formation of HSO_3^-.

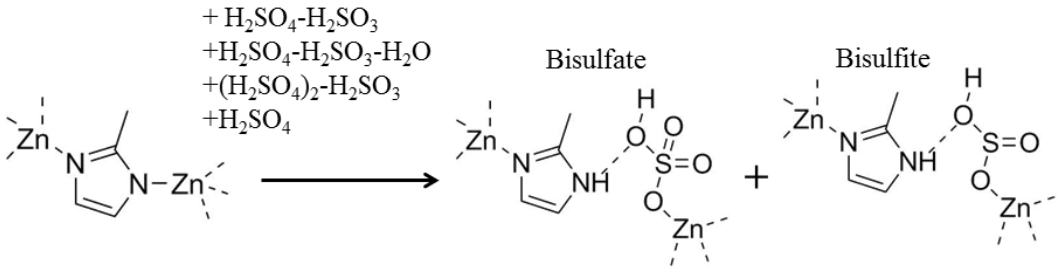

Figure 3.10. Schematic of reactants and product species generated during degradation of ZIF-8 under humid SO_2 exposure.

Based upon the foregoing discussion, **Figure 3.10** shows the proposed sequence of events. Control measurements with dry SO_2 or humid air indicate that these species cannot initiate the degradation reactions on their own. Under humid SO_2 exposure conditions in air, the formation of small amounts of several acidic species (sulfuric acid on its own, as

well as sulfuric-sulfurous complexes) is responsible for Zn-N bond cleavage and protonation of 2-mIm, leading to the formation of bisulfates and bisulfites. Upon reactivation, a considerable amount of these bisulfites and bisulfates are retained within the ZIF-8 structure. The "dangling" 2-mIm linkers resulting from the degradation reactions are highly likely to remain occluded within the ZIF-8 pores along with the introduced bisulfate/bisulfite species, thereby leading to considerable decreases in the pore volume. On the other hand, the aqueous phase SO_2 exposures involve only sulfurous (and not sulfuric) acid. It is suggested that water and HSO_3^- species cannot catalyze the cleavage of Zn-N bonds as efficiently as in the vapor exposure case. Furthermore, any free 2-mIm formed due to Zn-N bond cleavage at the external surfaces can be easily removed due to its high solubility in the aqueous phase, thereby allowing maintenance of pore volume and internal surface area.

3.4 Conclusions

This Chapter has examined the phenomenological and mechanistic aspects of the structural changes occurring in the MOF material ZIF-8 under exposure to the acid gas SO_2. I show that ZIF-8, known for its relatively high thermal and chemical stability among MOFs, retains bulk stability at 298 K upon humid air exposure and dry SO_2 exposure. Though there are changes observed on the surface of the ZIF-8 crystals on aqueous SO_2 exposure, the bulk properties like XRD spectra and BET surface areas are retained. However, ZIF-8 is susceptible to bulk degradation under long-term exposure to humidified SO_2. PXRD data shows a substantial decrease in relative crystallinity. Nitrogen physisorption measurements show considerable decreases in pore volume and internal surface area. FTIR, XPS, and EDX measurements were used to probe the compositional

and vibrational characteristics of the SO_2-exposed materials, and allowed us to postulate a degradation mechanism that is consistent with all the experimental observations. Sulfuric and sulfurous acids formed under humid SO_2 exposure conditions (*via* chemical reactions involving SO_2 and H_2O) are the species responsible for attacking the ZIF-8 structure. The initially surprising finding that ZIF-8 shows no bulk structural degradation in aqueous SO_2 solutions is also discussed. In conclusion, when ZIF-8 is considered for use in applications where it may be exposed to streams containing acid gases such as SO_2 at significant % R.H., a pre-treatment step will be required. Considering that dry acid gas does not affect the stability of ZIF-8 at least in ambient temperature conditions, a simple pre-treatment step involving drying/dehydration of the stream to remove water vapor may be sufficient (instead of more complex pre-treatments that attempt to remove the acid gas itself). To my knowledge this is the first experimental investigation that comprehensively evaluates and explains the acid gas stability of ZIF-8 under a number of different exposure conditions, thereby providing valuable information for the design and use of ZIFs in separation processes.

This Chapter establishes the foundations for a systematic investigation of acid gas stability of porous materials with the aid of the model material ZIF-8. Whether other ZIF materials with different linkers and topologies would undergo a similar fate on SO_2 gas exposure remains to be answered. The similarity or differences in stability of these materials on exposure to acid gases other than SO_2 is also an intriguing question. One may also ask about the kinetics of this degradation process and the correlation between microscopic changes in structural degradation with macroscopic observables such as the pore volume. In the next Chapter, I therefore expand this systematic study of acid gas

stability from the model ZIF-8 material to a diverse set of 16 porous ZIF materials with varying linkers and topologies. Through a suite of experimental and computational methods, the kinetic and thermodynamic acid gas stability of these 16 ZIFs are investigated in detail under different environments – humid air, liquid water, and acid gases CO_2 and SO_2 (dry, humid, and aqueous). In addition, I focus on the kinetics of ZIF degradation under exposure to humid SO_2, evaluate effective rate constants for acid gas degradation of ZIFs and correlate material properties to degradation rates through statistical analysis.

REFERENCES

1. Burtch, N. C.; Jasuja, H.; Walton, K. S., Water Stability and Adsorption in Metal-Organic Frameworks. *Chem. Rev.* **2014,** *114* (20), 10575-10612.

2. Gee, J. A.; Chung, J.; Nair, S.; Sholl, D. S., Adsorption and Diffusion of Small Alcohols in Zeolitic Imidazolate Frameworks ZIF-8 and ZIF-90. *J. Phys. Chem. C* **2013,** *117* (6), 3169-3176.

3. Hashimoto, Y.; Tanaka, S., A new method of generation of gases at parts per million levels for preparation of standard gases. *Environ. Sci. Technol.* **1980,** *14* (4), 413-416.

4. Jian, M.; Liu, B.; Liu, R.; Qu, J.; Wang, H.; Zhang, X., Water-based synthesis of zeolitic imidazolate framework-8 with high morphology level at room temperature. *RSC Adv.* **2015,** *5* (60), 48433-48441.

5. Barbosa, P.; Rosero-Navarro, N. C.; Shi, F.-N.; Figueiredo, F. M. L., Protonic Conductivity of Nanocrystalline Zeolitic Imidazolate Framework 8. *Electrochim. Acta* **2015,** *153*, 19-27.

6. Cheng, P.; Hu, Y. H., H_2O-Functionalized Zeolitic Zn(2-methylimidazole)2 Framework (ZIF-8) for H_2 Storage. *J. Phys. Chem. C* **2014,** *118* (38), 21866-21872.

7. Hu, Y.; Kazemian, H.; Rohani, S.; Huang, Y.; Song, Y., In situ high pressure study of ZIF-8 by FTIR spectroscopy. *Chem. Commun.* **2011,** *47* (47), 12694-12696.

8. Hachula, B.; Nowak, M.; Kusz, J., Crystal and Molecular Structure Analysis of 2-Methylimidazole. *J. Chem. Crystallogr.* **2010,** *40* (3), 201-206.

9. Joseph, J.; Jemmis, E. D., Red-, blue-, or no-shift in hydrogen bonds: A unified explanation. *J.Am.Chem.Soc.* **2007,** *129* (15), 4620-4632.

10. Miller, F. A.; Wilkins, C. H., Infrared spectra and characteristic frequencies of inorganic ions- their use in qualitative analysis. *Anal. Chem.* **1952,** *24* (8), 1253-1294.

11. Siriwardane, R. V.; Woodruff, S., FTIR characterization of the interaction of oxygen with zinc-sulfide *Ind. Eng. Chem. Res.* **1995,** *34* (2), 699-702.

12. Siriwardane, R. V.; Woodruff, S., In situ Fourier transform infrared characterization of sulfur species resulting from the reaction of water vapor and oxygen with zinc sulfide. *Ind. Eng. Chem. Res.* **1997,** *36* (12), 5277-5281.

13. J.K.Saha, J. P., Crystallization of zinc sulphate single crystals and its structural, thermal and optical characterization. *J. Bangladesh Acad. Sci.* **2011,** *35* (2), 203-210.

14. Sivanesan, G.; Kolandaivel, P.; Pandian, S. S., Laser Raman and FT-IR studies of pure and Zn-doped TGS. *Mater. Chem. Phys.* **1993,** *34* (1), 73-77.

15. N. Tugrul, A. S. K., E. Moroydor Derun, S. Piskin, The Determination of the Zinc Sulfate, Sodium Hydroxide and Boric Acid Molar Ratio on the Production of Zinc Borates. *Int.J.Chem.Mol.Nucl.Mater.Metall.Eng.* **2014,** *8* (7), 639-643.

16. Rajamanickam, N.; Rajashabala, S.; Ramachandran, K., On the structural and optical properties of nano-ZnO and its morphologies. *J. Lumin.* **2014,** *146*, 226-233.

17. Ashokkumar, M.; Muthukumaran, S., Microstructure, optical and FTIR studies of Ni, Cu co-doped ZnO nanoparticles by co-precipitation method. *Opt. Mater.* **2014,** *37*, 671-678.

18. Raja, K.; Ramesh, P. S.; Geetha, D., Synthesis, structural and optical properties of ZnO and Ni-doped ZnO hexagonal nanorods by Co-precipitation method. *Spectroc. Acta Pt. A-Molec. Biomolec. Spectr.* **2014,** *120*, 19-24.

19. Luanwuthi, S.; Krittayavathananon, A.; Srimuk, P.; Sawangphruk, M., In situ synthesis of permselective zeolitic imidazolate framework-8/graphene oxide composites: rotating disk electrode and Langmuir adsorption isotherm. *RSC Adv.* **2015,** *5* (58), 46617-46623.

20. Liu, J.; He, J.; Wang, L.; Li, R.; Chen, P.; Rao, X.; Deng, L.; Rong, L.; Lei, J., NiO-PTA supported on ZIF-8 as a highly effective catalyst for hydrocracking of Jatropha oil. *Sci. Rep.* **2016,** *6*.

21. Shipochka, M. G.; Stambolova, I. D.; Blaskov, V. N.; Stefanov, P. K., XPS investigation on the surface of ZnO photocatalytic films obtained by polymer modified spray pyrolysis. *Bulg. Chem. Commun.* **2013,** *45*, 105-109.

22. A. V. Naumkin, A. K.-V., S. W. Gaarenstroom, C. J. Powell, NIST X-ray Photoelectron Spectroscopy Database. In *http://srdata.nist.gov/xps/Default.aspx*, 2012.

23. Zhang, C.; Han, C.; Sholl, D. S.; Schmidt, J. R., Computational Characterization of Defects in Metal-Organic Frameworks: Spontaneous and Water-Induced Point Defects in ZIF-8. *J.Phys.Chem.Lett.* **2016,** *7* (3), 459-464.

24. Pang, S. H.; Han, C.; Sholl, D. S.; Jones, C. W.; Lively, R. P., Facet-Specific Stability of ZIF-8 in the Presence of Acid Gases Dissolved in Aqueous Solutions. *Chem. Mater.* **2016,** *28* (19), 6960-6967.

25. Eatough, D. J.; Caka, F. M.; Farber, R. J., The conversion of SO_2 to sulfate in the atmosphere. *Isr. J. Chem.* **1994,** *34* (3-4), 301-314.

26. Hudson, E., Katipovic, Kinetics of Sulfur Dioxide oxidation in Aqueous Solution. In *Internal Report*, U.S.E.P.A., Ed. 1979.

27. Scire, J. S.; Venkatram, A., The contribution of in-cloud oxidation of SO_2 to wet scavenging of sulfur in convective clouds *Atmos. Environ.* **1985,** *19* (4), 637-650.

28. Loerting, T.; Kroemer, R. T.; Liedl, K. R., On the competing hydrations of sulfur dioxide and sulfur trioxide in our atmosphere. *Chem. Commun.* **2000,** (12), 999-1000.

29. Tokunaga, O.; Nishimura, K.; Washino, M., Radiation treatment of exhaust gases. 2. Oxidation of sulfur-dioxide in moist mixture of oxygen and nitrogen *Int. J. Appl. Radiat. Isot.* **1978,** *29* (2), 87-90.

30. Flamm, D. L.; Bacon, D. D.; Kinsbron, E.; English, A. T., Chemical-reaction of sulfur-dioxide at high humidity and temperature - implications for accelerated testing *J. Electrochem. Soc.* **1981,** *128* (3), 679-685.

31. Sinha, R. K.; Scuderi, D.; Maitre, P.; Chiavarino, B.; Crestoni, M. E.; Fornarini, S., Elusive Sulfurous Acid: Gas-Phase Basicity and IR Signature of the Protonated Species. *J.Phys.Chem.Lett.* **2015,** *6* (9), 1605-1610.

32. Liu, J.; Fang, S.; Wang, Z.; Yi, W.; Tao, F.-M.; Liu, J.-y., Hydrolysis of Sulfur Dioxide in Small Clusters of Sulfuric Acid: Mechanistic and Kinetic Study. *Environ. Sci. Technol.* **2015,** *49* (22), 13112-13120.

33. Liu, J.; Fang, S.; Liu, W.; Wang, M.; Tao, F.-M.; Liu, J.-y., Mechanism of the Gaseous Hydrolysis Reaction of SO_2: Effects of NH_3 versus H_2O. *J. Phys. Chem. A* **2015,** *119* (1), 102-111.

34. Beilke, S.; Lamb, D.; Muller, J., Uncatalyzed oxidation of atmospheric SO_2 by oxygen in aqueous systems *Atmos. Environ.* **1975,** *9* (12), 1083-1090.

CHAPTER 4. ACID GAS STABILITY OF ZEOLITIC IMIDAZOLATE FRAMEWORKS: GENERALIZED KINETIC AND THERMODYNAMIC CHARACTERISTICS

4.1 Introduction*

In this Chapter I have systematically investigated the stability of 16 ZIFs under exposure to CO_2 and SO_2 gases in dry and humid environments, with data on aqueous-phase stability also provided for comparison. Observations from these experiments are used to quantify ZIF degradation on a common basis in terms of degradation rate constants. Among single-linker ZIFs, I have selected a variety of materials ranging from hydrophobic to hydrophilic with differing topologies (SOD, RHO, ANA), pore aperture sizes, and cage sizes (**Table B.1**, Appendix B). I have also included several "mixed-linker" ZIFs in GME and SOD topologies, which have more than one linker type within the same ZIF structure. I have first summarized extensive data on the structural and textural evolution of the ZIF materials under acid gas exposure (dry, humid, aqueous). I have then investigated the mechanistic basis of these observations through Fourier transform infrared spectroscopy (FTIR) and energy dispersive X-ray spectroscopy (EDX), and used it to extract quantitative kinetic parameters for acid gas degradation. For added mechanistic insight, I have also compared experimental observations with detailed computational investigations. Finally, I

* Work in this Chapter has been published previously in **S. Bhattacharyya**, R. Han, W.Kim, Y. Chiang, K.C.Jayachandrababu, J.T.Hungerford, M. R. Dutzer, C.Ma, K. S. Walton, D. S. Sholl, S. Nair, "Acid gas stability of zeoliic imidazolate frameworks: generalized kinetic and thermodynamic characteristics". *Chem.Mater.* **2018,** *30* (12), 4089-4101

have examined the possibility of quantitative stability correlations from the data, and assessed the validity of several well-known stability indicators proposed in the literature.

4.2 Experimental Methods

4.2.1 Materials

Zinc(II) nitrate hexahydrate (99%), 1-octanol (99%), benzimidazole (99%), ammonium hydroxide (28% NH_3) and imidazole-2-carboxaldehyde (97%) were purchased from Alfa Aesar; 2-methylimidazole (99%), 5-chlorobenzimidazole (96%), 5-aminoimidazole-4-carbonitrile (97%), 4-methyl-5-carboxaldehyde imidazole (99%), 2-ethylimidazole (98%) 4,5-dichloroimidazole (98%), toluene (99.8%), lanthanum hexaboride (LaB_6, 99%) powder, and sodium formate (99%) were obtained from Sigma-Aldrich; methanol (99.8%) and N,N-dimethylformamide (DMF) (99.8%) were obtained from BDH; 2-nitroimidazole (98%), 4-cyano imidazole (95%), 5-bromobenzimidazole (97%) were purchased from Oakwood Chemicals; and ethanol (200 proof) was obtained from Decon Labs. All chemicals were used as received. Ultra-high-purity air and N_2:CO_2:He (12:12:76 by volume) gas mixtures were purchased from Airgas. Deionized (DI) water was obtained with an EMD Millipore water purification system.

4.2.2 ZIF synthesis

The 16 ZIF materials were synthesized based upon procedures reported in several previous works.[1-10] ZIF-8 and ZIF-90 were synthesized by modifying the procedure reported by Gee *et al*.[1] For ZIF-8 synthesis, 0.972 g 2-methylimidazole and 1.614 g sodium formate were dissolved in 120 cc methanol and sonicated to dissolve completely. 1.764 g

zinc (II) nitrate was dissolved in 120 cc methanol added to the first solution. The combined solution was then heated in a glass jar to 363 K for 24 hours. The crystals were collected and washed with fresh methanol thrice and then air dried at 333 K. ZIF-8 was also synthesized without using sodium formate modulator by modifying the procedure reported by Zhang et al.[11] 1.176 g zinc (II) nitrate and 1.622 g 2-methylimidazole were individually dissolved in 80 cc methanol and then mixed together and stirred for 15 minutes. The crystals were collected and washed with fresh methanol thrice and then air dried at 333 K. Unless otherwise stated, ZIF-8 in this manuscript refers to crystals synthesized by the former method. ZIF-90 was synthesized by dissolving 11.904 g zinc (II) nitrate and 15.368 g imidazole-2-carboxaldehyde in 400 cc DMF. The solution was then heated to 393 K in an oil bath for 10 minutes and then cooled to ambient temperature. The crystals obtained were washed with methanol thrice and then air dried at 333 K.

For ZIF-14 synthesis, 1.923 g of 2-ethylimidazole was first dissolved in 50 cc water by stirring at room temperature. A mixture consisting of 1.487 g zinc (II) nitrate dissolved in 50 cc 1-Octanol was poured into the 2-ethylimidazole/ water solution and stirred at room temperature for 2.5 hours. The crystals were collected and washed with fresh methanol thrice and then air dried at 333 K.

ZIF-93 was synthesized by mixing 0.660 g 4-methylimidazole-5-carboxaldehyde in 20 cc DMF with 0.367 g zinc (II) acetate in 20 cc DMF. The combined solution was then transferred to a Teflon liner and sealed inside a Parr reactor at 358 K for 12 hours. The crystals were solvent exchanged with methanol for 24 hours before air drying at 333 K.[9]

ZIF-96 was synthesized by mixing 2.592 g 4-aminoimidazole-5-carbonitrile in 80 cc DMF with 1.47 g zinc (II) acetate in 80 cc DMF. The mixture was sealed and heated at 358 K for 12 hours. The crystals were solvent exchanged with methanol for 24 hours before air drying at 333 K.[9]

ZIF-71 was synthesized using the procedure followed by Zhang *et al*.[3] 297 mg zinc (II) acetate and 876 mg 4,5-dichloroimidazole were separately dissolved in 60 cc methanol. The zinc acetate solution was then added to the 4,5-dichloroimidazole solution and kept at room temperature without stirring for 24 hours. The crystals obtained were washed with methanol thrice and then air dried at 333 K.

SOD topology ZIF-71 was synthesized using the recent procedure reported by Wiebcke *et al*.[4] Zinc (II) nitrate (0.796 g) was dissolved in 100 cc 1-propanol. 4,5-dichloroimidazole (1.466 g) and 1-methylimidazole (0.88 g) were dissolved in 100 cc 1-propanol. The first solution was poured into the second solution and stirred for 48 hours at room temperature. Crystals were collected by centrifugation at 8500 rpm for 10 minutes, followed by washing with fresh methanol thrice. Crystals were air dried at 333 K.

ZIF-7 and ZIF-11 were synthesized according to the synthesis procedure reported by He *et al*.[2] For ZIF-7 synthesis, 1.8 g of benzimidazole was dissolved in 102 g of ethanol, followed by the addition of 0.9 g of ammonium hydroxide under stirring at room temperature. After that, 1.65 g of zinc acetate was added and stirred for 3 hours. The solution gradually turned into a milky suspension. The crystals were collected and washed with fresh methanol thrice and then air dried at 333 K. For ZIF-11 synthesis, 1.2 g of benzimidazole was dissolved in 68 g of ethanol, followed by the addition of 46 g of toluene and 0.6 g of ammonia hydroxide under

stirring at room temperature. After that, 1.1 g of zinc acetate was added and stirred for 3 hours at room temperature. The crystals were collected and washed with fresh methanol thrice and then air dried at 333 K.

ZIF-65 was synthesized according to synthesis procedure reported by Schoenecker *et al*.[5] Briefly, 3.675 g 2-nitroimidazole and 2.231 g zinc (II) nitrate were added to 200 ml DMF and heated at 100 °C for 24 hours. The crystals were solvent exchanged with methanol for 24 hours before air drying at 333 K.

ZIF-68 was synthesized by mixing together individual solutions of 0.543 g 2-nitroimidazole in 24 cc DMF, 0.189 g benzimidazole in 8 cc DMF and 0.476 g Zinc (II) nitrate in 8 cc DMF. The combined solution was then transferred to a Teflon liner and sealed inside a Parr reactor at 373 K for 72 hours. The crystals were solvent exchanged with methanol for 24 hours before air drying at 333 K.[10]

ZIF-69 was synthesized by mixing together individual solutions of 0.362 g 2-nitroimidazole in 16 cc DMF, 0.488 g 5-chlorobenzimidazole in 16 cc DMF and 0.476 g Zinc (II) nitrate in 8 cc DMF. The combined solution was then transferred to a Teflon liner and sealed inside a Parr reactor at 373 K for 72 hours. The crystals were solvent exchanged with methanol for 24 hours before air drying at 333 K.[10]

ZIF-81 was synthesized by mixing together individual solutions of 0.339 g 2-nitroimidazole in 15 cc DMF, 0.591 g 5-bromobenzimidazole in 15 cc DMF and 0.714 g Zinc (II) nitrate in 12 cc DMF. The combined solution was then transferred to a Teflon liner and sealed inside a Parr reactor at 363 K for 96 hours. The crystals were solvent exchanged with methanol for 24 hours before air drying at 333 K.[10]

ZIF-82 was synthesized by mixing together individual solutions of 0.339 g 2-nitroimidazole in 15 cc DMF, 0.279 g 5-cyanoimidazole in 15 cc DMF and 0.714 g Zinc (II) nitrate in 12 cc DMF. The combined solution was then transferred to a Teflon liner and sealed inside a Parr reactor at 373 K for 96 hours. The crystals were solvent exchanged with methanol for 24 hours before air drying at 333 K.[10]

Mixed-linker (hybrid) ZIF-8_{50}-90_{50} was synthesized using the procedure reported by Thompson *et al* and Eum *et al*.[6-8] 2.874 g 2-methylimidazole, 0.48 g imidazole-2-carboxaldehyde and 2.72 g sodium formate were dissolved in methanol by heating to 323 K under stirring and then cooled down to ambient temperature.2.974 g Zinc (II) nitrate was dissolved in water. Both solutions were mixed together under stirring. The solution was kept stirred for 24 hours. The crystals were then separated by centrifugation and washed with methanol thrice and then air dried at 333 K.

Mixed-linker (hybrid) ZIF-8_{15}-14_{85} was synthesized by the non-solvent induced crystallization (NSIC) method reported by Thompson *et al*.[7] A solution of 1.730 g 2-ethylimidazole, 0.164g of 2-methylimidazole and 1.360g of sodium formate was dissolved in 50 ml of water by stirring at room temperature. A solution of 1.487g zinc nitrate was prepared in 50 ml of water and added to the ligand solution followed by stirring at room temperature for 2.5 hours. The crystals were then separated by centrifugation and washed with methanol thrice and then air dried at 333 K. All dried crystals were activated by degassing at 453 K in vacuum for 24 hours.

4.2.3 Characterization

Activated ZIF samples before and after exposure to acid gases were characterized with powder X-ray diffraction (PXRD), nitrogen physisorption (NP) at 77 K or CO_2 physisorption at 273 K, energy dispersive X-ray spectroscopy (EDX), and fourier transform infrared spectroscopy (FTIR). PXRD measurements were conducted on an X'Pert Pro PANalytical x-ray diffractometer (Bragg-Brentano geometry, Cu Kα anode at 45 kV and 40 mA, X'celerator detector). PXRD patterns were collected with a step size of 0.02° 2θ and scan time of 10 s/step over 4-50° 2θ. The peak intensities were normalized with respect to the highest-intensity peak for each ZIF. Crystallite domain sizes and microstrains were estimated using the Williamson-Hall method, with a LaB_6 standard to determine instrumental contribution to peak broadening.[12-13] Textural analyses were conducted by NP at 77 K using a BET surface area analyzer (Tristar, Micromeritics). BET surface areas were calculated in individually determined pressure ranges.[14] EDX measurements were carried out with the LEO 1550 scanning electron microscope (Zeiss Electron Microscopy) and EDX analysis was done at 15 kV. Spectrometer gain and beam current were optimized with a Si wafer standard before sample measurements and the library calibration files of the Inca software (Oxford Instruments) were used to calculate elemental quantities. Areas of 100 μm×100 μm were selected for each EDX measurement and at least 10 independent areas were measured and averaged for each sample. FTIR spectroscopy was recorded by a Thermo Scientific Nicolet iS50 FT-IR equipped with an iS50 ATR module. Samples were analyzed in powder form from 550-4000 cm^{-1} with 96 scans with a resolution of 2 cm^{-1}. Water adsorption measurements were conducted with the IGAsorp DVS moisture sorption analyzer at 308 K. Each experiment was preceded by in

situ activation under a high-purity nitrogen stream at 383 K up to 12 hours. Adsorption data was collected at adsorbate relative humidities (P/P_0, where P_0 is the saturation vapor pressure of water) ranging from 0.05 to 0.95. Each data point was collected with sufficient time (1-6 hours) for reaching equilibration.

4.2.4 Acid Gas and Aqueous Acid Exposure

Dry sulfur dioxide (Airgas, anhydrous, 99.98% purity) adsorption isotherms were measured at 298 K for pressures ranging from 0 to approximately 2.5 bar using a lab-built volumetric system. Each sample (30-50 mg) was outgassed under dynamic vacuum at 453 K for 5 hours. SO_2 adsorption loading was determined by measuring the pressure drop in the sample cell, and this pressure drop was converted to moles using the Peng-Robinson equation of state. For humid SO_2 exposure, activated samples were exposed to varying concentrations (ppm) of SO_2 in air with relative humidity of 85% for different time intervals at room temperature (298 K). The acid gas mixture was prepared according to previous literature reports, with slight modifications.[15] The SO_2 gas was generated from a 400 mL aqueous solution of 0.5 mg/mL $NaHSO_3$ at a pH of 3.7 at 318 K. The temperature of the solution was maintained with a water bath (VWR). Air at 60 cc/min was bubbled through the solution and carried humid SO_2 gas stream to the exposure unit (Secador mini-desiccator). Gas concentration inside the transparent exposure unit was continuously monitored with the portable PAC 7000 SO_2 detector purchased from Dräger. Data from the detector was transferred to a computer after the exposure run was finished. A second SO_2 sensor was kept running outside the exposure unit for leak detection. Steady state levels of SO_2 and relative humidity were achieved within a few hours. The $NaHSO_3$ solution was refilled to maintain SO_2 level after every 2 days. The water bath, acid gas generator unit

and exposure unit were all placed inside a fume hood with a high exhaust rate, and handled with caution at all times. For humid CO_2 exposure, activated samples were exposed to a 12% CO_2/12% N_2/76% He stream humidified at a relative humidity of 90% for 3 days at 298 K. The dry gas mixture was bubbled at 60 cc/min through deionized water and the humid stream generated entered the exposure chamber (a Secador mini-desiccator). In all experiments, the relative humidity in the chamber was continuously monitored by a commercial available humidity sensor (Ambient Weather). All samples were re-activated at 453 K in vacuum for 24 hours after exposure and prior to characterization. For aqueous SO_2 exposures, dilute aqueous solutions of SO_2 were prepared by diluting a stock solution of aqueous SO_2 (6.2%, Sigma Aldrich). The SO_2 concentration of 2.5×10^{-5} mol/kg was determined based on the concentration in equilibrium with 20 ppm SO_2 in the vapor phase, according to Henry's law ($K_{H,\ SO2}$ = 1.25 mol/kg·bar). A solution at the desired concentration was introduced into a 60 mL glass vial with approximately 200 mg of ZIF-8 and sealed. The vials were briefly sonicated to ensure good dispersions of the particles within the solutions. After 5 days at room temperature, the resulting solids were centrifuged and washed with DI water and methanol. After exposure experiments, all samples were re-activated at 453 K in vacuum for 24 hours prior to characterization.

4.2.5 Computational Details

The experimentally reported structures of ZIF-7, ZIF-8, ZIF-11, ZIF-68, ZIF-69, ZIF-93, ZIF-96, ZIF-71, ZIF-81 and ZIF-90 were optimized with plane-wave density functional theory (DFT).[16-20] Theoretical SOD structures were generated for the ZIF-8_{15}-14_{85} SOD hybrid, ZIF-71 SOD, and ZIF-65 by replacing the methylimidazole in the ZIF-8 framework with a corresponding functionalized imidazole linker, and then re-optimizing

using DFT. Calculations were performed in the Vienna Ab-initio Simulation Package (VASP) with projector-augmented wave (PAW) method pseudopotentials[38] and the Perdew-Burke-Ernzerhof (PBE) generalized-gradient approximation (GGA) functional.[39] Atomic positions were first relaxed using a conjugate gradient algorithm with a cutoff energy of 480 eV until all forces were less than 0.05 eV/Å. Subsequently both atomic positions and lattice constants were optimized with the same cutoffs and tolerances. In all calculations, reciprocal space was sampled only at the Γ-point. The pK$_a$ values were calculated for the conjugated acids of the functionalized imidazolate linkers. Gaussian 09 was used to geometry-optimize the neutral and anionic linker fragments for each ZIF considered. Gas phase optimization was performed at the B3LYP/(6-311++G(d,p) level of theory using DFT. The free energy was a sum of the entropy, zero-point energy (ZPE), and thermal correction term. Aqueous solvation Gibbs energies were calculated using SMD.[21] Because the reference states of the gas (1 atm) and aqueous phase (1 M) were different, they are interconverted as follows:

$$\Delta G_{gas}(1\ M) = \Delta G_{gas}(1\ atm) + RT\ln(24.46) \qquad (1)$$

Experimental values for the proton free energies $G_{gas}(H^+)$ and $\Delta G_{solv}(H^+)$ were used: -6.28 kcal/mol[22] and -265.9 kcal/mol[23] respectively. A Born-Haber thermodynamic cycle was used to convert between the gas and aqueous phase free energies.[24]

$$pK_a = \left[G_{gas}(A^-) - G_{gas}(HA) + \Delta G_{solv}(A^-) - \Delta G_{solv}(HA) - 270.28\right]/1.364 \qquad (2)$$

Density Derived Electrostatic and Chemical (DDEC) net atomic charges were calculated using the Chargemol software developed by Manz and Limas.[25-26] Powder diffraction patterns were simulated in Mercury[27] with source wavelength λ = 1.54056 Å (Cu Kα

radiation). Hydrogen atoms were assigned isotropic atomic displacements of 0.06 Å; all other atoms were assumed to have 0.05 Å displacements. Peaks were assumed to be symmetric with pseudo-Voigt shape and 0.05° full width half maximum.

4.3 Results and Discussion

4.3.1 Overall Stability Behavior

Figure 4.1A-4.1C shows the PXRD patterns of all the ZIFs before and after a representative level of exposure to humid SO_2 or humid CO_2. The PXRD patterns of all the pristine ZIFs are consistent with the simulated patterns from their crystal structure and with previously reported experimental patterns. The PXRD patterns of all the ZIFs, with the exception of ZIF-71, were observed to be altered significantly under humid acid gas environments. Decreasing peak intensities and corresponding increases in amorphous background were observed upon both types of exposure **(Figure 4.1B**), and in addition new peaks were observed under humid CO_2 exposure corresponding to complex carbonate species[28] (**Figure 4.1C**).To better visualize these changes in peak intensities, the PXRD patterns in Appendix B have been presented on a logarithmic scale and normalized by the most intense Bragg peak. A detailed compilation of PXRD patterns under other exposure conditions is available in Appendix B grouped by each material **(Figures B.1, B.5, B.9, B.13, B.16, B.20, B.24, B.27, B.30, B.34, B.38, B.42, B.44, B.46, B.48, B.50)**. All the ZIFs that were exposed to dry SO_2 or dry CO_2 gases were observed to have unchanged PXRD patterns after exposure. Upon exposure to humid air for 5 days at 85% R.H, SOD-ZIF-71 underwent a partial phase transition to the nonporous material ZIF-72, while ZIF-65(Zn) also underwent a phase transition to a nonporous phase of unknown structure.[4] PXRD

patterns of GME topology ZIF-68, ZIF-69, ZIF-81 and ZIF-82 along with the RHO topology ZIF-96 were found to decrease significantly in intensity, indicating structural degradation, after a 5-day humid air exposure. The ZIFs that were unstable (structural degradation or phase transition) in humid air were not further investigated under exposure to humid acid gases. The results of ZIF exposure to pure water and aqueous SO_2 - while not the main focus of this work - were found to be identical, likely due to the small dissolved SO_2 concentration (20 ppm). While a few ZIFs such as ZIF-8, ZIF-90 and the ZIF-8_{50}-90_{50} hybrid had unchanged PXRD spectra under liquid exposure, a number of other ZIFs underwent phase changes[4, 29] to dense nonporous structures. Other ZIFs such as ZIF-14 and the hybrid ZIF-8_{15}-14_{85} retained most of their crystalline features but showed subtle changes in the PXRD patterns, especially at higher diffraction angles.

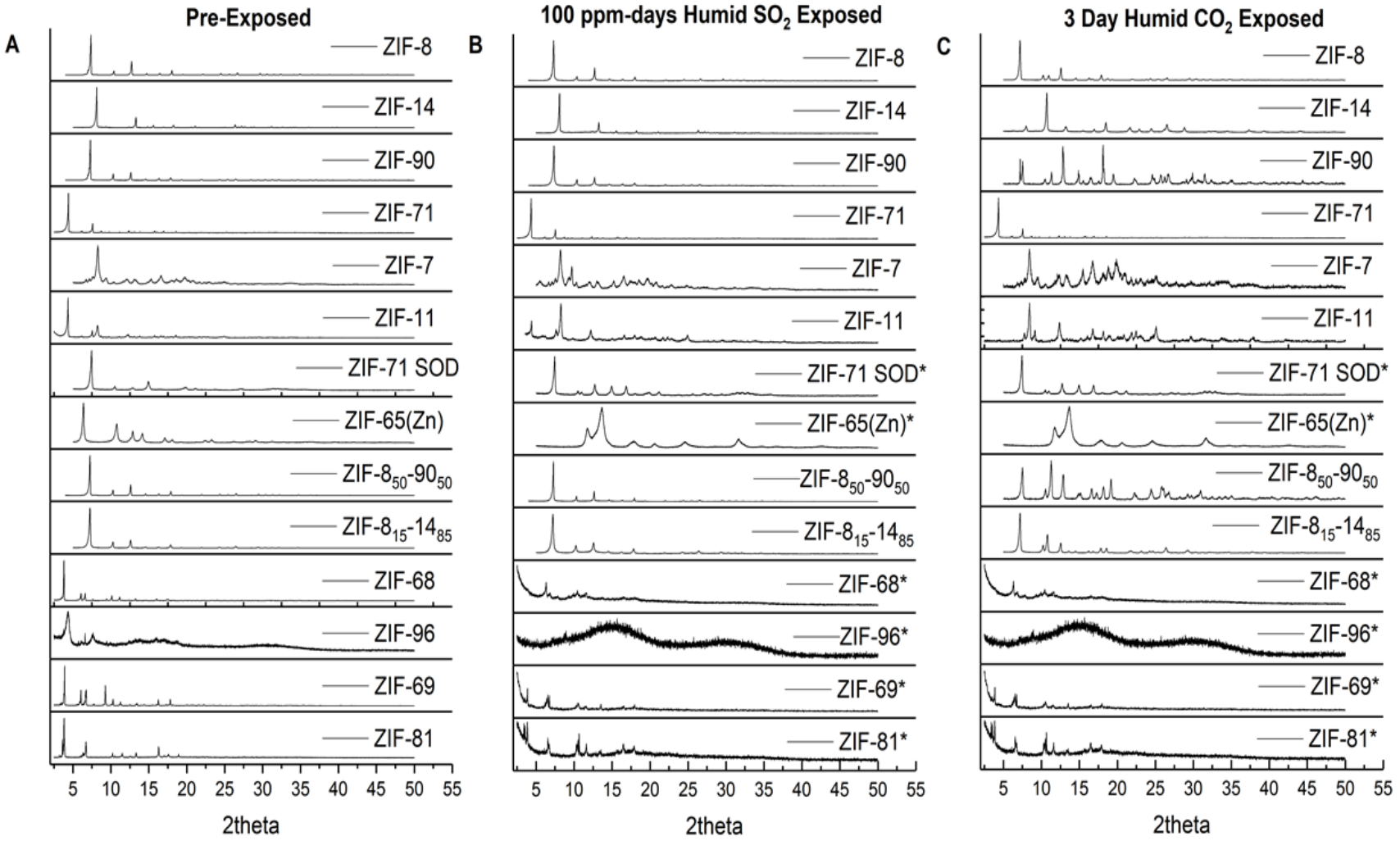

Figure 4.1. Normalized PXRD patterns of ZIFs investigated in this study under different conditions: A) Pre-exposure, B) 100 ppm-days humid SO_2 exposure, and C) 3-day humid CO_2 exposure. * Humid air PXRD patterns are showed in B) and C) for ZIFs unstable in humid air.

In addition to the bulk crystallinity measured by PXRD, analysis of the textural characteristics is important to evaluate stability.[30-31] To this end, pore volumes and BET surface areas of all the ZIFs were obtained from NP isotherms measured at 77 K. Changes in the pore volumes (in %) with respect to the pristine material, under different exposure conditions, are presented in **Figure 4.2**. A full collection of this data is available in Appendix B grouped by each material (**Figures B.2, B.6, B.10, B.14, B.25, B.28, B.31**, **B.35, B.39, B.43, B.45, B.47, B.49, B.51**). For the N_2-impermeable adsorbents ZIF-7 and ZIF-11, CO_2 physisorption at 273 K was used. All ZIFs exposed to dry acid gases (99.97% SO_2 or 12% CO_2) retain their pore volumes. Under humid air, GME topology ZIF-68, ZIF-69 and ZIF-81 along with the RHO topology ZIF-96 exhibit a complete reduction of their pore volume, in agreement with their PXRD spectra. As-synthesized ZIF-82 was found to be non-porous on activation pre-exposure. SOD-ZIF-71 and ZIF-65 (Zn) also show decreases in pore volume due to the previously discussed phase transitions, whereas all the other ZIFs maintain their pore volumes under the extended humid air exposure conditions used in this work. In this regard, it is significant that exposure to humid acid gases (SO_2 and CO_2) leads to a substantial drop in porosity of all the ZIFs investigated in this work with the exception of ZIF-71, in agreement with PXRD data from **Figure 4.1**. This destabilizing effect of humid acid gases is also observed in N_2-impermeable ZIF-7 and ZIF-11, as indicated by decreased CO_2 adsorption capacities at 273 K along with changes observed in their PXRD spectra. Under liquid water or aqueous SO_2 exposure, ZIF-8, ZIF-90 and ZIF-8_{50}-90_{50} retain their pore volumes, whereas ZIF-14 and ZIF-8_{15}-14_{85} register decreased pore volumes. In this work I did not find any changes to the bulk properties of ZIF-8 on long-term liquid water exposure, in contrast to other recent reports.[32-33]

Differences in the ZIF : water ratio may account for variations in the literature reports on liquid water stability of ZIFs, although this is not the main subject of the present work that focuses on acid gas stability of a larger collection of ZIFs.

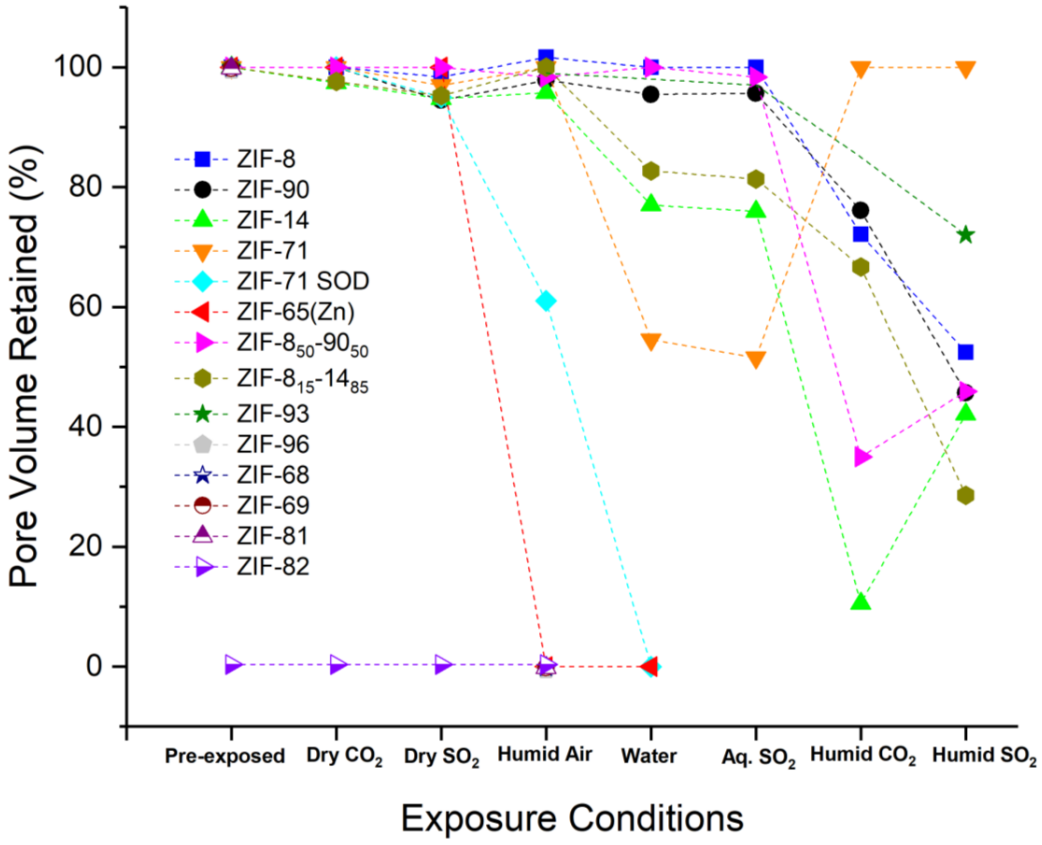

Figure 4.2. Retained pore volumes (%) as obtained from N_2 physisorption at 77 K for ZIFs under different exposure conditions. The dotted lines are included only for better visualization.

Table 4.1. Bulk stability chart of ZIF materials under different exposure modes at 298 K. Stability is denoted by color-coding: green: stable, yellow: phase change instability, red: degradation instability and gray: data not collected. The relative humidity was 85%, SO_2 concentration for humid SO_2 exposures was 20-40 ppm and CO_2 concentration was 12%.

Serial No.	Name	Imidazole linker substituent	Linker pK_a	Topology	Dry SO_2	Dry CO_2	Humid Air	Liq. Water	Aq. SO_2	Humid SO_2	Humid CO_2
1	ZIF-8	2-methyl	20.12	SOD							
2	ZIF-14	2-ethyl	19.56	ANA							
3	ZIF-$8_{15}14_{85}$	ZIF-8 & ZIF-14	19.56*	SOD							
4	ZIF-7	benzo	14.86	SOD							
5	ZIF-11	benzo	14.86	RHO							
6	ZIF-93	4-methyl 5-carboxaldeyhe	14.29	RHO							
7	ZIF-96	4- amino 5-carbonitrile	13.36	RHO							
8	ZIF-90	2-carboxaldehyde	13.58	SOD							
9	ZIF-$8_{50}90_{50}$	ZIF-8 & ZIF-90	13.58*	SOD							
10	ZIF-71	4,5-dichloro	11.01	RHO							
11	ZIF-71	4,5-dichloro	11.01	SOD							
12	ZIF-68	benzo & 2-nitro	10.22*	GME							
13	ZIF-69	5- chlorobenzo & 2-nitro	10.22*	GME							
14	ZIF-81	5-bromobenzo & 2-nitro	10.22*	GME							
15	ZIF-82	5-cyano & 2-nitro	10.22*	GME							
16	ZIF-65 (Zn)	2-nitro	10.22	SOD							

* For mixed-linker ZIFs, the lower of the two pK_a s of the ligands has been denoted.

The combined PXRD and the pore volume information allows us to construct a stability chart for the 16 ZIFs investigated in this work (**Table 4.1**). I have defined a ZIF to be "stable" under a particular exposure condition if it maintains its crystal structure and at least 90% of its pore volume. A number of reports propose that the linker pK_a is correlated with MOF/ZIF stability, with a higher linker pK_a being considered an indicator of higher stability.[22, 31] Hence, **Table 4.1** arranges the ZIFs in decreasing order of linker pK_a. Exposure conditions have been arranged from the left to right progressing from dry acid gas conditions to humid air, followed by water and aqueous SO_2, and lastly humid acid gas conditions. The topology of each ZIF is also shown. Instability of ZIFs as observed in this work is seen to be of two types: (i) instability due to degradation by attacking species, usually characterized by decreasing PXRD peak intensities and pore volumes; and (ii) instability due to phase change, characterized by a complete transformation in crystal structure on exposure and a total loss of pore volume upon complete transformation to the non-porous phase. These two modes of instability are shown in **Table 4.1** in red and yellow, respectively.

4.3.2 Chemical Changes: FTIR Spectroscopy

FTIR spectroscopy was used to examine the changes in the chemical bonding environments under different exposure conditions. Appendix B compiles the FTIR spectra for different ZIFs (**Figures B.3, B.7, B.11, B.15, B.18, B.22, B.26, B.29, B.32**, **B.36, B.40**). FTIR spectra for the GME topology ZIFs and ZIF-96 that degrade in humid air were not collected. In general, the FTIR spectra remain unchanged for all ZIFs that are stable under a particular exposure condition in **Table 4.1** above. For ZIFs undergoing phase transitions, only increases in absorbance intensities[12,44-49] are observed: e.g., SOD-ZIF-71, ZIF-65(Zn),

ZIF-7 and ZIF-11. These increased absorbance intensities upon phase change to dense materials are due to higher concentrations of chemical bonds in the chemically identical but nonporous/dense ZIFs. Much more pronounced changes are seen in the FTIR spectra for many materials after humid SO_2 and humid CO_2 exposures. **Figure 4.3** shows the spectra of ZIF-8, ZIF-14, ZIF-90 and ZIF-71 before and after exposure to humid CO_2 and humid SO_2. Under humid CO_2 exposure, new peaks around 1330 cm^{-1} and 1590 cm^{-1} corresponding to complex carbonate species are observed in ZIF-8, ZIF-14 and ZIF-90.[28, 34-35] Similar peaks are also observed in the FTIR spectra of ZIF-8_{50}-90_{50} and ZIF-8_{15}-14_{85}, which are unstable in humid CO_2. ZIF-7 and ZIF-11, however, do not show any major changes in their FTIR spectra on humid CO_2 exposure, even though the PXRD spectra and the CO_2 physisorption show clear signs of adsorbent degradation. No changes in the FTIR spectra were observed for ZIF-71. Under humid SO_2 exposures, formation of (bi)sulfite and (bi)sulfate species are observed in ZIF-8 and ZIF-14 (**Figure 4.3A-4.3B**), with the broad absorption region centered around 860 cm^{-1} comprising peaks at 946 cm^{-1} , 1018 cm^{-1} , 1167 cm^{-1} and 1094 cm^{-1} characteristic of (bi)sulfites[36] and peaks at 608 cm^{-1}, 983 cm^{-1}, 1055 cm^{-1} and 1112 cm^{-1} characteristic of (bi)sulfates.[37-39] In ZIF-90 (**Figure 4.3C**), the intensities of these new peaks under humid SO_2 exposure are much lower, while in ZIF-71 (**Figure 4.3D**) - which is "stable" under these exposure conditions - no new peaks are observed. All the other ZIFs exhibit (bi)sulfite and (bi)sulfate peaks under humid SO_2 exposures (Appendix B). In summary, all ZIFs investigated - with the notable exception of ZIF-71- were susceptible to degradation by humid SO_2, leading to the formation of (bi)sulfite and (bi)sulfate species, and decrease in crystallinity and porosity.

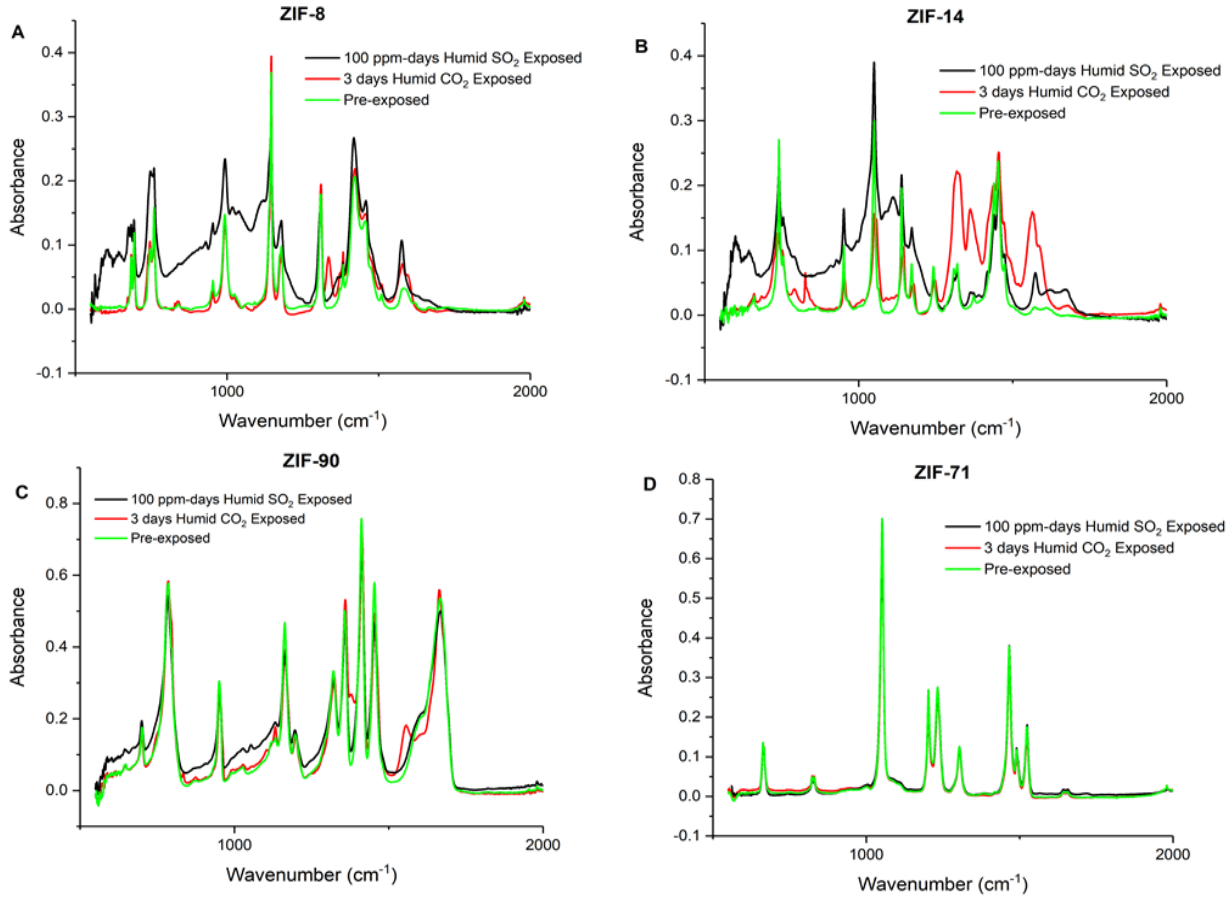

Figure 4.3. FTIR spectra of pre-exposed (green), 3 days humid CO_2-exposed (red), and 100 ppm-days humid SO_2-exposed (black) (A) ZIF-8, (B) ZIF-14, (C) ZIF-90, and (D) ZIF-71.

4.3.3 ZIF Degradation Kinetics

I proposed a mechanism in the previous Chapter of this thesis for degradation of ZIF-8 under humid SO_2 *via* formation of small amounts of sulfuric acid and sulfurous-sulfuric acid complexes that cleave the Zn-N coordinate bonds, protonate the imidazole linkers, and form (bi)sulfite/(bi)sulfate complexes. A thorough quantitative investigation into the kinetics of degradation of ZIFs can aid in understanding the role of different factors such as linker chemistry, topology, and pore sizes on the relative stabilities of ZIFs. Here I use energy dispersive X-ray (EDX) spectroscopy as a tool to measure SO_2 degradation kinetics and test its correlation with textural properties such as the pore volume. Pristine ZIFs have no sulfur (S) atoms, and therefore the quantity of S detected in the sample post-exposure is directly correlated to the formation of defect sites by (bi)sulfite and (bi)sulfate species. The Zn:S ratio is estimated for each ZIF at multiple exposure times, and is used to calculate the defect site density under the assumption that the incorporation of one S atom as (bi)sulfite/(bi)sulfate species is accompanied by the cleavage of one Zn-N bond. This assumption is consistent with the mechanism proposed earlier.

The humid SO_2 degradation kinetics of a selected set of ZIFs (1-6, 8-10 in **Table 4.1**) with respect to decreases in pore volume and corresponding increases in S content (and hence cleaved Zn-N bonds) are summarized in **Figures 4.4A-4.4B**. The detailed degradation kinetics are presented in Appendix B grouped by material (**Figures B.4, B.8, B.12, B.19, B.23, B.37, B.41**). All unstable ZIFs progressively lose their pore volume over time on humid SO_2 exposure, with the highest rate of loss of pore volume for ZIF-14 and the hybrid ZIF-8_{15}-14_{85} (**Figure 4.4A**). Only ZIF-71 maintains its pore volume over 10 days of exposure, while ZIF-8, ZIF-90 and ZIF-8_{50}-90_{50} approach a complete loss of pore

volume within 10 days (200 ppm-days) of humid SO_2 exposure. However, analysis of the corresponding increase of S content over time (**Figure 4.4B**) presents a very different microscopic picture. For example, ZIF-8 has the highest rate of incorporation of S atoms with a calculated Zn:S ratio of 1.8 (6.67 S atoms per unit cell, equivalent to only 14% of all Zn-N bonds cleaved) at complete pore volume loss (**Figure B.4**). In ZIF-90 the amount of S incorporation and the resulting cleaved Zn-N bonds is only 2% at complete pore volume loss (**Figure B.12**), with the other ZIFs showing values in the 4-10% range. The comparison of pore volume loss versus extent of bond cleavage for each ZIF (e.g., **Figure B.4**) strongly suggests that bulk textural measurements cannot be used as a substitute for microscopic chemical measurements if quantitative kinetic information is desired. To determine kinetic rate constants for defect formation in ZIFs from our experimental data, the following approach was adopted. The total number of available attack sites per unit volume (P_o) in a pristine ZIF can be calculated from the number of Zn-N bonds per unit volume. At any time, some of these sites have been degraded to create defect sites of concentration C and remaining pristine sites of concentration P:

$$P_o = P + C \tag{3}$$

The rate of defect site formation in a ZIF is assumed to be first order in the pristine site density and in the concentration of acid protons, leading to the following results:

$$\frac{dC}{dt} = -\frac{dP}{dt} = kP \tag{4}$$

$$C = P_o\,(1 - e^{-kt}) \tag{5}$$

Fitting equation (5) to the experimental defect densities measured by EDX analysis at multiple times (*e.g.*, **Figure 4.4B**) yields the degradation rate constants under humid SO_2

(**Table 4.2**). The rate constant for ZIF-8 is the highest (0.0146 day^{-1}) and is 7.3 times higher than that of ZIF-93 or ZIF-90 which have the lowest value (~0.002 day^{-1}). ZIF-7 and ZIF-11 have similar rate constants while that of ZIF-8_{50}-90_{50} is significantly closer to ZIF-90 than to ZIF-8.

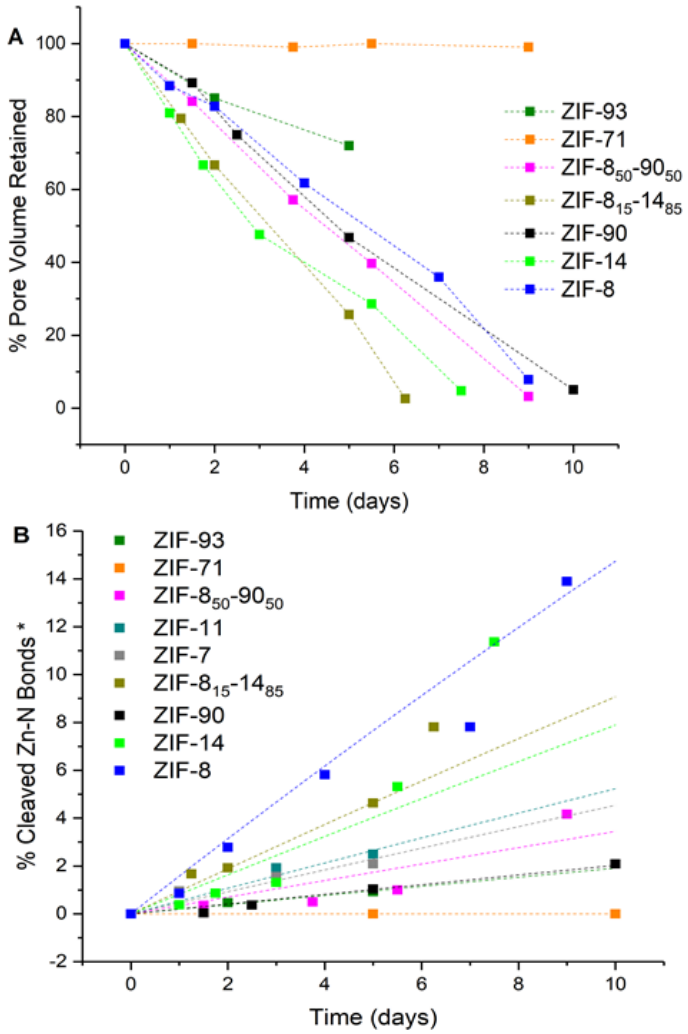

Figure 4.4. SO_2 degradation kinetics of ZIFs showing: (A) the decrease in pore volume over time, and (B) the corresponding increase in defect sites (cleaved Zn-N bonds) for each ZIF. Dotted lines in (A) are for visual aid and in (B) indicate fitted curves for observed degradation rate constants using equation (5). *Cleaved Zn-N bonds were calculated from the experimental Zn:S ratio assuming that one S atom incorporation led to one Zn-N bond cleavage.

Table 4.2. Degradation rate constants of ZIFs exposed to humid SO_2. *These values are from Morris *et al.*[40]

Serial No.	Material	Observed Rate Const. k (day^{-1}) ($\times 10^{-3}$)	Adsorbed Water at 85% R.H. (mmol/g)	Pore Vol. (cc_{pores}/g)	Pore Vol. (cc_{pores}/cc_{zif})	Adsorbed Water corrected for Pore Vol. ($mmol/cc_{pores}$)	Steric Index (Å)	XRD Crystallite Size (nm)	pK_a
1	**ZIF-8**	14.6	0.36	0.6	0.55	0.6	319	104	20.12
2	**ZIF-14**	9.5	1.5	0.22	0.24	6.8	386	116	19.56
3	**ZIF-8_{15}-14_{85}**	11.5	0.6	0.41	0.44	1.5	376	54	19.56
4	**ZIF-7**	4.6	1.03	0.2*	0.25	5.1	679	42	14.86
5	**ZIF-11**	5.4	1.06	0.46*	0.46	2.3	679	154	14.86
6	**ZIF-93**	1.9	17	0.31	0.31	55	524	42	14.29
8	**ZIF-90**	2.0	21	0.45	0.5	46.7	327	110	13.58
9	**ZIF-8_{50}-90_{50}**	3.6	19.5	0.6	0.61	32.5	323	114	13.58
10	**ZIF-71**	~0	0.17	0.35	0.41	0.5	461	185	11.01

4.3.4 Defect Thermodynamics - Computational Insights[#]

To obtain additional insight into the effects of linker chemistry on acid gas induced degradation, periodic DFT calculations were used to compare single Zn-N bond cleavage reactions and the resulting dangling-linker defect formation energies in the five single-linker SOD ZIF structures investigated in this work, along with the mixed-linker SOD ZIF-8_{15}-14_{85}. SOD structures have many fewer atoms per unit cell than ANA, GME, or RHO polymorphs, making these calculations tractable. Experimental synthesis of SOD-ZIF-71 has been reported, though its crystal structure is not fully resolved.[4] More recently, multiple accessible isomorphs of SOD-ZIF-71 have been reported.[41] Two such isomorphs, SOD-I-ZIF-71 and SOD-II-ZIF-71, whose simulated XRD patterns are in close agreement with our synthesized material (**Figure B.52**) were investigated. The lower defect formation energy in either structure is reported as the theoretical minimum for SOD-ZIF-71. I have defined the defect formation energy (**Table 4.3**) as the difference between the energy of a ZIF containing an acidified dangling-linker defect and the energy of the pristine ZIF plus the isolated acid gas molecule.[42-43] Negative values correspond to thermodynamically favorable defect formation, implying that the structure is more thermodynamically unstable. As noted above, no degradation of ZIFs is observed in dry SO_2 or CO_2, and the formation of reactive acid gas complexes (by acid gas molecules along with water vapor) is required to cleave the Zn-N bond.[44-46] In the case of humid SO_2, where various reactive complexes can form through interactions of SO_2 and water vapor, several simplified molecules as the attacking species were considered and the lowest defect formation energy

[#]The computational work reported in this subsection was performed by Rebecca Han

among them reported, since that indicates the likely experimental degradation path. Specifically, the following attacking species were considered: H_2O (for humid air); H_2SO_3, H_2SO_4 and SO_2-H_2O (for humid SO_2); and H_2CO_3 (for humid CO_2). Multiple initial geometries were explored in order to find the lowest energy structures reported below.

Table 4.3. Dangling-linker defect formation energies (eV) of SOD ZIFs computed using DFT. The color scheme – green (stable), yellow (phase change) and red (unstable) – reflects the experimental stability observations from Table 4.1.

Name	Exposure Condition		
	Humid Air	**Humid SO_2**	**Humid CO_2**
ZIF-8	0.61	-0.59	-0.57
ZIF-14	0.72	-0.20	0.20
ZIF-7	0.27	-0.80	-0.32
ZIF-90	0.25	-0.02	0.25
ZIF-71(SOD)	-0.04	-0.53	-0.04
ZIF-65(Zn)	0.74	-0.47	-0.31

Although the defect formation energies presented in **Table 4.3** only concern thermodynamic effects and do not give any information about the kinetics of degradation (**Table 4.2**), they display interesting correlations with our experimental observations of ZIF stability (**Table 4.1**). ZIF-8, ZIF-14, ZIF-7, and ZIF-90 are all predicted to be thermodynamically unfavorable to dangling-linker defects when attacked by H_2O alone (humid air) but are thermodynamically favorable to attack by humid SO_2. Both predictions

are in agreement with our experimental observations. SOD-ZIF-71 is thermodynamically favorable to Zn-N bond cleavage in all three exposures, consistent with its experimental propensity to undergo phase transitions to nonporous structures (which also requires Zn-N bond cleavage)[17] under all three conditions. ZIF-65(Zn) is an outlier when comparing the humid air predictions with experimental results. It is important to note that the as-synthesized ZIF-65(Zn) crystal structure matches well with the simulated XRD patterns, but changes to an unknown (non-SOD) structure during activation (**Figure B.27**) upon removal of all the solvent (dimethylformamide) molecules from the pores.[47] This is indicated by the disappearance of the 1670 cm^{-1} FTIR peak corresponding to the C=O stretch of DMF (**Figure B.53**) upon activating at 453 K.[48] The assumption of the original SOD crystal structure of ZIF-65(Zn) in defect formation energy calculations likely results in the observed deviation. Nevertheless, the material is correctly predicted to be thermodynamically favorable towards degradation in humid SO_2 and CO_2. The only significant inconsistency between **Table 4.3** and **Table 4.1** is the prediction that ZIF-14 and ZIF-90 are thermodynamically stable under humid CO_2 exposures whereas they are experimentally unstable. However, their predicted thermodynamic instability in humid SO_2 is consistent with observations. These findings indicate that the assumption of H_2CO_3 as the sole attacking species during humid CO_2 exposure may not be valid. However, in this work this has not been investigated further. The foregoing experimental results also indicate that RHO-ZIF-71 is very stable in relation to the other materials. Defect formation energy calculations could not be carried out for RHO ZIFs in this work due to prohibitive computational costs associated with their large unit cells.

4.3.5 Stability Analysis: Thermodynamic Stability Indicators

A synergistic analysis of all the results obtained from the library of data on 16 different ZIFs allow me to obtain new insights on the different factors influencing the relative stability among ZIF adsorbents. A number of stability indicators for ZIFs/MOFs have been discussed in literature, often in the context of water induced MOF degradation.[31] Higher coordination numbers of the metal center of a MOF or high oxidation state of the metal or metal cluster have been correlated with more stable MOFs.[49] However, in the present work all the ZIFs have the same Zn^{2+} metal center and tetrahedral coordination, and so this factor cannot explain the observed large variations in stability. The strength of the metal-linker coordination bond is also considered a key factor in determining MOF/ZIF stability. However, quantifying this concept is challenging. The linker pK$_a$ (i.e., its relative ease of protonation) has been used as an indicator for the strength of the Zn-N coordination bond, with a higher value correlated with higher thermodynamic stability.[22, 31] This is derived from the Lewis acid-base theory wherein the basicity of the conjugated base (i.e. ability of the nitrogen atom to donate electrons and form a Zn-N coordination bond) of a weaker acid (*i.e.,* low K$_a$ of the protonated ZIF linker) is stronger than that of the conjugated base of a stronger acid. The pK$_a$ values for all the ZIF linkers are shown in **Table 4.1**. Contrary to previous expectations, it is clear that pK$_a$ does not correlate strongly with the experimental observations of ZIF stability under water or acid gases. While ZIF-8 with the highest ligand pK$_a$ (20.12) is stable in water, ZIF-14 and ZIF-8_{15}-14_{85} with pK$_a$ values (19.56) close to ZIF-8 are unstable. Low pK$_a$ values correlate with phase transitions in aqueous solutions for both ZIF-71 (11.01) and ZIF-65(Zn) (10.22), but not in ZIF-7 (14.86) - which changes phase but has a higher pK$_a$ than ZIF-90 (13.58) which is stable against

phase transitions in aqueous solutions. Thus the correlation with pK$_a$ is not strong for water exposure of ZIFs. As for the humid acid gas exposures, there seems no correlation with high pK$_a$ and stability, with the most stable RHO-ZIF-71(11.01) having one of the lowest pK$_a$ values. Higher electron densities (more negative charge) on the coordinating atom of MOF linkers have also been correlated with higher stability of the coordination bond.[22] DDEC charges (**Table B.2**) of the N atoms in the DFT-optimized ZIF-8 and ZIF-71(SOD) materials were therefore calculated to determine whether there is a significant difference in the charge distributions. However, negligible variations (on the order of 0.01e) were found across ZIF-8 and ZIF-71, indicating that the charge distribution cannot explain the large stability differences between the two.

4.3.6 Statistical Analysis of Kinetic Stability

With previously proposed indicators for thermodynamic stability such as ligand pK$_a$ and electron density unable to explain the observed trends in acid gas stability behavior, I also examined other factors. MOFs that are stable under high humidity but that degrade under liquid water have been termed as "kinetically stable".[31] Among the ZIFs investigated here, ZIF-14, ZIF-8$_{15}$-14$_{85}$, ZIF-7, ZIF-11 and ZIF-71 all come under this definition. In the literature (as reviewed by Burtch *et al*)[19], hydrophobicity has often been associated with kinetic stability in the context of water exposure, based on the hypothesis that a hydrophobic linker prevents water from reaching the vicinity of the MOF metal center. Since kinetic rate constants for water vapor degradation in MOFs are not available, only qualitative assessments of water stability have been made thus far. However, I am in a position - notably in the context of humid acid gas stability - to assess relative kinetic stability of ZIFs in a quantitative manner. Indeed, RHO-ZIF-71 is the most hydrophobic

material in this set (**Figure B.54**) with a water uptake at 85% R.H of only 0.19 mmol/g. However, a number of other ZIFs in this work are also hydrophobic (< 1 mmol/g water adsorbed at 85% R.H.) but are all unstable under humid acid gas exposure. Hence, a fundamental feature of the present work is the distinction between thermodynamic (equilibrium) indicators of stability versus the kinetics of degradation, which in most cases determines the practically useful lifetime of the material. Based upon **Figure 4.4**, and the fairly small fractions (<10%) of cleaved Zn-N bonds in the ZIFs, it appears that the degradation processes are far from equilibrium.

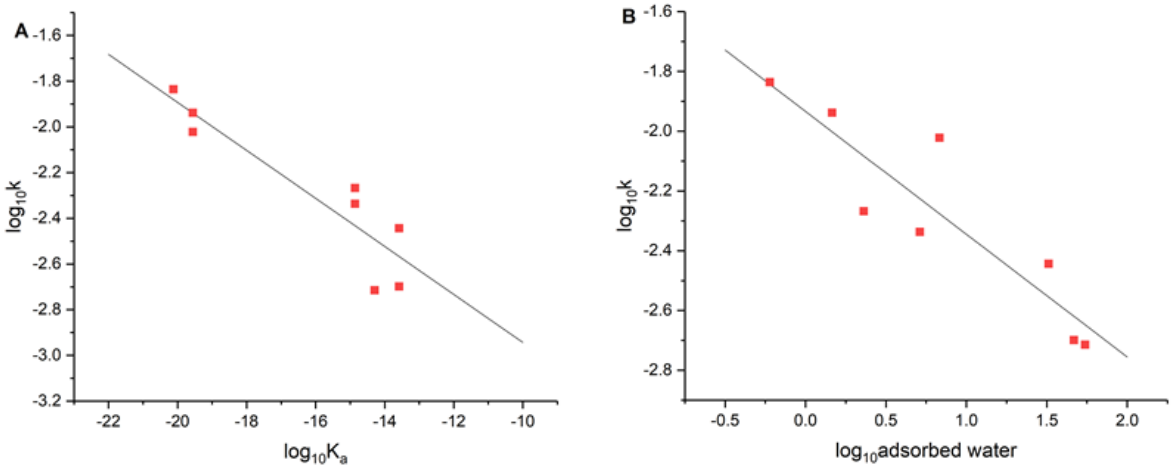

Figure 4.5. Power-law correlations ($k = ax^b$ plotted on logarithmic scale) between the experimentally observed degradation rate constants and x = linker K_a (A) or adsorbed water uptake at 85% R.H. (B), in ZIFs that measurably degraded under humid SO_2 exposure. Symbols: experimental data, Lines: correlation fits. The parameter values and regression coefficient (a, b, R^2) are (1.02×10^{-4}, -0,105, 0.83) and (1.16×10^{-2}, -0.41, 0.82) in the two correlations shown in (A) and (B) respectively.

In the above context of kinetic stability, I therefore carried out a statistical analysis of how different measurable variables associated with the structure of the ZIFs affect their degradation rate under humid SO_2 exposure. The variables (x) chosen for this analysis include the pore volume, the K_a of the constituent linkers, the quantity of adsorbed water under the exposure conditions (85% R.H.), crystallite size, and a recently proposed numerical measure of the linker shape and size called the steric index.[50] For each ZIF that degrades measurably under humid SO_2, I have listed these properties in **Table 4.2**. Williamson-Hall plots were used to determine crystallite size and microstrain after accounting for the small instrumental contribution to peak broadening (**Figure B.55** and **Table B.3**). To examine the correlation between these variables and the degradation rate constant, I assumed a simple power law dependence of the form $k = ax^b$. Analysis of the dependence of the rate constant on these variables was conducted by linear regression, as shown in **Figure 4.5** and **Figure B.56**.

Steric effects could be hypothesized to slow down the rate of degradation by impeding access to the Zn-N coordination bond sites, and inversely a larger pore volume can be hypothesized to accelerate degradation. Similarly, smaller crystallite sizes have been associated with increased thermal or structural instability in a variety of materials.[51-53] Our analysis (**Figure B.56**) shows that there is no correlation between the degradation rate constant with either the ZIF pore volume, linker steric indices, or the primary crystallite sizes (very low R^2 values of 0.001, 0.04, and 0.032 respectively) of the ZIFs that degrade under humid SO_2. In contrast with the dissolution of MOFs in liquid acids (wherein primary crystallite sizes and surface areas may have an appreciable effect), our hypothesis is that the kinetic degradation rate constants for acid gas exposure (as measured in this work)

reflect the intrinsic acid stability of the Zn-N bonds in the different crystal structures, independent of crystallite effects. This is corroborated by the lack of correlation with crystallite sizes in **Figure B.56**.

On the other hand, **Figure 4.5** reveals strong correlations ($R^2 > 0.8$) of the degradation rate constant with the linker K_a and the adsorbed water quantity at the 85% R.H. of the experiments. Remarkably, while high linker pK_a has been previously associated with higher thermodynamic stabilities of MOFs and ZIFs in the literature, I find a strong correlation between pK_a and the degradation rate constant with a *negative* proportionality, i.e., a high linker pK_a (low K_a) correlates to faster degradation under humid SO_2 exposure. The adsorbed water quantity also shows a strong correlation with a *negative* proportionality, *i.e.*, lower water uptake is correlated with faster degradation rates in humid SO_2. Additionally, the linker K_a and the adsorbed water uptake variable have no mutual correlation (**Figure B.56D**). A dual power-law fitting ($k = ax_1^b x_2^c$) of the degradation rate constant with these two variables leads to an even stronger correlation ($R^2 = 0.94$) albeit with three fitting parameters (**Figure B.57**).

4.3.7 Overall Implications and New Insights

As explained earlier, the defect densities obtained from the S incorporation measurements revealed that only 14% of the Zn-N bonds of ZIF-8 were cleaved directly by the time of complete pore volume loss. Although I assumed direct cleavage of one Zn-N coordination bond with one S-containing species, indirect Zn-N bond cleavages could result as well from the additional strain on the crystal structure due to incorporation of the (bi)sulfite/(bi)sulfate group at the defect site. Recently, a method called “solvent assisted

crystal redemption" (SACRed) was developed to reverse acid-gas induced damage in ZIFs and recover surface area and pore volume.[54] Using deuterated 2-methylimidazole linkers, it was estimated that 34% of dangling ZIF-8 linkers were replaced through SACRed for a "completely degraded" (*i.e.*, zero pore volume as measured by NP) ZIF-8 material. This linker replacement allowed a remarkable full recovery of pore volume. It is therefore significant to note that complete loss of NP pore volume can be observed with only a fraction of the coordination bonds cleaved. However, acid gas attack can still continue to occur. Indeed, **Figure 4.4B** does not indicate any decrease in the rate of Zn-N bond cleavage at long measurement times, and in fact shows an acceleration for some of the ZIF materials. A likely reason for this effect is that the structure becomes more hydrophilic as dangling-linker defects are created. For example, upon defect formation the ZIF-8 structure turns gradually more hydrophilic with a 22-fold higher uptake of water after 150 ppm-days of humid SO_2 exposure than in the pristine material (**Figure B.54**). The case of RHO-ZIF-71 (whose degradation rate was too slow to measure and hence cannot be correlated) warrants a separate comment. ZIF-71 has the lowest pK_a of all the linkers investigated in this study and therefore should indeed have the lowest degradation rate, in agreement with the correlation in **Figure 4.5A**. However, ZIF-71 is also a highly hydrophobic material with the lowest water uptake (~0.17 mmol/g) among all the investigated ZIFs. Visual analysis of the cross-section of the ZIF-71 unit cell suggests that the 4,5-dichloro substituents in the imidazole group in RHO-ZIFs should impart a strong steric protection to the Zn-N bonds, unlike the case of 2-substituted SOD-ZIFs (**Figure B.58**). The stability of RHO-ZIF-71 hence likely results from a synergistic combination of multiple factors including high hydrophobicity and steric effects. It is also important to mention that there are differences

of methodology in the synthesis of each ZIF material. Considerations such as different linker deprotonation equilibrium constants (K_a) and solubilities necessitate addition of coordination modulators/deprotonators and the use of different solvents and temperatures.[2, 7, 55] Since these synthesis variations in the literature have already led to the synthesis of high-quality ZIF samples, in this work I have adopted these previously established synthesis protocols and find that the pristine ZIF samples do not show any unusual XRD, physisorption, or FTIR characteristics indicative of a higher level of defects. To test the sensitivity of the degradation rates to differences in synthesis procedure, I synthesized ZIF-8 with and without the sodium formate coordination modulator (see SI for details). The two materials were then simultaneously exposed to humid SO_2 and found no significant difference in the rate of S incorporation (Zn:S ratio) during degradation (**Figure B.59**), thus further corroborating the hypothesis that the observed degradation behavior is intrinsic to the ZIF structure and composition rather than influenced by possibly differing levels of defects in the pristine materials.

Our overall analysis leads us to propose a division of the investigated ZIFs into three broad classes: **(I)** highly hydrophobic ZIFs with low pK_a, essentially impermeable to any hydrophilic attacking species under our exposure conditions, and hence kinetically stable (e.g. RHO-ZIF-71); **(II)** hydrophobic ZIFs with high pK_a that still uptake significant water at high R.H. and have a high degradation rate constant (e.g. ZIF-14, ZIF-8); and **(III)** hydrophilic ZIFs whose pores are essentially filled with liquid-like water under the exposure conditions and have a lower rate of degradation than hydrophobic ZIFs (e.g. ZIF-93, ZIF-90 etc.). The relatively higher kinetic stability of ZIFs of class **III** compared to those of class **II –** as seen in **Table 4.2** and the correlation in **Figure 4.5 –** is surprising but

may have multiple possible explanations. For example, ZIF-8 is often considered as a typical example of a hydrophobic "stable" ZIF with the highest linker pK_a among those investigated in this work. However, hydrophilic ZIFs such as ZIF-90 or ZIF-93 have polar functional groups which could interact strongly with SO_2-containing species along with water and shield the imidazole backbone and the Zn-N coordination bond from direct acid gas attack. The presence of liquid-like water in these ZIFs may also lead to a higher fraction of the less potent sulfurous acid (through SO_2 dissolution in water) as the attacking species, as compared to hydrophobic ZIFs in which more potent sulfuric-sulfurous acid complexes form as found by us recently for ZIF-8.[30]

To complete our present investigation, dry SO_2 adsorption isotherms were also measured up to high (2.5 bar) pressures at 298 K (**Figure B.60**). ZIFs with polar linkers such as ZIF-90 and ZIF-65(Zn) have a higher SO_2 uptake at low pressures than other ZIFs due to stronger interactions with the polar SO_2 molecules (**Table B.4**).[56] Dry SO_2 gas strongly interacts with oxygen in MOFs through its S atom, and can hydrogen bond with C-H groups in aromatic rings and alkyl groups through its O atoms.[57-58] Such interactions of MOFs with dry acid gases could be hypothesized to result in irreversible adsorption and degradation of the crystal structure.[59-62] However, my results show that all the ZIFs investigated in this work remain stable after exposure to pure SO_2 gas up to 2.5 bar, and the best-performing materials such as ZIF-65(Zn) can be utilized in SO_2-containing feed streams under dry conditions. A practical implication of the dry-SO_2 stability of ZIFs is that the presence of humidity along with the acid gas is critical for degradation to occur. Hence, many process streams may only require a simpler dehydration (water removal) pretreatment, rather than more complex desulfurization pretreatments or pursuit of

ZIFs/MOFs with extremely high humid SO_2 stability. The performance of ZIF-65(Zn) and ZIF-90 at 0.1 bar and 1 bar are comparable with the highest reported SO_2 uptakes in the literature for MOFs (**Table B.4**).[57-58, 61] The SO_2 saturation uptake of ZIF-65(Zn) (13.7 mmol/g at 2.7 bar) is the highest reported for any MOF to the best of our knowledge, and the shape of the isotherm suggests a framework flexibility effect due to SO_2 uptake.

4.4 Conclusions

I have conducted a systematic and quantitative investigation of the structural and chemical changes occurring in a library of 16 different ZIF materials under exposure to the acid gases CO_2 and SO_2 in this Chapter. Observations for each ZIF under a particular exposure condition have been summarized in the form of a color-coded "stability chart", which is a useful resource for evaluation of ZIFs for separation applications in which acid gases are a significant factor. All ZIFs investigated under dry CO_2 and SO_2 were observed to be stable under such exposure conditions. ZIF-90 and ZIF-65(Zn) had dry SO_2 uptakes comparable with the highest reported in MOF literature. A number of ZIFs underwent transformations to non-porous phases on humid air or water exposure while all GME topology ZIFs investigated in this work degraded under humid air exposure. However, ZIFs investigated in this work were susceptible to bulk degradation under long-term exposure to humidified CO_2 or SO_2 with the exception of ZIF-71. FTIR measurements were used to probe the mechanistic aspects of the CO_2/SO_2-induced degradation, and S incorporation post-exposure to humid SO_2 was quantified through EDX. This allowed a kinetic study of ZIF degradation under humid SO_2, and rate constants for humid SO_2-induced degradation have been measured for the first time. Various conventional indicators of thermodynamic and kinetic stability were evaluated to explain the observed humid acid gas stability, but

none were able to satisfactorily explain the observations. On the other hand, due to the examination of multiple ZIF materials in this work, I was able to examine statistical correlations of the rate constant with chemical and structural variables associated with the ZIFs. This analysis revealed surprisingly strong correlations of the degradation rate with the linker K_a and ZIF hydrophilicity with *negative* proportionalities. To the best of my knowledge, this is the first generalized study that provides quantitative insights on the stability of a diverse range of ZIF materials under acid gas (CO_2, SO_2) exposure.

An important feature of this Chapter is the stability chart, which allows researchers to choose ZIFs exhibiting stability under their particular application process condition for further investigation. For example, humid air stable ZIFs such as ZIF-7, ZIF-11, ZIF-71 etc. should not be used for any practical application where they are exposed to liquid water as they are prone to phase changes under those conditions. One can conclude from this Chapter in general that ZIFs are prone to degradation under high humidity in the presence of acid gases such as SO_2 and CO_2. However, ZIF-71 exhibits enhanced stability under such conditions compared to the other ZIFs investigated. Another important general conclusion of this thesis so far has been the stability of ZIF materials towards dry SO_2 or CO_2 even at high concentrations. Whether other toxic and reactive acid gases would behave similarly with ZIF materials remains an open question. It may be possible to impart stability to an incoming humid process stream containing a mixture of different acid gases by removing or reducing the water content to an appropriate level if ZIFs are demonstrated to be stable to other dry acid gases as well. Nitrogen dioxide (NO_2) is one such major acid gas that is usually present in process streams containing SO_2 or CO_2. In the next chapter, I systematically investigate the interactions of dry and humid NO_2 gas with 3 carefully

chosen ZIF materials (ZIF-8, ZIF-90 and ZIF-71) to establish similarities and/or differences of ZIF interactions with other acid gases such as CO_2 and SO_2.

REFERENCES

1. Gee, J. A.; Chung, J.; Nair, S.; Sholl, D. S., Adsorption and Diffusion of Small Alcohols in Zeolitic Imidazolate Frameworks ZIF-8 and ZIF-90. *J. Phys. Chem. C* **2013,** *117* (6), 3169-3176.

2. He, M.; Yao, J. F.; Liu, Q.; Zhong, Z. X.; Wang, H. T., Toluene-assisted synthesis of RHO-type zeolitic imidazolate frameworks: synthesis and formation mechanism of ZIF-11 and ZIF-12. *Dalton Trans.* **2013,** *42* (47), 16608-16613.

3. Zhang, K.; Lively, R. P.; Dose, M. E.; Brown, A. J.; Zhang, C.; Chung, J.; Nair, S.; Koros, W. J.; Chance, R. R., Alcohol and water adsorption in zeolitic imidazolate frameworks. *Chem. Commun.* **2013,** *49* (31), 3245-3247.

4. Schweinefuss, M. E.; Springer, S.; Baburin, I. A.; Hikov, T.; Huber, K.; Leoni, S.; Wiebcke, M., Zeolitic imidazolate framework-71 nanocrystals and a novel SOD-type polymorph: solution mediated phase transformations, phase selection via coordination modulation and a density functional theory derived energy landscape. *Dalton Trans.* **2014,** *43* (9), 3528-3536.

5. Schoenecker, P. M. High-throughput synthesis and application development of water-stable MOFs, Ph.D. Thesis. Georgia Institute of Technology, Atlanta, U.S.A., 2012.

6. Eum, K.; Jayachandrababu, K. C.; Rashidi, F.; Zhang, K.; Leisen, J.; Graham, S.; Lively, R. P.; Chance, R. R.; Sholl, D. S.; Jones, C. W.; Nair, S., Highly Tunable Molecular Sieving and Adsorption Properties of Mixed-Linker Zeolitic Imidazolate Frameworks. *J.Am.Chem.Soc.* **2015,** *137* (12), 4191-4197.

7. Thompson, J. A.; Blad, C. R.; Brunelli, N. A.; Lydon, M. E.; Lively, R. P.; Jones, C. W.; Nair, S., Hybrid Zeolitic Imidazolate Frameworks: Controlling Framework Porosity and Functionality by Mixed-Linker Synthesis. *Chem. Mater.* **2012,** *24* (10), 1930-1936.

8. Thompson, J. A.; Brunelli, N. A.; Lively, R. P.; Johnson, J. R.; Jones, C. W.; Nair, S., Tunable CO_2 Adsorbents by Mixed-Linker Synthesis and Postsynthetic Modification of Zeolitic Imidazolate Frameworks. *J. Phys. Chem. C* **2013,** *117* (16), 8198-8207.

9. Morris, W.; Leung, B.; Furukawa, H.; Yaghi, O. K.; He, N.; Hayashi, H.; Houndonougbo, Y.; Asta, M.; Laird, B. B.; Yaghi, O. M., A Combined Experimental-Computational Investigation of Carbon Dioxide Capture in a Series of Isoreticular Zeolitic Imidazolate Frameworks. *J.Am.Chem.Soc.* **2010,** *132* (32), 11006-11008.

10. Banerjee, R.; Furukawa, H.; Britt, D.; Knobler, C.; O'Keeffe, M.; Yaghi, O. M., Control of Pore Size and Functionality in Isoreticular Zeolitic Imidazolate Frameworks and their Carbon Dioxide Selective Capture Properties. *J.Am.Chem.Soc.* **2009,** *131* (11), 3875-3877.

11. Zhang, C.; Lively, R. P.; Zhang, K.; Johnson, J. R.; Karvan, O.; Koros, W. J., Unexpected Molecular Sieving Properties of Zeolitic Imidazolate Framework-8. *J.Phys.Chem.Lett.* **2012,** *3* (16), 2130-2134.

12. Mote, V.; Purushotham, Y.; Dole, B., Williamson-Hall analysis in estimation of lattice strain in nanometer-sized ZnO particles. *J.Th.App.Phy.* **2012,** *6* (1), 1-8.

13. Thompson, J. A.; Chapman, K. W.; Koros, W. J.; Jones, C. W.; Nair, S., Sonication-induced Ostwald ripening of ZIF-8 nanoparticles and formation of ZIF-8/polymer composite membranes. *Microporous Mesoporous Mater.* **2012,** *158*, 292-299.

14. Walton, K. S.; Snurr, R. Q., Applicability of the BET method for determining surface areas of microporous metal-organic frameworks. *J.Am.Chem.Soc.* **2007,** *129* (27), 8552-8556.

15. Hashimoto, Y.; Tanaka, S., A new method of generation of gases at parts per million levels for preparation of standard gases. *Environ. Sci. Technol.* **1980,** *14* (4), 413-416.

16. Park, K. S.; Ni, Z.; Cote, A. P.; Choi, J. Y.; Huang, R. D.; Uribe-Romo, F. J.; Chae, H. K.; O'Keeffe, M.; Yaghi, O. M., Exceptional chemical and thermal stability of zeolitic imidazolate frameworks. *Proc. Natl. Acad. Sci. U. S. A.* **2006,** *103* (27), 10186-10191.

17. Banerjee, R.; Phan, A.; Wang, B.; Knobler, C.; Furukawa, H.; O'Keeffe, M.; Yaghi, O. M., High-throughput synthesis of zeolitic imidazolate frameworks and application to CO_2 capture. *Science* **2008,** *319* (5865), 939-943.

18. Morris, W.; Doonan, C. J.; Furukawa, H.; Banerjee, R.; Yaghi, O. M., Crystals as molecules: Postsynthesis covalent functionalization of zeolitic imidazolate frameworks. *J.Am.Chem.Soc.* **2008,** *130* (38), 12626-12627.

19. First, E. L.; Floudas, C. A., MOFomics: Computational pore characterization of metal–organic frameworks. *Microporous Mesoporous Mater.* **2013,** *165*, 32-39.

20. https://github.com/numat/RASPA2/tree/master/structures/mofs/cif.

21. Marenich, A. V.; Cramer, C. J.; Truhlar, D. G., Universal Solvation Model Based on Solute Electron Density and on a Continuum Model of the Solvent Defined by the Bulk Dielectric Constant and Atomic Surface Tensions. *J. Phys. Chem. B* **2009,** *113* (18), 6378-6396.

22. Lu, P.; Wu, Y.; Kang, H.; Wei, H.; Liu, H.; Fang, M., What can pKa and NBO charges of the ligands tell us about the water and thermal stability of metal organic frameworks? *J. Mater. Chem. A* **2014,** *2* (38), 16250-16267.

23. Namazian, M.; Zakery, M.; Noorbala, M. R.; Coote, M. L., Accurate calculation of the pKa of trifluoroacetic acid using high-level ab initio calculations. *Chem. Phys. Lett.* **2008,** *451* (1), 163-168.

24. Liptak, M. D.; Shields, G. C., Accurate pKa Calculations for Carboxylic Acids Using Complete Basis Set and Gaussian-n Models Combined with CPCM Continuum Solvation Methods. *J.Am.Chem.Soc.* **2001,** *123* (30), 7314-7319.

25. Manz, T. A., Limas, N.G., DDEC6: A Method for Computing Even-Tempered Net Atomic Charges in Periodic and Nonperiodic Materials. arXiv:1512.08270, 2015.

26. Manz, T. A.; Sholl, D. S., Chemically Meaningful Atomic Charges That Reproduce the Electrostatic Potential in Periodic and Nonperiodic Materials. *J. Chem. Theory Comput.* **2010,** *6* (8), 2455-2468.

27. Macrae, C. F.; Bruno, I. J.; Chisholm, J. A.; Edgington, P. R.; McCabe, P.; Pidcock, E.; Rodriguez-Monge, L.; Taylor, R.; van de Streek, J.; Wood, P. A., Mercury CSD 2.0 - new features for the visualization and investigation of crystal structures. *J. Appl. Crystallogr.* **2008,** *41* (2), 466-470.

28. Mottillo, C.; Friscic, T., Carbon Dioxide Sensitivity of Zeolitic Imidazolate Frameworks. *Angew. Chem., Int. Ed.* **2014,** *53* (29), 7471-7474.

29. Zhao, P.; Lampronti, G. I.; Lloyd, G. O.; Wharmby, M. T.; Facq, S.; Cheetham, A. K.; Redfern, S. A. T., Phase Transitions in Zeolitic Imidazolate Framework 7: The Importance of Framework Flexibility and Guest-Induced Instability. *Chem. Mater.* **2014,** *26* (5), 1767-1769.

30. Bhattacharyya, S.; Pang, S. H.; Dutzer, M. R.; Lively, R. P.; Walton, K. S.; Sholl, D. S.; Nair, S., Interactions of SO_2-Containing Acid Gases with ZIF-8: Structural Changes and Mechanistic Investigations. *J. Phys. Chem. C* **2016,** *120* (48), 27221-27229.

31. Burtch, N. C.; Jasuja, H.; Walton, K. S., Water Stability and Adsorption in Metal-Organic Frameworks. *Chem. Rev.* **2014,** *114* (20), 10575-10612.

32. Zhang, H.; Liu, D.; Yao, Y.; Zhang, B.; Lin, Y. S., Stability of ZIF-8 membranes and crystalline powders in water at room temperature. *J. Membr. Sci.* **2015,** *485*, 103-111.

33. Liu, X.; Li, Y.; Ban, Y.; Peng, Y.; Jin, H.; Bux, H.; Xu, L.; Caro, J.; Yang, W., Improvement of hydrothermal stability of zeolitic imidazolate frameworks. *Chem. Commun.* **2013,** *49* (80), 9140-9142.

34. Bhattacharyya, S.; Jayachandrababu, K. C.; Chiang, Y.; Sholl, D. S.; Nair, S., Butanol Separation from Humid CO_2-Containing Multicomponent Vapor Mixtures by Zeolitic Imidazolate Frameworks. *ACS Sustainable Chem. Eng.* **2017,** *5* (10), 9467-9476.

35. Liu, H.; Guo, P.; Regueira, T.; Wang, Z.; Du, J.; Chen, G., Irreversible Change of the Pore Structure of ZIF-8 in Carbon Dioxide Capture with Water Coexistence. *J. Phys. Chem. C* **2016,** *120* (24), 13287-13294.

36. Miller, F. A.; Wilkins, C. H., Infrared spectra and characteristic frequencies of inorganic ions- their use in qualitative analysis. *Anal. Chem.* **1952,** *24* (8), 1253-1294.

37. J.K.Saha, J. P., Crystallization of zinc sulphate single crystals and its structural, thermal and optical characterization. *J. Bangladesh Acad. Sci.* **2011,** *35* (2), 203-210.

38. Sivanesan, G.; Kolandaivel, P.; Pandian, S. S., Laser Raman and FT-IR studies of pure and Zn-doped TGS. *Mater. Chem. Phys.* **1993,** *34* (1), 73-77.

39. N. Tugrul, A. S. K., E. Moroydor Derun, S. Piskin, The Determination of the Zinc Sulfate, Sodium Hydroxide and Boric Acid Molar Ratio on the Production of Zinc Borates. *Int.J.Chem.Mol.Nucl.Mater.Metall.Eng.* **2014,** *8* (7), 639-643.

40. Morris, W.; He, N.; Ray, K. G.; Klonowski, P.; Furukawa, H.; Daniels, I. N.; Houndonougbo, Y. A.; Asta, M.; Yaghi, O. M.; Laird, B. B., A Combined Experimental-Computational Study on the Effect of Topology on Carbon Dioxide Adsorption in Zeolitic Imidazolate Frameworks. *J. Phys. Chem. C* **2012,** *116* (45), 24084-24090.

41. Springer, S.; Baburin, I. A.; Heinemeyer, T.; Schiffmann, J. G.; van Wullen, L.; Leoni, S.; Wiebcke, M., A zeolitic imidazolate framework with conformational variety: conformational polymorphs versus frameworks with static conformational disorder. *Crystengcomm* **2016,** *18* (14), 2477-2489.

42. Han, C.; Zhang, C.; Tyminska, N.; Schmidt, J. R.; Sholl, D. S., Insights into the Stability of Zeolitic Imidazolate Frameworks in Humid Acidic Environments from First Principles Calculations. *J. Phys. Chem. C* **2018**.

43. Zhang, C.; Han, C.; Sholl, D. S.; Schmidt, J. R., Computational Characterization of Defects in Metal-Organic Frameworks: Spontaneous and Water-Induced Point Defects in ZIF-8. *J.Phys.Chem.Lett.* **2016,** *7* (3), 459-464.

44. Bernard, J.; Seidl, M.; Kohl, I.; Liedl, K. R.; Mayer, E.; Gálvez, Ó.; Grothe, H.; Loerting, T., Spectroscopic Observation of Matrix-Isolated Carbonic Acid Trapped from the Gas Phase. *Angew. Chem., Int. Ed.* **2011,** *50* (8), 1939-1943.

45. Flamm, D. L.; Bacon, D. D.; Kinsbron, E.; English, A. T., Chemical reaction of Sulfur-Dioxide at high humidity and temperature - implications for accelerated testing. *J. Electrochem. Soc.* **1981,** *128* (3), 679-685.

46. Liu, J.; Fang, S.; Wang, Z.; Yi, W.; Tao, F.-M.; Liu, J.-y., Hydrolysis of Sulfur Dioxide in Small Clusters of Sulfuric Acid: Mechanistic and Kinetic Study. *Environ. Sci. Technol.* **2015,** *49* (22), 13112-13120.

47. Tu, M.; Wiktor, C.; Rosler, C.; Fischer, R. A., Rapid room temperature syntheses of zeolitic-imidazolate framework (ZIF) nanocrystals. *Chem. Commun.* **2014,** *50* (87), 13258-13260.

48. Öztürk, Z.; Hofmann, J. P.; Lutz, M.; Mazaj, M.; Logar, N. Z.; Weckhuysen, B. M., Controlled Synthesis of Phase-Pure Zeolitic Imidazolate Framework Co-ZIF-9. *Eur. J. Inorg. Chem.* **2015,** *2015* (9), 1625-1630.

49. Low, J. J.; Benin, A. I.; Jakubczak, P.; Abrahamian, J. F.; Faheem, S. A.; Willis, R. R., Virtual High Throughput Screening Confirmed Experimentally: Porous Coordination Polymer Hydration. *J. Am. Chem. Soc.* **2009,** *131* (43), 15834-15842.

50. Yang, J.; Zhang, Y.-B.; Liu, Q.; Trickett, C. A.; Gutiérrez-Puebla, E.; Monge, M. Á.; Cong, H.; Aldossary, A.; Deng, H.; Yaghi, O. M., Principles of Designing Extra-Large Pore Openings and Cages in Zeolitic Imidazolate Frameworks. *J.Am.Chem.Soc.* **2017,** *139* (18), 6448-6455.

51. Kim, U.-J.; Eom, S. H.; Wada, M., Thermal decomposition of native cellulose: Influence on crystallite size. *Polym. Degrad. Stab.* **2010,** *95* (5), 778-781.

52. Korotcenkov, G.; Cho, B. K., The role of grain size on the thermal instability of nanostructured metal oxides used in gas sensor applications and approaches for grain-size stabilization. *Prog. Cryst. Growth Charact. Mater.* **2012,** *58* (4), 167-208.

53. Praserthdam, P.; Phungphadung, J.; Tanakulrungsank, W., Effect of crystallite size and calcination temperature on the thermal stability of single nanocrystalline chromium oxide: expressed by novel correlation. *Mater. Res. Innovations* **2003,** *7* (2), 118-123.

54. Jayachandrababu, K. C.; Bhattacharyya, S.; Chiang, Y.; Sholl, D. S.; Nair, S., Recovery of Acid-Gas-Degraded Zeolitic Imidazolate Frameworks by Solvent-Assisted Crystal Redemption (SACRed). *ACS Appl. Mater. Interfaces* **2017,** *9* (40), 34597-34602.

55. Cravillon, J.; Schroder, C. A.; Bux, H.; Rothkirch, A.; Caro, J.; Wiebcke, M., Formate modulated solvothermal synthesis of ZIF-8 investigated using time-resolved in situ X-ray diffraction and scanning electron microscopy. *Crystengcomm* **2012,** *14* (2), 492-498.

56. Fioretos, K. A.; Psofogiannakis, G. M.; Froudakis, G. E., Ab-Initio Study of the Adsorption and Separation of NO_x and SO_x Gases in Functionalized IRMOF Ligands. *J. Phys. Chem. C* **2011,** *115* (50), 24906-24914.

57. Yang, S.; Sun, J.; Ramirez-Cuesta, A. J.; Callear, S. K.; DavidWilliam, I. F.; Anderson, D. P.; Newby, R.; Blake, A. J.; Parker, J. E.; Tang, C. C.; Schröder, M., Selectivity and direct visualization of carbon dioxide and sulfur dioxide in a decorated porous host. *Nat Chem* **2012,** *4* (11), 887-894.

58. Savage, M.; Cheng, Y.; Easun, T. L.; Eyley, J. E.; Argent, S. P.; Warren, M. R.; Lewis, W.; Murray, C.; Tang, C. C.; Frogley, M. D.; Cinque, G.; Sun, J.; Rudić, S.; Murden, R. T.; Benham, M. J.; Fitch, A. N.; Blake, A. J.; Ramirez-Cuesta, A. J.; Yang, S.; Schröder, M., Selective Adsorption of Sulfur Dioxide in a Robust Metal–Organic Framework Material. *Adv. Mater.* **2016,** *28* (39), 8705-8711.

59. Ebrahim, A. M.; Levasseur, B.; Bandosz, T. J., Interactions of NO_2 with Zr-Based MOF: Effects of the Size of Organic Linkers on NO_2 Adsorption at Ambient Conditions. *Langmuir* **2013,** *29* (1), 168-174.

60. Petit, C.; Levasseur, B.; Mendoza, B.; Bandosz, T. J., Reactive adsorption of acidic gases on MOF/graphite oxide composites. *Microporous Mesoporous Mater.* **2012,** *154*, 107-112.

61. Tan, K.; Canepa, P.; Gong, Q.; Liu, J.; Johnson, D. H.; Dyevoich, A.; Thallapally, P. K.; Thonhauser, T.; Li, J.; Chabal, Y. J., Mechanism of Preferential Adsorption of SO_2 into Two Microporous Paddle Wheel Frameworks M(bdc)(ted)$_{0.5}$. *Chem. Mater.* **2013,** *25* (23), 4653-4662.

62. Dathe, H.; Jentys, A.; Lercher, J. A., Sulfate formation on SO_x trapping materials studied by Cu and S K-edge XAFS. *Phys. Chem. Chem. Phys.* **2005,** *7* (6), 1283-1292.

CHAPTER 5. NO_X STABILITY OF ZEOLITIC IMIDAZOLATE FRAMEWORKS

5.1 Introduction

In this Chapter, I systematically investigate the reaction mechanisms of dry and humid NO_x with ZIFs and their impact on the stability of these materials. Here, a material's stability is defined in terms of the retention of its crystal structure and pore volume.[1] The mechanisms of ZIF interaction with (and degradation by) NO_x are shown to be strikingly different from the mechanisms of interaction with CO_2 or SO_x.[2-4] Many of the mechanistic findings of this Chapter can be expected to be applicable to a wider variety of MOFs. In the previous Chapter on SO_x stability of ZIFs, I studied a large set of more than 15 ZIF materials.[2] These results motivated me to study three representative ZIFs with respect to interaction with NO_x. ZIF-8 and ZIF-90 were selected because they had the highest and lowest measurable degradation rate constants in humid SO_x. ZIF-71 was also selected because it showed no measurable degradation in the presence of humid SO_x. These ZIFs are therefore expected to encompass the different outcomes possible upon NO_x exposure. The main topological characteristics of the three ZIF structures are shown in **Table C.1** (Appendix C).

5.2 Experimental Methods

5.2.1 Materials

Zinc(II) nitrate hexahydrate (99%) and imidazole-2-carboxaldehyde (97%) were obtained from Alfa Aesar. 2-methylimidazole (99%), 4,5-dichloroimidazole (98%) and

sodium formate (99%) were purchased from Sigma-Aldrich while methanol (99.8%) and N,N-dimethylformamide (DMF) (99.8%) were purchased from BDH. Chemicals were used as received. Deionized (DI) water from the EMD Millipore water purification system and ultra-high purity air (76.5-80.5% N_2, 19.5-23.5% O_2) from Airgas were used in this work.

5.2.2 Synthesis of ZIF adsorbents

The synthesis protocol reported by Gee *et al* was modified to synthesize ZIF-8 and ZIF-90 in this work.[5] For ZIF-8 synthesis, a solution of 0.972 g 2-methylimidazole and 1.614 g sodium formate in 120 cc methanol was mixed with another solution of 1.764 g zinc (II) nitrate in 120 cc methanol, followed by heating at 363 K for 24 hours. The collected crystals were washed three times with methanol and air dried at 333 K.

ZIF-90 synthesis was carried out by adding 11.904 g zinc (II) nitrate and 15.368 g imidazole-2-carboxaldehyde to 400 cc DMF and heating the solution to 393 K in an oil bath for 20 minutes. The solution was then cooled to ambient temperature and left to crystallize for 4 days. The collected crystals were washed three times with methanol and air dried at 333 K.

The synthesis protocol reported by Zhang *et al*.[6] was modified in order to synthesize ZIF-71 in this work. Two 60 cc methanol solutions were prepared containing 297 mg zinc (II) acetate and 876 mg 4,5-dichloroimidazole. The two solutions were then mixed and kept without stirring for 24 hours under ambient conditions. The collected crystals were washed three times with methanol and air dried at 333 K.

Activation of crystals post air-drying was carried out by degassing in vacuum at 453 K for 24 hours.

5.2.3 Characterization

Activated ZIF samples were characterized using powder X-ray diffraction (PXRD), nitrogen physisorption (NP) at 77 K, *in-situ* and *ex-situ* Fourier transform infrared spectroscopy (FTIR) and scanning electron microscopy (SEM). An X'Pert Pro PANalytical X-ray Diffractometer operating with a Cu anode at 45 kV and 40 mA was used for collecting PXRD patterns with a scan time of 10 s/step and a step size of 0.02 degrees 2θ over the range of 2.5-50 degrees 2θ. A BET surface area analyzer (Tristar, Micromeritics) was used to measure surface area and pore volume using NP at 77 K using individually determined pressure ranges.[7] SEM measurements were carried out with a LEO 1530 scanning electron microscope (Zeiss Electron Microscopy). Samples were coated with gold by sputtering for 60 seconds under vacuum and a 15 kV accelerating voltage was used for imaging. A Thermo Scientific Nicolet iS50 FT-IR equipped with an iS50 ATR module was used for *ex-situ* FTIR spectra collection. Powder ZIF samples were directly analyzed from 550-4000 cm^{-1} with 32 scans at a 2 cm^{-1} resolution.

5.2.4 In-situ Diffuse Reflectance Infrared Fourier Transform Spectroscopy

The *in-situ* Diffuse Reflectance Infrared Fourier Transform Spectroscopy (DRIFTS) experiments were performed on a FTIR spectrometer (Thermo, Nicolet iS50) equipped with a liquid nitrogen cooled MCT/A detector, a diffuse reflectance accessory (Praying Mantis, Harrick), and a high temperature reaction chamber (HVC, Harrick). The chamber used in NO_2 exposure experiments was coated with SilcoNert. KBr was loaded

into the chamber before each sample and measured as IR background. Pre-activated ZIF samples were loaded into the sample chamber and reactivated *in situ* at 383 K under 20 cc min^{-1} He flow for 3 hours. After cooling to 298 K, the He gas was switched to 20 cc min^{-1} 1000 ppm NO_2 with balance N_2. IR spectra was recorded at pre-programmed intervals with 32 scans and 4 cm^{-1} resolution for the duration of exposure.

5.2.5 Dry NO_2 Exposure

100 mg powder samples were placed in a fritted 6 mm × 4 mm × 4.5 in. (O.D. x I.D. x L) quartz glass thermal desorption tube (Supelco). The packed bed was placed in a custom-made fixed-bed gas exposure setup. To ensure safe hazardous gas testing, the entire fixed-bed system was housed in a well-ventilated chemical hood, with real-time gas sensors for safety. An upstream pressure gauge was utilized to confirm the absence of detectable pressure drop during gas exposure. Additionally, outlet lines were fed to a 1N NaOH solution to scrub eluted acid gas streams. Packed samples were flushed with ultra-high purity nitrogen (Airgas) at 75 cc min^{-1} and activated *in-situ* for 2 hours at 453 K. After cooling to ambient conditions, 1000 ppm NO_2 gas in balance N_2, (Airgas), was passed through the fixed-bed at a flow rate of 75c min^{-1} for about 2 hours and 25 min (100 ppm-days of NO_2 gas exposure). Upon completion of the exposure, the bed was flushed with N_2 for 30min and the sample removed for further characterization.

5.2.6 Humid NO_2 Exposure

Activated samples were exposed to ~20 (ppm) of NO_2 in air at 75% relative humidity (R.H.) for 5 days (~100 ppm-days) at 298 K. The NO_2 gas was generated from a 400 cc aqueous solution of 0.5 mg/mL $NaNO_2$ at a pH of 4.0 at 318 K in accordance with

reported literature.[8] Air at 40 cc min^{-1} was bubbled through the solution and carried humid NO_2 gas stream into the exposure unit (Secador mini-desiccator), where the portable PAC 7000 NO_2 detector (Dräger) measured the NO_2 concentrations at regular intervals. The R.H. was monitored inside the transparent exposure unit using a humidity sensor (Ambient Weather). The $NaNO_2$ solution was refilled every 24 hours and the custom-made unit was placed inside a fume hood for safe operation. Samples following exposure were re-activated at 453 K for 24 hours in vacuum.

5.2.7 Computational Details

The experimentally reported structure of ZIF-8 was optimized with plane-wave density functional theory (DFT).[9-13] Calculations were performed in the Vienna Ab-initio Simulation Package (VASP) with projector-augmented wave (PAW) method pseudopotentials39 and the Perdew-Burke-Ernzerhof (PBE) generalized-gradient approximation (GGA) functional40. Atomic positions were first relaxed using a conjugate gradient algorithm with a cutoff energy of 480 eV until all forces were less than 0.05 eV/Å. Subsequently both atomic positions and lattice constants were optimized with the same cutoffs and tolerances. In all calculations, reciprocal space was sampled only at the Γ-point.

5.3 Results and Discussion

The crystallinity of the three ZIFs before and after exposure to different conditions were characterized using PXRD (**Figure 5.1**)**,** with the patterns normalized with respect to the most intense Bragg peak for each ZIF. PXRD patterns of these three ZIFs exposed to humid air, dry and humid SO_2 are reproduced from my previous work and included in **Figure 5.1**.[2-3] Here and below, exposure to acid gases is denoted in units of ppm-days.

With 100 ppm-days of exposure to dry NO_2, significant changes to the PXRD patterns are observed for ZIF-8 and ZIF-90. The PXRD patterns exhibit a progressive increase in the background signal, indicating structural degradation. The changes in the PXRD pattern of ZIF-71 are slower, but after exposures of 1000 ppm-days, peak intensities decrease considerably (**Figure 5.1** and **Figure C.1**). This behavior is quite different from exposure to dry SO_2, for which all three ZIFs are very stable.[2] Under humid NO_2 exposures at 75% R.H. for 100 ppm-days, the 3 ZIFs exhibit distinctive changes in their PXRD patterns. In ZIF-8, the change in its PXRD pattern is less discernable under humid NO_2 than similar dry NO_2 exposures, indicating slower degradation in the presence of humidity. ZIF-90, however, exhibits increased changes under humid NO_2 exposure. The ZIF-71 PXRD pattern after 100 ppm-days humid NO_2 exposure indicates transformation to a different crystalline phase corresponding to the non-porous lcs topology ZIF-72.[14] Phase transformations like this have been observed for ZIFs exposed to humid SO_2, but ZIF-71 remains stable under humid SO_2.[2-3] These results indicate that the interactions of NO_2 with ZIFs are strikingly different than for SO_2 or CO_2.

Figure C.2 and **Table C.2** show results from nitrogen physisorption (NP) isotherms at 77 K of the exposed materials. Decreasing NP profiles are observed for ZIF-8 and ZIF-90 upon NO_2 exposure, with a greater decrease observed in ZIF-8 on dry exposure than on humid exposure. In contrast, ZIF-90 exhibits a near-complete loss of porosity on humid NO_2 exposure, consistent with the significantly altered PXRD pattern of ZIF-90 (**Figure 5.1**) on humid NO_2 exposure. For ZIF-71, NP profiles exhibit no significant change on 100 ppm-day dry NO_2 exposure but decrease considerably after1000 ppm-day exposure. After humid NO_2 exposure of ZIF-71, no porosity in NP is observed,

in agreement with the transformation to nonporous ZIF-72 seen with PXRD. These PXRD and NP results show that none of three ZIFs are stable to NO_2 exposure under either dry or humid (75% R.H.) conditions. This behavior is in sharp contrast to my previous SO_2 exposure observations (reproduced in **Figure C.2**).

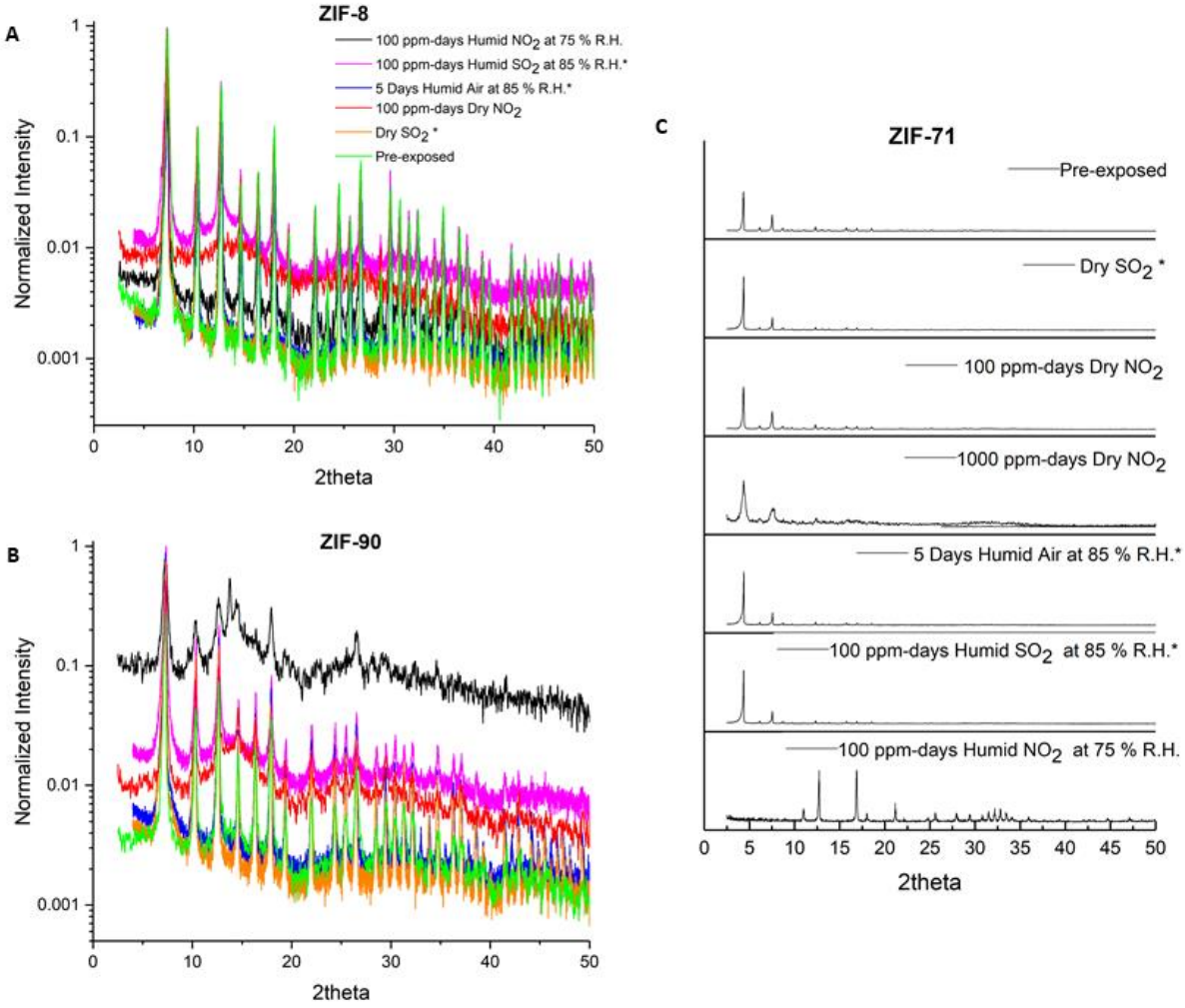

Figure 5.1. Normalized PXRD patterns of A) ZIF-8, B) ZIF-90 and C) ZIF-71 after exposure to dry and humid NO_2 compared to pre-exposed samples. Figure legends in A and B are same. *PXRD patterns of ZIFs on exposure to humid air, dry and humid SO_2 are reproduced for comparison from previous work.[2]

To probe the chemical bonding changes in ZIFs due to NO_2 exposure, *in situ* FTIR spectroscopy was carried out on each ZIF over a 5-hr exposure to 1000 ppm dry NO_2. The temporal evolution of the several new peaks observed upon dry NO_2 exposure are shown in the difference spectra (**Figures 5.2A-5.2F**) obtained by subtracting the spectra at each time from the initial spectrum. Absorbance peaks in the difference spectra (marked in black) signify formation of new chemical species, while negative peaks (marked in red) indicate reduced concentration of pre-existing moieties in the ZIF due to gas exposure. The raw FTIR spectra are available in **Figure C.3**. In ZIF-8, reduced intensities observed at 760 and 1146 cm^{-1} correspond to aromatic C-H bending vibrations while those at 1310, 1430 and 1459 cm^{-1} correspond to the C-H bending of the methyl group.[15] The intensity reduction observed at 990 cm^{-1} can be attributed to imidazole ring twisting while those at 2930 and 3135 cm^{-1} are due to the aliphatic and aromatic C-H stretch respectively.[15-16] ZIF-90 and ZIF-71 also show reduced intensities for aromatic and aliphatic C-H bending and stretching vibrations. In ZIF-90, the reduction observed at 1700 cm^{-1} corresponds to the C=O stretch. In ZIF-71, which has no aliphatic C-H groups, only one major peak reduction is observed at 3130 cm^{-1}, which corresponds to the aromatic C-H stretch. The difference spectra in all three ZIFs point to strong interactions/reactions of NO_2 with the aromatic (and aliphatic) C-H groups in imidazole rings.

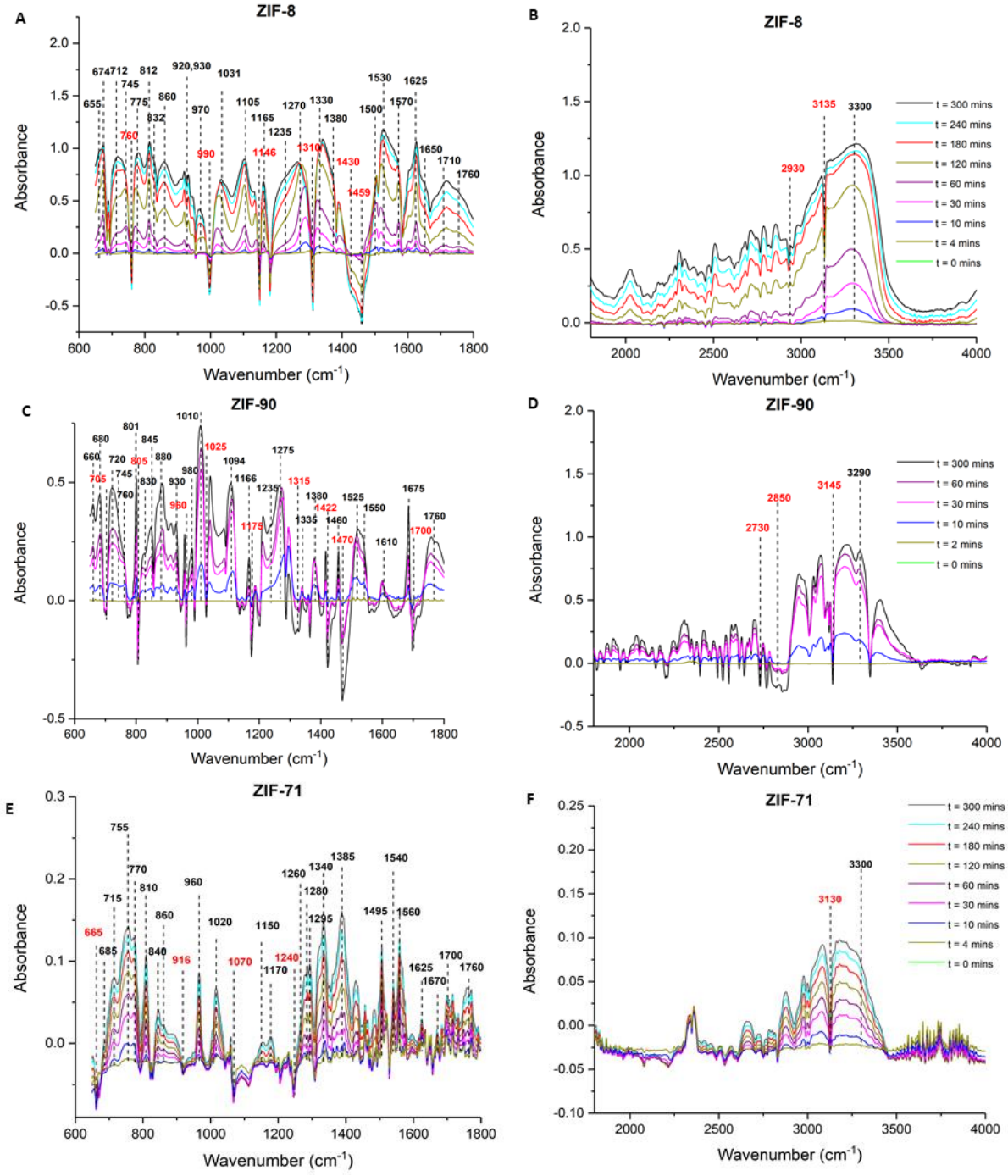

Figure 5.2. *In situ* FTIR difference spectra of ZIFs exposed to 1000 ppm dry NO_2 over 5 hours. Decreasing peaks are marked in red. Time intervals of the FTIR spectra are identical in **A** and **B** (ZIF-8), **C** and **D** (ZIF-90) and **E** and **F** (ZIF-71).

The large number of overlapping new peaks observed on dry NO_2 exposure to the ZIFs makes unique peak attribution to new chemical species a difficult task. Analysis of the FTIR results aided by literature references allows me to make the peak assignments detailed in **Table C.3**, which highlights unambiguously attributable peaks in green. Exposure to dry NO_2 leads to formation of diverse set of new species in the ZIF materials including both organic and inorganic species, strongly suggesting attack of NO_2 on the imidazole linkers as well as the Zn-N coordination bonds. My analysis points to the formation of nitro-, organic nitrite, nitrosamine, nitramine and inorganic nitrate groups upon the dry NO_2 exposure of ZIFs. The data is also consistent with the presence of organic nitrates and inorganic nitrites, although there are not individual peaks that can be unambiguously associated with these groups alone. In addition to the assignments in **Table C.3**, the peak at 1760 cm^{-1} is likely due to adsorbed N_2O_4 species[17] while the peak around 1700 cm^{-1} observed in ZIF-8 and ZIF-71 is likely due to adsorbed nitrous acid.[18-20]

Since the *in situ* DRIFTS cell is not compatible with corrosive humid acid gas mixtures, I used *ex situ* ATR FTIR spectroscopy to investigate changes in ZIFs exposed to humid NO_2 mixtures (**Figure C.4**). To confirm qualitative agreement between these two methods, I also measured the *ex situ* ATR FTIR spectra of dry NO_2 exposed ZIFs (**Figure C.5**) for comparison with **Figure C.3**. The new peaks marked in **Figure C.4** that are observed in *ex situ* FTIR of the un-reactivated ZIFs after dry NO_2 exposure match those observed in the *in situ* DRIFTS experiments. **Figure C.6** shows the *ex situ* FTIR spectra after reactivation of the ZIFs at 180 °C under vacuum for 24 hours. Comparison of the *ex situ* spectra before (**Figure C.5**) and after reactivation leads to the important observation

that reactivation after NO_2 exposure does not lead to complete removal of the new chemical species formed during the exposure. That is, a permanent alteration to the chemical structure resulted even upon dry NO_2 exposure of all three ZIFs. The FTIR spectra of ZIF-8 and ZIF-90 on humid NO_2 exposure at 75% R.H. are in general agreement with those obtained after dry NO_2 exposure. Absorbance changes for these ZIFs upon humid NO_2 exposures are less intense than the equivalent dry exposures. In ZIF-90, on humid NO_2 exposure, I observe a substantial decrease in the bending and stretching vibrations associated with the imidazole ring, compared to equivalent dry exposure. This is best exemplified by the sharp decrease in absorbance around 1590 cm^{-1}, which likely corresponds to the C=N stretch of the imidazole ring in ZIF-90, in analogy with reported studies of ZIF-8.[16] However, the FTIR spectrum of ZIF-71 on humid NO_2 exposure is significantly different from the equivalent dry NO_2 exposure. No significant changes are observed on a 100 ppm-day dry NO_2 exposed ZIF-71 by *ex-situ* FTIR. However, even a 100 ppm-day exposure of ZIF-71 to humid NO_2 at 75% R.H. leads to significant changes. The absorbance intensities associated with the imidazole ring vibrations of the pre-exposed ZIF-71 increase further on humid NO_2 exposure. I have shown from PXRD (**Figure 5.1**) that ZIF-71 undergoes a complete phase change under these exposure conditions. Therefore, the observed increase in absorbance intensities are due to the dense, nonporous ZIF-72 structure having a higher concentration of chemical bonds. Additionally, a peak at 1385 cm^{-1} corresponding to inorganic nitrate formation is also observed on 100 ppm-day humid NO_2 exposure in ZIF-71.

The morphological changes in the ZIF materials on exposure to dry and humid NO_2 were examined by SEM (**Figure C.7**). ZIF-8 shows significant changes upon 400 ppm-

days dry NO_2 exposure with many irregular fragments and a general absence of the crystal facets present in the pre-exposed material. Even though ZIF-71 loses around half of its BET surface area upon 1000 ppm-days dry NO_2 exposure, no significant morphological changes are observed. In contrast, after a 100 ppm-days humid NO_2 exposure, the ZIF-71 crystals are strongly etched and cavities are visible within the crystals. The color of each exposed ZIF powder sample also changes on these NO_2 exposures and are depicted in **Figure C.8**.

Humid NO_2 exposure therefore has remarkably different effects on the three ZIFs I investigated. In hydrophobic ZIF-8, the presence of humidity tempers the deleterious effect observed with dry NO_2 and slows the degradation process. This is similar to earlier reports for UiO-66, another hydrophobic material.[21] In hydrophilic ZIF-90, humidity accelerates the framework degradation by NO_2. Finally, in the hydrophobic ZIF-71, the synergy of humidity and NO_2 drives a phase change towards the nonporous ZIF-72 framework, an outcome that is different from the degradation route observed under prolonged dry NO_2 exposures in the same material.

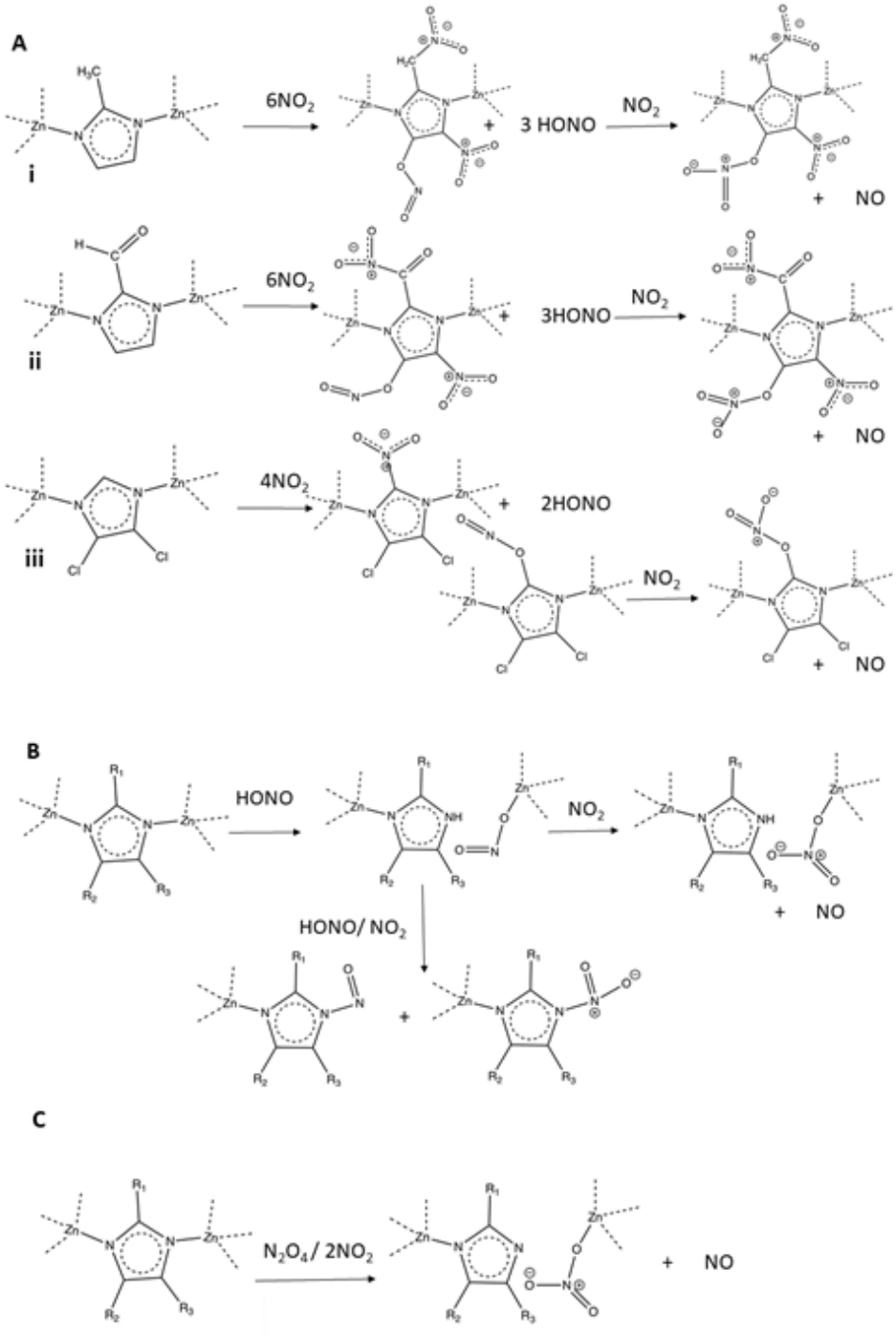

Figure 5.3. Schematic of reactants and product species generated during degradation of ZIFs under dry NO_2 exposure. Stoichiometrically balanced reactions of ZIF-8 (**i**), ZIF-90 (**ii**) and ZIF-71 (**iii**) are individually shown in **5.3A**, while **5.3B** and **5.3C** are valid for any of the 3 ZIFs (designated by general functional groups R_1, R_2 and R_3).

Based upon consideration of all the foregoing results as well as literature information on reactivity of NO_2, I propose the mechanisms depicted in **Figure 5.3** for degradation of ZIFs by *dry* NO_2. The FTIR investigation has revealed several reactions such as NO_2 addition to unsaturated bonds, hydrogen abstraction, and radical dimerization in addition to its strong oxidizing action.[22-24] NO_2 has been observed to react with unsaturated organics in the gas phase at ambient temperature forming nitrates or nitrites by free radical hydrogen abstraction and addition reactions, with the hydrogen abstraction route preferred at lower concentrations (~1000 ppm).[25-26] Nitrous acid (HONO), which forms as the result of hydrogen abstraction by NO_2, has been observed to be produced with a near 100% yield on reactions of NO_2 with dry soot at ambient conditions.[27] Formation of nitrites, nitrates, nitro- and nitramine groups have been reported on gas-phase reactive adsorption of NO_2 on aromatics, polymers, hydrocarbon soots and other carbonaceous materials at ambient temperature.[22, 28-34] The presence of aromatic imidazole groups in ZIFs create the strong possibility of similar mechanisms of NO_2 interaction with these materials at ambient conditions. The FTIR analysis shows a strong decrease in aromatic and aliphatic C-H stretching and bending vibrations in all three ZIFs on dry NO_2 exposure. Additionally, the FTIR spectra has evidence of adsorbed HONO (1700 cm^{-1} stretch), consistent with the free radical H-abstraction mechanism.[18-20] While the addition reaction of NO_2 directly to the aromatic ring is possible, the low NO_2 concentrations, the reduction in C-H bond stretches in the FTIR, as well as HONO formation point towards the H-abstraction mechanism dominating under the conditions in this work. Such a mechanism (**Figure 5.3A**) proceeds with NO_2 abstracting H from the organic linker of a ZIF to form HONO, allowing additional NO_2 free radicals to react with the imidazole radical that was created,

forming nitro, organic nitrite or nitrate species.[22, 25] The HONO formed can dissociate to create NO and a reactive hydroxyl radical[27, 35], which can initiate a chain reaction with other free radicals such as NO_2 or carry out H-abstraction reactions itself forming water.

The decreased crystallinity of the ZIFs after exposure to dry NO_2 exposure (**Figure 5.1**), as well as the presence of inorganic nitrites and nitrates, are consistent with cleavage of Zn-N bonds. HONO produced in the H-abstraction mechanism can attack the Zn-N bonds (**Figure 5.3B**) protonating the imidazole N and forming an inorganic nitrite, which can then be oxidized by NO_2 to form an inorganic nitrate.[36] NO_2 or HONO can then react with the protonated N of the imidazole forming nitramines and nitrosamines.[37-40] Thus, the free radical H-abstraction mechanism satisfactorily explains the formation of organic N-containing groups observed in the FTIR spectra leading to the creation of functionalized imidazole species, whereas formation of the observed inorganic nitrates, nitrosamines, nitramines and inorganic nitrites can result from secondary reactions with HONO produced by the above mechanism.

In addition to the two mechanisms already discussed, NO_2 is also a strong oxidizing agent that has been observed to oxidize ionic salts such as iodides, chlorides and bromides in the dark at ppm concentrations forming inorganic nitrites, which can be further oxidized by NO_2 to nitrates with the evolution of NO.[36, 41-42] Reactive adsorption of NO_2 on metals (including Zn) and metal oxides has been observed to proceed at ambient temperature *via* disproportionation of two NO_2 molecules or the N_2O_4 dimer on the active site to form a surface nitrate and evolve NO.[43-48] Thus, the metal centers in ZIFs are a third route for NO_2 interactions, leading to Zn-N bond cleavage (**Figure 5.3C**).

ZIF-71 is the most stable of the three ZIFs under dry NO_2 exposure. This observation provides indirect evidence regarding which of the mechanisms listed above is dominant. ZIF-71 has only one aromatic C-H group per linker, unlike ZIF-8 or ZIF-90 linkers which have multiple aromatic (two each) and aliphatic (three and one, respectively) C-H bonds. I therefore think the dominant mechanism for ZIF degradation in this work is likely H-abstraction from the organic imidazole group by NO_2 augmented by Zn-N bond cleavage of the ZIF by the resulting acidic species. While direct attack by reactive NO_2 adsorption on Zn sites cannot be ruled out, the lack of similar reactivity and speciation of the three ZIFs make this mechanism a minor contributor to the overall degradation at best.

Additional insights into NO_2 induced degradation can be obtained through periodic DFT calculations to compute defect formation energies. Defect formation energies for specific reactions of ZIF-8 in dry and humid NO_2 environments were computed by subtracting the total energy of the products from the reactants and are tabulated in Appendix C (**Table C.4)**.[49-50] Negative values of the defect formation energy imply a thermodynamically favorable degradation reaction. The predictions of the reaction mechanism of ZIF-8 from the defect formation energies are in agreement with my proposed reaction mechanism based on experimental observations. The H-abstraction reactions by NO_2 in ZIF-8 forming nitro or nitrite groups along with HONO are all thermodynamically favorable (**Reactions 1-3, Table C.4**). Attack on the ZIF-8 structure by HONO or HNO_3 forming inorganic nitrites or nitrates are also favorable (**Reactions 4-5, Table C.4**). Interestingly, the direct oxidation of Zn by the reactive adsorption of NO_2 on the metal

[#]The computational work reported in this subsection was performed by Rebecca Han

center in ZIF-8is not favored according to the simulation results (**Reaction 6, Table C.4**). Computational investigations of defect formation energies for ZIF-90 is expected to yield similar information and was not carried out. Unfortunately, the high computational costs associated with large unit cells of the RHO topology of ZIF-71 render calculations for this material infeasible.

All of the mechanistic discussion above focused on exposure to dry NO_2. Under *humid* conditions, the mechanism of ZIF degradation by NO_2 has an additional contribution. The reaction of NO_2 and water vapor in dark atmospheric smog chambers has been reported to be a heterogeneous surface reaction with the reactor walls leading to formation of gaseous nitrous acid and adsorbed nitric acid in the absence or presence of O_2.[51-55] This surface-catalyzed nitric acid formation proceeds under humid conditions with any reactor surface (pyrex glass, quartz, teflon)[51-52] and was also demonstrated to form on hydrated silica surfaces, activated carbon, alumina and glass beads.[56-57] A detailed mechanism for this reaction was proposed, in which NO_2 was adsorbed into the aqueous surface film in the form of N_2O_4, with the HONO product either desorbing into the gas phase or reacting further to form NO.[55, 58] Nitric acid remains adsorbed on the surface.

My FTIR investigation indicates that the presence of humidity can impede the reaction of NO_2 with hydrophobic ZIFs (**Figure 5.3**) such as ZIF-8 *via* competitive adsorption of NO_2 and water. This is also seen in previous reports on UiO-66 and Cu-BTC that were degraded significantly more under dry NO_2 exposures.[21, 59] However in hydrophilic ZIF-90, dissolution of NO_2 in the water-filled pores under humid exposure conditions leads to nitric acid formation (**Eqn 1**) and aids in faster degradation of the ZIF-90 structure, as evidenced by an enhanced reduction of the stretches associated with the

imidazole ring (**Figure C.4**). Reductions in intensity of the new peaks formed around 1290 cm^{-1} on humid NO_2 exposure of ZIF-90 compared to its dry exposures suggest that the sites of interaction of nitric acid with the ZIF-90 structure differ from those of dry NO_2 whose action is impeded by water. The hydrophobic ZIF-71 undergoes a phase transformation to nonporous ZIF-72 upon humid NO_2 exposure, which is not observed under dry exposure conditions. This phase transformation is also observed in ZIF-71 on prolonged exposure to liquid water but not under humid air exposure.[2] The surprising phase transformation in ZIF-71 under humid NO_2 points to bond cleavages induced by small amounts of adsorbed nitric acid formed under humid NO_2 exposure, and is supported by the presence of inorganic nitrates in its FTIR spectra and the absence of nitro-, nitramine, organic nitrites and nitrate groups (**Figure C.4**). Similar actions of adsorbed nitric acid are also expected in hydrophobic ZIF-8, but unlike ZIF-71 it does not undergo a phase transformation and instead degrades slowly.

5.4 Conclusions

I have conducted the first systematic investigation of the effects of dry and humid NO_2 gas on three representative ZIFs, chosen carefully based upon my previous work. All the ZIFs investigated are shown to be unstable under prolonged dry or humid NO_2 exposures. The hydrophobic ZIF-8 degrades faster under dry NO_2 exposure than the hydrophilic ZIF-90, but inversely degrades more slowly than ZIF-90 under humid NO_2 exposure. Hydrophobic ZIF-71 shows the slowest degradation under dry NO_2 exposure but undergoes a structural transformation to the nonporous but chemically identical ZIF-72 on prolonged humid NO_2 exposure. These unexpected findings are entirely in contrast with the interactions of dry or humid SO_2 with ZIFs. The presence of various nitro-, organic and

inorganic nitrites and nitrates, nitrosamines and nitramines were confirmed by FTIR measurements, which revealed the mechanisms of ZIF degradation by dry and humid NO_2. DFT simulations on defect energy formation were carried out which supported experimental observations. The formation of nitrous acid in dry NO_2 exposures points to the free radical H-abstraction mechanism of NO_2 as the major interaction route under both dry and humid conditions, with possible minor contributions from NO_2 disproportionation on the Zn metal center. In comparison to dry or humid SO_2, the free radical NO_2 is a much more aggressive acid gas whose presence would require new approaches to stabilize ZIF/MOF materials.

This Chapter highlights striking differences in the reactivity of NO_2 towards ZIFs compared to another common pollutant and acid gas, SO_2. My previous studies on ZIF-SO_2 interactions also show that dry SO_2 gas at ambient temperature does not degrade ZIFs, with degradation only observed under humid conditions.[3] The much higher reactivity of dry NO_2 compared to dry SO_2 can be attributed to its free radical nature, and I can envision similar mechanisms of NO_2 attack on other ZIFs and MOFs which make NO_2 a much more potent hindrance to widespread use of MOFs in acid gas-related applications. Previous Chapters in this thesis report SO_2 interactions with ZIFs under dry conditions or at high humidity (85% R.H.). The stability of ZIFs observed under dry SO_2 exposure indicate that water removal from the incoming process stream could impart stability to these materials. In the next Chapter of my thesis, I investigate the effect of humidity on the humid SO_2 induced degradation of ZIF-8 by conducting equivalent SO_2 exposures at 25%, 50%, 75% and 95% R.H. and develop a predictive model of ZIF-8 stability under SO_2 exposure across a range of R.H. conditions.

REFERENCES

1. Burtch, N. C.; Jasuja, H.; Walton, K. S., Water Stability and Adsorption in Metal-Organic Frameworks. *Chem. Rev.* **2014,** *114* (20), 10575-10612.

2. Bhattacharyya, S.; Han, R.; Kim, W.-G.; Chiang, Y.; Jayachandrababu, K. C.; Hungerford, J. T.; Dutzer, M. R.; Ma, C.; Walton, K. S.; Sholl, D. S.; Nair, S., Acid Gas Stability of Zeolitic Imidazolate Frameworks: Generalized Kinetic and Thermodynamic Characteristics. *Chem. Mater.* **2018,** *30* (12), 4089-4101.

3. Bhattacharyya, S.; Pang, S. H.; Dutzer, M. R.; Lively, R. P.; Walton, K. S.; Sholl, D. S.; Nair, S., Interactions of SO_2-Containing Acid Gases with ZIF-8: Structural Changes and Mechanistic Investigations. *J. Phys. Chem. C* **2016,** *120* (48), 27221-27229.

4. Bhattacharyya, S.; Jayachandrababu, K. C.; Chiang, Y.; Sholl, D. S.; Nair, S., Butanol Separation from Humid CO_2-Containing Multicomponent Vapor Mixtures by Zeolitic Imidazolate Frameworks. *ACS Sustainable Chem. Eng.* **2017,** *5* (10), 9467-9476.

5. Gee, J. A.; Chung, J.; Nair, S.; Sholl, D. S., Adsorption and Diffusion of Small Alcohols in Zeolitic Imidazolate Frameworks ZIF-8 and ZIF-90. *J. Phys. Chem. C* **2013,** *117* (6), 3169-3176.

6. Zhang, K.; Lively, R. P.; Dose, M. E.; Brown, A. J.; Zhang, C.; Chung, J.; Nair, S.; Koros, W. J.; Chance, R. R., Alcohol and water adsorption in zeolitic imidazolate frameworks. *Chem. Commun.* **2013,** *49* (31), 3245-3247.

7. Walton, K. S.; Snurr, R. Q., Applicability of the BET method for determining surface areas of microporous metal-organic frameworks. *J.Am.Chem.Soc.* **2007,** *129* (27), 8552-8556.

8. Hashimoto, Y.; Tanaka, S., A new method of generation of gases at parts per million levels for preparation of standard gases. *Environ. Sci. Technol.* **1980,** *14* (4), 413-416.

9. Park, K. S.; Ni, Z.; Cote, A. P.; Choi, J. Y.; Huang, R. D.; Uribe-Romo, F. J.; Chae, H. K.; O'Keeffe, M.; Yaghi, O. M., Exceptional chemical and thermal stability of zeolitic imidazolate frameworks. *Proc. Natl. Acad. Sci. U. S. A.* **2006,** *103* (27), 10186-10191.

10. Banerjee, R.; Phan, A.; Wang, B.; Knobler, C.; Furukawa, H.; O'Keeffe, M.; Yaghi, O. M., High-throughput synthesis of zeolitic imidazolate frameworks and application to CO_2 capture. *Science* **2008,** *319* (5865), 939-943.

11. Morris, W.; Doonan, C. J.; Furukawa, H.; Banerjee, R.; Yaghi, O. M., Crystals as molecules: Postsynthesis covalent functionalization of zeolitic imidazolate frameworks. *J.Am.Chem.Soc.* **2008,** *130* (38), 12626-12627.

12. First, E. L.; Floudas, C. A., MOFomics: Computational pore characterization of metal–organic frameworks. *Microporous Mesoporous Mater.* **2013,** *165*, 32-39.

13. https://github.com/numat/RASPA2/tree/master/structures/mofs/cif.

14. Schweinefuss, M. E.; Springer, S.; Baburin, I. A.; Hikov, T.; Huber, K.; Leoni, S.; Wiebcke, M., Zeolitic imidazolate framework-71 nanocrystals and a novel SOD-type polymorph: solution mediated phase transformations, phase selection via coordination modulation and a density functional theory derived energy landscape. *Dalton Trans.* **2014,** *43* (9), 3528-3536.

15. Cheng, P.; Hu, Y. H., H_2O-Functionalized Zeolitic Zn(2-methylimidazole)2 Framework (ZIF-8) for H_2 Storage. *J. Phys. Chem. C* **2014,** *118* (38), 21866-21872.

16. Hu, Y.; Kazemian, H.; Rohani, S.; Huang, Y.; Song, Y., In situ high pressure study of ZIF-8 by FTIR spectroscopy. *Chem. Commun.* **2011,** *47* (47), 12694-12696.

17. Bibart, C. H.; Ewing, G. E., Vibrational-spectrum, torsional potential, and binding of gaseous N_2O_4. *J.Chem.Phys.* **1974,** *61* (4), 1284-1292.

18. Al-Abadleh, H. A.; Grassian, V. H., Heterogeneous reaction of NO_2 on hexane soot: A Knudsen cell and FT-IR study. *J. Phys. Chem. A* **2000,** *104* (51), 11926-11933.

19. Zawadzki, J.; Wisniewski, M.; Skowronska, K., Heterogeneous reactions of NO_2 and NO-O_2 on the surface of carbons. *Carbon* **2003,** *41* (2), 235-246.

20. Kagann, R. H.; Maki, A. G., Infrared absorption intensities of nitrous acid (HONO) fundamental bands. *J. Quant. Spectrosc. Radiat. Transfer* **1983,** *30* (1), 37-44.

21. Ebrahim, A. M.; Levasseur, B.; Bandosz, T. J., Interactions of NO_2 with Zr-Based MOF: Effects of the Size of Organic Linkers on NO_2 Adsorption at Ambient Conditions. *Langmuir* **2013,** *29* (1), 168-174.

22. Gray, P.; Yoffe, A. D., The Reactivity And Structure Of Nitrogen Dioxide. *Chem. Rev.* **1955,** *55* (6), 1069-1154.

23. Bernard, F.; Cazaunau, M.; Mu, Y.; Wang, X.; Daële, V.; Chen, J.; Mellouki, A., Reaction of NO_2 with Selected Conjugated Alkenes. *J. Phys. Chem. A* **2013,** *117* (51), 14132-14140.

24. Kaupp, G.; Schmeyers, J., Gas/Solid Reactions with Nitrogen Dioxide. *J. Org. Chem* **1995,** *60* (17), 5494-5503.

25. Pryor, W. A.; Lightsey, J. W.; Church, D. F., Reaction of Nitrogen-Dioxide with alkenes and poly-unsaturated fatty acids - addition and hydrogen abstraction mechanisms. *J.Am.Chem.Soc.* **1982,** *104* (24), 6685-6692.

26. Giamalva, D. H.; Kenion, G. B.; Church, D. F.; Pryor, W. A., Rates and mechanisms of reactions of nitrogen dioxide with alkenes in solution. *J.Am.Chem.Soc.* **1987,** *109* (23), 7059-7063.

27. Aubin, D. G.; Abbatt, J. P. D., Interaction of NO_2 with Hydrocarbon Soot: Focus on HONO Yield, Surface Modification, and Mechanism. *J. Phys. Chem. A* **2007,** *111* (28), 6263-6273.

28. Akhter, M. S.; Chughtai, A. R.; Smith, D. M., Reaction of hexane soot with nitrogen dioxide/nitrogen oxide (N_2O_4). *J. Phys. Chem.* **1984,** *88* (22), 5334-5342.

29. Azambre, B.; Collura, S.; Trichard, J. M.; Weber, J. V., Nature and thermal stability of adsorbed intermediates formed during the reaction of diesel soot with nitrogen dioxide. *Appl. Surf. Sci.* **2006,** *253* (4), 2296-2303.

30. Kirchner, U.; Scheer, V.; Vogt, R., FTIR spectroscopic investigation of the mechanism and kinetics of the heterogeneous reactions of NO_2 and HNO_3 with soot. *J. Phys. Chem. A* **2000,** *104* (39), 8908-8915.

31. Davydov, E. Y.; Gaponova, I. S.; Pokholok, T. V.; Vorotnikov, A. P.; Pariiskii, G. B.; Zaikov, G. E., Features of mechanism of free radical initiation in polymers under exposure to nitrogen oxides. *Polym. Adv. Technol.* **2008,** *19* (6), 475-484.

32. Gao, X.; Liu, S.; Zhang, Y.; Luo, Z.; Ni, M.; Cen, K., Adsorption and reduction of NO_2 over activated carbon at low temperature. *Fuel Process. Technol.* **2011,** *92* (1), 139-146.

33. Jeguirim, M.; Tschamber, V.; Brilhac, J. F.; Ehrburger, P., Interaction mechanism of NO_2 with carbon black: effect of surface oxygen complexes. *J. Anal. Appl. Pyrolysis* **2004,** *72* (1), 171-181.

34. Zhang, W.-J.; Bagreev, A.; Rasouli, F., Reaction of NO_2 with Activated Carbon at Ambient Temperature. *Ind. Eng. Chem. Res.* **2008,** *47* (13), 4358-4362.

35. Akhter, M. S.; Chughtai, A. R.; Smith, D. M., The Structure of Hexane Soot II: Extraction Studies. *Appl. Spectrosc.* **1985,** *39* (1), 154-167.

36. Erinn, O. N.; Z., H. R., Production of molecular iodine from the heterogeneous reaction of nitrogen dioxide with solid potassium iodide. *J. Geophys. Res.: Atmos.* **2011,** *116* (D1).

37. Challis, B. C.; Kyrtopoulos, S. A., The chemistry of nitroso-compounds. Part 11. Nitrosation of amines by the two-phase interaction of amines in solution with gaseous oxides of nitrogen. *J. Chem. Soc., Perkin Trans. 1* **1979,** (0), 299-304.

38. Turney, T. A.; Wright, G. A., Nitrous Acid And Nitrosation. *Chem. Rev.* **1959,** *59* (3), 497-513.

39. Zhao, Y.-L.; Garrison, S. L.; Gonzalez, C.; Thweatt, W. D.; Marquez, M., N-Nitrosation of Amines by NO_2 and NO: A Theoretical Study. *J. Phys. Chem. A* **2007,** *111* (11), 2200-2205.

40. Grosjean, D., Atmospheric Chemistry of Toxic Contaminants. 6. Nitrosamines: Dialkyl Nitrosamines and Nitrosomorpholine. *J. Air Waste Manage. Assoc.* **1991,** *41* (3), 306-311.

41. Li, H.; Zhu, T.; Ding, J.; Chen, Q.; Xu, B., Heterogeneous reaction of NO_2 on the surface of NaCl particles. *Sci. China, Ser. B: Chem.* **2006,** *49* (4), 371-378.

42. Vogt, R.; Finlayson-Pitts, B. J., A Diffuse Reflectance Infrared Fourier Transform Spectroscopic Study of the Surface Reaction of NaCl with Gaseous NO_2 and HNO_3. *J. Phys. Chem.* **1994,** *98* (14), 3747-3755.

43. Forzatti, P.; Castoldi, L.; Nova, I.; Lietti, L.; Tronconi, E., NO_x removal catalysis under lean conditions. *Catal. Today* **2006,** *117* (1), 316-320.

44. Despres, J.; Koebel, M.; Krocher, O.; Elsener, M.; Wokaun, A., Storage of NO_2 on BaO/TiO_2 and the influence of NO. *Appl. Catal. B-Environ.* **2003,** *43* (4), 389-395.

45. Grossale, A.; Nova, I.; Tronconi, E., Role of Nitrate Species in the "NO_2-SCR" Mechanism over a Commercial Fe-zeolite Catalyst for SCR Mobile Applications. *Catal. Lett.* **2009,** *130* (3-4), 525-531.

46. Rodriguez, J. A.; Jirsak, T.; Dvorak, J.; Sambasivan, S.; Fischer, D., Reaction of NO_2 with Zn and ZnO: Photoemission, XANES, and Density Functional Studies on the Formation of NO_3. *J. Phys. Chem. B* **2000,** *104* (2), 319-328.

47. Tournas, A. D.; Potts, A. W., Surface reactions of NO_2 with machined Zn, Cd, Cu and Ag surfaces studied by He I/II photoelectron spectroscopy. *J. Electron Spectrosc. Relat. Phenom.* **1993,** *66* (1), 167-174.

48. Apostolescu, N.; Schröder, T.; Kureti, S., Study on the mechanism of the reaction of NO_2 with aluminium oxide. *Appl. Catal. B-Environ.* **2004,** *51* (1), 43-50.

49. Han, C.; Zhang, C.; Tyminska, N.; Schmidt, J. R.; Sholl, D. S., Insights into the Stability of Zeolitic Imidazolate Frameworks in Humid Acidic Environments from First Principles Calculations. *J. Phys. Chem. C* **2018**.

50. Zhang, C.; Han, C.; Sholl, D. S.; Schmidt, J. R., Computational Characterization of Defects in Metal-Organic Frameworks: Spontaneous and Water-Induced Point Defects in ZIF-8. *J.Phys.Chem.Lett.* **2016,** *7* (3), 459-464.

51. Febo, A.; Perrino, C., Prediction and experimental evidence for high air concentration of nitrous acid in indoor environments. *Atmos. Environ. Part A* **1991,** *25* (5), 1055-1061.

52. Kleffmann, J.; Becker, K. H.; Wiesen, P., Heterogeneous NO_2 conversion processes on acid surfaces: possible atmospheric implications. *Atmos. Environ.* **1998,** *32* (16), 2721-2729.

53. Sakamaki, F.; Hatakeyama, S.; Akimoto, H., Formation of nitrous acid and nitric oxide in the heterogeneous dark reaction of nitrogen dioxide and water vapor in a smog chamber. *Int. J. Chem. Kinet.* **1983,** *15* (10), 1013-1029.

54. Svensson, R.; Ljungström, E.; Lindqvist, O., Kinetics of the reaction between nitrogen dioxide and water vapour. *Atmos. Environ.* **1987,** *21* (7), 1529-1539.

55. Finlayson-Pitts, B. J.; Wingen, L. M.; Sumner, A. L.; Syomin, D.; Ramazan, K. A., The heterogeneous hydrolysis of NO_2 in laboratory systems and in outdoor and indoor atmospheres: An integrated mechanism. *Phys. Chem. Chem. Phys.* **2003,** *5* (2), 223-242.

56. Goodman, A. L.; Underwood, G. M.; Grassian, V. H., Heterogeneous Reaction of NO_2: Characterization of Gas-Phase and Adsorbed Products from the Reaction, $2NO_2(g) + H_2O(a) \rightarrow HONO(g) + HNO_3(a)$ on Hydrated Silica Particles. *J. Phys. Chem. A* **1999,** *103* (36), 7217-7223.

57. Gundel, L. A.; Guyot-Sionnest, N. S.; Novakov, T., A Study of the Interaction of NO_2 with Carbon Particles. *Aerosol Sci. Technol.* **1989,** *10* (2), 343-351.

58. Ramazan, K. A.; Syomin, D.; Finlayson-Pitts, B. J., The photochemical production of HONO during the heterogeneous hydrolysis of NO_2. *Phys. Chem. Chem. Phys.* **2004,** *6* (14), 3836-3843.

59. Levasseur, B.; Petit, C.; Bandosz, T. J., Reactive Adsorption of NO_2 on Copper-Based Metal-Organic Framework and Graphite Oxide/Metal-Organic Framework Composites. *ACS Appl. Mater. Interfaces* **2010,** *2* (12), 3606-3613.

CHAPTER 6. THE EFFECT OF RELATIVE HUMIDITY ON ACID GAS STABILITY OF ZIF-8

6.1 Introduction

In the previous literature studies of MOF stability to SO_2 or NO_2 summarized in Chapter 1, as well as in Chapters 2-5 of this thesis, experimental data is reported either for dry acid gases or at a fixed high value of relative humidity (R.H.) (~ 70-85%). This does not allow any insight on the important effects of R.H. on the acid gas stability of MOFs. In previous Chapters of this thesis, I have established that SO_2 or CO_2 (but not NO_2) does not affect ZIF stability even at high concentrations under dry conditions but considerable degradation is observed on long term exposure (~5 days) of ZIFs in the presence of high humidity (~85 % R.H.) with even trace amounts (~20 ppm) of SO_2 present. It may therefore be hypothesized that removing the moisture from process gas streams could impart stability to ZIFs towards acid gases such as SO_2 or CO_2. Removal of moisture from an incoming process stream will add a parasitic cost to the overall plant economics and therefore it is important to evaluate the minimum water removal necessary, or the maximum operable R.H. level at which the adsorbent can exhibit long term stability towards the acid gas.

In this Chapter, I have investigated the effect of humid SO_2 gas on the bulk stability of ZIF-8 at R.H. levels of 25%, 50%, 75% and 95%. Bulk stability has been defined similar to the previous Chapters, namely retention of crystal structure and porosity of the porous ZIF.[1-3] After a systematic investigation of the bulk stability, mechanistic aspects of the degradation process are investigated *via* FTIR. Kinetics of the humid SO_2 induced degradation process at different R.H.s are then ascertained through EDX investigations of

S incorporation in the ZIF structure.[2] Finally, I carry out a statistical analysis on the dependence of the degradation rate on various variables, allowing a prediction of ZIF stability across a range of R.H. conditions. To my knowledge, this is the first experimental study of the stability of any MOF across different R.H. conditions on SO_2 exposure and this approach can be generalized for other MOFs/ZIFs to predict their stability to acid gases across a wide range of R.H.

6.2 Experimental Methods

6.2.1 Materials

Zinc(II) nitrate hexahydrate (99%), 2-methylimidazole (99%) and methanol (99.8%) were purchased from Alfa Aesar, Sigma-Aldrich and BDH respectively and used as received. Ultra-high-purity air was purchased from Airgas. Deionized (DI) water from an EMD Millipore water purification system was used in all experiments.

6.2.2 ZIF-8 synthesis

The reported synthesis procedure of Gee *et al*. was modified to synthesize ZIF-8.[4] Briefly, 0.972 g 2-methylimidazole and 1.614 g sodium formate were dissolved in 120 cc methanol. 1.764 g zinc (II) nitrate dissolved in 120 cc methanol was then added to the first solution followed by heating at 363 K for 24 hours. The collected crystals were washed three times with methanol and then air dried at 333 K.

6.2.3 Characterization

Activated ZIF-8 samples before and after exposure to acid gases were characterized with powder X-ray diffraction (PXRD), nitrogen physisorption (NP) at 77 K, fourier transform infrared spectroscopy (FTIR), and energy dispersive X-ray spectroscopy (EDX). PXRD measurements were conducted on an X'Pert Pro PANalytical x-ray diffractometer (Cu Kα anode at 45 kV and 40 mA, X'celerator detector) with a step size of 0.02° 2θ and scan time of 10 s/step from 2.5-50° 2θ. Pore volume was analyzed by NP at 77 K (Tristar, Micromeritics). FTIR spectroscopy was carried out using a Thermo Scientific Nicolet iS50 FT-IR with an iS50 ATR module. Powder samples were analyzed from 550-4000 cm^{-1} with 32 scans with a resolution of 2 cm^{-1}. EDX measurements were carried out with the LEO 1550 scanning electron microscope (Zeiss Electron Microscopy) at 15 kV. A Si wafer standard was used to optimize the spectrometer gain before sample measurements and elemental quantities were calculated with the help of library calibration files of the Inca software (Oxford Instruments).

6.2.4 SO_2 Exposure with Varying Humidity

Activated samples were exposed to ~100 ppm-days of SO_2 (~20 ppm for 5 days) in air at 298 K at different relative humidities (R.H.). The SO_2 gas was generated from a 400 cc dilute $NaHSO_3$ solution (~ 0.5 mg/cc) at a pH of 3.7 at 318 K.[5] Air was bubbled through the solution and carried humid SO_2 gas into the exposure unit (Secador mini-desiccator), where SO_2 concentrations were measured at regular intervals by the portable PAC 7000 SO_2 detector (Dräger). A second dry air line was mixed with the incoming humid SO_2 gas line and their flowrates adjusted individually to generate different levels of R.H within the

transparent exposure unit. The R.H. was monitored using a humidity sensor (Ambient Weather). The solution was refilled after regular intervals and the unit was placed inside a fume hood for operational safety. Around 150-200 mg ZIF-8 sample was placed in a 250 ml borosilicate glass flask for the exposure inside the unit and was re-activated in vacuum at 453 K after the exposure for one day before characterization.

6.3 Results and Discussion

The crystalline structure of ZIF-8 was investigated using PXRD (**Figure 6.1**) before and after humid SO_2 exposures**,** with patterns normalized with respect to the most intense Bragg peak at 7.33° 2θ corresponding to the (011) plane.[3] The PXRD intensities are represented in the logarithmic scale for ease of visualization of subtle changes during the exposure. The PXRD patterns in **Figure 6.1** clearly indicate that the crystallinity of ZIF-8 progressively decreases with increasing R.H. at a constant SO_2 exposure of 100 ppm-days. Increasing baseline intensities especially around 13° 2θ reflect a growing amorphous character and evidence of a degrading crystal structure with rising R.H.

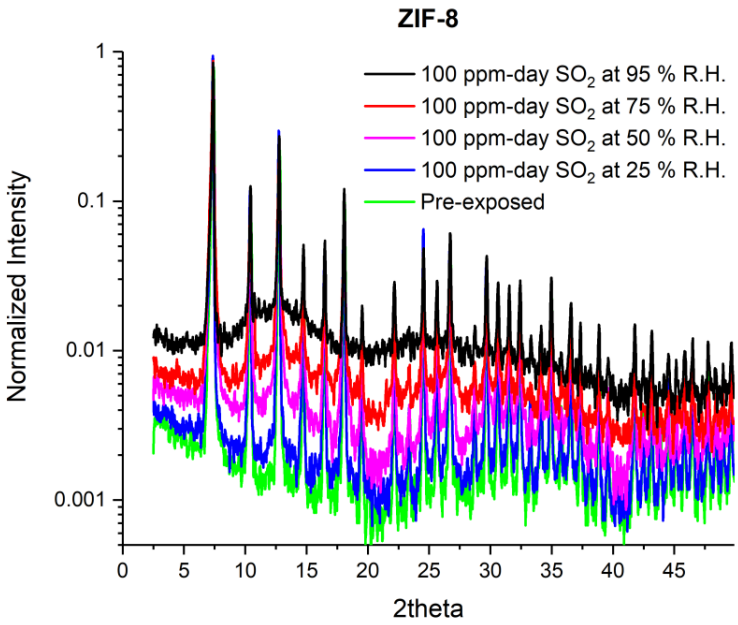

Figure 6.1. Normalized PXRD patterns of ZIF-8 after exposure to 100 ppm-day humid SO_2 at different R.H. levels compared to pre-exposed samples.

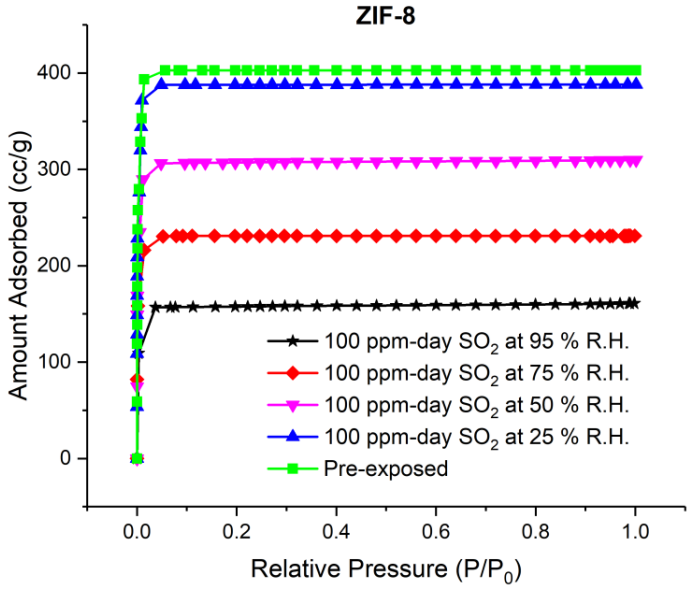

Figure 6.2. N_2 physisorption at 77 K in pre-exposed and reactivated ZIF-8 after different exposure protocols.

To further evaluate the bulk stability of ZIF-8, NP was conducted at 77 K (**Figure 6.2**).[1] The measured BET surface areas and pore volumes from the NP are tabulated in **Table 6.1**. These results clearly show decreasing porosity of the material with a progressive increase in R.H. at a constant SO_2 exposure of 100 ppm-days, in agreement with the changes observed in the PXRD patterns. For a 100 ppm-day SO_2 exposure, ZIF-8 retains almost all of its porosity at 25% R.H., which drops progressively to ~40% at 95% R.H.

Table 6.1. Textural characteristics of ZIF-8 after exposure to 100 ppm SO_2 at varying R.H. BET surface area is reported as a percentage relative to the pre-exposed ZIF-8.

Exposure Condition	R.H. (%)	Relative BET SA	Pore Vol. (cc/g)
Pre-exposed	NA	100	0.62
100 ppm-day SO_2	25	91±8	0.59±0.03
100 ppm-day SO_2	50	67±8	0.44±0.06
100 ppm-day SO_2	75	53±4	0.36±0.04
100 ppm-day SO_2	95	36±5	0.28±0.03

Mechanistic investigations of the humid SO_2 induced degradation process of ZIF-8 with varying R.H. were carried out using FTIR spectroscopy. The results are shown in **Figure 6.3**. The change in the FTIR pattern of ZIF-8 is subtle for SO_2 exposure at 25% R.H. but substantial changes in the pattern are observed at higher humidities. As the R.H. progressively increases, the effect of long term SO_2 exposure on the ZIF-8 structure becomes more marked, in agreement with bulk stability observations from PXRD and NP shown earlier in this Chapter. The changes in **Figure 6.3**, described in detail in Chapter 2

of this thesis, are consistent with an increasing presence of (bi)sulfite and (bi)sulfate groups, along with NH and OH stretches, as the R.H. is increased from 25% to 95% at constant (100 ppm-days) overall SO_2 exposure.[2-3] The significant changes in the FTIR pattern of ZIF-8 after humid SO_2 exposure at different humidities also suggest that S-containing species are not completely removed from the ZIF-8 structure even after reactivation.

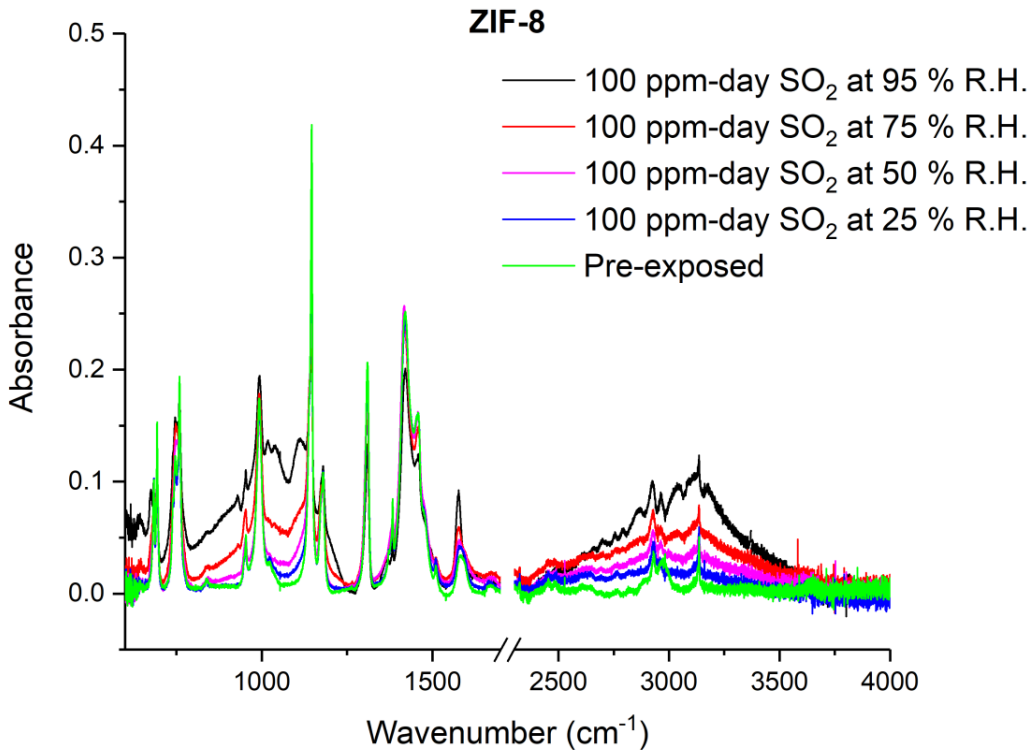

Figure 6.3. FTIR spectra of reactivated ZIF-8 after exposure to 100 ppm SO_2 gas under varying R.H. levels of 25%, 50%, 75%, and 95% compared to pre-exposed ZIF-8.

For a quantitative analysis of the kinetics of humid SO_2 induced ZIF-8 degradation under varying R.H., energy dispersive X-ray (EDX) spectroscopy was used to quantify the

residual S within ZIF-8 after exposure.[2] As pristine ZIF-8 has no S content, any S detected by EDX in a partially degraded ZIF can be directly correlated to defect site creation, and the calculated elemental Zn:S ratio can be used for a quantitative estimation of the defect site density. The percentage of Zn-N bonds that were cleaved was estimated under the assumption that each S atom incorporated within the ZIF-8 structure post reactivation cleaves one Zn-N bond. The degradation kinetics of ZIF-8 depicting the decrease in the macroscopic parameter of pore volume and corresponding increase in the microscopic parameter of cleaved Zn-N bonds is shown in **Figure 6.4.** It is observed that exposure to 100 ppm-days SO_2 with increasing R.H. leads to an increase in the defect site density along with a decrease in pore volumes. Calculations from EDX results show that the number of cleaved Zn-N bonds increase from ~0.6% for SO_2 exposure at 25% R.H. to ~4% for the same exposure at 95% R.H (**Table 6.2**).

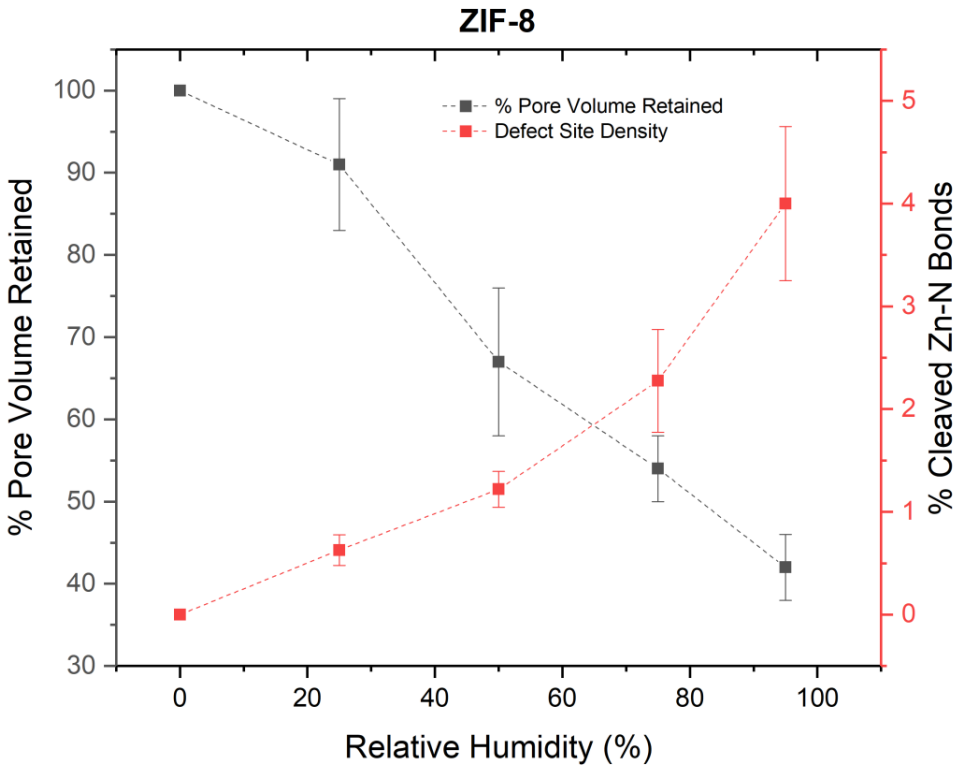

Figure 6.4. Degradation kinetics of ZIF-8 exposed to 100 ppm SO_2 at different R.H. levels showing the decrease in pore volume and the corresponding increase in defect sites (cleaved Zn-N bonds) with increasing R.H. Dotted lines are for visual aid. Cleaved Zn-N bonds were calculated from the experimental Zn:S ratio assuming that one S atom incorporation led to one Zn-N bond cleavage.

The quantitative analysis of the degradation of ZIF-8 to humid SO_2 can be extended to yield kinetic rate constants for the degradation process (**Table 6.2**).[2] At any time, the sum of the defect site concentration (C) and the concentration of the pristine sites left (P) equals the total number of available attack sites per unit volume of ZIF-8 (P_o).

$$P_o = P + C \tag{1}$$

If a first order rate of defect site formation is assumed, the following equations are obtained:

$$\frac{dC}{dt} = -\frac{dP}{dt} = kP \quad (2)$$

$$C = P_o\,(1 - e^{-kt}) \quad (3)$$

Known values of time (t) and the defect site concentration (C/P_o) at that time, as measured by EDX, were substituted in equation (3) to yield a degradation rate constant (k) at different R.H. levels (**Table 6.2**).Not surprisingly, the calculated rate constants for the degradation of ZIF-8 increase with increasing R.H., consistent with the observations from PXRD, NP, FTIR and EDX reported earlier in this Chapter. The calculated degradation rate constant at 95% R.H. is ~6 times higher than that at 25% R.H., clearly establishing the important role of R.H. in the humid SO_2 induced degradation of ZIF-8.

Table 6.2. Degradation rate constants of ZIF-8 calculated using equation (3) after exposure to 100 ppm SO_2 (20 ppm for 5 days) at varying R.H.

Exposure R.H. (%)	**Zn:S Ratio**	**Cleaved Zn-N bonds (%)**	**Rate Constant × 10^{-3}(day^{-1})**
0	∞	0	0
25	39.8±7.7	0.63±0.15	1.26
50	20.5±3.4	1.3±0.175	2.45
75	11.6±3.3	2.275±0.5	4.6
95	6.5±1.4	4±0.75	8.2

The experimental observations in this Chapter clearly illustrate the effect of R.H. in accelerating the degradation of ZIF-8 under SO_2 exposure. At the exposure temperature (298 K), the vapor pressure of water is 23.8 torr,[6] which corresponds to a water content of 3.13% at 100% R.H. assuming an ideal gas mixture. Relative to the 20 ppm of SO_2 inside

the exposure unit, water is in large excess at all the experimental data points, including at the 25% R.H. level. SO_2 would therefore be the limiting reactant of any hypothetical homogeneous gas phase oxidation reaction with water and/or the O_2 in the carrier gas. My experimental evidence in this Chapter of increasing reaction rates with increasing humidity is in contradiction with such a mechanism. Heterogeneous SO_2 oxidation sites may be provided by foreign particles such as activated carbon, metal oxides, or transition metals including Zn, the metal center in ZIF-8.[7-10] Clean polycrystalline Zn can oxidize dry SO_2 gas at ambient temperature to form adsorbed sulfites and sulfates.[9-10] The reaction is proposed to proceed *via* disproportionation of SO_2 on the Zn surface at 300 K forming chemisorbed S and O species, with further interaction of SO_2 and the chemisorbed O leading to formation of adsorbed sulfites and sulfates.[9] However the inertness of ZIFs towards dry SO_2 does not support such a reaction mechanism. The interaction of SO_2 with soot, char and activated carbon has interesting similarities with the observations of my present work.[11-13] Dry SO_2 physisorbs on activated carbon, but increasing humidity results in its reactive adsorption, forming sulfates and sulfuric acid on the carbon surface.[11] Similar reactive adsorption of SO_2 with increasing humidity have also been observed in char and soot.[12-13] Adsorbed water, O_2, and SO_2 on the carbon surface have been proposed to be involved in this heterogeneous conversion to H_2SO_4 across all these carbonaceous materials.[11-13] While the atmospheric conversion of SO_2 to sulfuric acid proceeds photochemically *via* its oxidation by OH radicals,[14-15] experimental evidence has also been reported of SO_2 conversion to sulfuric acid in the dark (no external irradiation) under high R.H. air flow.[7] Clustering of SO_2 with gas phase water molecules (large cluster sizes resulting at higher R.H.) was proposed to facilitate SO_2 oxidation, resulting in H_2SO_4

aerosol droplet formation, whose surface then acts as heterogeneous reaction sites for subsequent SO_2 oxidation.[7, 14, 16] The oxidation of SO_2 to H_2SO_4 in my experiments likely results from one/more of the above heterogeneous reaction pathways. It is therefore likely that the R.H. (a measure of the total water content within the exposure unit) and the resulting adsorbed water within ZIF-8 (ascertainable at the desired R.H. with the aid of an experimentally measured water adsorption isotherm) are important variables affecting the rate of degradation of ZIF-8 on humid SO_2 exposure.

It is useful to explore correlations that can account for my experimental data and to consider the implication of these correlations for other exposure conditions. In this Chapter, I have assumed a simple power law dependence of the form $k = ax^b$ to examine such correlations with R.H. and the adsorbed water. The water adsorption isotherm of ZIF-8, measured up to 90% R.H. due to condensation issues within the measurement chamber, is reproduced from Chapter 3 of this thesis for the analysis (**Figure 6.5**). The adsorbed amount of water is estimated from the isotherm by piece wise linear interpolation using the Matlab Curve Fitting Toolbox. For exposures corresponding to 95% R.H., the value of water uptake at the last experimental isotherm point of 90% R.H. was used. For the case of adsorbed water, fitting was conducted both with and without this last data point, since the effects of capillary condensation in the ZIF-8 sample make it unclear if this data point corresponds to an intrinsic property of ZIF-8 or to more macroscopic properties of the powder used in the adsorption experiment. The results, obtained by linear regression using the Matlab Curve Fitting Toolbox, are shown in **Figure 6.6**. The equation is consistent with the limiting case of 0% R.H. where ZIF-8 is stable *(k = 0)* under SO_2 exposure. It is evident from **Figure 6.6** that the degradation rate constant is strongly correlated with both R.H.

and the corresponding adsorbed water within the material (R^2 >0.95). Furthermore, the correlation between adsorbed water and the degradation rate is not significantly affected by the (non)inclusion of the data point at 95% R.H corresponding to the capillary condensation region.

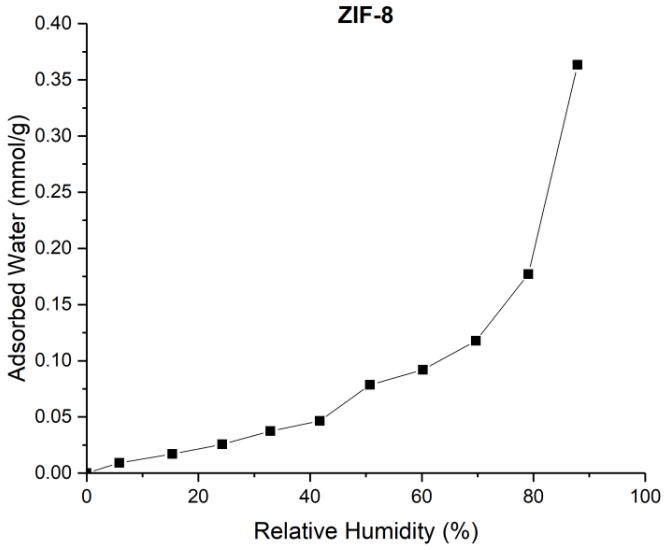

Figure 6.5. Water adsorption isotherm of ZIF-8. Experimental data points are shown linearly connected piecewise.

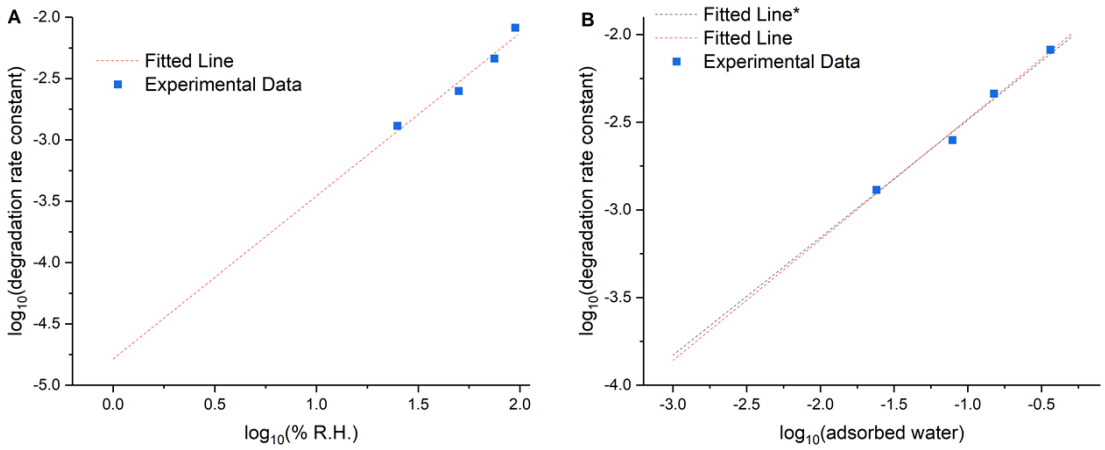

Figure 6.6. Power-law correlations ($k = ax^b$ plotted on logarithmic scale) between the experimentally observed degradation rate constant (k) and x = %R.H. (A) or adsorbed water uptake with and without (*) the data point corresponding to 95 %R.H. (B) in ZIF-8. Symbols: experimental data, Dashed lines: correlation fits. The parameter values and regression coefficient (a, b, R^2) are (1.64×10^{-5}, 1.328, 0.96) in the correlation shown in (A), and (1.614×10^{-2}, 0.69, 0.99) and (1.53×10^{-2}, 0.67, 0.98) in the correlations shown in (B).

The functional stability of a material in an environment that might cause degradation can be defined by the time over which the material can maintain a desired performance level. For a porous material, the retained pore volume on exposure can be an effective indicator of its functional stability. For a desired performance threshold (retained pore volume), the durability (time duration of use) of a porous material at a particular R.H. under continuous SO_2 exposure can be calculated by rearranging equation (3) in the form:

$$t = -\left(\frac{1}{k}\right) ln\,(1 - C/P_o) \qquad (4)$$

The corresponding approximate value of C/P_o or fractional amount of defect sites for a desired performance threshold can be deduced from **Figure 6.4**. For example, for a 75% or a 50% performance cut off, the mean C/P_o values are 0.011 and 0.031 respectively.

The fitted lines in **Figure 6.6** can be extrapolated below 25% R.H. to predict the degradation rate, and by extension, the durability of ZIF-8 at a desired performance threshold. The predicted durability of ZIF-8 under a continuous exposure of 20 ppm SO_2 with varying R.H. for a desired performance threshold is shown in **Figure 6.7.** Independent predictions of the degradation rate to calculate the durability at different R.H.s were made using the correlations with adsorbed water (method 1) and R.H. (method 2) (**Figure 6.6**). For method 1, the average of the values from the correlations obtained with and without the data point corresponding to capillary condensation (95% R.H.) was used. Differences in the value of the degradation rate, and by extension the material durability, are observed on extrapolation of the fitted data up to 1% R.H. in **Figure 6.6** and **Figure 6.7** by the different methods. The predicted degradation rates (and material durability) from methods 1 and 2 vary by less than a factor of 2 for R.H. above ~10%. The two methods differ more strongly at lower R.H. (**Figure 6.6**). A comparison of the predicted durability of ZIF-8 with varying R.H. at the performance thresholds in **Figure 6.7** are tabulated in **Table 6.3**. For example, at 20% R.H., method 1 predicts ZIF-8 to be stable for 5.5, 9.8, 16, and 27.2 days at material performance thresholds of 90%, 75%, 60% and 50% respectively while method 2 predicts its durability to be 7.4, 12, 21.1, and 35.9 days for the same performance thresholds.

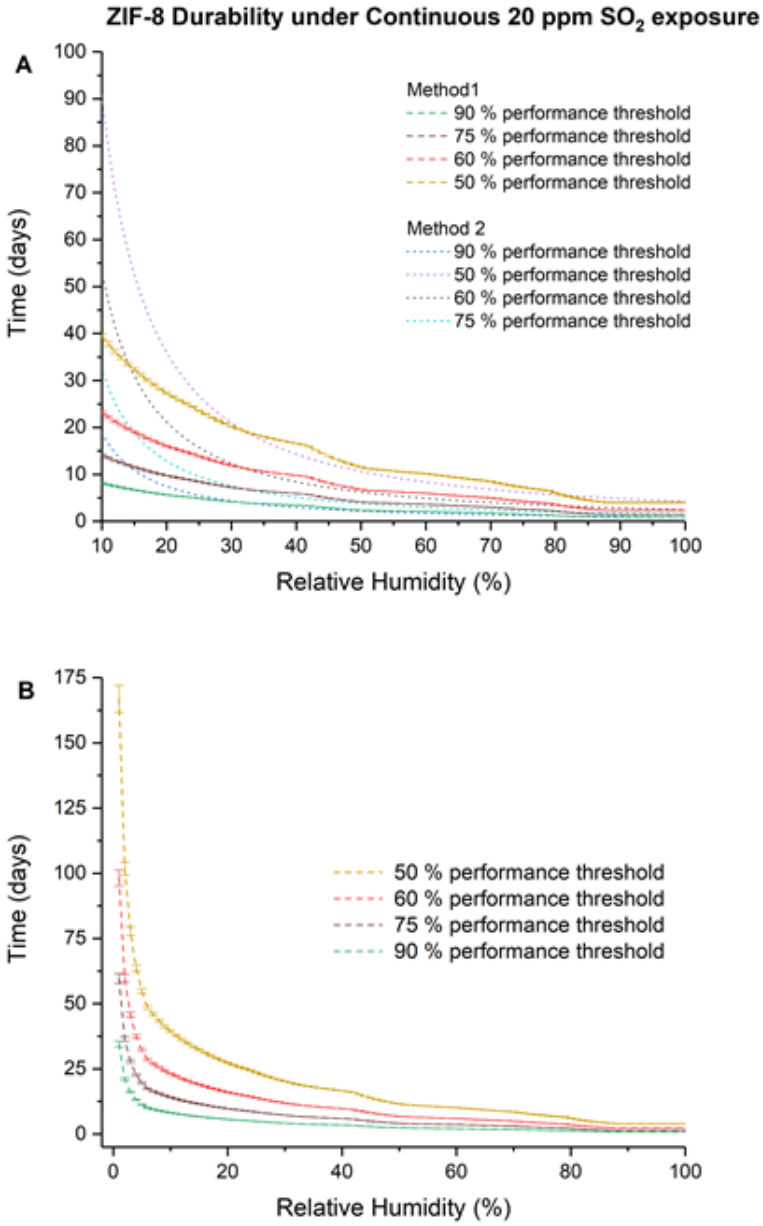

Figure 6.7. Durability of ZIF-8 (days) at different performance levels (% retained pore volume) under continuous exposure of 20 ppm SO_2 with varying R.H from (A) 10-100 % using methods 1 and 2 and (B) 1-100% using method 1. In method 1, rate constants at different R.H. are predicted using the correlation with adsorbed water, while in method 2, predictions use the correlation with R.H.

Table 6.3. Predictions of ZIF-8 durability (days) at different R.Hs for different performance thresholds (% retained pore volume) under continuous SO_2 exposure as predicted by methods 1 (M-1) and 2 (M-2).

Exposure R.H. (%)	Material Performance Threshold							
	90%		75%		60%		50%	
	M-1	M-2	M-1	M-2	M-1	M-2	M-1	M-2
20	5.5	7.4	9.8	12	16	21.1	27.2	35.9
15	6.7	10.9	11.6	18.8	19	31	32.3	52.6
10	9.1	18.6	14.1	32.2	23.2	53	39.4	90.1
5	11.3	46.8	19.6	81	32.2	133	54.8	226
1	34.5	397	59.6	686	98.1	1129	166.8	1919

Table 6.3 tabulates the predicted stability (durability) of ZIF-8 for pre-determined performance thresholds with varying R.H. It is important to note the limitations and uncertainties associated with the mathematical analysis. From **Table 6.3** one can observe how different correlations to predict the degradation rate *(k)*, fitted with a high degree of confidence to experimental data points, can differ significantly by an order of magnitude when extrapolated to low values of R.H.(~1%). Since ZIF-8 is stable under dry SO_2 exposure, k tends to 0 (and durability tends to ∞) as R.H. tends to 0%. The resulting exponential nature of the material durability curve makes predicting stability thresholds at low values of R.H. mathematically uncertain. Measurements of the microscopic parameter of fractional bonds disrupted (C/P_o) from repeated experiments in this Chapter show large error bars especially when the material is considerably degraded. This may imply that

differing amounts of disrupted bonds are able to result in similar observable pore volume losses. This can lead to additional uncertainty in the predictions. The degradation rate constants are calculated here using a single data point of 5 days in humid SO_2 at a particular R.H. and assume a constant rate of degradation for the material throughout the degradation process. The SO_2 concentration throughout the exposures in this work was maintained at 20 ppm and hence the vertical axis of **Figure 6.7** can be expressed in ppm-days (time (days) × 20 ppm). Such a representation would imply that exposure at a fixed value of ppm-days would result in the same effect on ZIF-8 stability, regardless of the individual variations of time and SO_2 concentration. While this hypothesis has been successfully proven for SO_2 concentrations in the 10-80 ppm range (due to limitations of the SO_2 detector range), this has not been shown directly at higher SO_2 concentrations. Most importantly, the predictions assume no reaction energy barrier for the reaction of ZIF-8 with SO_2 and humid air to proceed. It is possible that SO_2 may react appreciably with ZIF-8 only after meeting a certain R.H. threshold. For example, no measurable reactive adsorption is observed for activated carbon and humid SO_2 at 6% R.H.[11] Practical considerations such as maintaining a constant SO_2 concentration of 20 ppm while diluting the incoming stream to very low R.H. levels, exposure apparatus availability for exposing a material for a time period long enough to ensure detectable S concentrations by EDX at the resulting low degradation rates, make it difficult to examine the predicted material durability at R.H. levels lower than 25% experimentally.

6.4 Conclusions

In this Chapter, a quantitative investigation of the degradation occurring in ZIF-8 on exposure to the acid gas SO_2 at different R.H. levels (ranging from 25-95%) has been conducted. Bulk stability of ZIF-8 investigated with PXRD and NP indicates increasing amorphous character and decreasing porosity on exposure to SO_2 as the R.H. gradually increases. These observations are corroborated by mechanistic investigations using FTIR and EDX, which indicate an increasing rate of degradation of ZIF-8 with a rise in R.H. The reaction of ZIF-8 and SO_2 likely proceeds *via* one or more heterogeneous pathways, and rate constants for the humid SO_2 induced degradation of ZIF-8 were measured from S incorporation in the structure using EDX. Statistical correlations of the measured rate constant with variables such as the R.H. and adsorbed water were examined, revealing strong correlations of the degradation rate with both of these variables. The correlations were extended to predict the degradation rate and hence, ZIF-8 durability, at pre-determined performance thresholds (% pore volume retained) under humid SO_2 exposure at R.H. values beyond the experimental range. The validity and limitations of the prediction were also discussed. To the best of my knowledge, this is the first experimental study of any MOF/ZIF stability across varying R.H. conditions on SO_2 exposure. The detailed analysis of the kinetics of ZIF-8 degradation in this work allows for predictions of material durability at chosen R.H. levels. The experimental observations and stability predictions for ZIF-8 from this Chapter should be applicable for different realistic process streams that contain humid SO_2 and unreacted O_2 and this approach can be generalized to study and predict the stability of other porous materials of interest to acid gases under varying humidity.

REFERENCES

1. Burtch, N. C.; Jasuja, H.; Walton, K. S., Water Stability and Adsorption in Metal-Organic Frameworks. *Chem. Rev.* **2014,** *114* (20), 10575-10612.

2. Bhattacharyya, S.; Han, R.; Kim, W.-G.; Chiang, Y.; Jayachandrababu, K. C.; Hungerford, J. T.; Dutzer, M. R.; Ma, C.; Walton, K. S.; Sholl, D. S.; Nair, S., Acid Gas Stability of Zeolitic Imidazolate Frameworks: Generalized Kinetic and Thermodynamic Characteristics. *Chem. Mater.* **2018,** *30* (12), 4089-4101.

3. Bhattacharyya, S.; Pang, S. H.; Dutzer, M. R.; Lively, R. P.; Walton, K. S.; Sholl, D. S.; Nair, S., Interactions of SO_2-Containing Acid Gases with ZIF-8: Structural Changes and Mechanistic Investigations. *J. Phys. Chem. C* **2016,** *120* (48), 27221-27229.

4. Gee, J. A.; Chung, J.; Nair, S.; Sholl, D. S., Adsorption and Diffusion of Small Alcohols in Zeolitic Imidazolate Frameworks ZIF-8 and ZIF-90. *J. Phys. Chem. C* **2013,** *117* (6), 3169-3176.

5. Hashimoto, Y.; Tanaka, S., A new method of generation of gases at parts per million levels for preparation of standard gases. *Environ. Sci. Technol.* **1980,** *14* (4), 413-416.

6. Dortmund Data Bank. 2017 ed.; http://www.ddbst.com/, 2017.

7. Flamm, D. L.; Bacon, D. D.; Kinsbron, E.; English, A. T., Chemical-reaction of sulfur-dioxide at high humidity and temperature - implications for accelerated testing *J. Electrochem. Soc.* **1981,** *128* (3), 679-685.

8. Urone, P.; Lutsep, H.; Noyes, C. M.; Parcher, J. F., Static studies of sulfur dioxide reactions in air. *Environ. Sci. Technol.* **1968,** *2* (8), 611-618.

9. Chaturvedi, S.; Rodriguez, J. A.; Jirsak, T.; Hrbek, J., Surface Chemistry of SO_2 on Zn and ZnO: Photoemission and Molecular Orbital Studies. *J. Phys. Chem. B* **1998,** *102* (36), 7033-7043.

10. Tournas, A. D.; Potts, A. W., Surface reaction of SO_2 with machined (polycrystalline) Zn, Cd, Cu and Ag surfaces studied by He I/II photoelectron spectroscopy. *J. Electron Spectrosc. Relat. Phenom.* **1995,** *73* (2), 231-238.

11. Zhang, P.; Wanko, H.; Ulrich, J., Adsorption of SO_2 on Activated Carbon for Low Gas Concentrations. *Chem. Eng. Technol.* **2007,** *30* (5), 635-641.

12. Lizzio, A. A.; DeBarr, J. A., Mechanism of SO_2 Removal by Carbon. *Energy Fuels* **1997,** *11* (2), 284-291.

13. Zhao, Y.; Liu, Y.; Ma, J.; Ma, Q.; He, H., Heterogeneous reaction of SO_2 with soot: The roles of relative humidity and surface composition of soot in surface sulfate formation. *Atmos. Environ.* **2017,** *152*, 465-476.

14. Tachikawa, H., Water-Accelerated OH Addition to Sulfur Dioxide SO_2: Direct Ab Initio Molecular Dynamics (AIMD) Study. *J. Phys. Chem. A* **2014,** *118* (18), 3230-3236.

15. Benson, D. R.; Young, L.-H.; Kameel, F. R.; Lee, S.-H., Laboratory-measured nucleation rates of sulfuric acid and water binary homogeneous nucleation from the SO_2 + OH reaction. *Geophys. Res. Lett.* **2008,** *35* (11).

16. Marvin, C. D.; Reiss, H., Cloud chamber study of the gas phase photooxidation of sulfur dioxide. *J.Chem.Phys.* **1978,** *69* (5), 1897-1918.

CHAPTER 7. CONCLUSIONS AND OUTLOOK

7.1 Conclusions and impacts of this work

This thesis has developed a fundamental basis for understanding and controlling acid gas interactions with ZIF materials. These advances are a significant step on the road to fulfilling the great potential of ZIFs as high-performance materials for energy efficient industrial separations under process conditions containing different acid gases. The new and systematized knowledge generated in this work helps create a significantly better understanding of the behavior of these materials towards the acid gases CO_2, SO_2, and NO_2, and will aid in the design of robust materials for chemical separations. The main conclusions and impacts of the thesis are summarized in more specific terms below.

In Chapter 2, I explored the separation performance of seven representative ZIF materials towards 1-butanol separation utilizing a novel hybrid separation approach, coupling vapor-phase breakthrough experiments with gas stripping. ZIF-8 was found to be the most butanol selective material under inert gas stripping. The impact of the acid gas CO_2 generated during the fermentation process on the ZIF materials was then evaluated under high humidity, and only ZIF-71 was determined to be stable under such conditions. All other ZIFs formed complex carbonates with a corresponding decrease in butanol uptake and porosity. The study was extended to a multicomponent model ABE aqueous solution with CO_2 stripping, and ZIF-71 was still found to be highly butanol-selective. This is the first reported study on any MOF being evaluated for vapor-phase biobutanol separations. Significantly, it established the importance of stability as a performance metric while choosing materials for a practical application. Without stability considerations, ZIF-8

performed best towards biobutanol separations, but its instability to humid CO_2 made ZIF-71 the material of choice for this application. The results of this Chapter raised fundamental questions concerning the stability of ZIFs to other, stronger acid gases such as SO_2, and NO_2 which were investigated in the later Chapters.

In Chapter 3, I investigated the structural and mechanistic aspects of the changes occurring in a model ZIF material (ZIF-8) under exposure to the acid gas SO_2. ZIF-8, known for its relatively high thermal and chemical stability among MOFs, retained bulk stability upon humid air exposure and dry SO_2 exposure but was susceptible to bulk degradation under long-term exposure to humidified SO_2, exhibiting decreased crystallinity and porosity. Multiple mechanistic investigations were consistent with a mechanism of ZIF-8 degradation *via* formation of sulfuric and sulfurous acids (*via* chemical reactions involving SO_2 and H_2O). This is the first experimental investigation that comprehensively evaluated and explained the acid gas (SO_2) stability of any ZIF material under a number of different exposure conditions, and provided valuable information for the design and use of ZIFs in separation processes.

In Chapter 4, I expanded the study of acid gas stability from the model ZIF-8 material to a generalized and systematic investigation involving a diverse set of 16 porous ZIF materials with varying linkers and topologies under different environments – humid air, liquid water, and acid gases CO_2 and SO_2 (dry, humid, and aqueous). Observations for each ZIF under a particular exposure condition were summarized in the form of a color-coded stability chart, which is a useful resource for evaluation of ZIFs for separation applications in which acid gases are a significant factor. All ZIFs investigated under dry CO_2 and SO_2 were observed to be stable under such exposure conditions, but, with the

exception of ZIF-71, were susceptible to bulk degradation under long-term exposure to humidified CO_2 or SO_2. Quantifying elemental S incorporation post-exposure to humid SO_2 through EDX allowed a kinetic study of ZIF degradation, with rate constants for the humid SO_2-induced degradation measured for the first time. Conventional indicators of thermodynamic and kinetic stability were unable to satisfactorily explain the observations. Due to the evaluation of multiple ZIF materials in this work, I was able to examine statistical correlations of the rate constant with chemical and structural variables associated with the ZIFs which revealed surprisingly strong correlations of the degradation rate with the linker K_a and ZIF hydrophilicity with *negative* proportionalities. This is the first generalized study providing quantitative insights on the stability of a diverse range of ZIF materials under acid gas (CO_2, SO_2) exposure. An important practical contribution of this chapter is the stability chart, allowing researchers to choose ZIFs exhibiting stability under their particular application process condition for further investigation. This chapter also indicates that, in general ZIFs are prone to degradation under high humidity in the presence of acid gases such as SO_2 and CO_2.

In Chapter 5, I conducted a systematic investigation of the effects of dry and humid NO_2 gas on a limited set of representative ZIFs, chosen carefully based upon the findings from the larger set of ZIFs employed in Chapter 4. All the ZIFs investigated were found to be unstable under prolonged dry or humid NO_2 exposures. Humid NO_2 caused greater damage in hydrophilic ZIF-90, while dry NO_2 affected hydrophobic ZIF-8 more. ZIF-71 had the highest relative stability under dry NO_2 exposure but underwent phase transformation under humid NO_2 exposure. Permanent alteration of the chemical structure of the 3 ZIFs was confirmed through FTIR measurements, with formation of new N-

containing species. DFT simulations on defect energy formation were carried out which supported experimental observations. H-abstraction by the free radical NO_2 was proposed as the major reaction mechanism under dry exposure, while adsorbed nitric acid led to additional reaction pathways under humid exposures, especially in hydrophilic materials. The unexpected findings of this work highlight striking differences in ZIF stability towards dry NO_2 compared to the other acid gases SO_2 and CO_2, which are detrimental only under humid exposure conditions. In comparison to dry or humid SO_2, the free radical NO_2 is a much more aggressive acid gas whose presence may require different approaches to stabilize ZIF/MOF materials.

In Chapter 6, I considered the important effect of water vapor concentration in enabling the attack of acid gas species on ZIF materials. Towards this end, a quantitative investigation of the degradation of ZIF-8 upon exposure to the acid gas SO_2 at different R.H. levels of 25%, 50%, 75% and 95% was conducted. Bulk stability of ZIF-8 investigated with PXRD and NP indicated increasing amorphous character and decreasing porosity on exposure to SO_2 as the R.H. gradually increased. These observations are corroborated by mechanistic investigations using FTIR and EDX, which indicate an increasing rate of degradation of ZIF-8 with a rise in R.H. The reaction of ZIF-8 and SO_2 likely proceeds *via* one or more heterogeneous pathways, and rate constants for the humid SO_2 induced degradation of ZIF-8 were measured from S incorporation in the structure using EDX. Statistical correlations of the measured rate constant with variables such as the R.H. and adsorbed water were examined, revealing strong correlations of the degradation rate with both of these variables of interest. The correlations were extended to predict the degradation rate and hence, ZIF-8 durability, at pre-determined performance thresholds (%

pore volume retained) under humid SO_2 exposure at R.H. values beyond the experimental range. The validity and limitations of the prediction were also discussed. This is the first experimental study of any MOF/ZIF stability across varying R.H. conditions on SO_2 exposure. The detailed analysis of the kinetics of ZIF-8 degradation in this work allows for predictions of material durability at chosen R.H. levels. The experimental observations and stability predictions for ZIF-8 from this chapter should be applicable for realistic process streams that contain humid SO_2 with unreacted O_2 and this approach can be generalized to study and predict the stability of other porous materials of interest to acid gases under varying humidity.

7.2 Outlook and Future Work

Theoretical and experimental studies on other types of MOFs recently conducted by my collaborators at Georgia Tech have been consistent with the findings of my work on ZIFs. Theoretical investigations into the energetics of defect formation in ZIF-8 by various attacking acidic species have indicated that missing linker and dangling linker defects are the most energetically favorable.[1-3] Favorable dangling linker defect formation energies have been reported for ZIF-8 reacting with bronsted acid species such as sulfurous and sulfuric acids that may form *in situ* under humid SO_2 exposure conditions, but not with humidity or dry SO_2 alone.[3] Experimental studies by collaborators have also shown that humid (~80-85% R.H.) SO_2 gas even at ppm-levels is particularly detrimental to stability of MOFs such as MIL-125, defective UiO-66, MOF nanosheets, and DMOFs.[4-6] This consistency in the stability observations across a variety of MOF species and my in-depth study of ZIFs gives direct proof of the wider applicability of the present work beyond ZIF

materials. The generalized insights obtained in this thesis result in a number of promising and impactful research avenues, which are discussed below.

7.2.1 Imparting stability to ZIF materials towards phase transitions

This thesis has explored in detail different acid gas specific ZIF interactions which enhance our fundamental knowledge on ZIF-acid gas interactions. As discussed in Chapter 4 of the thesis, stability of a ZIF on acid gas exposure can be either due to degradation of the crystal structure by the attacking species, or a result of crystal phase transformation.[7] In Chapter 2 of this thesis, while investigating the humid CO_2 stability of ZIF materials, I discovered that the hybrid ZIF-8_{55}-71_{45} (SOD topology) material was stable under humid air unlike one of its parent materials ZIF-71 (SOD), which undergoes a phase transformation under these conditions.[8] This gives direct evidence that doping of a ZIF can impart stability to it towards phase transformation. Interestingly, ZIF-8_{55}-71_{45} hybrids were observed to be unstable to humid CO_2 which indicates that, while incorporation of phase-stable ZIF-8 imparted phase transformation stability to ZIF-71(SOD), the relative inertness towards acid gases of ZIF-71(SOD) did not translate to the hybrid material synthesized. This doping approach can be extended to other ZIFs unstable in humid air or water. ZIF-65(Zn) is particularly interesting in this regard as it has the highest reported SO_2 adsorption capacity for any MOF under dry conditions. However it is unstable under humid air and water rendering it of no practical use to acid gas capture. Stabilizing it by doping with another humidity stable ZIF such as ZIF-8 can unlock the full potential of this material towards acid gas capture applications. Inspiration for the design of robust materials to acid gases can be drawn from the design of water stable MOFs, although critical differences exist.[9-11] Often post-synthetic modifications using hydrophobic linkers are used as a stabilization

strategy for MOFs against water. An analogous strategy for acid gas stability would rely on preventing access of the attacking species inside the MOF pores, which cannot be used if the attacking species itself is the desired adsorbate (*eg.* acid gas capture). Another difference is the formation of secondary attacking species in the presence of humidity and acid gases, whose concentrations, and even, exact structures can be complex and difficult to predict. Deliberate design of ZIFs/MOFs that are robust towards acid gases and still maintain the desired functionality - while not a direct focus of this thesis - is expected to be a key topic for future investigations.

7.2.2 Explaining the high stability of ZIF-71

A number of stability indicators explored in Chapter 4 were unable to satisfactorily explain the observed acid gas stability of ZIF-71. The statistical correlation of the numerical degradation rates with material properties revealed a surprising *negative correlation* of the reaction rate with the linker K_a.[7] While high linker *p*K_a has been traditionally associated with a stronger MOF coordination bond, this thesis shows that ZIFs comprised of lower *p*K_a linkers such as ZIF-71 have higher relative stability to the humid SO_2 acid gas.[12] Similar observations have been reported recently on the acid stability of MOF materials consisting of low *p*K_a linkers such as carboxylates.[11] It has been proposed from experimental observations that MOFs comprised of soft acids (*eg.* Zn^{2+}) and soft bases such as imidazoles with relatively high linker *p*K_as exhibit increased stability under basic environments while lower linker *p*K_a carboxylate based MOFs with hard acid sites (*eg.* Zr^{4+}) are more stable under acidic solutions.[11, 13-14] Relatively high *p*K_a values of imidazolate linkers in materials such as ZIF-8 are believed to lead to a stronger coordination bond, but they also indicate strong affinity between the linkers and protons,

which can destabilize the system in the presence of acids.[11] While the observations behind this hypothesis are strictly true for acidic solutions, evaluating acid gas stability of other ZIFs with lower *p*K_a linkers should be explored in designing acid gas stable ZIF materials in future work.

7.2.3 The complex role of material hydrophilicity

Statistical correlations of the degradation rate in Chapter 4 of this thesis link the material hydrophilicity to a slower rate of degradation on humid SO_2 exposure.[7] Hydrophilic ZIFs such as ZIF-90 and ZIF-93 have two of the lowest degradation rates for humid SO_2. However, the ZIF-90 framework is severely destroyed on exposure to humid NO_2 gases (Chapter 5) which contradicts the findings in Chapter 4. This apparent discrepancy may be addressed by a closer inspection of the acidic species produced on humid SO_2 and NO_2 exposures within hydrophilic materials. Hydrophilic ZIFs undergo complete pore filling at high R.H. conditions and acidic species are likely to form *via* dissolution of the acid gases in the water-filled pores that approach bulk conditions. The dissolution of SO_2 in water yields sulfurous acid, a comparatively weaker acid than nitric acid that is formed when NO_2 dissolves in water.[15-16] Under the conditions of this study, oxidation of the sulfurous acid solution to sulfuric acids is unlikely. Thus, the thesis results highlight the complex role of material hydrophilicity on material stability; this difference in the potency of SO_2 and NO_2 under humid conditions in a hydrophilic material will hold true for all materials, beyond just ZIFs.

7.2.4 Understanding the progress of defects in the degradation reaction

A careful analysis of the crystal structure of ZIF-8 post humid SO_2 degradation shows that even on complete loss of pore volume, ZIF-8's crystal structure is not severely altered. Consistent with the PXRD results, my EDX analysis indicates that only 14% of the bonds are cleaved at complete loss of pore volume and this number is similar or even smaller for other ZIFs degraded by humid SO_2 (Chapter 4). The relative maintenance of the crystal structure and the low bond cleavage % at complete loss of pore volume for a ZIF indicates that pore blockage by humid SO_2 attack is the possible dominant degradation pathway. This indicates that the surface of a ZIF material is likely degraded first by humid SO_2 and the resulting small fraction of broken bonds can block off the internal bulk porosity of the material. The recently reported solvent assisted crystal redemption (SACRed) process for the recovery of acid gas degraded ZIFs also reported only 34% of linker replacement to recover a completely degraded ZIF-8 sample.[17] The surface of ZIF-8 has been computationally shown to be more reactive than its bulk and ongoing investigations into the defect propagation within ZIF structures could shed more light towards a better understanding of the degradation process.[3] Water adsorption, which is correlated with a higher SO_2 degradation rate (Chapter 6), can be significant on the surface of a hydrophobic material such as ZIF-8 due to terminal –N-H functionalities of the imidazole linker.[18] Experimentally verifying the distribution of defective and pristine imidazole linkers within a ZIF after humid SO_2 degradation can also aid in determining the nature and progress of this heterogeneous degradation reaction. Nuclear magnetic resonance (NMR), which has been successfully used to probe linker distribution within the ZIF structure, may be advantageously utilized for this purpose in the future.[19]

7.2.5 Evaluation of other reaction parameters

In Chapter 6, I establish that the reaction between SO_2 and ZIFs in humid air is a heterogeneous reaction, with oxidation of SO_2 to sulfuric acid facilitated either by formation of water clusters within the exposure unit or by the surface of the ZIF *via* reactive adsorption.[20] The role of oxygen in this reaction has not been extensively investigated in my thesis and can be done in future work. SO_2, water, and/or O_2 adsorbed on the ZIF surface likely react forming sulfuric acids on the ZIF surface, similar to the reactions on soot or activated carbon. The use of O_2 as the carrier gas in this work makes the thesis results applicable to practical conditions where SO_2 in combustion process streams always contain excess O_2.

Exposure to acid gases in this thesis has been conducted by spreading equal amounts of ZIF samples in a chemically inert borosilicate glass container.[21] All standard laboratory surfaces adsorb water under high R.H. and may promote heterogeneous surface reactions.[22] Compared to a gas breakthrough setup, my exposure unit has a higher proportion of materials exposed to the support surface. This dependence of the surface properties of the container on the observed degradation rate was not evaluated in this thesis and can be done in future work.

In addition, the effect of temperature on the degradation rate of humid acid gases should be evaluated in future work. Realistic flue gas temperatures for CO_2 capture processes are higher than ambient temperatures and these can be expected to have non-trivial effects on the observed reaction rate. ZIFs may be more susceptible to dry acid gases at a higher temperature but the effects of humid acid gases are not straightforward to

predict. While reaction rates may increase with an increase in temperature, the adsorption of species is always exothermic and shows the opposite trend. Indeed if the adsorbed water within ZIF materials decrease significantly at higher temperatures, the resulting humid acid degradation process might mirror the results of the dry acid gas. The limitation of the structural materials of my exposure setup prevented an investigation of the acid gas stability of ZIF materials at higher temperatures. It is recommended that this study be carried out to ascertain material stability under more realistic process conditions.

7.2.6 Extending the quantitative approach to acid gas degradation

A highlight of this thesis is the emergence of a quantitative approach to the stability of ZIFs through an evaluation of degradation reaction rates. This approach has been demonstrated on different ZIF materials towards the acid gas SO_2 with great success. However the underlying method evaluates reaction rates from introduced elemental S within the ZIF framework. This works successfully for all materials which do not already contain S atoms in their structure, as accurately quantifying excess S introduced into the structure of such a material through this method is fraught with uncertainty. Conversely, this method could not be applied to evaluate the degradation rate of ZIFs (which already have N in their framework) under NO_2 exposure. However, for a vast number of MOFs and other materials which do not contain structural N, the method will be able to accurately determine the rate of NO_2 degradation. FTIR spectroscopy could be used by integrating specific peak areas characteristic to the degradation mechanism, but accurate quantification of integrated areas across materials need to account for differences in polarizability. Future research is recommended in order to establish complementary methods to determine degradation reaction rates in such cases where EDX cannot be accurately used.

7.2.7 Improvement of the predictive acid gas degradation model

The predictive models for ZIF stability to humid SO_2 developed in Chapter 6 of this thesis is the first of its kind and can be further improved. The durability chart is strictly established for a process stream of 20 ppm SO_2 gas but the Y-axis of the chart can be represented both as time and ppm-days. Such a representation (ppm-days) is practically useful as a measure of the total quantity of exposure, but holds true only if individual variations of SO_2 concentration and exposure time do not alter their combined effect at a constant value of ppm-days. Exposure experiments of ZIF-8 conducted at 10 ppm and 80 ppm SO_2 concentration for 2 days and 6 hours respectively showed good agreement with the observed degradation at 20 ppm for 1 day. The limitations of my sensor prevent further investigation of the SO_2 concentration range but is highly recommended in future studies. The variation in the predictions of the two correlations at low R.H.s can be properly addressed by SO_2 exposure experiments at lower R.H. Experiments at lower R.H.s are practically difficult but could establish minimum humidity thresholds for the ZIF-8 degradation reaction to humid SO_2. Such a study was not feasible in my exposure unit but is recommended in future work. The predictive models assume a constant rate of degradation at a certain R.H. which should also be validated in future work. Additionally, the effect of R.H. on hydrophilic materials such as ZIF-90 may be significantly different from ZIF-8 due to pore filling effects. This effect may also be evaluated in future work and a predictive model established to extend the scope of the conclusions of this study.

In conclusion, this thesis has significantly expanded the boundaries of knowledge on stability of ZIF materials to the acid gases SO_2 and NO_2 and the observations and findings of this thesis are relevant to all separation processes containing one or more of

these species where the use of ZIF materials are envisioned. The a) detailed mechanistic insights from this thesis on ZIF stability to these gases under different conditions, b) volume of new observations on a large dataset of ZIF materials towards humidity, water and acid gas stability, c) the quantitative approach towards MOF/ZIF stability by estimation of degradation rates, d) new insights obtained from statistical correlations between degradation rates and material properties, and e) initial development of predictive models towards acid gas stability, makes this work critical to the intelligent design of stable MOFs and ZIFs towards acid gases in the near future.

REFERENCES

1. Han, R.; Sholl, D. S., Computational Model and Characterization of Stacking Faults in ZIF-8 Polymorphs. *J. Phys. Chem. C* **2016,** *120* (48), 27380-27388.

2. Zhang, C.; Han, C.; Sholl, D. S.; Schmidt, J. R., Computational Characterization of Defects in Metal-Organic Frameworks: Spontaneous and Water-Induced Point Defects in ZIF-8. *J.Phys.Chem.Lett.* **2016,** *7* (3), 459-464.

3. Han, C.; Zhang, C.; Tymińska, N.; Schmidt, J. R.; Sholl, D. S., Insights into the Stability of Zeolitic Imidazolate Frameworks in Humid Acidic Environments from First-Principles Calculations. *J. Phys. Chem. C* **2018,** *122* (8), 4339-4348.

4. Elder, A. C.; Bhattacharyya, S.; Nair, S.; Orlando, T. M., Reactive Adsorption of Humid SO_2 on Metal–Organic Framework Nanosheets. *J. Phys. Chem. C* **2018,** *122* (19), 10413-10422.

5. Jiao, Y.; Liu, Y.; Zhu, G.; Hungerford, J. T.; Bhattacharyya, S.; Lively, R. P.; Sholl, D. S.; Walton, K. S., Heat-Treatment of Defective UiO-66 from Modulated Synthesis: Adsorption and Stability Studies. *J. Phys. Chem. C* **2017,** *121* (42), 23471-23479.

6. Mounfield, W. P.; Han, C.; Pang, S. H.; Tumuluri, U.; Jiao, Y.; Bhattacharyya, S.; Dutzer, M. R.; Nair, S.; Wu, Z.; Lively, R. P.; Sholl, D. S.; Walton, K. S., Synergistic Effects of Water and SO_2 on Degradation of MIL-125 in the Presence of Acid Gases. *J. Phys. Chem. C* **2016,** *120* (48), 27230-27240.

7. Bhattacharyya, S.; Han, R.; Kim, W.-G.; Chiang, Y.; Jayachandrababu, K. C.; Hungerford, J. T.; Dutzer, M. R.; Ma, C.; Walton, K. S.; Sholl, D. S.; Nair, S., Acid Gas Stability of Zeolitic Imidazolate Frameworks: Generalized Kinetic and Thermodynamic Characteristics. *Chem. Mater.* **2018,** *30* (12), 4089-4101.

8. Bhattacharyya, S.; Jayachandrababu, K. C.; Chiang, Y.; Sholl, D. S.; Nair, S., Butanol Separation from Humid CO_2-Containing Multicomponent Vapor Mixtures by Zeolitic Imidazolate Frameworks. *ACS Sustainable Chem. Eng.* **2017,** *5* (10), 9467-9476.

9. Howarth, A. J.; Liu, Y.; Li, P.; Li, Z.; Wang, T. C.; Hupp, J. T.; Farha, O. K., Chemical, thermal and mechanical stabilities of metal–organic frameworks. *Nat. Rev. Mater.* **2016,** *1*, 15018.

10. Bosch, M.; Zhang, M.; Zhou, H.-C., Increasing the Stability of Metal-Organic Frameworks. *Adv. Chem.* **2014,** *2014*, 8.

11. Yuan, S.; Feng, L.; Wang, K.; Pang, J.; Bosch, M.; Lollar, C.; Sun, Y.; Qin, J.; Yang, X.; Zhang, P.; Wang, Q.; Zou, L.; Zhang, Y.; Zhang, L.; Fang, Y.; Li, J.; Zhou, H. C., Stable Metal-Organic Frameworks: Design, Synthesis, and Applications. *Adv Mater* **2018,** *0* (0), 1704303.

12. Lu, P.; Wu, Y.; Kang, H.; Wei, H.; Liu, H.; Fang, M., What can pKa and NBO charges of the ligands tell us about the water and thermal stability of metal organic frameworks? *J. Mater. Chem. A* **2014,** *2* (38), 16250-16267.

13. Wang, K.; Lv, X.-L.; Feng, D.; Li, J.; Chen, S.; Sun, J.; Song, L.; Xie, Y.; Li, J.-R.; Zhou, H.-C., Pyrazolate-Based Porphyrinic Metal–Organic Framework with Extraordinary Base-Resistance. *J.Am.Chem.Soc.* **2016,** *138* (3), 914-919.

14. Morris, W.; Volosskiy, B.; Demir, S.; Gándara, F.; McGrier, P. L.; Furukawa, H.; Cascio, D.; Stoddart, J. F.; Yaghi, O. M., Synthesis, Structure, and Metalation of Two New Highly Porous Zirconium Metal–Organic Frameworks. *Inorg. Chem.* **2012,** *51* (12), 6443-6445.

15. Gray, P.; Yoffe, A. D., The Reactivity And Structure Of Nitrogen Dioxide. *Chem. Rev.* **1955,** *55* (6), 1069-1154.

16. Bhattacharyya, S.; Pang, S. H.; Dutzer, M. R.; Lively, R. P.; Walton, K. S.; Sholl, D. S.; Nair, S., Interactions of SO_2-Containing Acid Gases with ZIF-8: Structural Changes and Mechanistic Investigations. *J. Phys. Chem. C* **2016,** *120* (48), 27221-27229.

17. Jayachandrababu, K. C.; Bhattacharyya, S.; Chiang, Y.; Sholl, D. S.; Nair, S., Recovery of Acid-Gas-Degraded Zeolitic Imidazolate Frameworks by Solvent-Assisted Crystal Redemption (SACRed). *ACS Appl. Mater. Interfaces* **2017,** *9* (40), 34597-34602.

18. Zhang, K.; Lively, R. P.; Zhang, C.; Koros, W. J.; Chance, R. R., Investigating the Intrinsic Ethanol/Water Separation Capability of ZIF-8: An Adsorption and Diffusion Study. *J. Phys. Chem. C* **2013,** *117* (14), 7214-7225.

19. Jayachandrababu, K. C.; Verploegh, R. J.; Leisen, J.; Nieuwendaal, R. C.; Sholl, D. S.; Nair, S., Structure Elucidation of Mixed-Linker Zeolitic Imidazolate Frameworks by Solid-State ^{1}H CRAMPS NMR Spectroscopy and Computational Modeling. *J.Am.Chem.Soc.* **2016,** *138* (23), 7325-7336.

20. Flamm, D. L.; Bacon, D. D.; Kinsbron, E.; English, A. T., Chemical-reaction of sulfur-dioxide at high humidity and temperature - implications for accelerated testing *J. Electrochem. Soc.* **1981,** *128* (3), 679-685.

21. Glass, P., Technical information: pyrex glass. http://www.pegasus-glass.com/Portals/0/technical_infopyrex.pdf.

22. Sumner, A. L.; Menke, E. J.; Dubowski, Y.; Newberg, J. T.; Penner, R. M.; Hemminger, J. C.; Wingen, L. M.; Brauers, T.; Finlayson-Pitts, B. J., The nature of water on surfaces of laboratory systems and implications for heterogeneous chemistry in the troposphere. *Phys. Chem. Chem. Phys.* **2004,** *6* (3), 604-613.

APPENDIX A. SUPPORTING INFORMATION (CHAPTER 2)

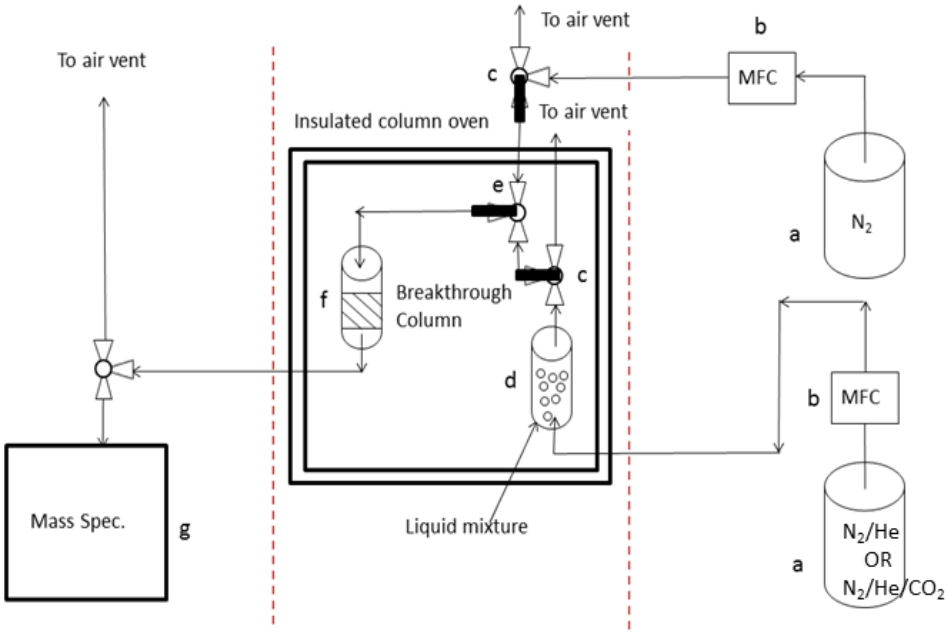

Figure A.1. Schematic of the vapor breakthrough apparatus used for butanol separation from dilute aqueous solutions and ABE mixtures.

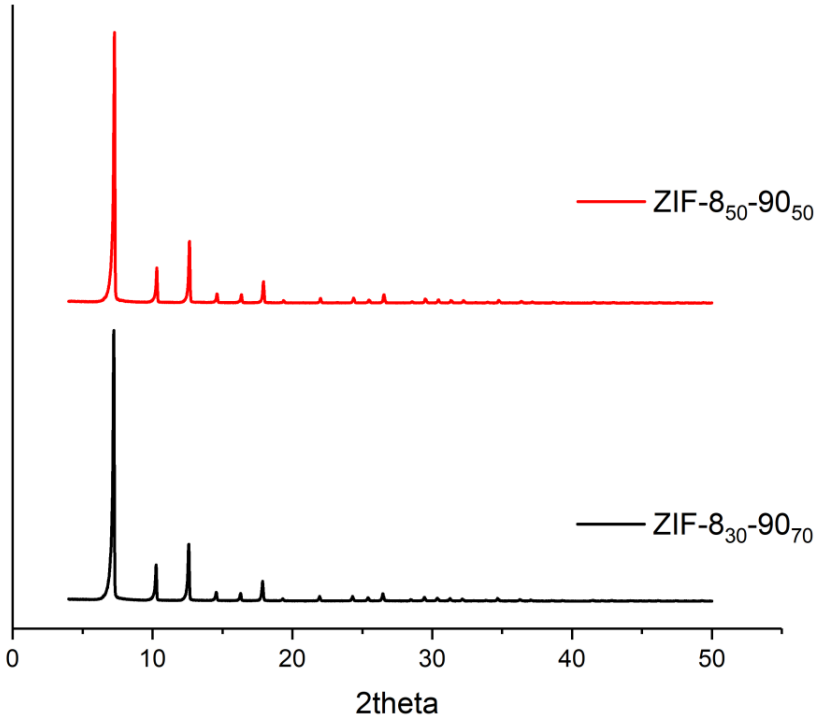

Figure A.2. PXRD patterns of ZIF-8_{50}-90_{50} and ZIF-8_{30}-90_{70}.

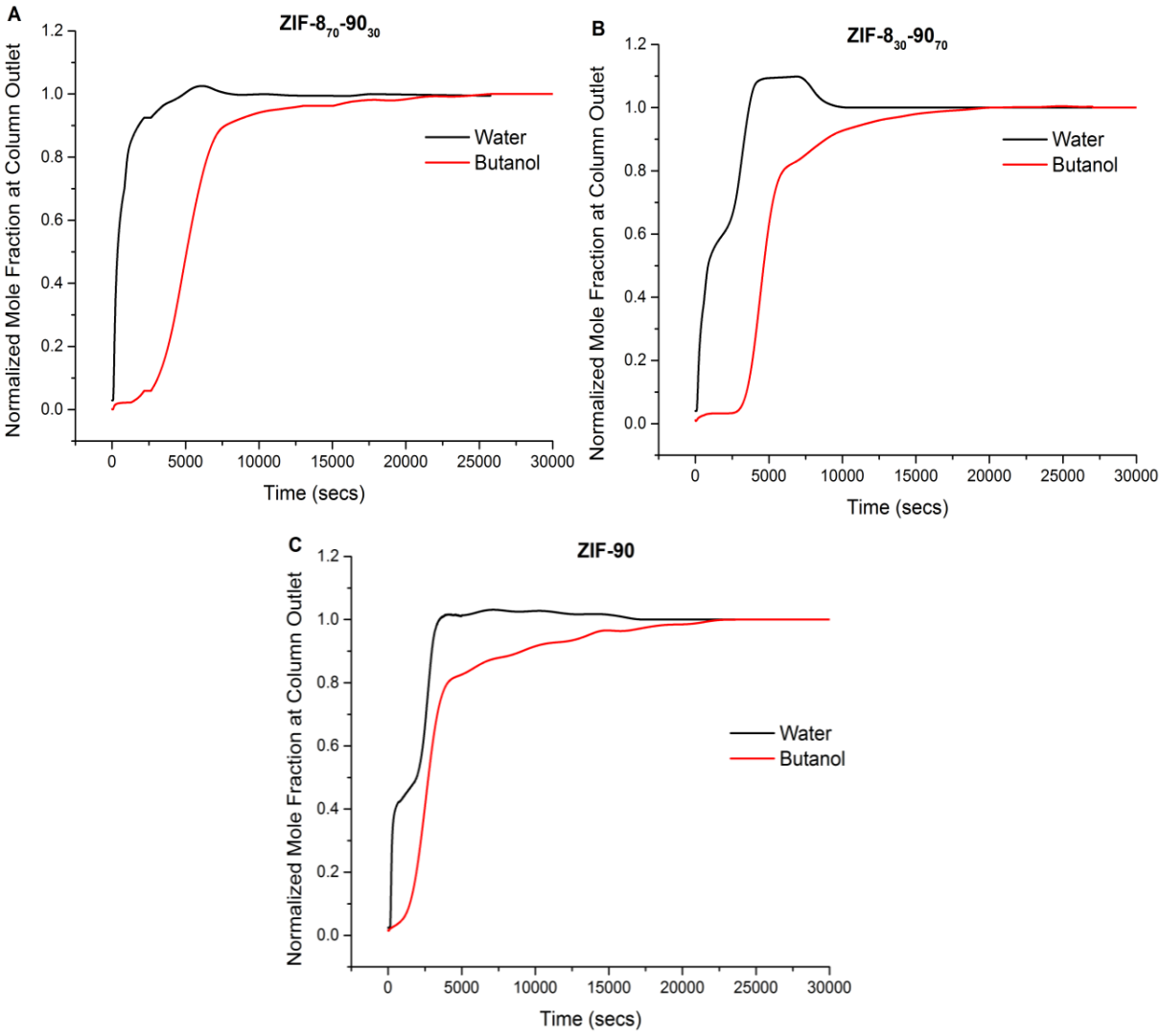

Figure A.3. Breakthrough curves showing the normalized vapor-phase mole fractions of water and butanol at the outlet of the packed bed adsorber with a step input of the equilibrated vapor phase from a 1 mol% butanol/water solution, at a total pressure of 1 atm, temperature of 308 K, and flowrate of 22 cc/min. The three adsorbents shown are: A) ZIF-8$_{70}$-90$_{30}$, B) ZIF-8$_{30}$-90$_{70}$, and C) ZIF-90.

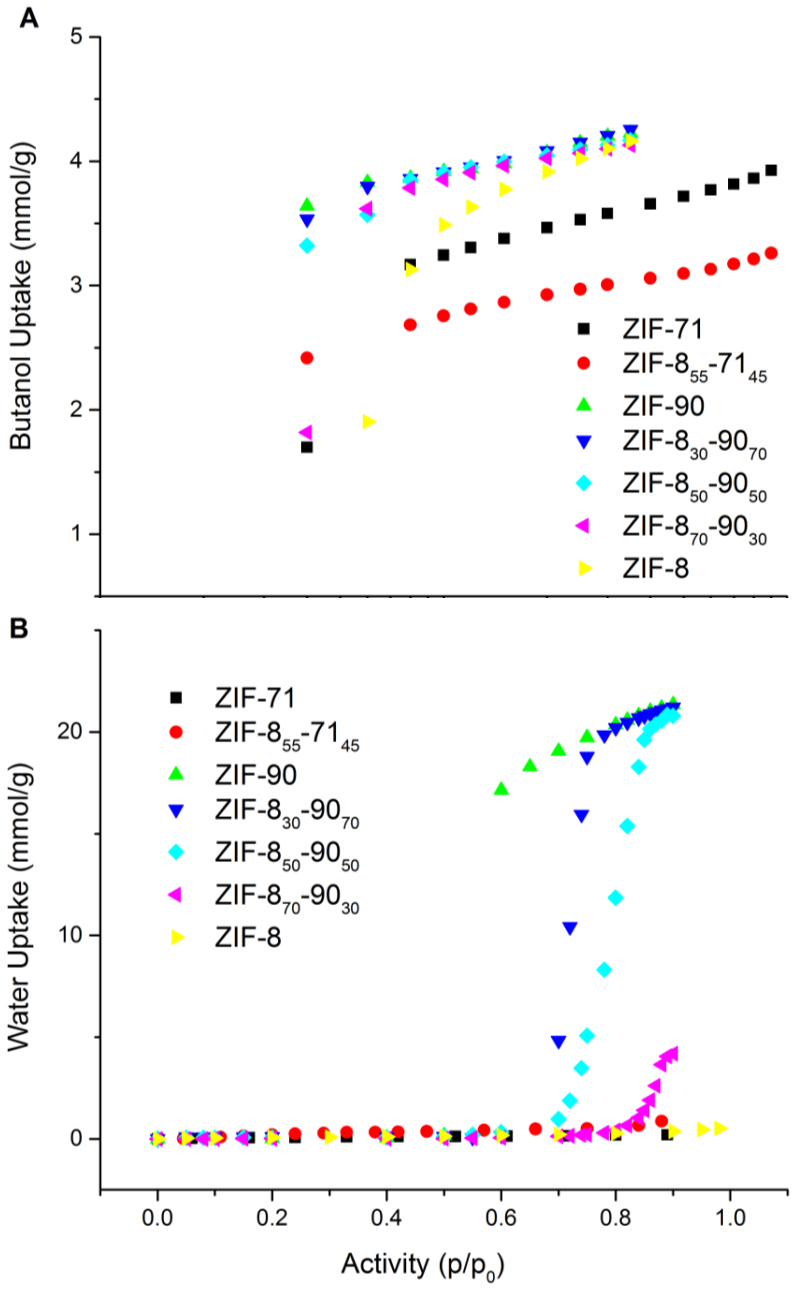

Figure A.4. A) Butanol and B) water single-component adsorption isotherms for all the seven adsorbents.

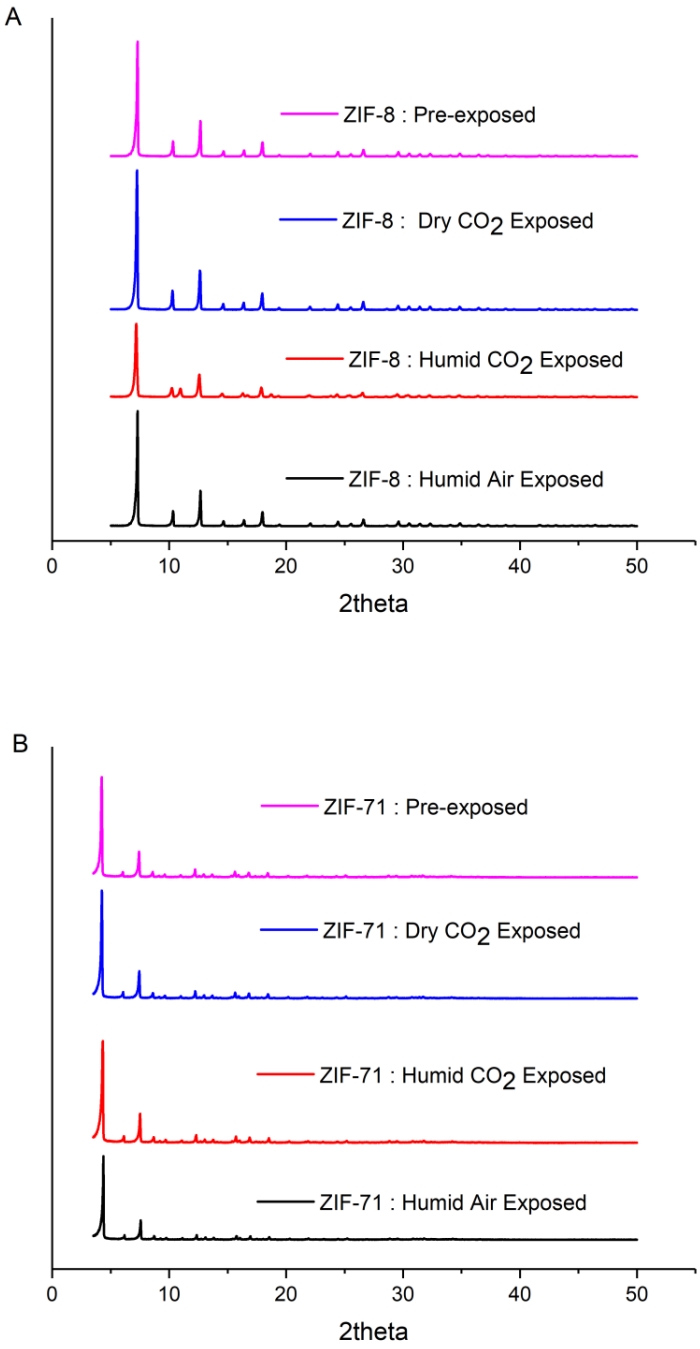

Figure A.5. PXRD patterns of ZIF-8 and ZIF-71 before and after exposure to different gas environments.

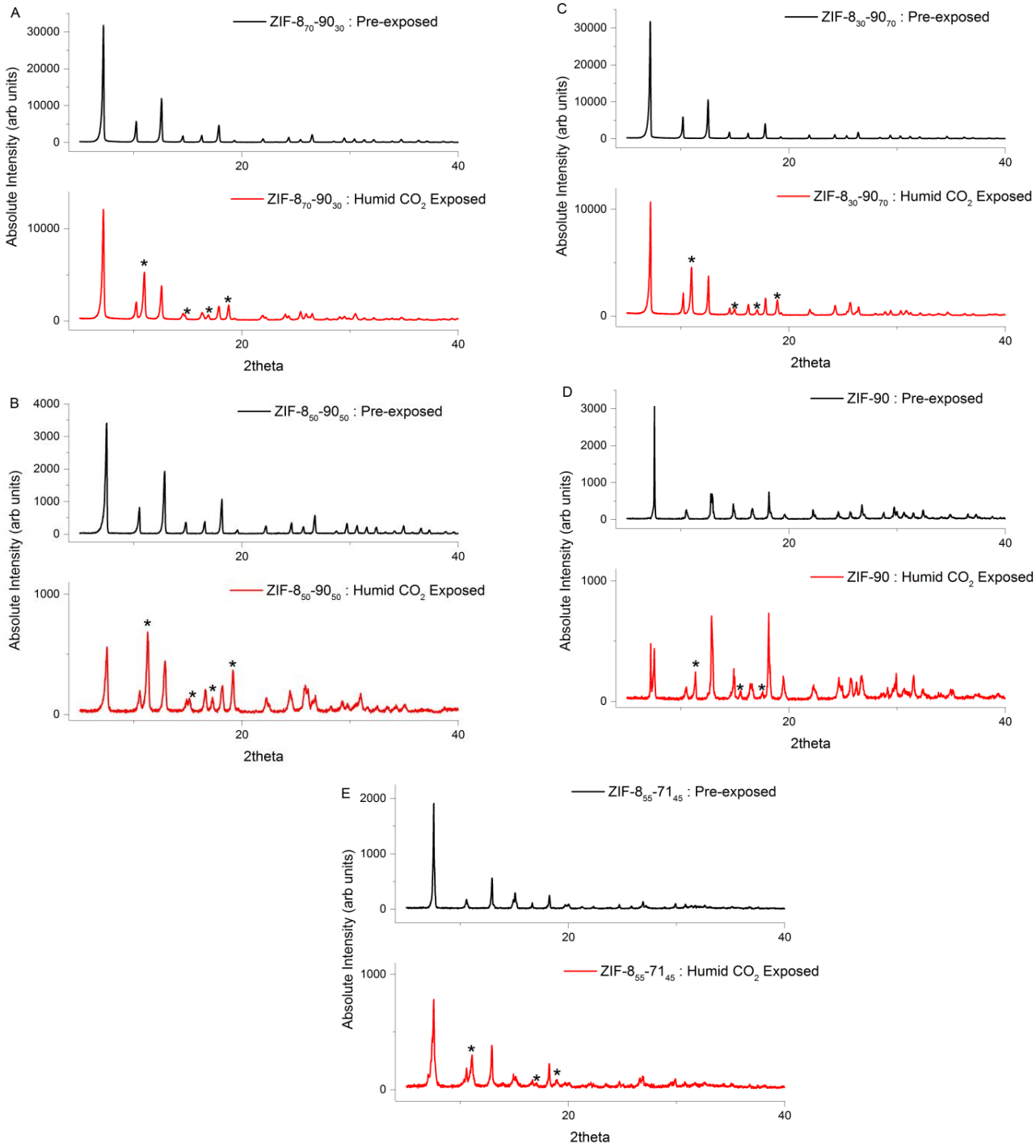

Figure A.6. PXRD patterns of A) ZIF-8$_{70}$-90$_{30}$, B) ZIF-8$_{50}$-90$_{50}$, C) ZIF-8$_{30}$-90$_{70}$, D) ZIF-90, and E) ZIF-8$_{55}$-71$_{45}$ before and after exposure to humid CO_2. Peaks corresponding to carbonate formation are marked (*).

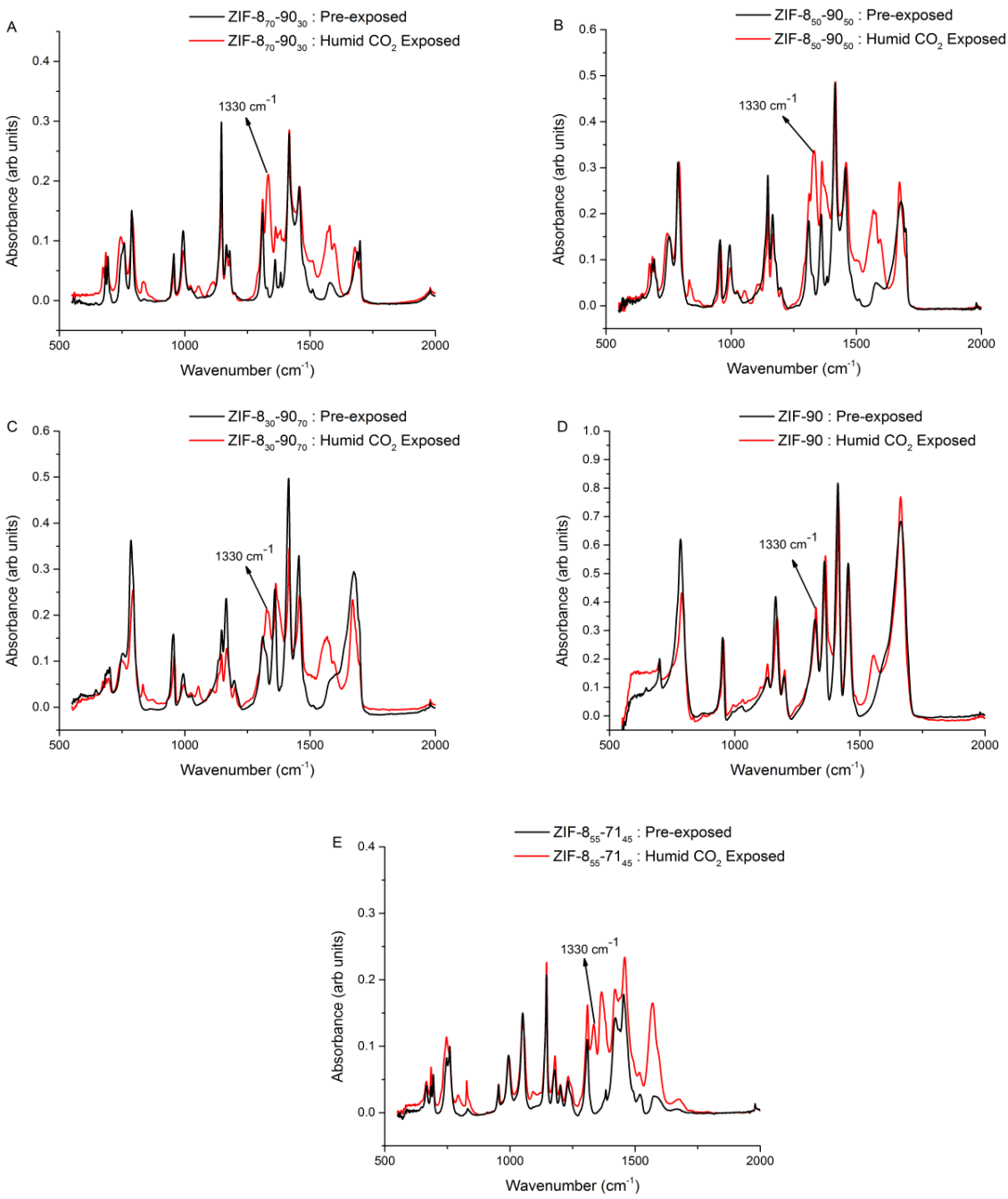

Figure A.7. FTIR spectra of A) ZIF-8$_{70}$-90$_{30}$, B) ZIF-8$_{50}$-90$_{50}$, C) ZIF-8$_{30}$-90$_{70}$, D) ZIF-90, and E) ZIF-8$_{55}$-71$_{45}$ before and after exposure to humid CO_2. The peak at 1330 cm^{-1} signifying complex carbonate formation is highlighted.

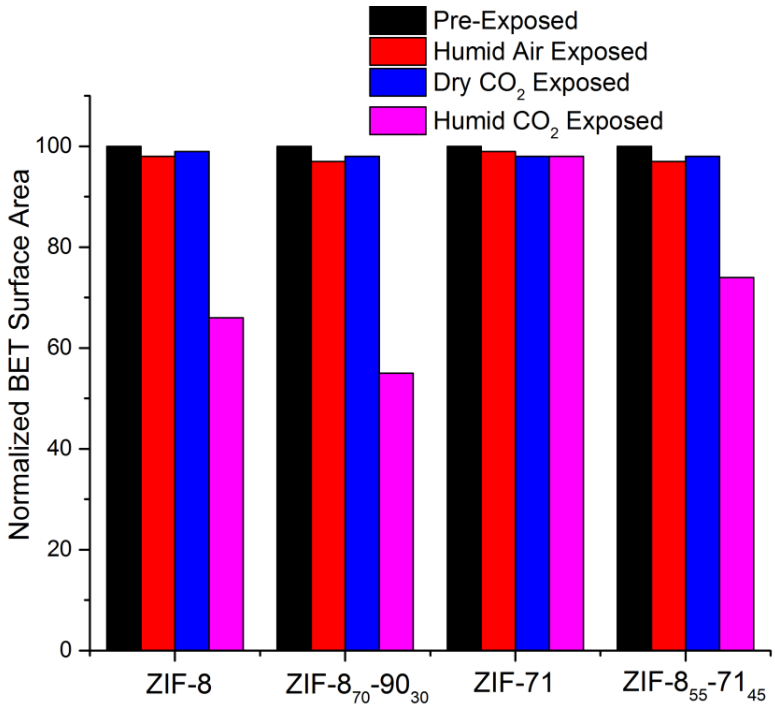

Figure A.8. Normalized BET surface areas of ZIF-8, ZIF-8_{70}-90_{30}, ZIF-71 and ZIF-8_{55}-71_{45} under different exposure conditions.

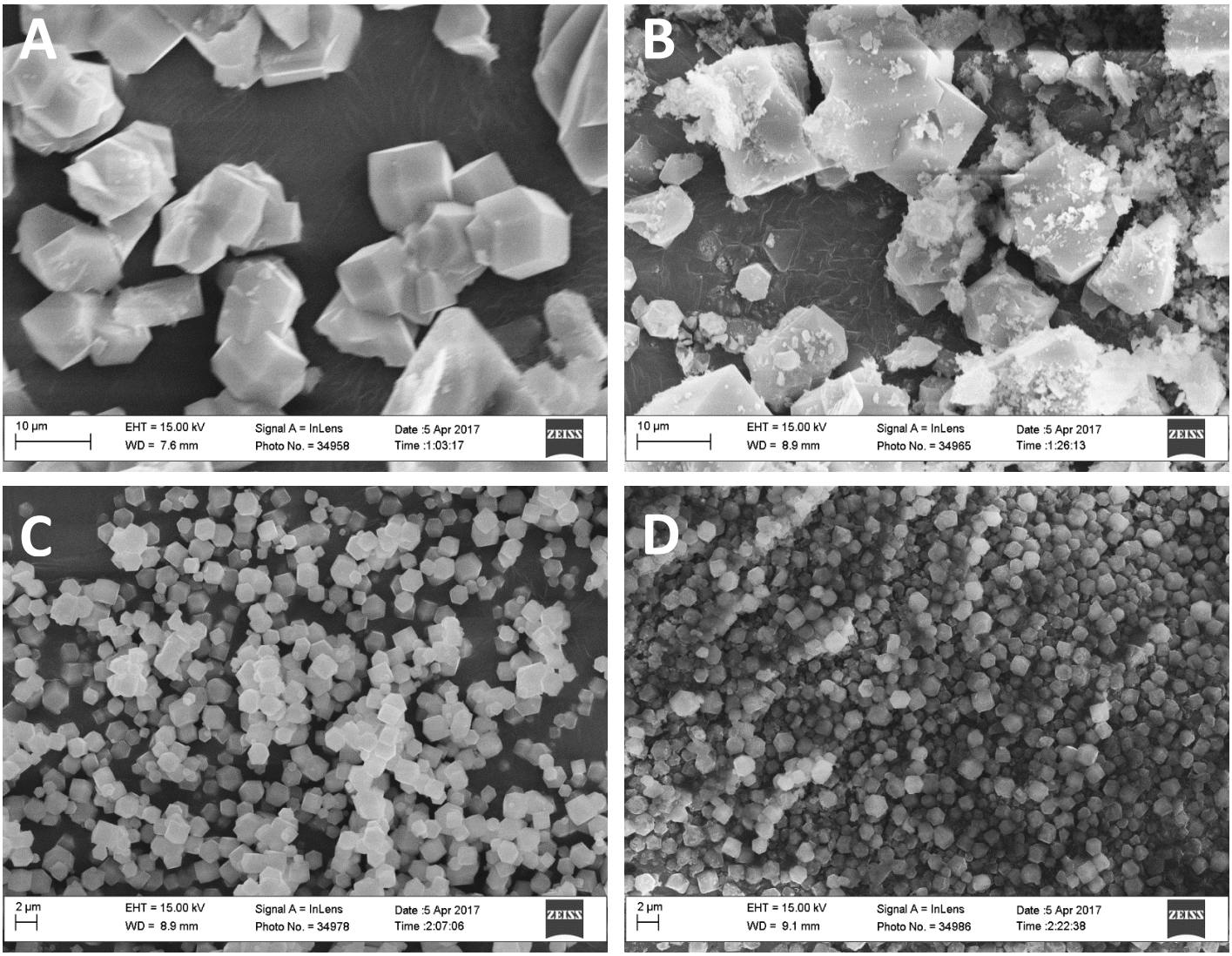

Figure A.9. SEM images of A) pre-exposed ZIF-8, B) 3.6 $\times 10^5$ ppm-days humid CO_2 exposed and reactivated ZIF-8, C) pre-exposed ZIF-71 and D) 3.6 $\times 10^5$ ppm-days humid CO_2 exposed and reactivated ZIF-71.

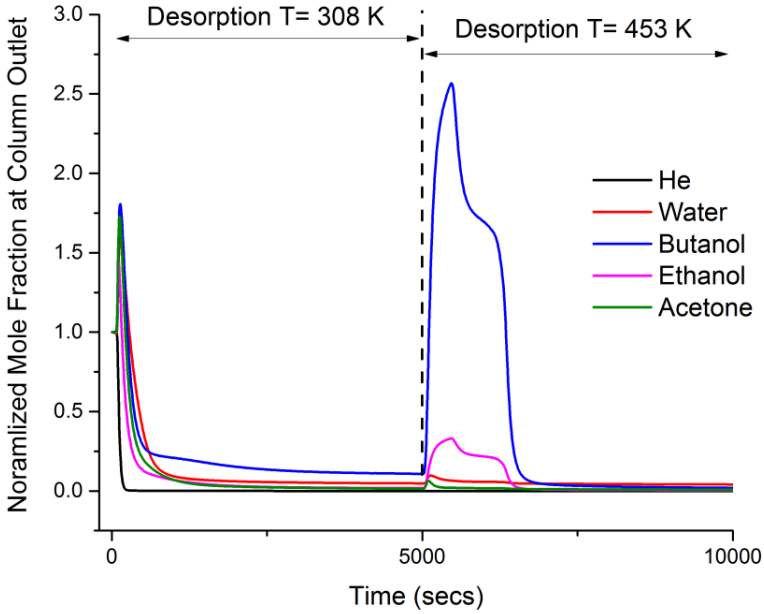

Figure A.10. Desorption profile of ZIF-71 sequentially at 308 K and 453 K after an ABE breakthrough run.

Table A.1. Advantages and challenges of various single-stage processes for butanol recovery in ABE fermentation

Separation Method	Advantages	Challenges
Gas stripping	Simplicity, low equipment cost, no toxicity	Low selectivity, foaming
Liquid-liquid extraction	High selectivity	Emulsion formation, extractant cost, toxicity to cells, high post-purification cost
Adsorption	Low energy costs, moderate selectivity	Material cost, adsorbent stability and biocompatibility, fouling, desorption
Pervaporation	High selectivity	Material cost, membrane stability and biocompatibility, fouling

Table A.2. Amounts of reagents used to synthesize mixed-linker ZIF-8_x-90_{100-x}.

Reagent	**ZIF-8_{70}-90_{30}**	**ZIF-8_{50}-90_{50}**	**ZIF-8_{30}-90_{70}**
$Zn(NO_3)_2.6H_2O$	2.974 g	2.974 g	2.974 g
2-methylimidazole	3.072 g	2.874 g	2.464 g
Imidazole-2-carboxaldehyde	0.252 g	0.480 g	0.962 g
Sodium formate	2.72 g	2.72 g	2.72 g

Table A.3. Vapor phase pressure, mole fractions and activity coefficients of butanol and water as calculated using the Mixture Property Predictor of the Dortmund Databank Software and Separation Technology (DDBST).

Total pressure (KPa)	Butanol liquid mole fraction	Butanol Activity Coefficient	Butanol vapor mole fraction	Water liquid mole fraction	Water Activity Coefficient	Water vapor mole fraction	Gas stripping separation factor
6.3	0.01	38.85	0.1127	0.99	1.001	0.8873	12.57

The gas stripping separation factor for butanol is defined as:

$$\alpha = \frac{\frac{y}{1-y}}{\frac{x}{1-x}}$$

where y is the mole fraction of butanol in the vapor phase and x is the mole fraction of butanol in the liquid phase.

Table A.4. Salient properties of the model ABE mixture components.

Component	Vapor Pressure at 308.15 K (kPa)	Boiling Point (K)
1-Butanol	1.827	390.2
Acetone	46.253	329.7
Ethanol	13.72	351.6
Water	5.639	373.2

Table A.5. Vapor phase pressure and mole fractions of butanol, acetone, ethanol and water as calculated using the Mixture Property Predictor of the Dortmund Databank Software and Separation Technology (DDBST). A= Acetone, B= 1-Butanol, E= Ethanol and W=Water.

Gas stripping separation factor	Total Pressure (KPa)	Liquid Phase Mole Fractions (A/B/E/W)	Activity Coefficients (A/B/E/W)	Vapor Phase Mole Fractions (A/B/E/W)
7.45	8.858	0.006/ 0.01/ 0.0025/ 0.9815/	8.94/ 34.06/ 5.88/ 1.0	0.28/ 0.0703/ 0.0228/ 0.6268

Table A.6. Comparison of BET surface areas and pore volumes of the adsorbents after activation.

Adsorbent	BET Surface Area (m^2/g)	Pore Volume (cm^3/g)
ZIF-8	1380	0.61
ZIF-8_{70}-90_{30}	1310	0.61
ZIF-8_{50}-90_{50}	1350	0.61
ZIF-8_{30}-90_{70}	1250	0.55
ZIF-90	1000	0.48
ZIF-71	850	0.34
ZIF-8_{55}-71_{45}	630	0.29

Table A.7. Experimental butanol and water loadings and butanol/water adsorption selectivities during binary breakthrough from a 11:89 butanol/water vapor mixture carried by a 90:10 N_2/He inert gas stream. IAST-predicted selectivities are shown for comparison.

Adsorbent	Butanol Loading (mmol/g)	Water loading (mmol/g)	Butanol/Water Selectivity (Experimental)	Butanol/Water Selectivity (IAST)
ZIF-8	4.0 ± 0.2	1.7 ± 0.6	21 ± 5	668
ZIF-8_{70}-90_{30}	4.3 ± 0.2	2.5 ± 0.8	15 ± 4	128
ZIF-8_{50}-90_{50}	4.1 ± 0.3	3.4 ± 0.5	10 ± 2	7
ZIF-8_{30}-90_{70}	3.9 ± 0.4	5.7 ± 0.5	5 ± 1	6
ZIF-90	3.0 ± 0.2	9.9 ± 1.8	2 ± 0	4
ZIF-71	3.7 ± 0.2	2.8 ± 0.8	11 ± 3	603
ZIF-8_{55}-71_{45}	3.4 ± 0.3	1.4 ± 0.3	17 ± 3	528

Table A.8. Adsorbate loadings and butanol/water adsorption selectivity of ZIF-71 upon breakthrough of a CO_2-enriched gas (12% CO_2/12% N_2/76% He) sparged through a 1% butanol in water solution at 308 K and 1 bar. The butanol/water ratio in the feed vapor-gas mixture is 11:89 as shown in Table A.3.

Adsorbent	Butanol Loading (mmol/g)	Water loading (mmol/g)	Butanol/Water Adsorption Selectivity (Experimental)
ZIF-71	3.2 ± 0.2	3.3± 0.2	8 ± 2

Table A.9. Adsorbate loadings and butanol/water adsorption selectivity of ZIF-71 upon breakthrough of a CO_2-enriched gas (12% CO_2/12% N_2/76% He) sparged through a dilute ABE model solution containing 1 mol% butanol, 0.6 mol% acetone and 0.25 mol % ethanol at 308 K and 1 bar. The composition of organics and water in the feed vapor-gas mixture remains as shown in Table A.5.

Butanol Loading (mmol/g)	**Water/Ethanol/Acetone loadings (mmol/g)**	**Butanol Adsorption Selectivity over Water/Acetone/Ethanol**	**Butanol/All Adsorption Selectivity**
3.1 ± 0.1	3.3 ± 0.2 / 0.34 ± 0.2 / 2.6 ± 0.1	7 ± 2 / 4 ± 1 / 3 ± 1	6 ± 1

APPENDIX B. SUPPORTING INFORMATION (CHAPTER 4)

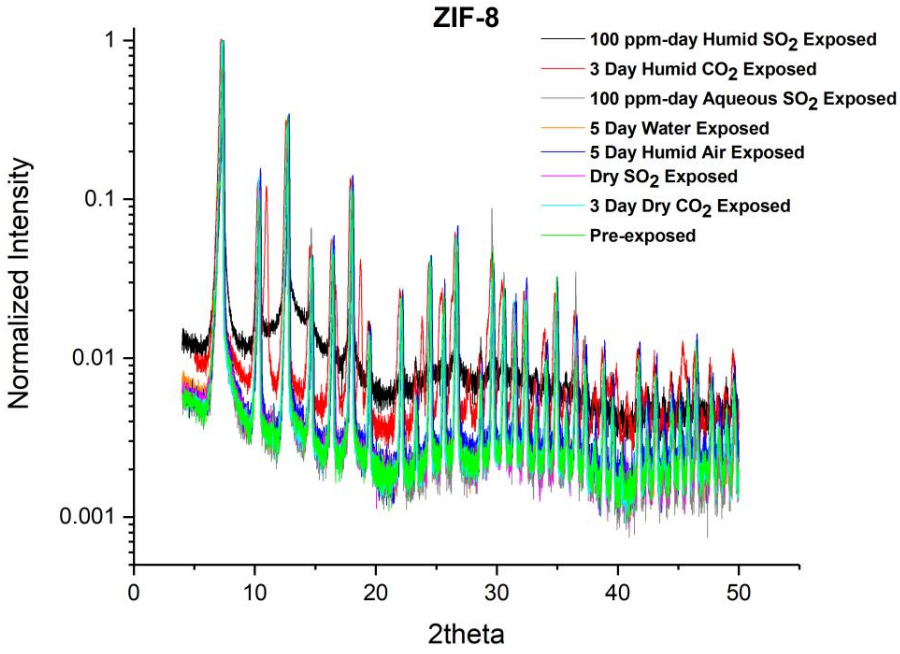

Figure B.1. PXRD patterns of ZIF-8 under different exposure conditions.

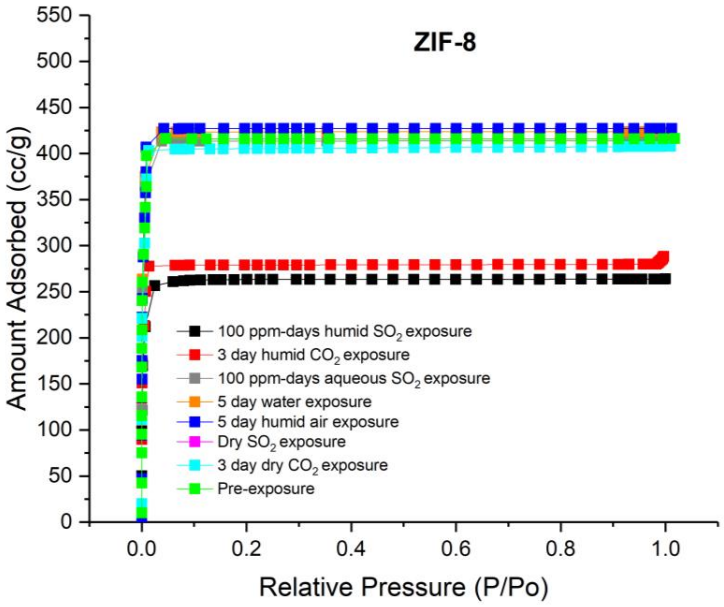

Figure B.2. N_2 physisorption at 77 K in ZIF-8 under different exposure conditions.

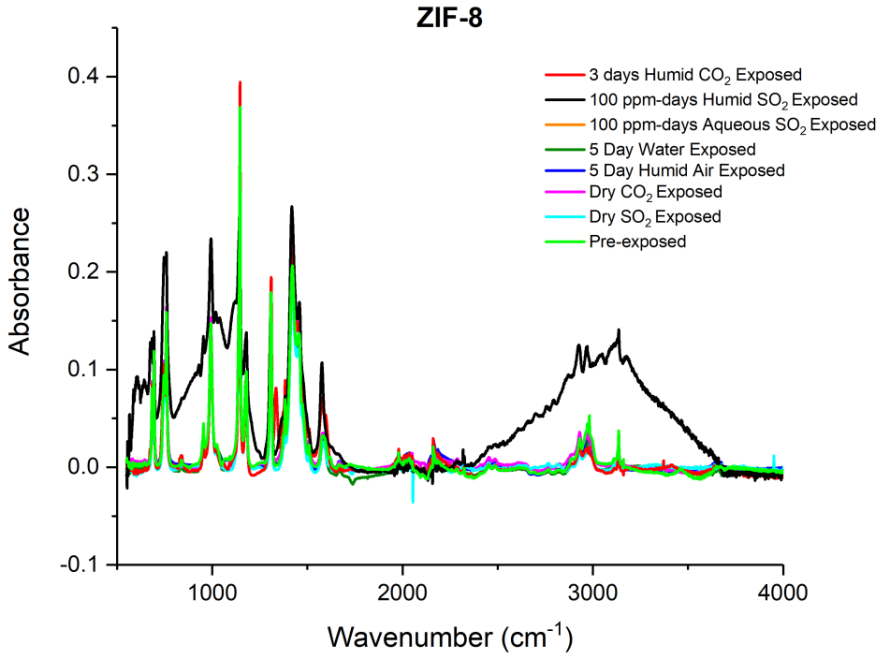

Figure B.3. FTIR spectra of ZIF-8 under different exposure conditions.

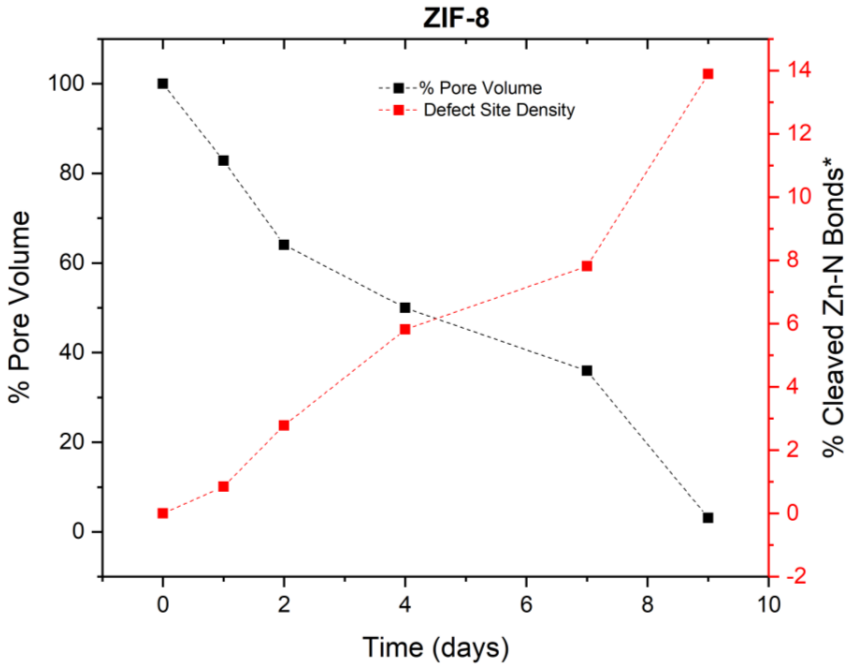

Figure B.4. Degradation kinetics of ZIF-8 showing the decrease in pore volume over time and the corresponding increase in defect sites (cleaved Zn-N bonds). Dotted lines are for visual aid.*Cleaved Zn-N bonds were calculated from the experimental Zn:S ratio assuming that one S atom incorporation led to one Zn-N bond cleavage.

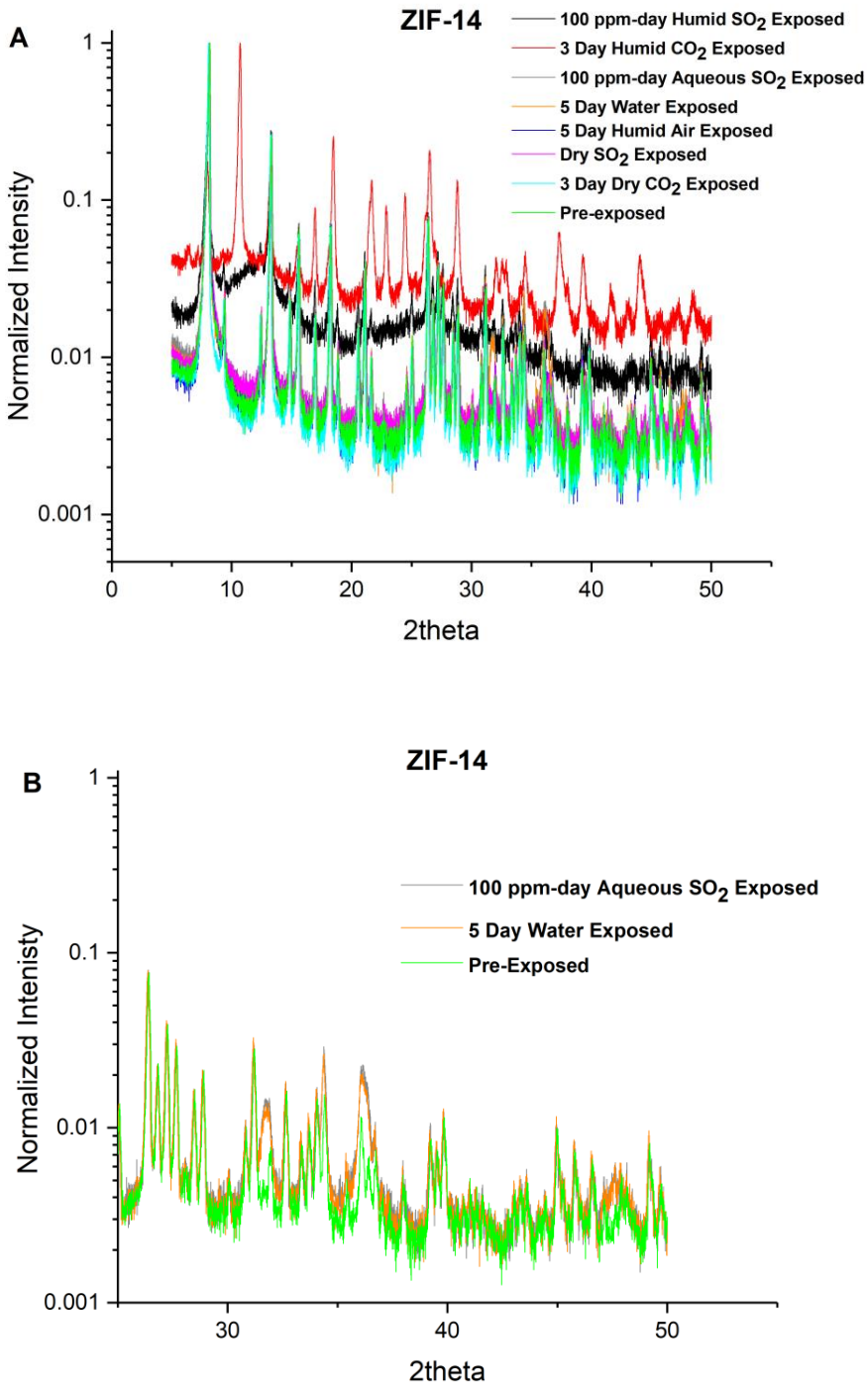

Figure B.5. PXRD patterns of ZIF-14 under different exposure conditions.

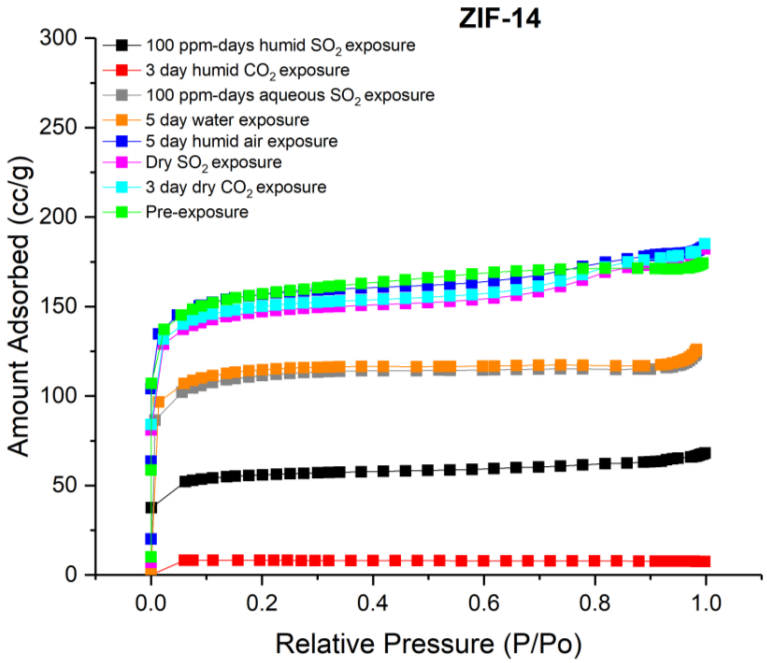

Figure B.6. N_2 physisorption at 77 K in ZIF-14 under different exposure conditions.

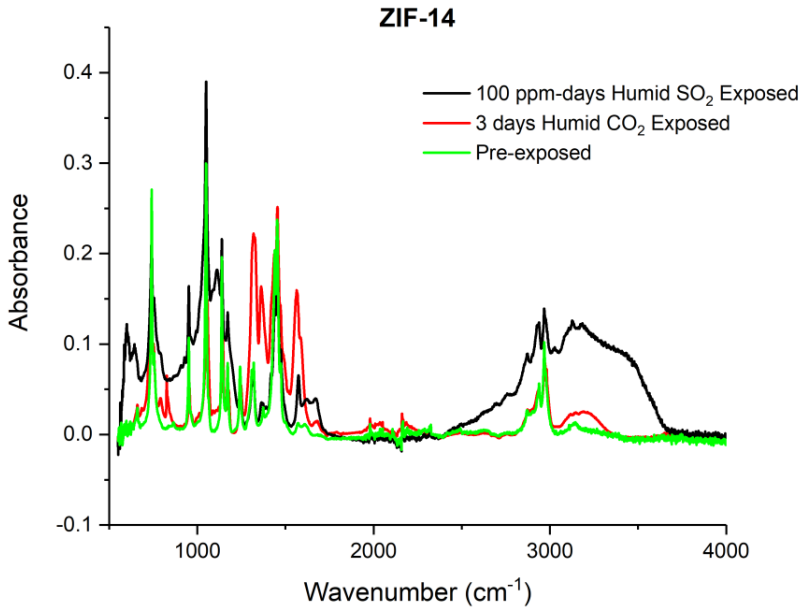

Figure B.7. FTIR spectra of ZIF-14 under different exposure conditions.

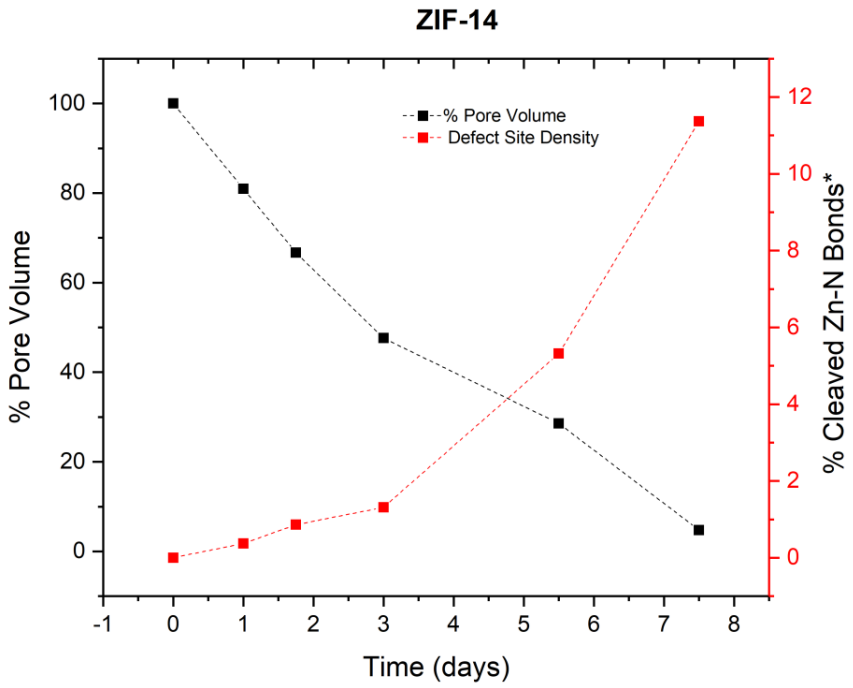

Figure B.8. Degradation kinetics of ZIF-14 showing the decrease in pore volume over time and the corresponding increase in defect sites (cleaved Zn-N bonds). Dotted lines are for visual aid. *Cleaved Zn-N bonds were calculated from the experimental Zn:S ratio assuming that one S atom incorporation led to one Zn-N bond cleavage.

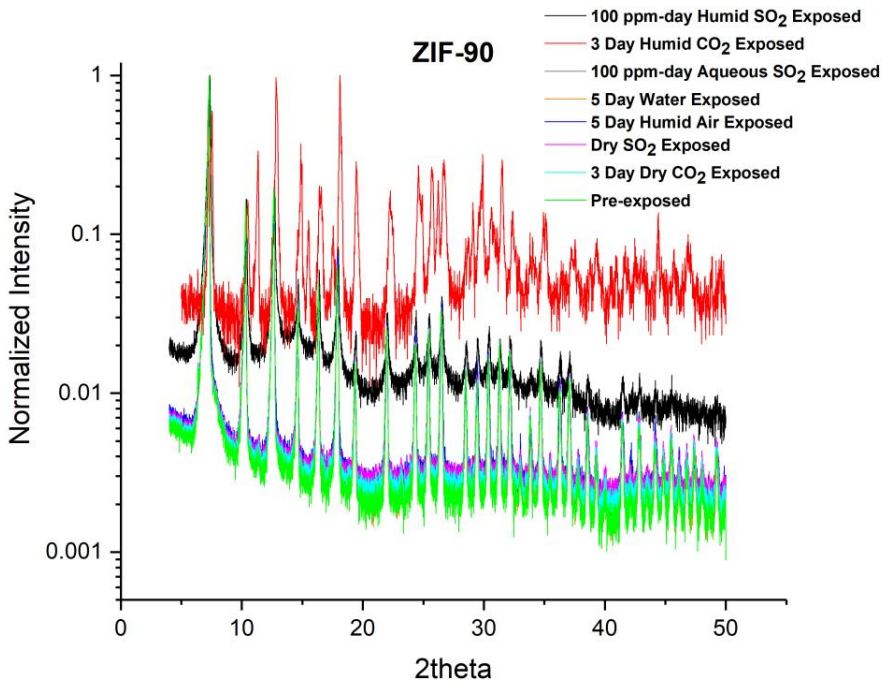

Figure B.9. PXRD patterns of ZIF-90 under different exposure conditions.

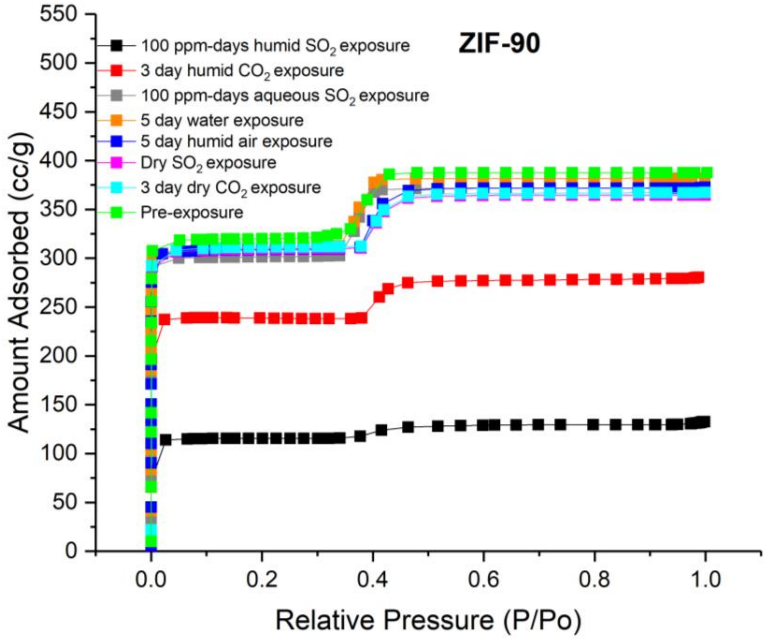

Figure B.10. N_2 physisorption at 77 K in ZIF-90 under different exposure conditions.

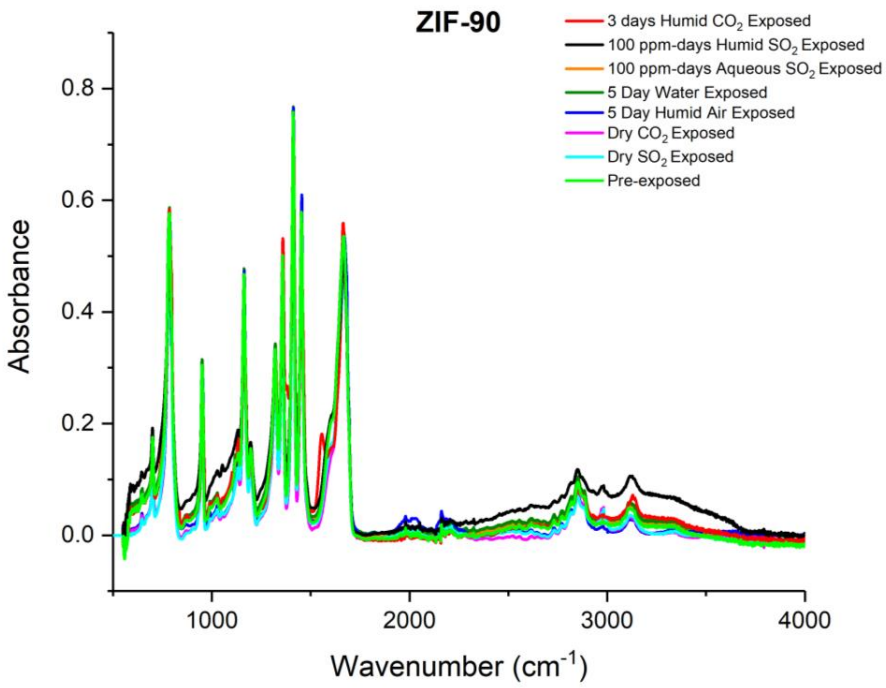

Figure B.11. FTIR spectra of ZIF-90 under different exposure conditions.

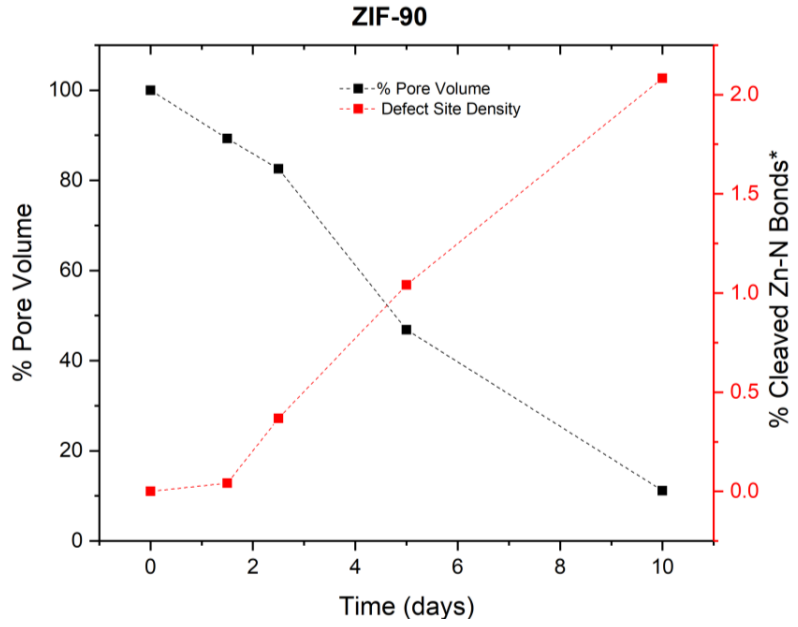

Figure B.12. Degradation kinetics of ZIF-90 showing the decrease in pore volume over time and the corresponding increase in defect sites (cleaved Zn-N bonds). Dotted lines are for visual aid. *Cleaved Zn-N bonds were calculated from the experimental Zn:S ratio assuming that one S atom incorporation led to one Zn-N bond cleavage.

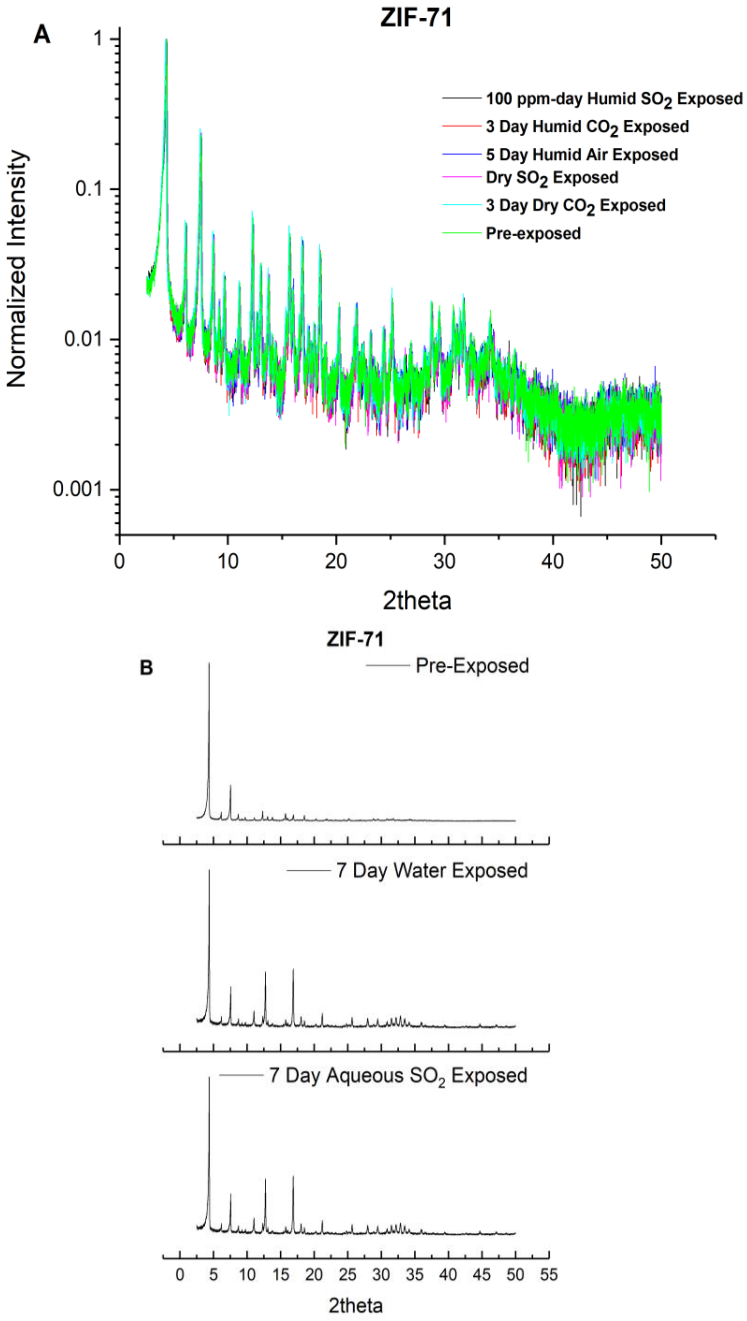

Figure B.13. PXRD patterns of ZIF-71 under different exposure conditions.

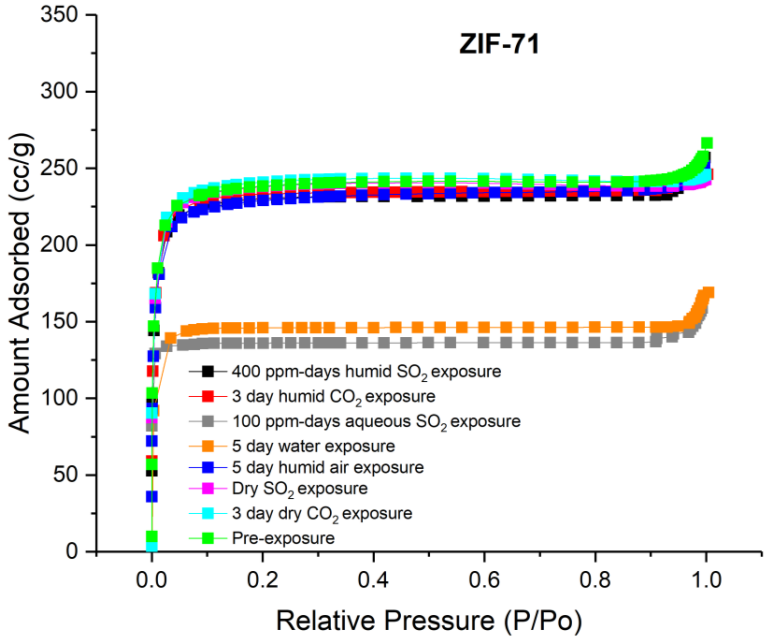

Figure B.14. N_2 physisorption at 77 K in ZIF-71 under different exposure conditions.

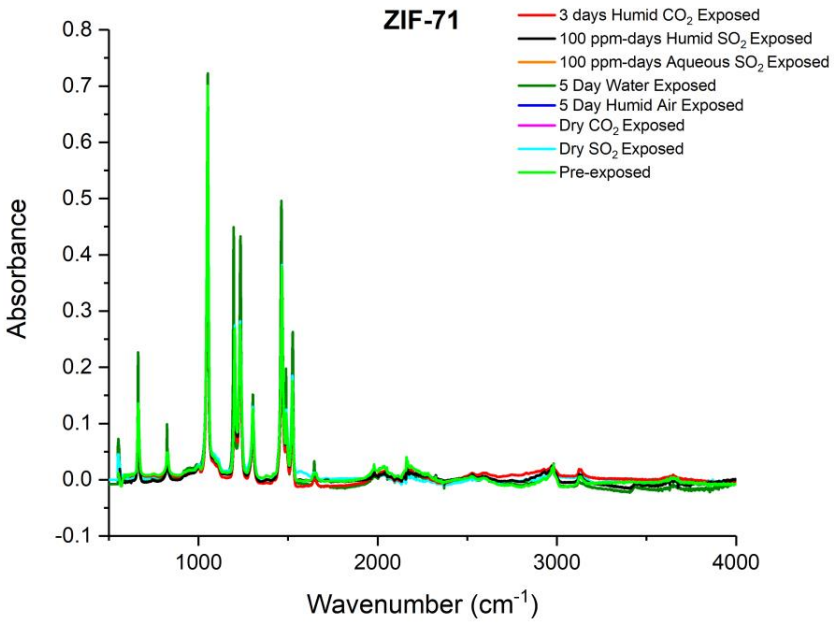

Figure B.15. FTIR spectra of ZIF-71 under different exposure conditions.

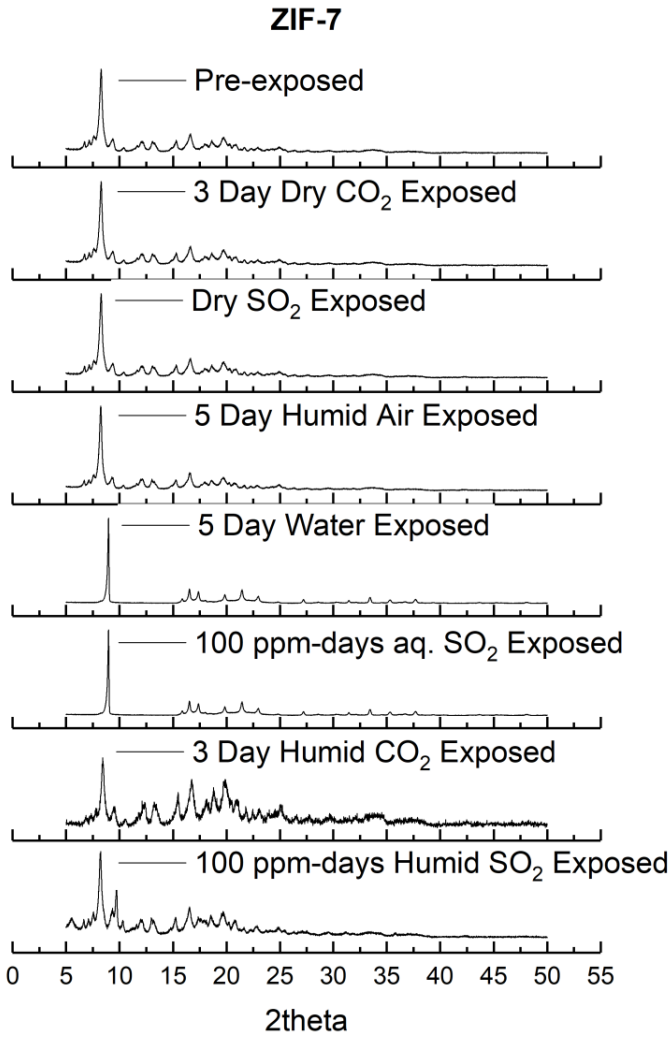

Figure B.16. PXRD patterns of ZIF-7 under different exposure conditions.

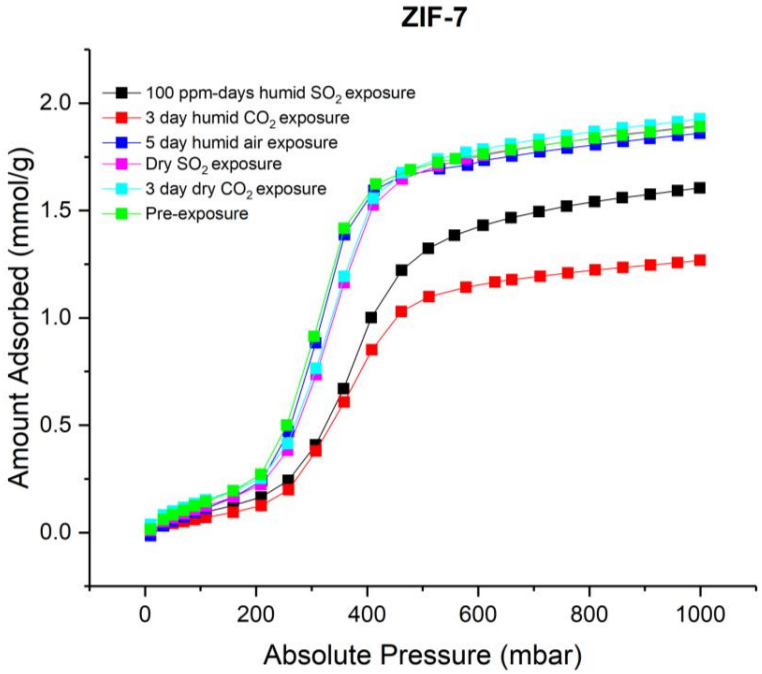

Figure B.17. CO_2 physisorption at 273 K in ZIF-7 under different exposure conditions.

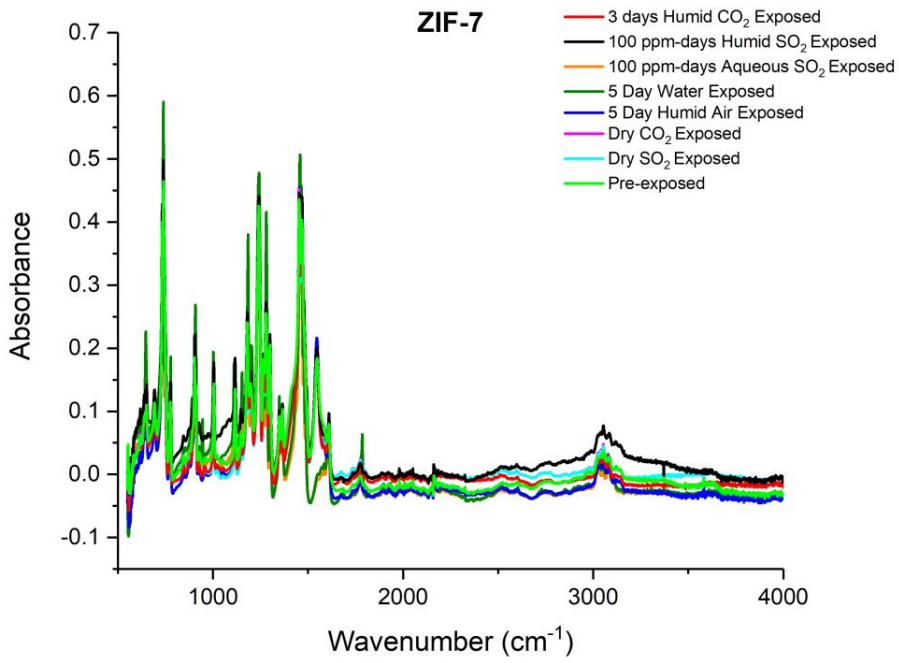

Figure B.18. FTIR spectra of ZIF-7 under different exposure conditions.

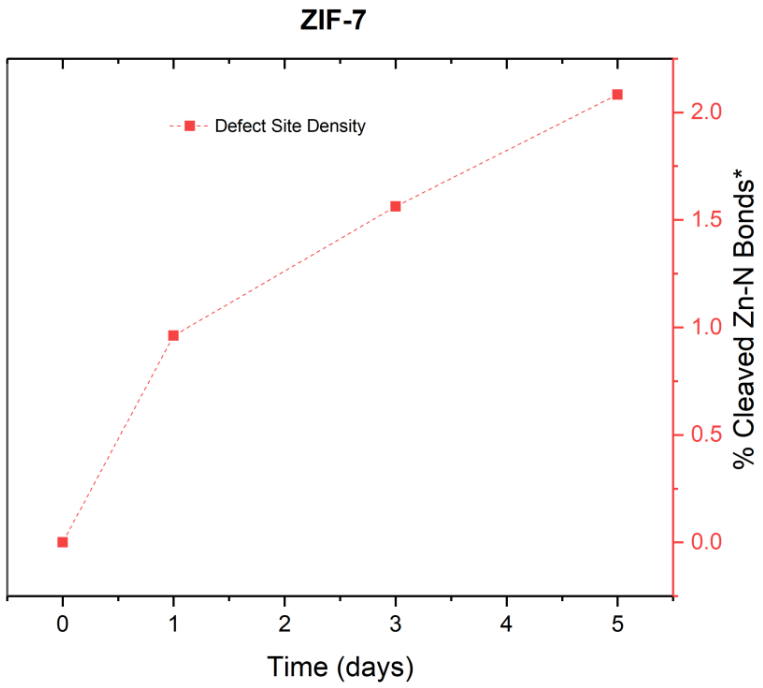

Figure B.19. Degradation kinetics of ZIF-7 showing the increase in defect sites with time (cleaved Zn-N bonds). Dotted lines are for visual aid.*Cleaved Zn-N bonds were calculated from the experimental Zn:S ratio assuming that one S atom incorporation led to one Zn-N bond cleavage.

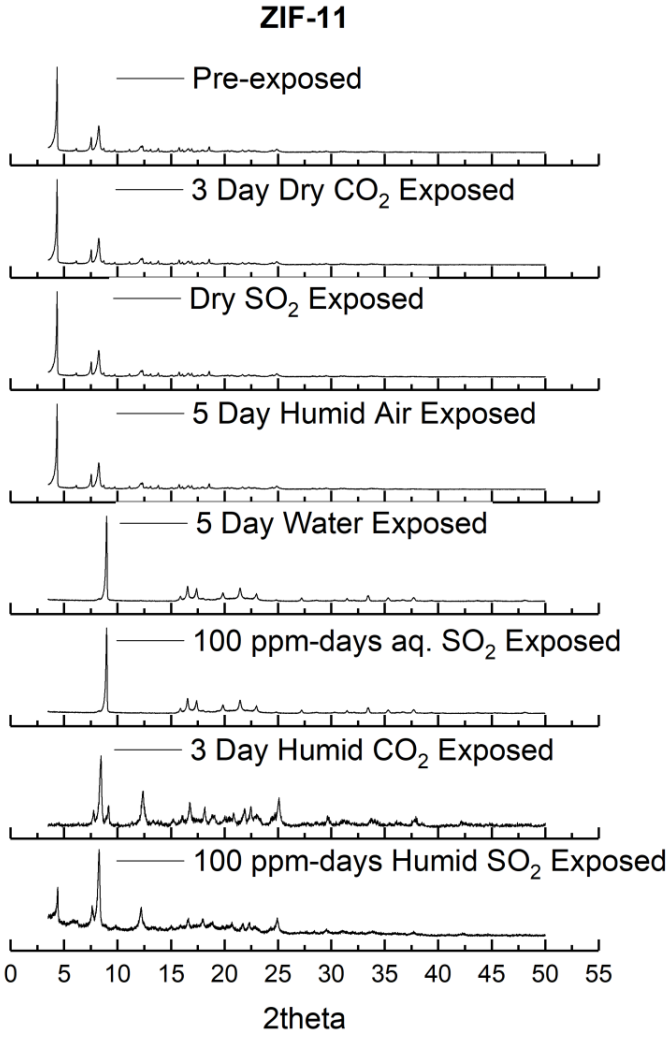

Figure B.20. PXRD patterns of ZIF-11 under different exposure conditions.

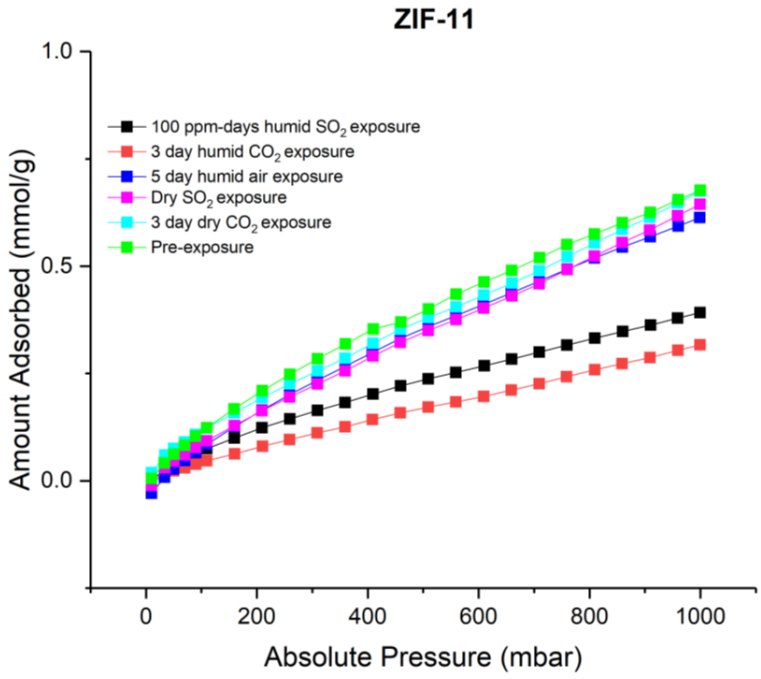

Figure B.21. CO_2 physisorption at 273 K in ZIF-11 under different exposure conditions.

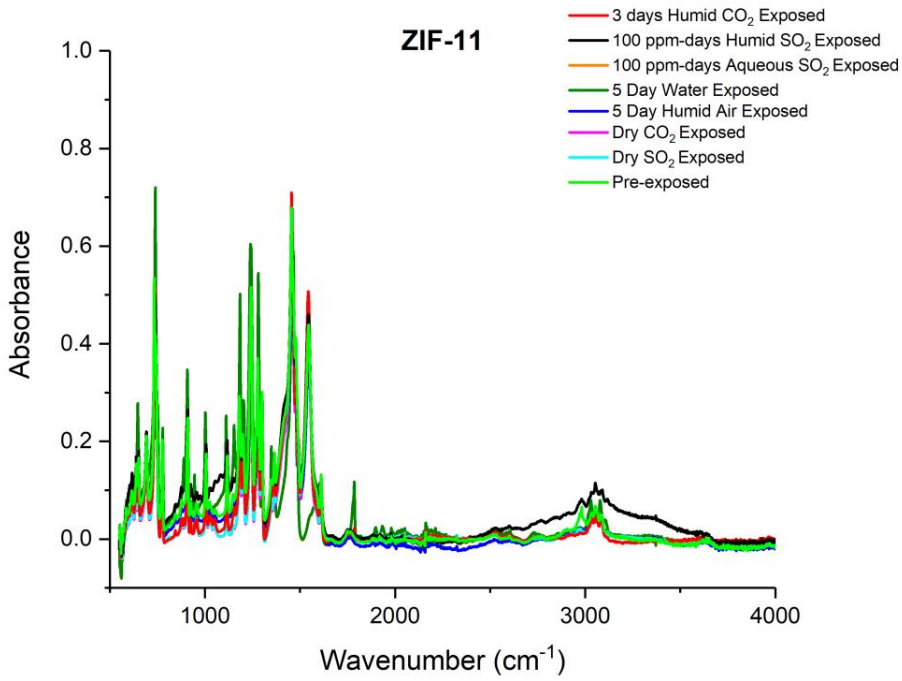

Figure B.22. FTIR spectra of ZIF-11 under different exposure conditions.

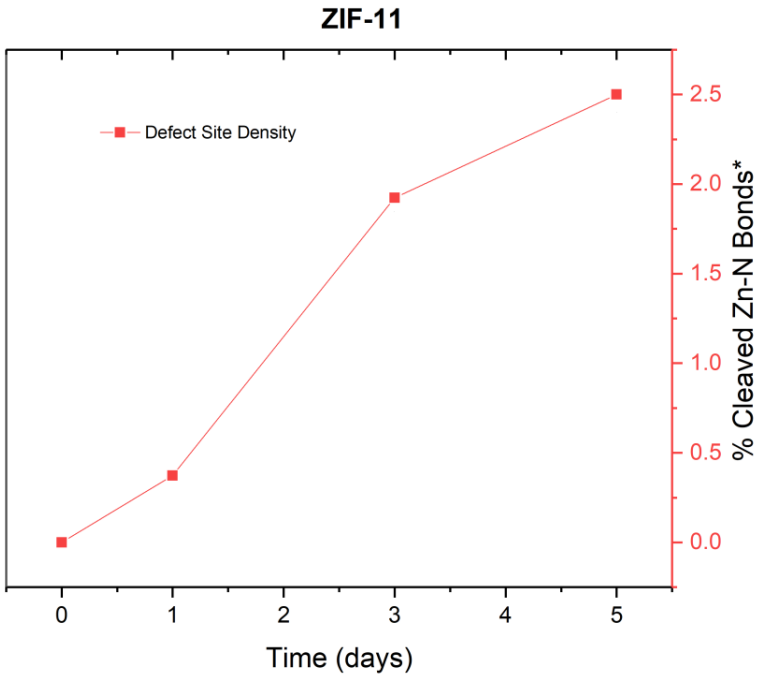

Figure B.23. Degradation kinetics of ZIF-11 showing the increase in defect sites with time (cleaved Zn-N bonds). Dotted lines are for visual aid.*Cleaved Zn-N bonds were calculated from the experimental Zn:S ratio assuming that one S atom incorporation led to one Zn-N bond cleavage.

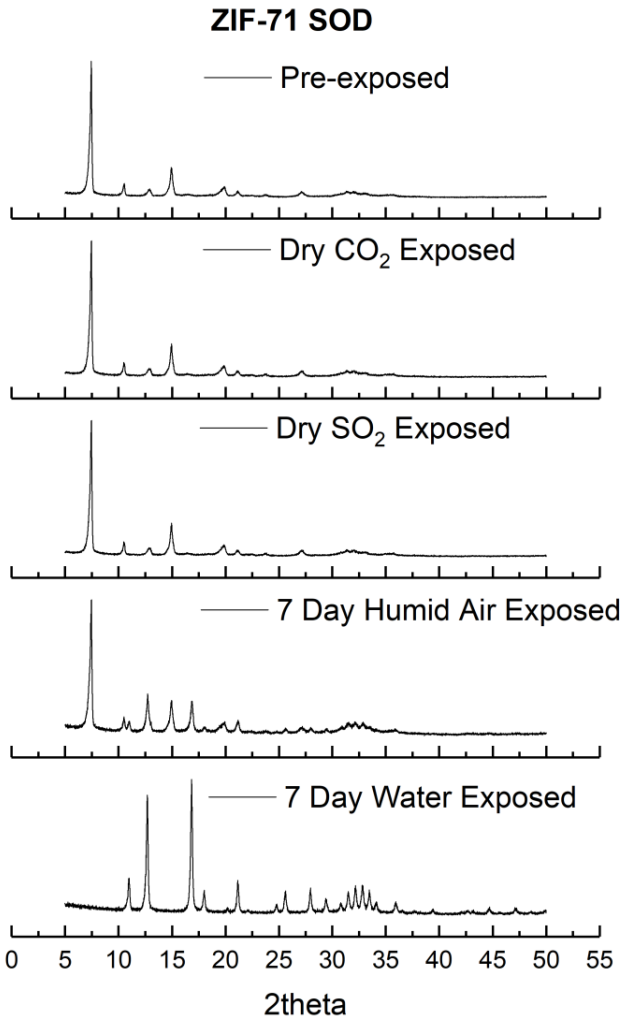

Figure B.24. PXRD patterns of ZIF-71 (SOD) under different exposure conditions.

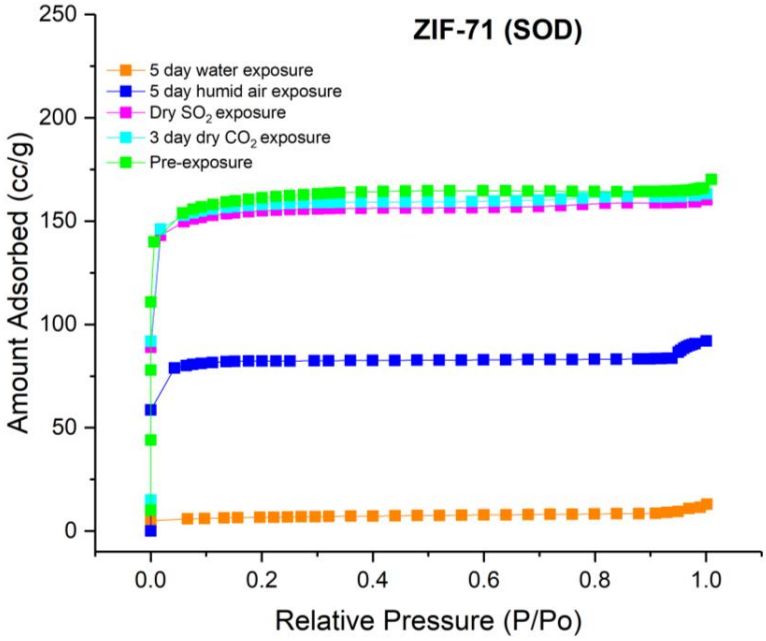

Figure B.25. N_2 physisorption at 77 K in ZIF-71 (SOD) under different exposure conditions.

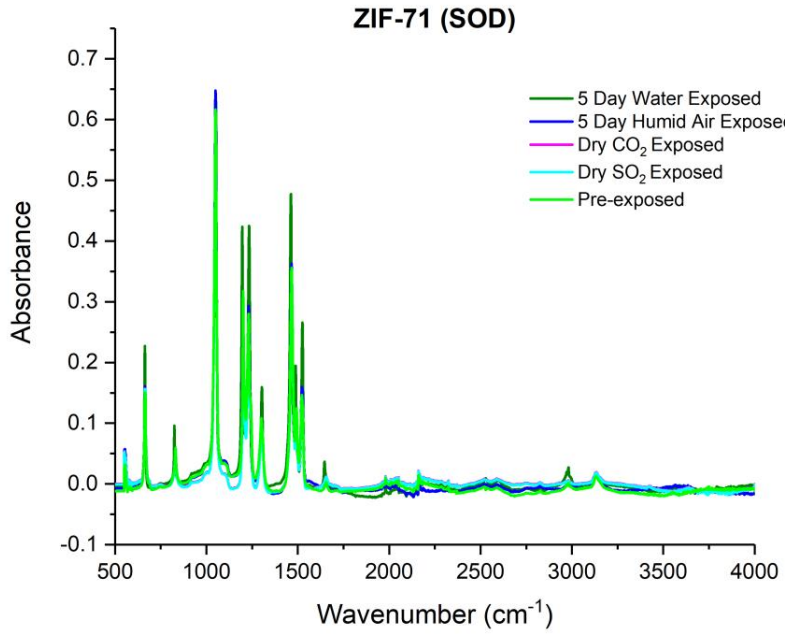

Figure B.26. FTIR spectra of ZIF-71 (SOD) under different exposure conditions.

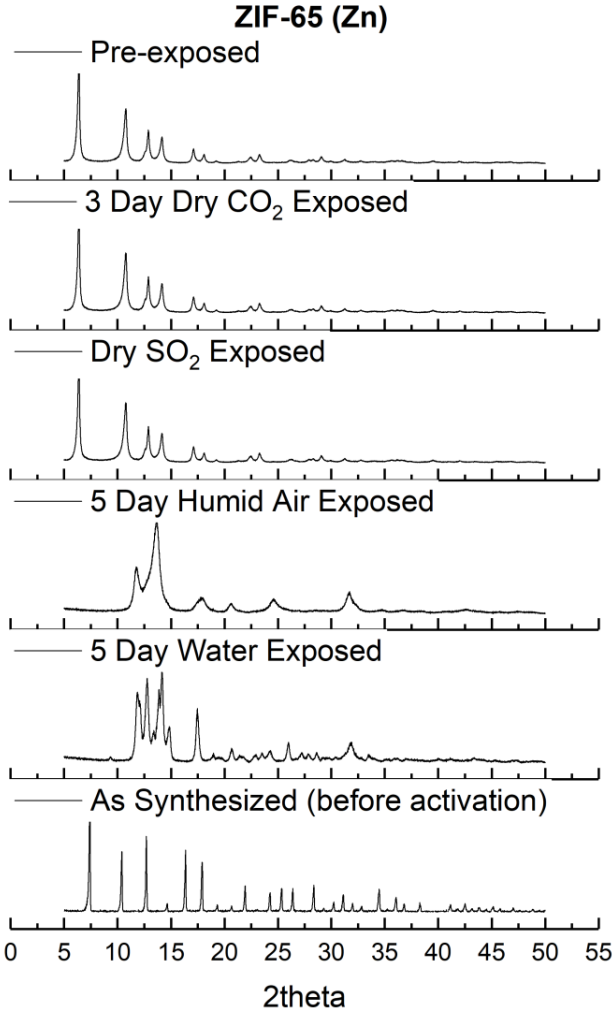

Figure B.27. PXRD patterns of ZIF-65(Zn) under different exposure conditions.

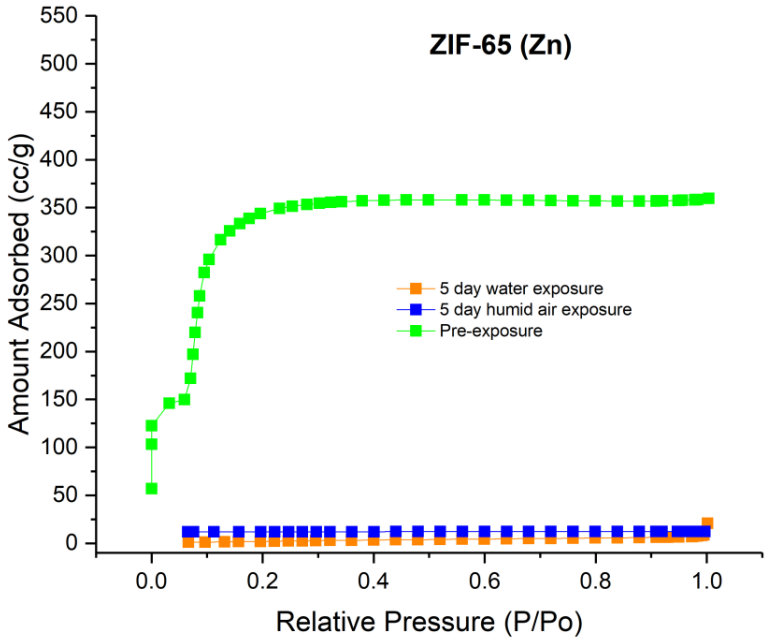

Figure B.28. N_2 physisorption at 77 K in ZIF-65(Zn) under different exposure conditions.

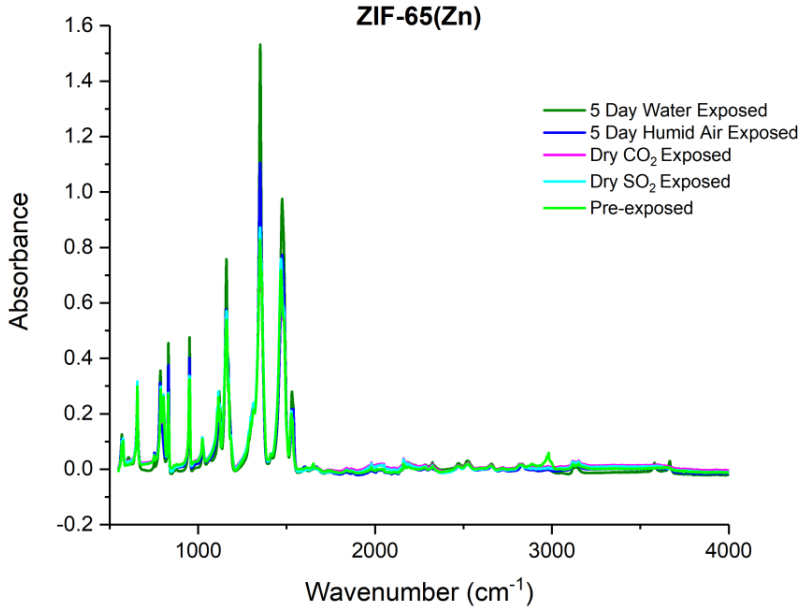

Figure B.29. FTIR spectra of ZIF-65 (Zn) under different exposure conditions.

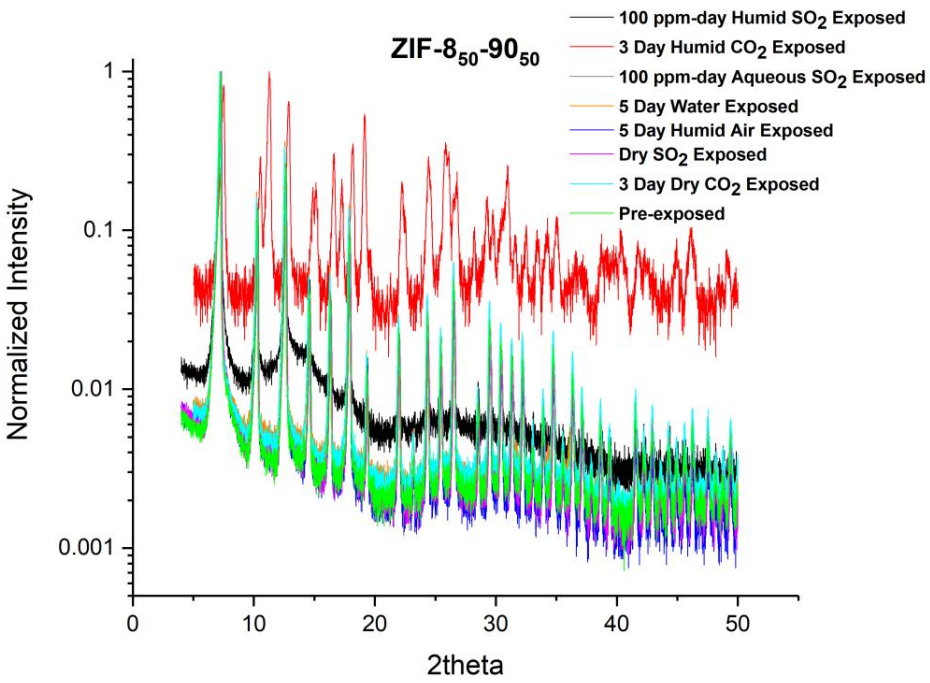

Figure B.30. PXRD patterns of ZIF-8$_{50}$-90$_{50}$ under different exposure conditions.

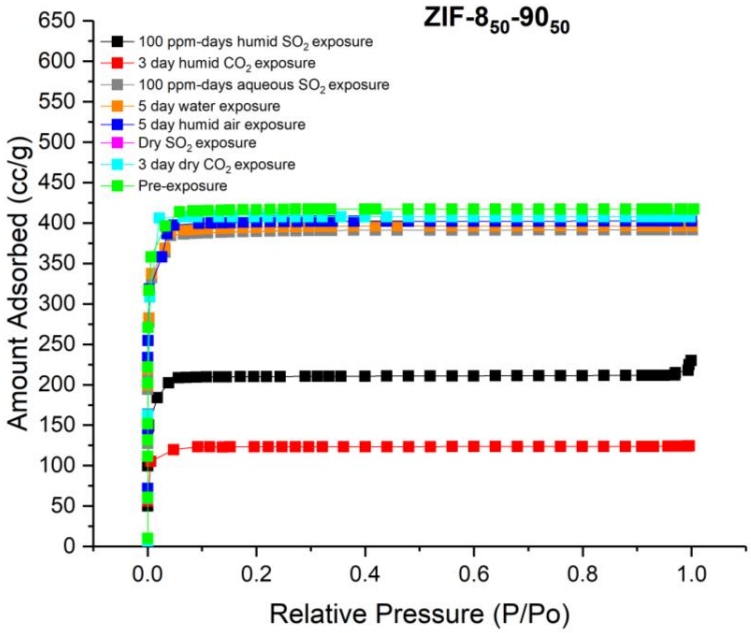

Figure B.31. N_2 physisorption at 77 K in ZIF-8$_{50}$-90$_{50}$ under different exposure conditions.

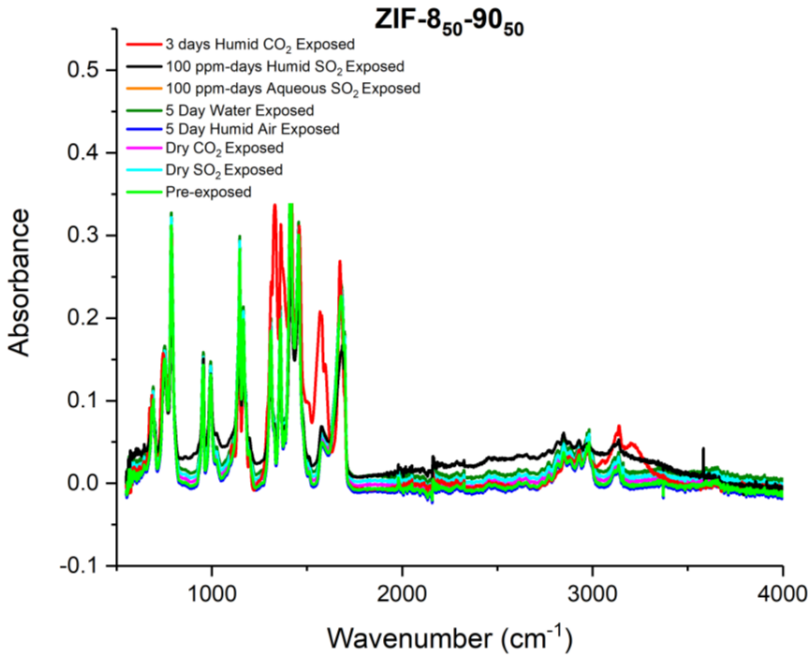

Figure B.32. FTIR spectra of ZIF-8$_{50}$-90$_{50}$ under different exposure conditions.

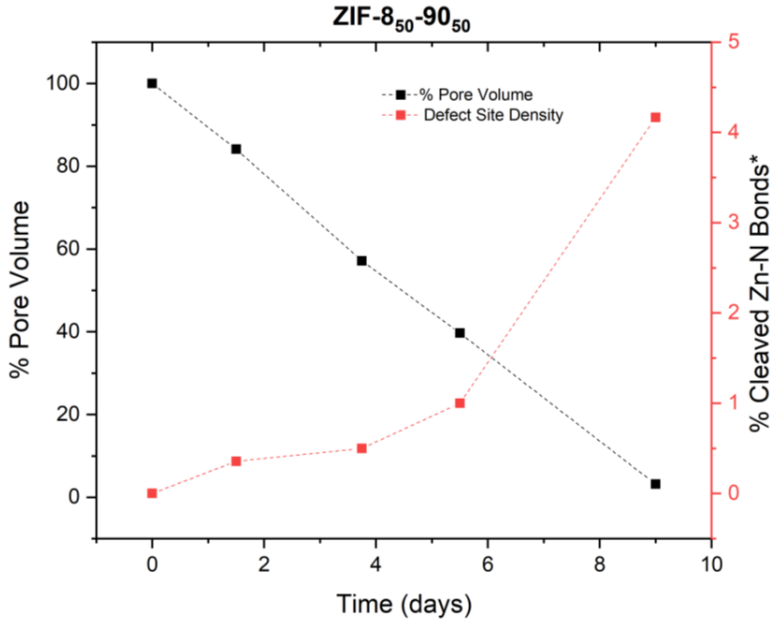

Figure B.33. Degradation kinetics of ZIF-8$_{50}$-90$_{50}$ showing the decrease in pore volume over time and the corresponding increase in defect sites (cleaved Zn-N bonds). Dotted lines are for visual aid.*Cleaved Zn-N bonds were calculated from the experimental Zn:S ratio assuming that one S atom incorporation led to one Zn-N bond cleavage.

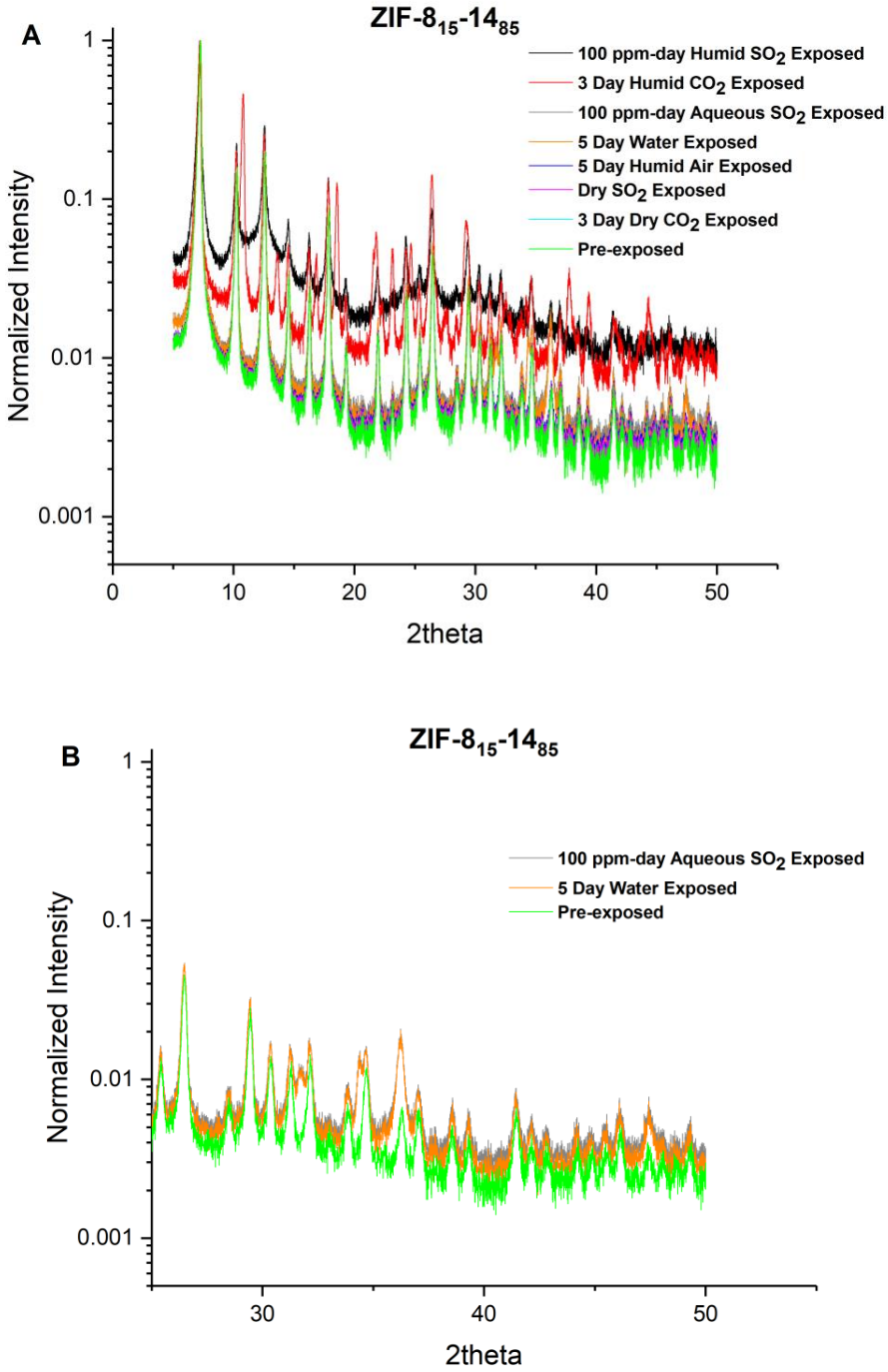

Figure B.34. PXRD patterns of ZIF-8_{15}-14_{85} under different exposure conditions.

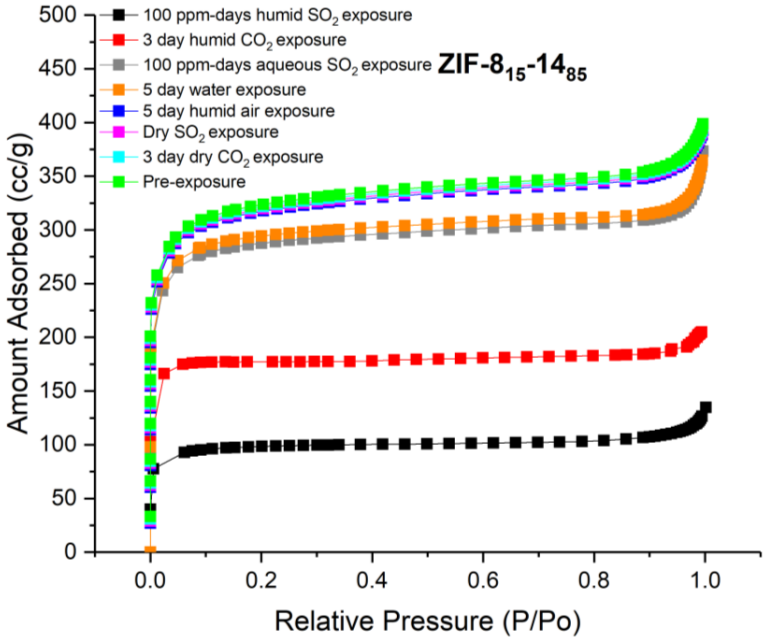

Figure B.35. N_2 physisorption at 77 K in ZIF-8_{15}-14_{85} under different exposure conditions.

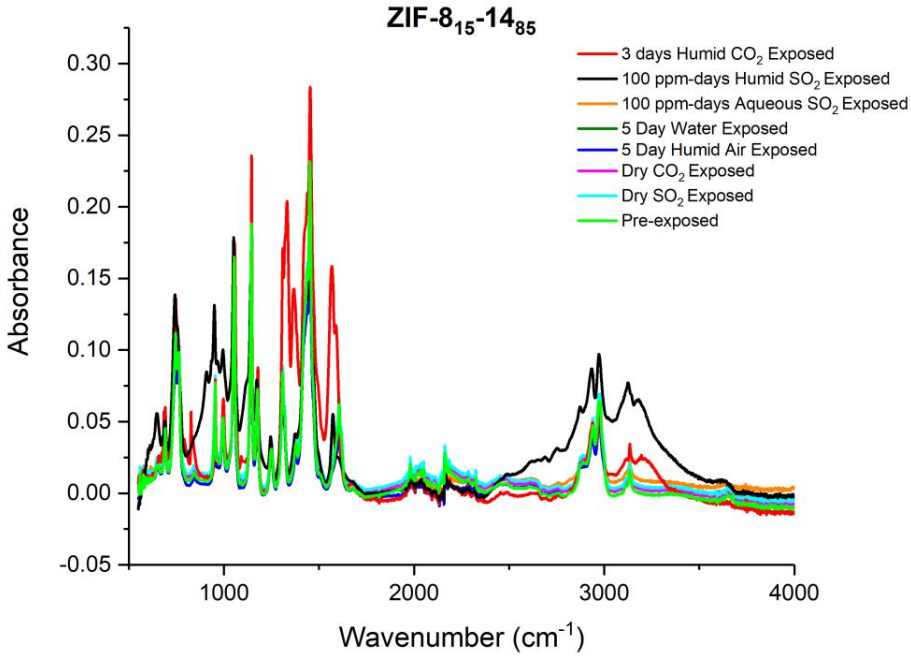

Figure B.36. FTIR spectra of ZIF-8_{15}-14_{85} under different exposure conditions.

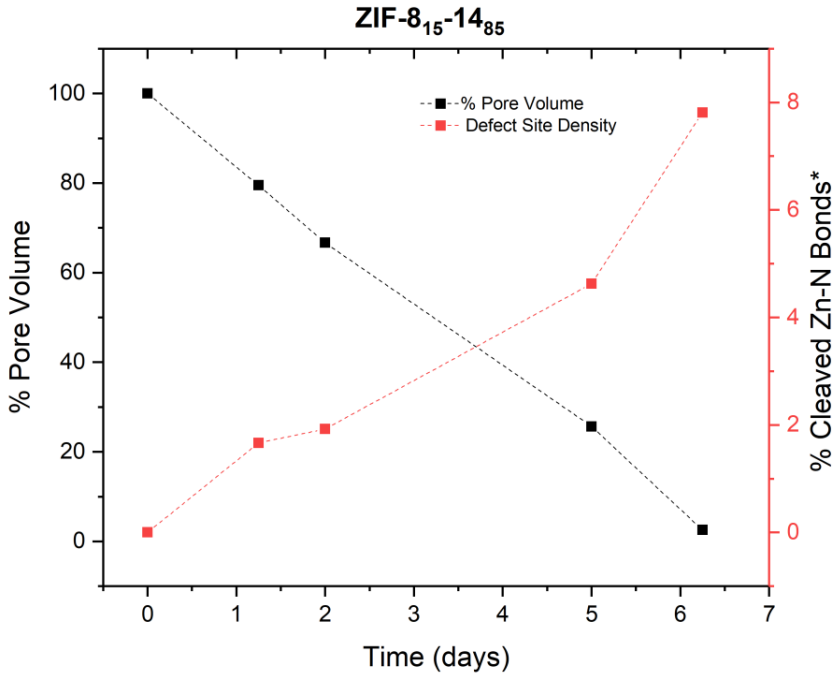

Figure B.37. Degradation kinetics of ZIF-8_{15}-14_{85} showing the decrease in pore volume over time and the corresponding increase in defect sites (cleaved Zn-N bonds). Dotted lines are for visual aid.*Cleaved Zn-N bonds were calculated from the experimental Zn:S ratio assuming that one S atom incorporation led to one Zn-N bond cleavage.

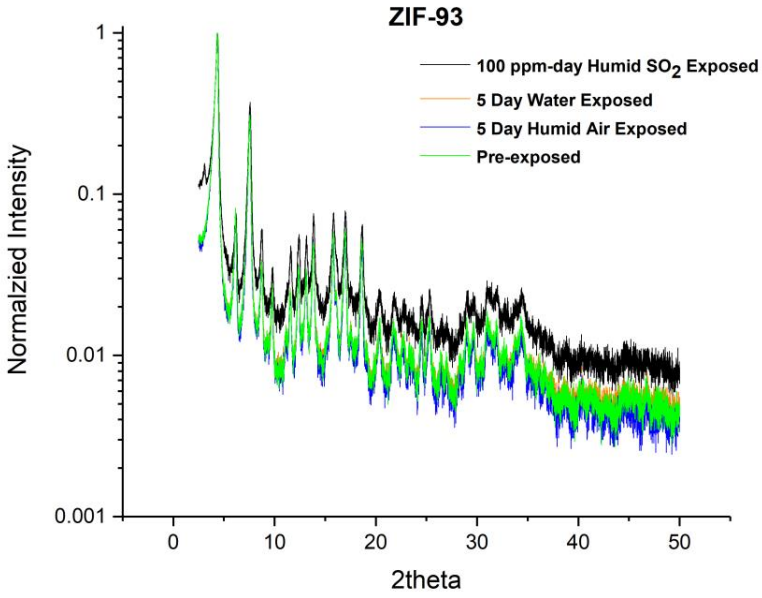

Figure B.38. PXRD patterns of ZIF-93 under different exposure conditions.

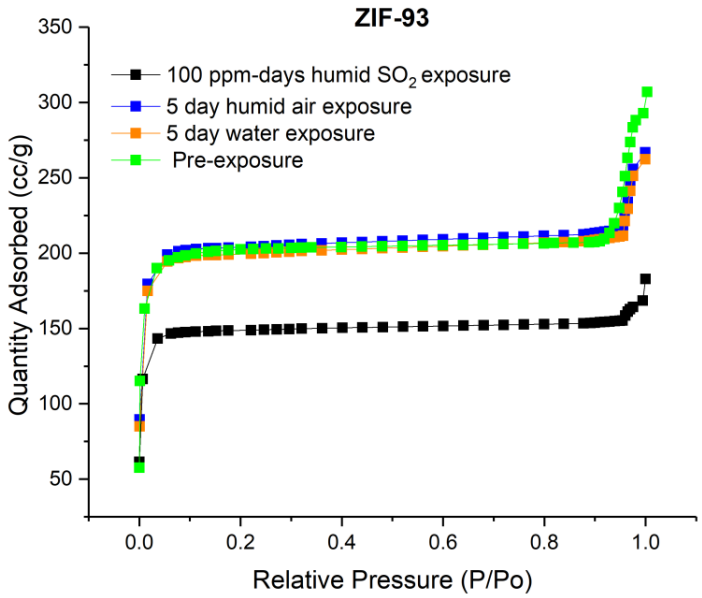

Figure B.39. N_2 physisorption at 77 K in ZIF-93 under different exposure conditions.

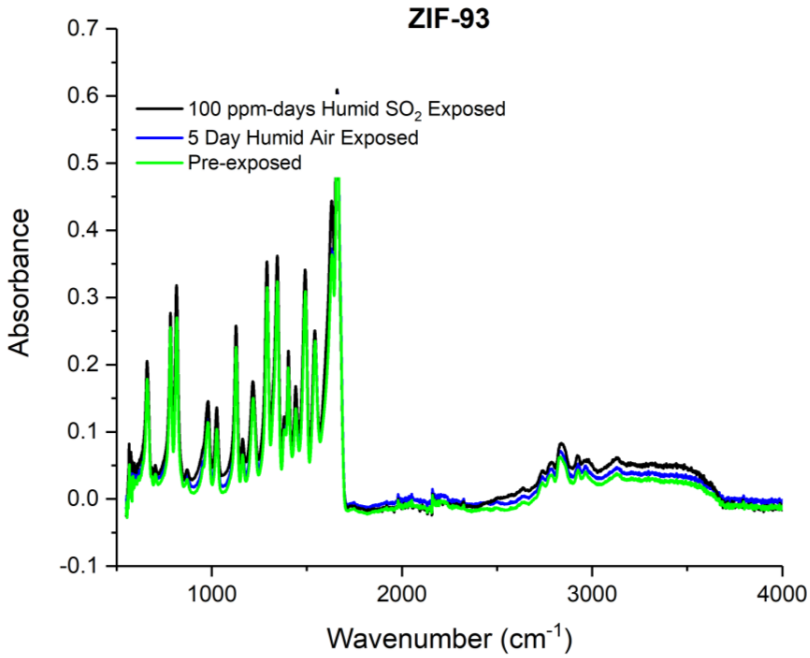

Figure B.40. FTIR spectra of ZIF-93 under different exposure conditions.

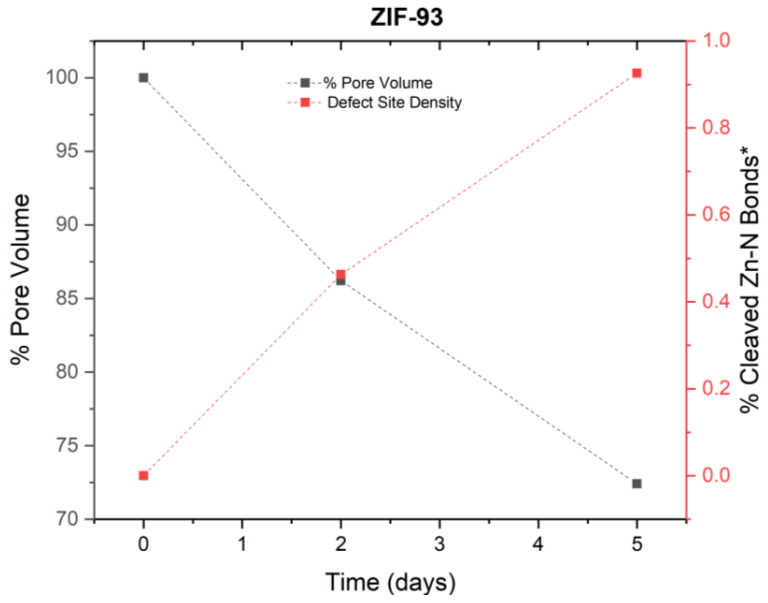

Figure B.41. Degradation kinetics of ZIF-93 showing the decrease in pore volume over time and the corresponding increase in defect sites (cleaved Zn-N bonds). Dotted lines are for visual aid.*Cleaved Zn-N bonds were calculated from the experimental Zn:S ratio assuming that one S atom incorporation led to one Zn-N bond cleavage.

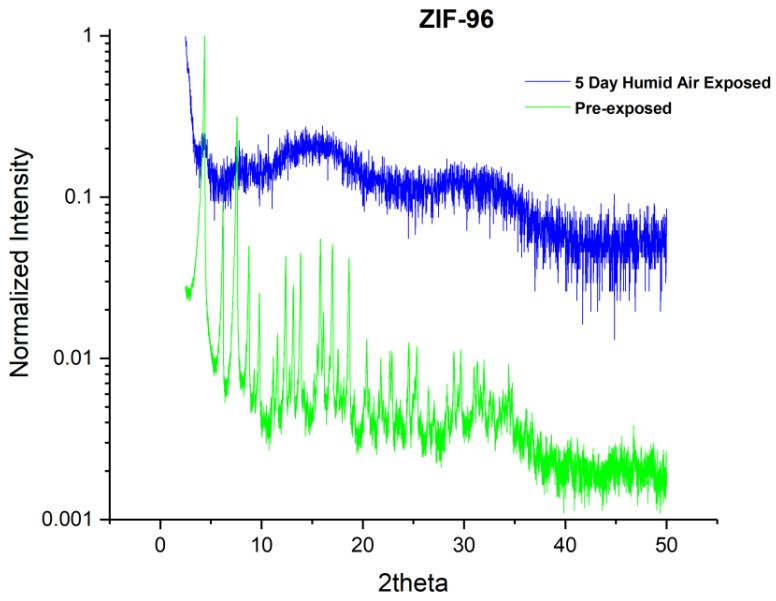

Figure B.42. PXRD patterns of ZIF-96 under different exposure conditions.

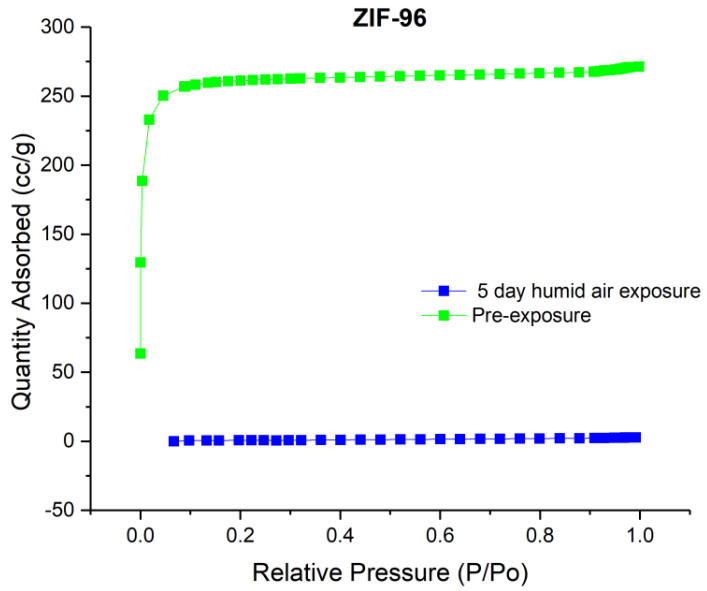

Figure B.43. N_2 physisorption at 77 K in ZIF-96 under different exposure conditions.

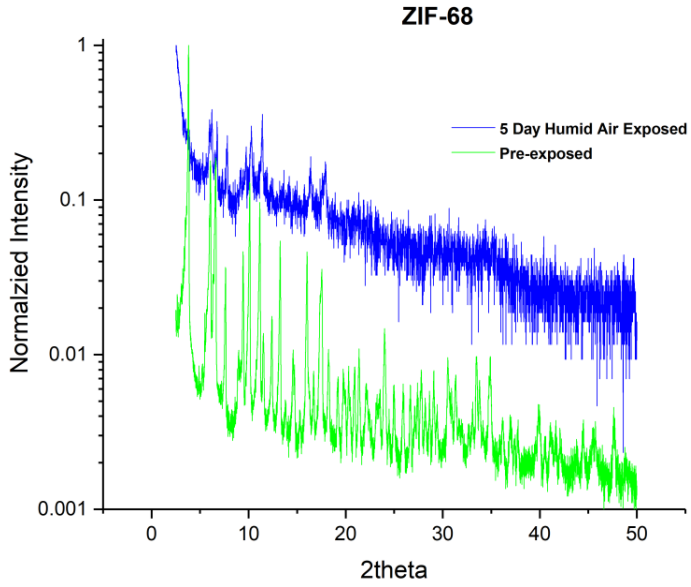

Figure B.44. PXRD patterns of ZIF-68 under different exposure conditions.

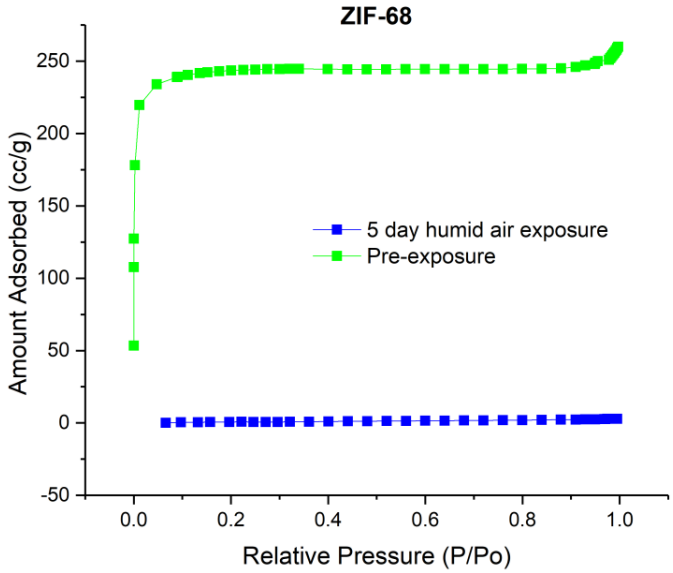

Figure B.45. N_2 physisorption at 77 K in ZIF-68 under different exposure conditions.

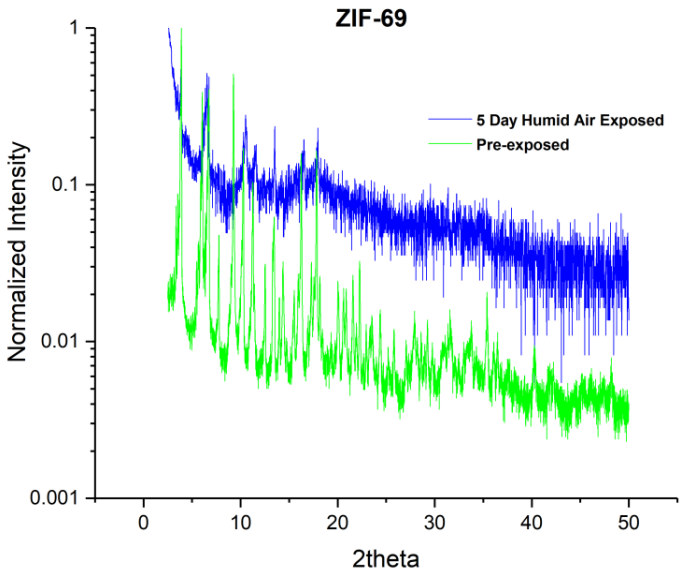

Figure B.46. PXRD patterns of ZIF-69 under different exposure conditions.

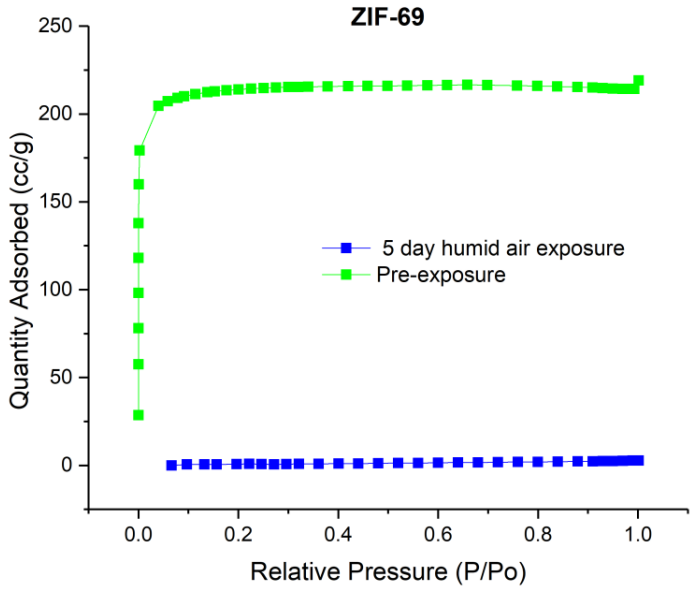

Figure B.47. N_2 physisorption at 77 K in ZIF-69 under different exposure conditions.

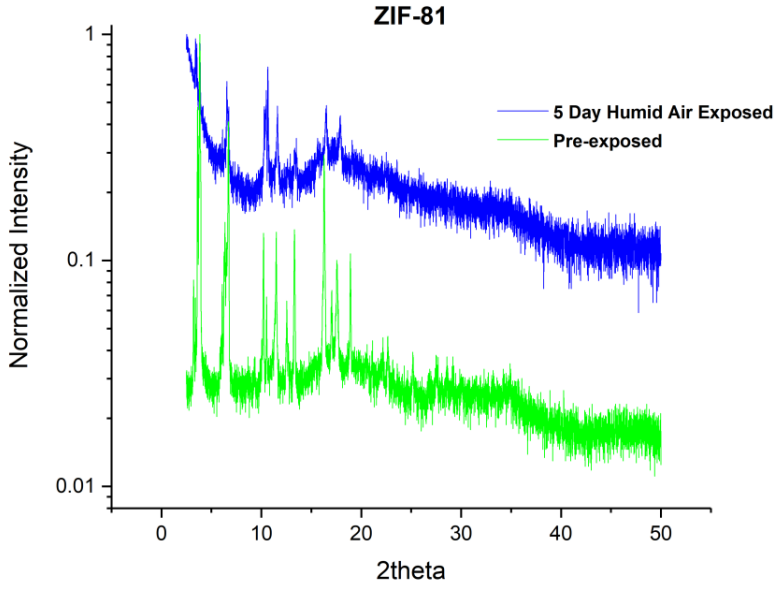

Figure B.48. PXRD patterns of ZIF-81 under different exposure conditions.

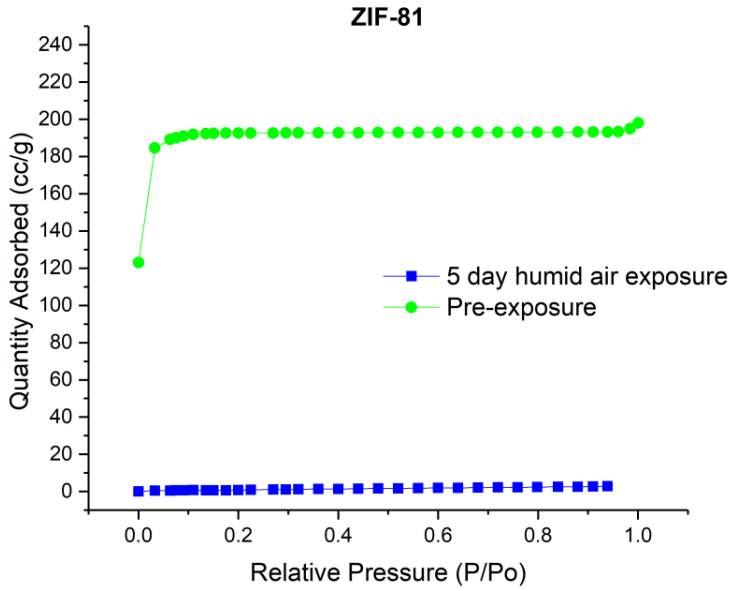

Figure B.49. N_2 physisorption at 77 K in ZIF-81 under different exposure conditions.

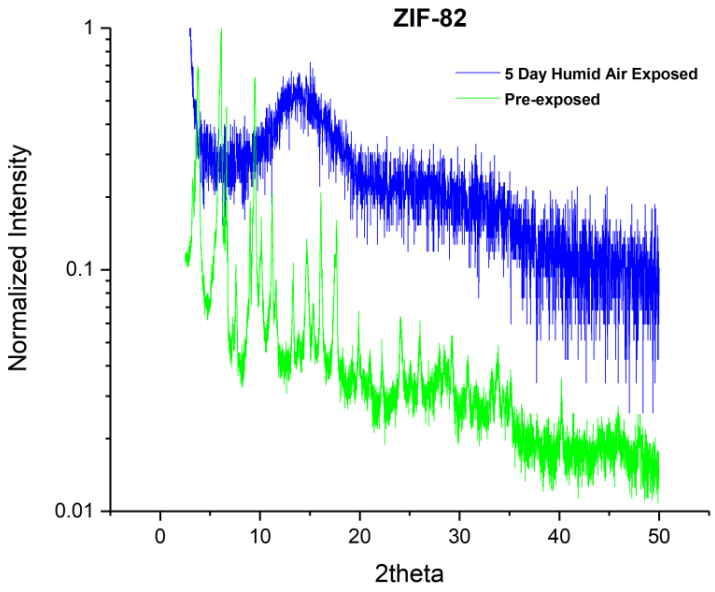

Figure B.50. PXRD patterns of ZIF-82 under different exposure conditions.

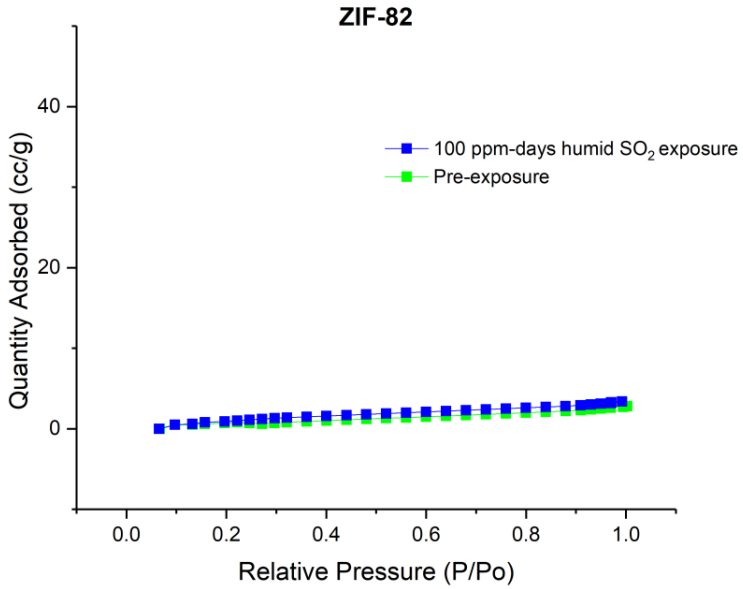

Figure B.51. N_2 physisorption at 77 K in ZIF-82 under different exposure conditions.

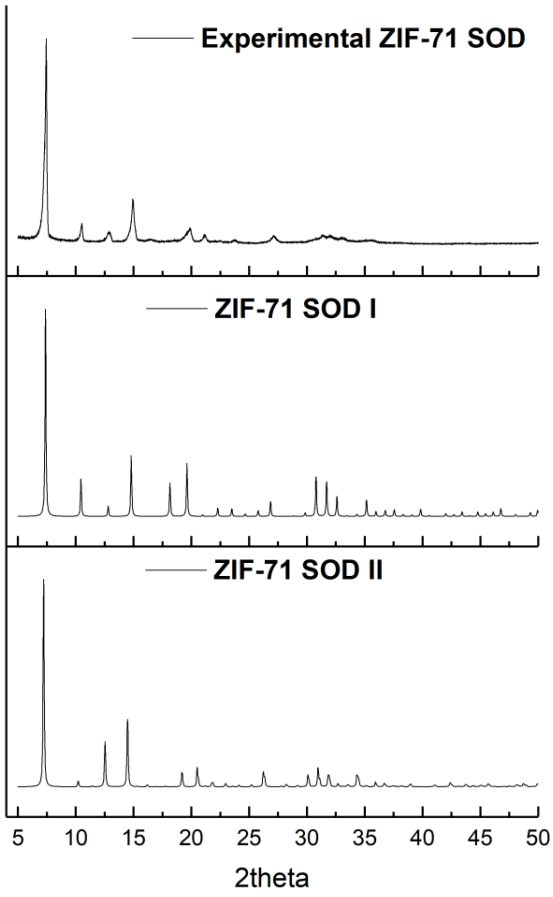

Figure B.52. PXRD patterns of ZIF-71 SOD isomorphs compared with experimentally synthesized ZIF-71 SOD.

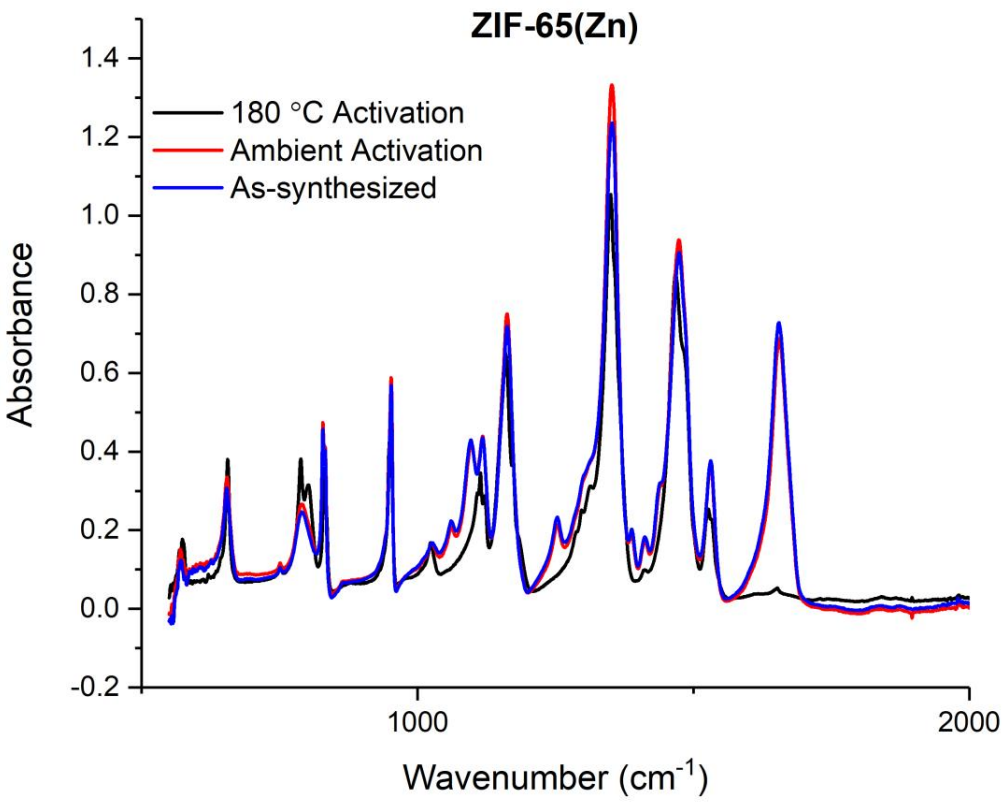

Figure B.53. FTIR spectra of as-synthesized ZIF-65 and its evolution on activation under vacuum at room temperature and at 453 K.

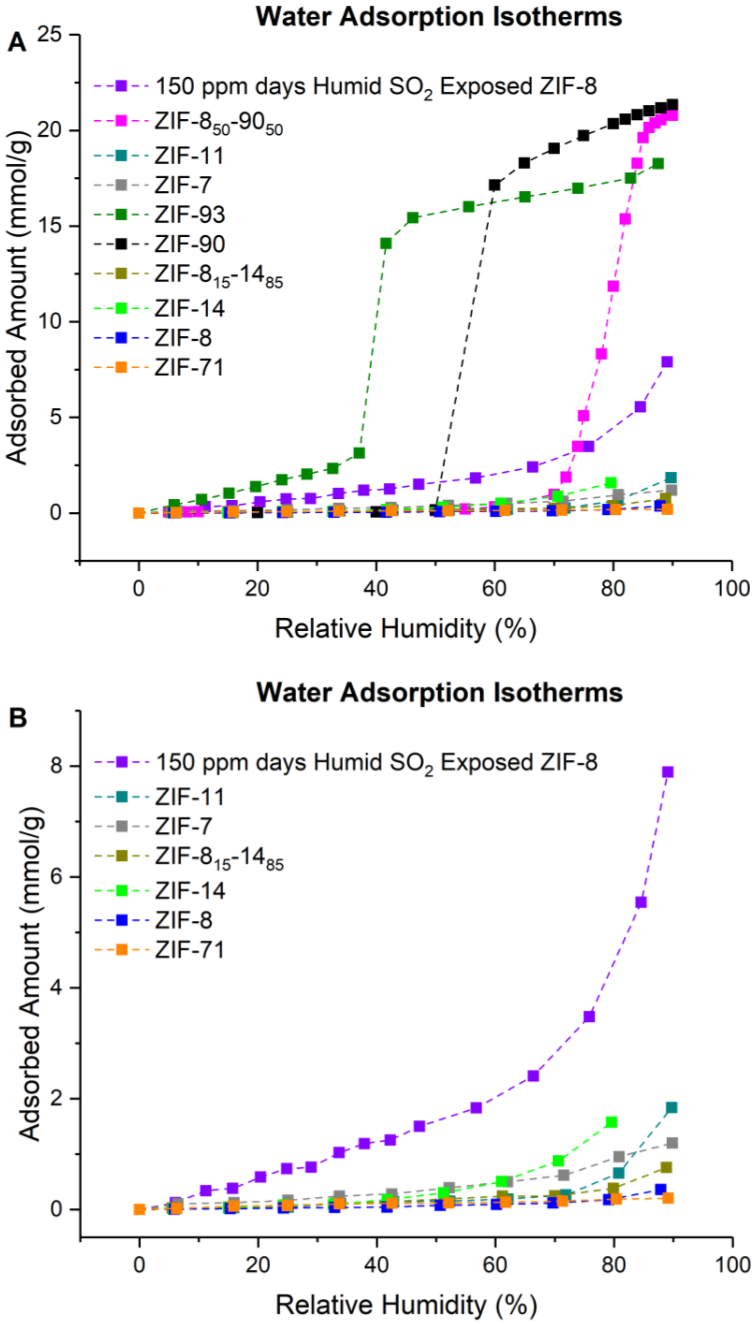

Figure B.54. Water adsorption isotherms of all ZIFs (**A**) and without ZIF-90, ZIF-93, ZIF-8_{50}-90_{50} (**B**). Closed symbols correspond to the experimental adsorption isotherms. Dashed lines are for visual reference only.

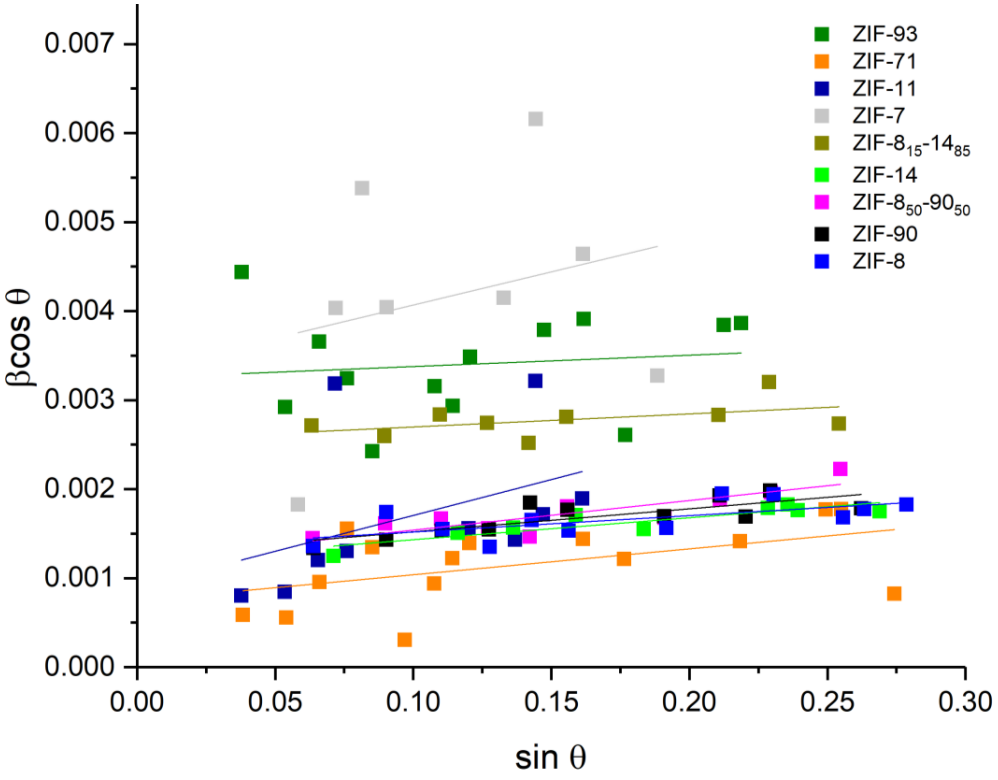

Figure B.55. Williamson-Hall Plot to evaluate crystallite sizes. The full width at half maxima (FWHM) for the peaks were adjusted for instrumental broadening using a LaB_6 standard.

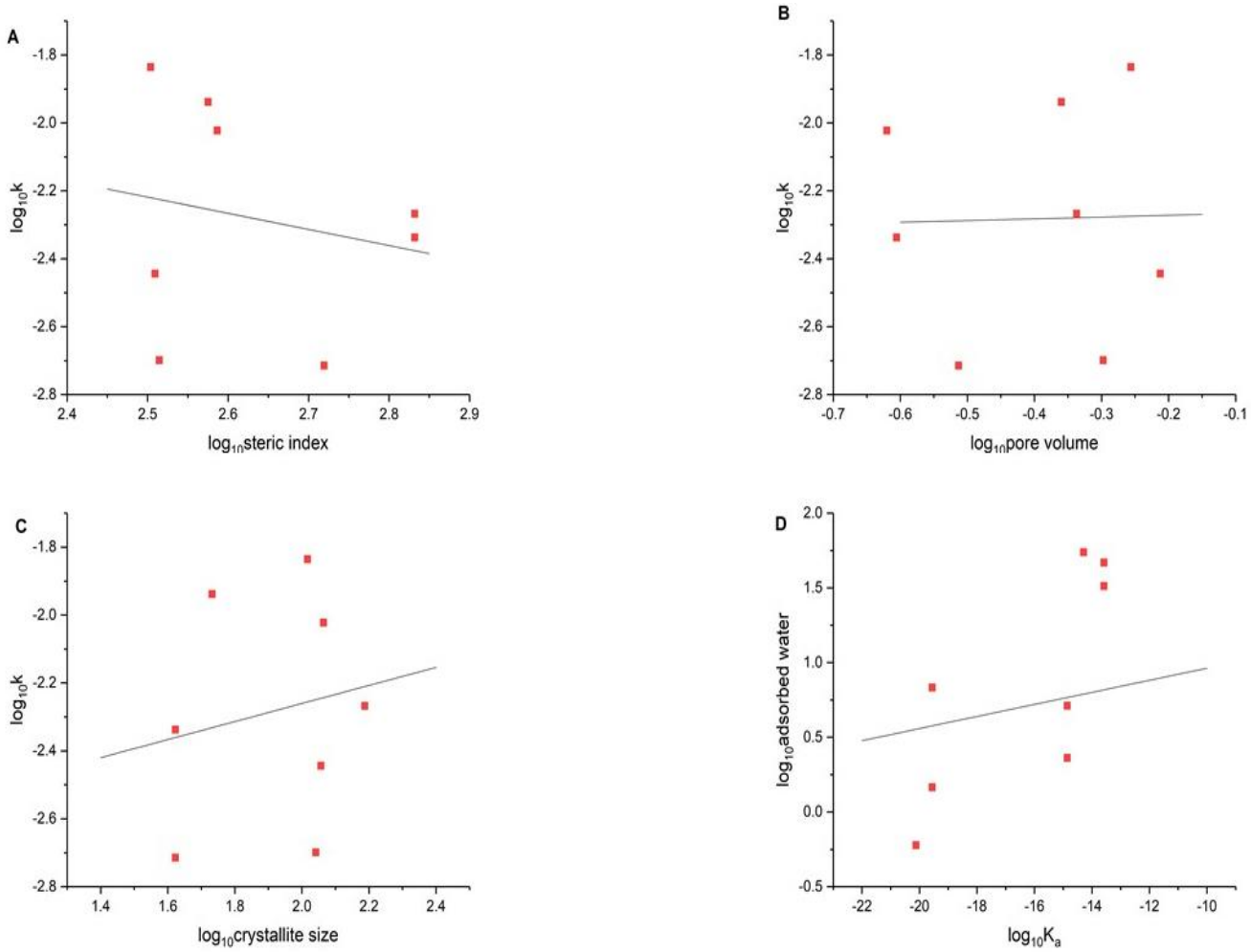

Figure B.56. Power-law correlations ($k = ax^b$ plotted on logarithmic scales) between the experimentally observed degradation rate constants and x = Steric Index (A), Pore Volume (B), and Crystallite Size (C) in ZIFs that measurably degraded under humid SO_2 exposure. Similar correlation (D) between linker K_a and adsorbed water in those ZIFs are also shown. Symbols: experimental data, Lines: correlation fits. The parameter values and regression coefficient (a, b, R^2) are (0.0933, -0.47, 0.04), (5.5×10^{-3}, 0.051, 0.0006), (0.0016, 0.27, 0.0316) and (63.24, 0.07, 0.08) respectively in the three correlations shown in (A), (B) and (C) respectively.

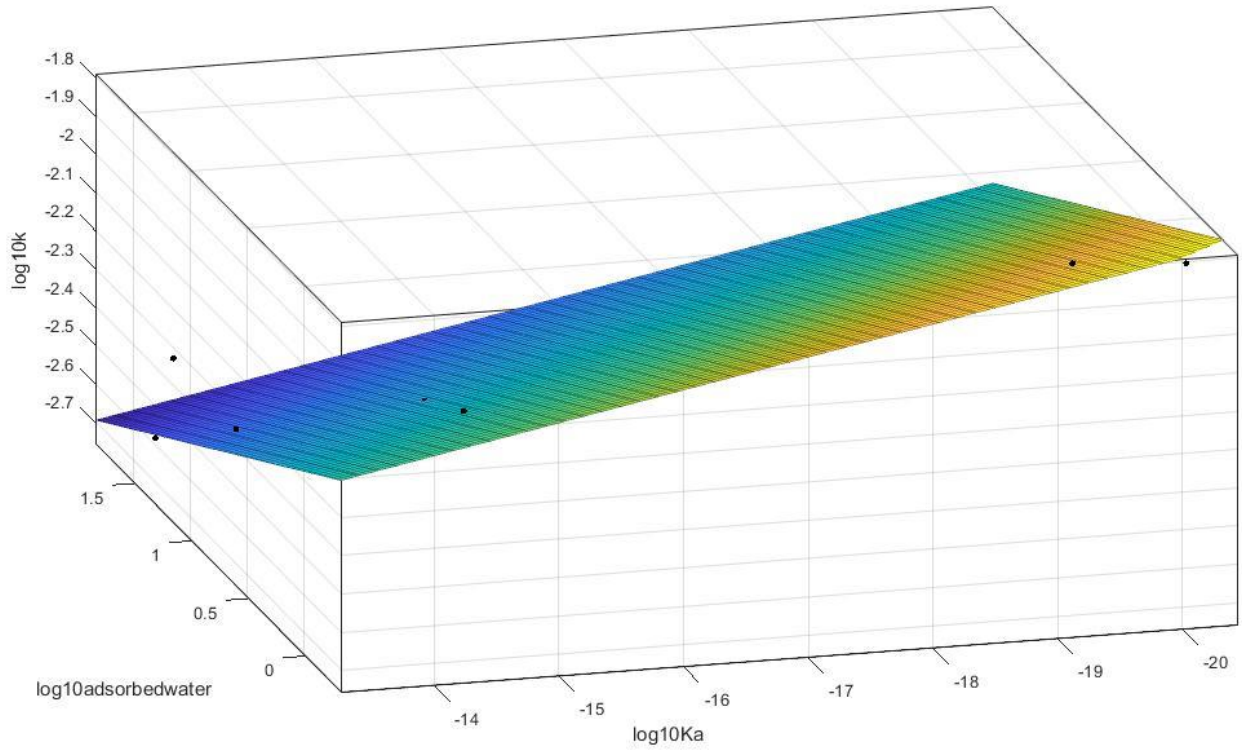

Figure B.57. Power-law correlation ($k = ax_1^b x_2^c$ plotted on logarithmic scales) between the experimentally observed degradation rate constants and x_1 = linker K_a and x_2 = adsorbed water in ZIFs that measurably degraded under humid SO_2 exposure. The parameter values and regression coefficient (a, b, c, R^2) are (8.15×10^{-4}, -0.06, -0.23, 0.94).

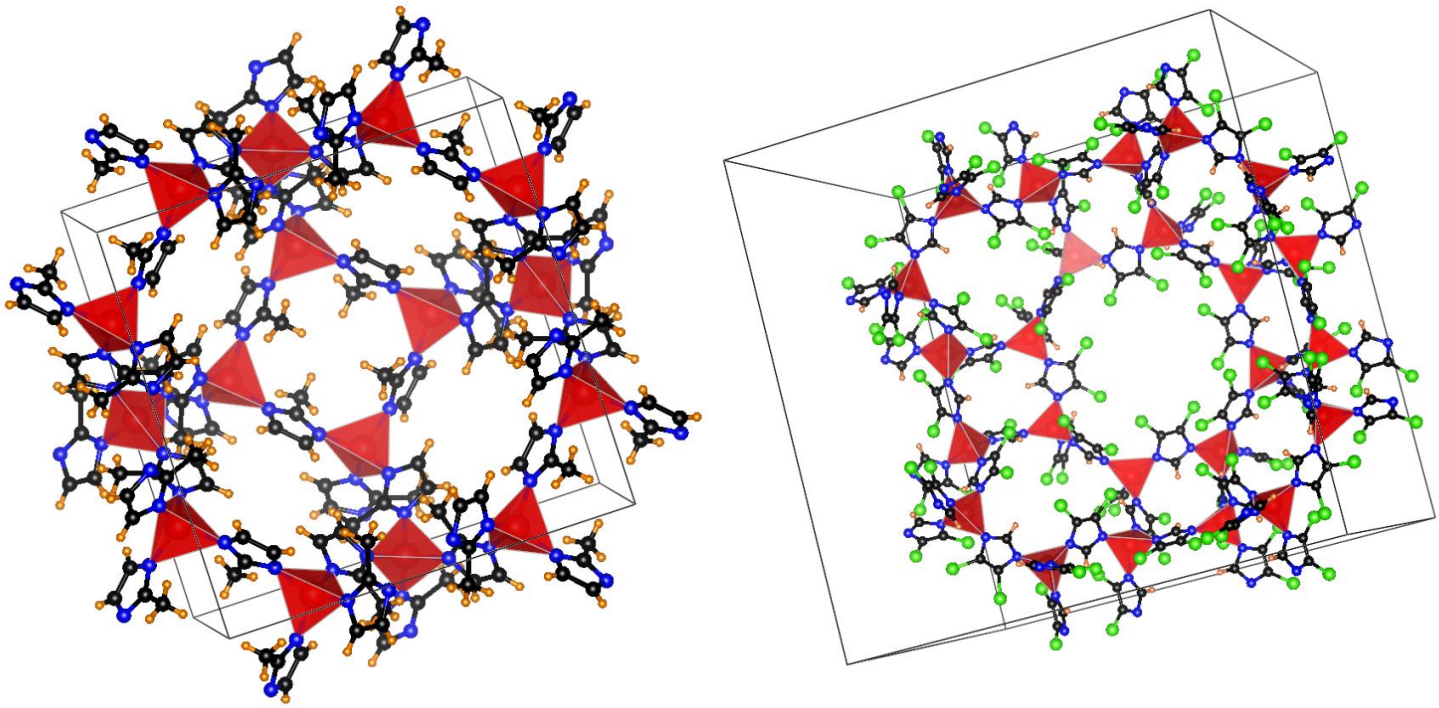

Figure B.58. Cross-sectional view of the unit cell of SOD topology ZIF-8 (left) and RHO topology ZIF-71 (right). Atoms are color coded as follows: Carbon (black), Nitrogen (blue), Hydrogen (orange), Zinc (red) and Chlorine (green).

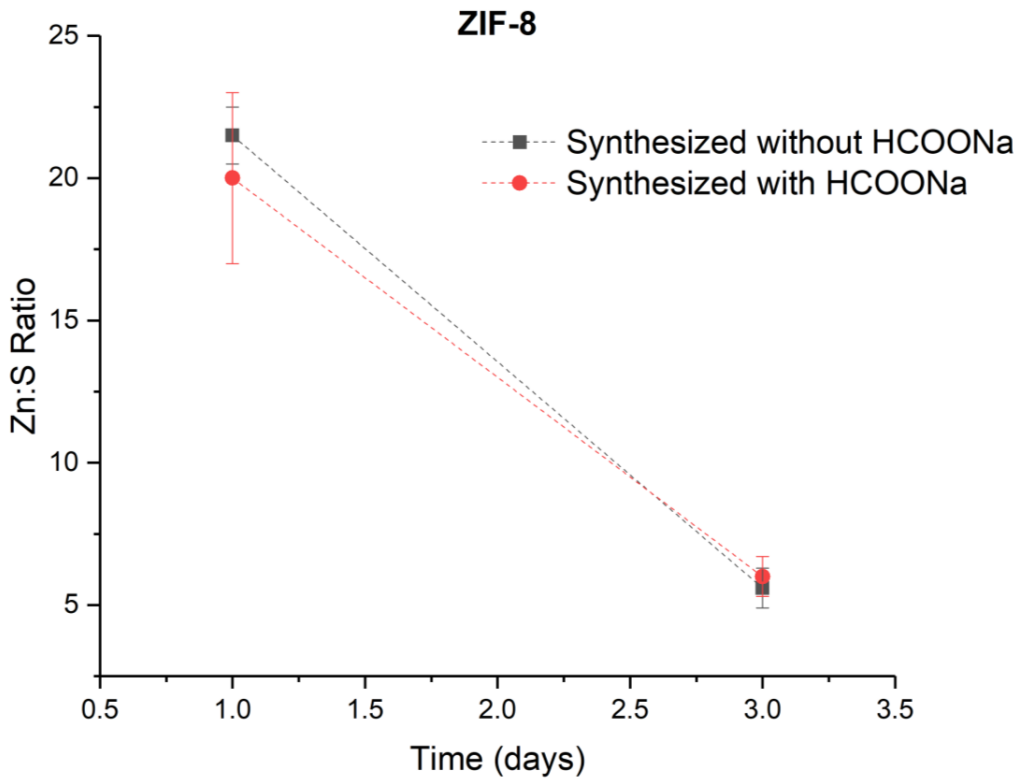

Figure B.59. S incorporation upon humid SO_2 exposure in ZIF-8 synthesized with and without sodium formate as modulator. Dotted lines are for visual reference.

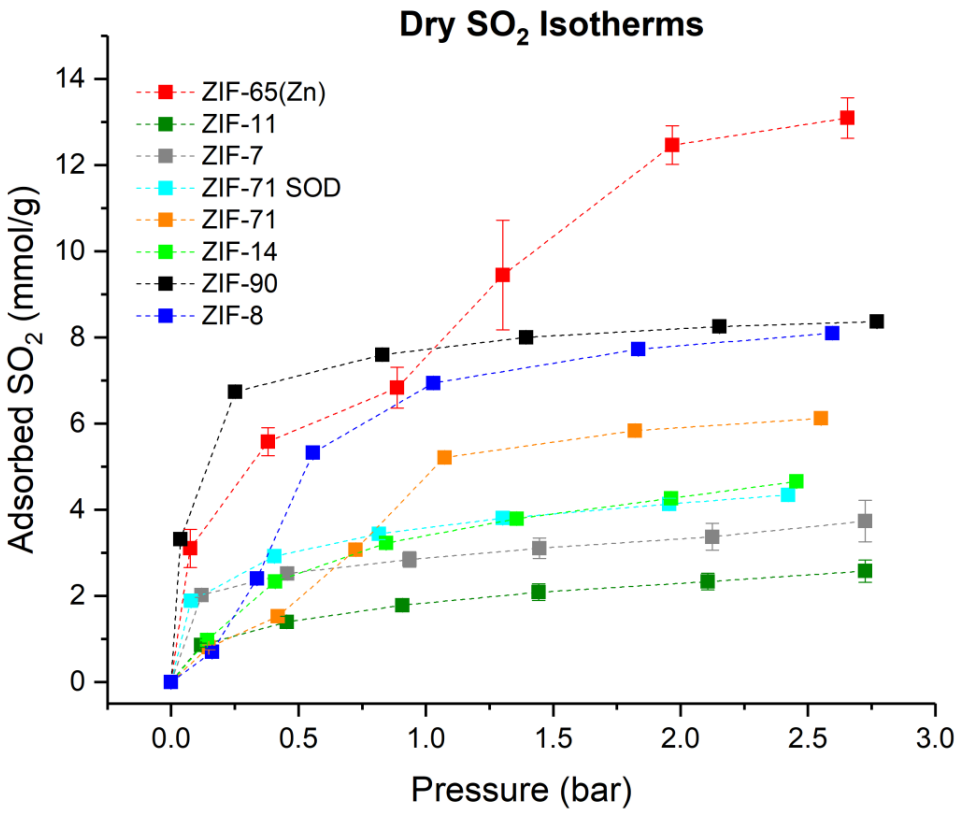

Figure B.60. SO_2 adsorption isotherms of different ZIFs investigated in this work. Closed symbols correspond to the experimental adsorption isotherms. Dashed lines are for visual reference only.

Table B.1. Characteristics of the single-linker ZIFs investigated in the thesis as detailed in Chapter 4. This table does not include the mixed-linker GME and SOD topology ZIFs

Adsorbent Name	Linker	Topology	Pore Aperture (Å)	Cage Size (Å)
ZIF-8	2-methyl imidazole	SOD	3.4	11.6
ZIF-14	2-ethyl imidazole	ANA	2.2	2.2
ZIF-7	benzimidazole	SOD	2.9	4.31
ZIF-11	benzimidazole	RHO	3	14.6
ZIF-90	2-carboxaldehyde imidazole	SOD	3.5	11.2
ZIF-71	4,5-dichloroimidazole	RHO	4.2	16.5
ZIF-71	4,5-dichloroimidazole	SOD	3.2	8.6
ZIF-65(Zn)	2-nitroimidazole	SOD	3.4	10.4
ZIF-93	4-methyl 5-carboxaldehyde imidazole	RHO	3.5	16.9

Table B.2. Calculated DDEC charges on the coordinating N atom of the imidazole linker for different ZIFs investigated in the thesis in Chapter 4.

Adsorbent	Average N Charge (Hartree atomic units)
ZIF-8	-0.36
ZIF-14	-0.35
ZIF-7	-0.36
ZIF-90	-0.30
ZIF-71	-0.35
ZIF-65	-0.06

Table B.3. Crystallite domain sizes and microstrain of ZIFs that degrade under humid SO_2 evaluated using the Williamson-Hall Method.

Serial No.	Material	Crystallite Size (nm)	Microstrain ($\times 10^{-3}$)
1	**ZIF-8**	104	1.8
2	**ZIF-14**	116	2.5
3	**ZIF-8_{15}-14_{85}**	54	1.5
4	**ZIF-7**	42	7.4
5	**ZIF-11**	154	5.8
6	**ZIF-93**	42	1.3
8	**ZIF-90**	110	2.6
9	**ZIF-8_{50}-90_{50}**	114	3.3
10	**ZIF-71**	185	2.9

Table B.4. SO_2 uptakes from adsorption isotherms of different ZIFs at 0.1, 1, and 2.5 bar and 298 K. The highest uptakes are highlighted for each pressure. * Measured at 1.73 bar.

Adsorbent	SO_2 uptake (mmol/g)		
	0.1 bar	1 bar	2.5 bar
ZIF-11	0.7	1.8	2.5
ZIF-7	1.7	2.9	3.6
ZIF-71 SOD	1.9	3.5	4.3
ZIF-14	0.7	3.4	4.6
ZIF-71	0.6	4.7	6
ZIF-8	0.4	6.8	8.1
ZIF-90	**4.3**	7.5	8.3
ZIF-65(Zn)	3.3	**7.7**	**12.9**
MFM-300(Al) [1-2]		7.1	
MFM-300(In) [1]		8.3	
$Ni(bdc)(ted)_{0.5}$ [3]	4.5	9.97	10.88*
Mg-MOF-74 [3]	6.4	8.6	

REFERENCES

1. Savage, M.; Cheng, Y.; Easun, T. L.; Eyley, J. E.; Argent, S. P.; Warren, M. R.; Lewis, W.; Murray, C.; Tang, C. C.; Frogley, M. D.; Cinque, G.; Sun, J.; Rudić, S.; Murden, R. T.; Benham, M. J.; Fitch, A. N.; Blake, A. J.; Ramirez-Cuesta, A. J.; Yang, S.; Schröder, M., Selective Adsorption of Sulfur Dioxide in a Robust Metal–Organic Framework Material. *Adv. Mater.* **2016,** *28* (39), 8705-8711.

2. Yang, S.; Sun, J.; Ramirez-Cuesta, A. J.; Callear, S. K.; DavidWilliam, I. F.; Anderson, D. P.; Newby, R.; Blake, A. J.; Parker, J. E.; Tang, C. C.; Schröder, M., Selectivity and direct visualization of carbon dioxide and sulfur dioxide in a decorated porous host. *Nat Chem* **2012,** *4* (11), 887-894.

3. Tan, K.; Canepa, P.; Gong, Q.; Liu, J.; Johnson, D. H.; Dyevoich, A.; Thallapally, P. K.; Thonhauser, T.; Li, J.; Chabal, Y. J., Mechanism of Preferential Adsorption of SO_2 into Two Microporous Paddle Wheel Frameworks M(bdc)(ted)$_{0.5}$. *Chem. Mater.* **2013,** *25* (23), 4653-4662.

APPENDIX C. SUPPORTING INFORMATION (CHAPTER 5)

Table C.1. Topological characteristics of the ZIF structures investigated in this work.

Material	Imidazolate Linker	Topology	Pore Aperture (Å)	Cage Size (Å)
ZIF-8	2-methyl imidazole	SOD	3.4	11.6
ZIF-90	2-carboxaldehyde imidazole	SOD	3.5	11.2
ZIF-71	4,5-dichloroimidazole	RHO	4.2	16.5

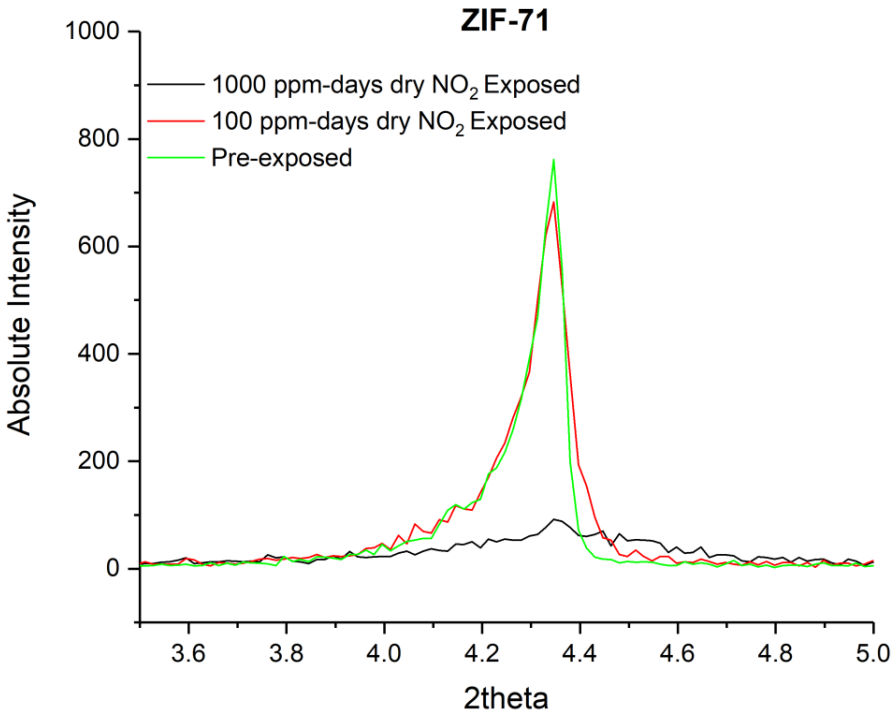

Figure C.1. The (110) PXRD peak of ZIF-71 on exposure to increasing dosage of dry NO_2 compared to the pre-exposed sample.

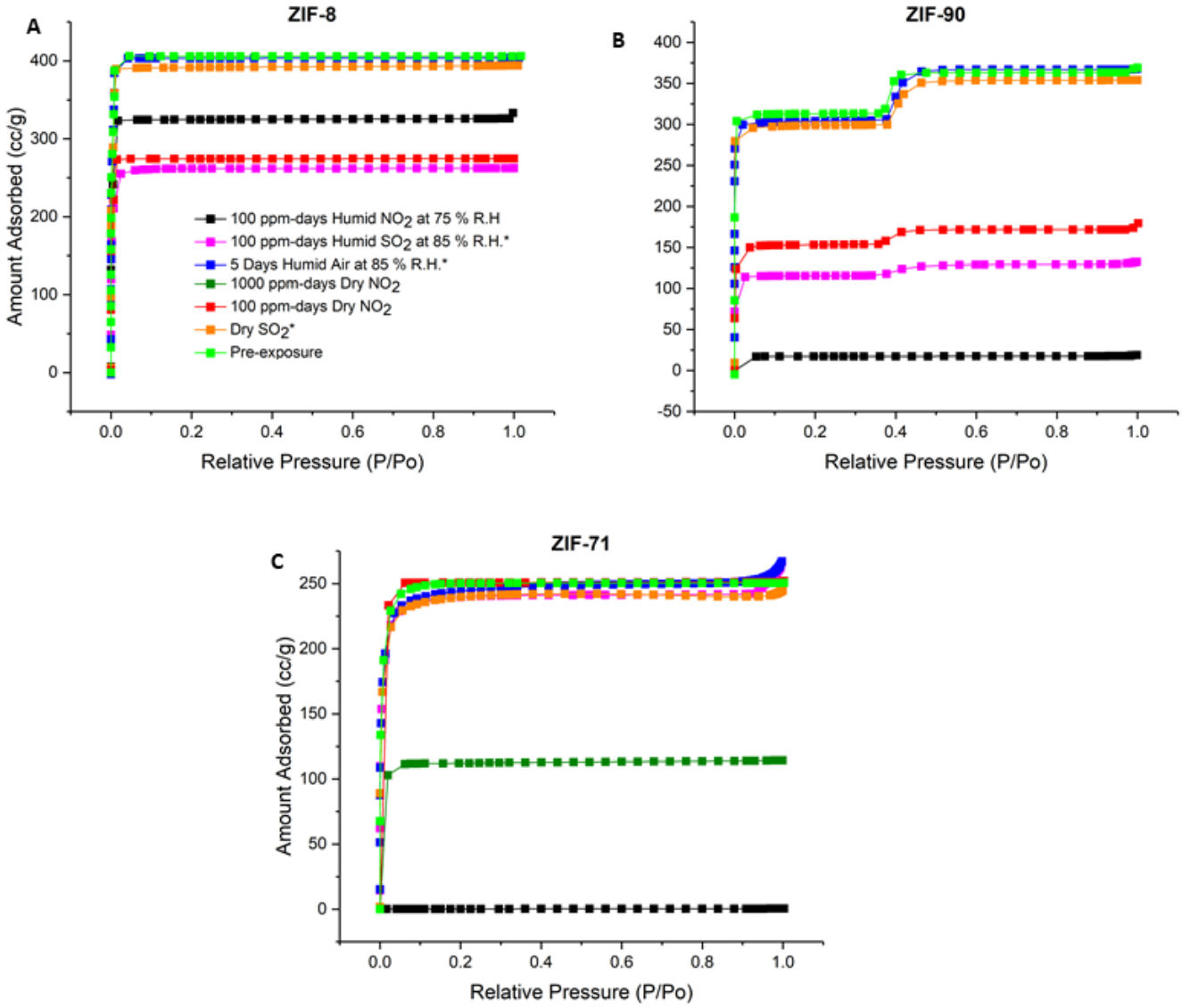

Figure C.2. N_2 physisorption at 77 K in pre-exposed and reactivated ZIFs after different exposure protocols. Figure legends are same in all. 1000 ppm-days dry NO_2 exposure was only carried out in C) ZIF-71. * Data reproduced from previous work for comparison[1]

Table C.2. Textural characteristics of pre-exposed ZIFs and ZIFs after different exposure experiments. The BET surface area is reported as a percentage relative to pre-exposed ZIF-8.
* Previously reported data[1]
# Phase-change
[a] Average SO_2 concentration during dry SO_2 isotherm measurements

Exposure Condition	Exposed Time (days)	Conc.	Overall Exposure (ppm-days)	Relative BET SA			Pore Vol. (cc/g)		
				ZIF-8	ZIF-90	ZIF-71	ZIF-8	ZIF-90	ZIF-71
Pre	NA	NA	NA	100	100	100	0.62	0.45	0.37
Dry SO_2*	0.15	99.8%	[a]1.8×10^5	98	99	98	0.6	0.44	0.34
Dry NO_2	0.1	1000 ppm	100	65	53	99	0.41	0.25	0.36
Dry NO_2	1	1000 ppm	1000	N/A	N/A	45	N/A	N/A	0.17
Humid Air*	5	0	0	99	98	99	0.61	0.44	0.33
Humid SO_2*	5	20 ppm	100	61	50	97	0.38	0.22	0.34
Humid NO_2	5	20 ppm	100	81	3	0[#]	0.49	0.04	0[#]

Table C.3. Functional groups attributed to new FTIR peaks in ZIFs following 200 ppm-days dry NO_2 exposure. Same peaks are observed on humid NO_2 exposure except in ZIF-71. Peaks without overlaps that can be unambiguously assigned are highlighted green.

Functional Groups with References	ZIF-8	ZIF-90	ZIF-71	Expected Range of Peaks
Organic Groups				
Nitro[2-6]	1530	1525	1540	1485-1570 (asym. NO_2 str.)
	1330	masked	1340	1320-1370 (sym. NO_2 str.)
	1031	1010	1020	865-1180 (aromatic C-N str.)
	920, 930	930	NA	850-1000 (aliphatic C-N str.)
	832	830	840	830-865 (NO_2 def.)
	655	660	NA	605-670 (NO_2 def. aliphatic)
Nitrite[2-7]	1650	1675	1670	1610-80 (N=O str.)
	812	801	810	750-850 (N-O str.)
	674	680	685	615-690 (O-N=O def.)
	1105	1094	1150	1000-1300 (C-O)
Nitrate[4-7]	1625	1610	1625	1615-1660 (asym. NO_2 str.)
	1270	1270	1280	1270-1300 (sym. NO_2 str.)
	860	845	860	840-870 (N-O str.)
	745	745	755	745-765 (NO_2 def.)
	712	720	715	680-720 (NO_2 def.)
	1105	1094	1150	1000-1300 (C-O)
Nitramine[2-3, 6, 8]	1570	1550	1560	1530-1630 (asym. NO_2 str.)
	1270	1275	1295	1260-1315 (sym. NO_2 str.)
	970	980	960	925-1030 (N-N str.)
	775	760	770	755-775 (NO_2 def.)
Nitrosamine[6, 9]	1500	1460	1495	1450-1500 (N=O str.)

	970 1165	980 1166	960 1170	925-1030 (N-N str.) 1160-1200 (C-N str.)
Inorganic Groups				
Nitrate[6, 10-11]	1380 860 712	1380 845 720	1385 860 715	1350-1410 (asym. NO_3 str.) ~800-860 ~710-730
Nitrite[6]	1235 812	1235 801	1260 810	1235-1275 (asym. NO_2 str.) 800-835

Peaks appearing at 1500-1600 cm^{-1} arise from the asymmetric NO_2 stretch of nitro- groups or nitramines, with the nitro- stretch usually present in the lower wavenumber range of 1500-1540 cm^{-1} and the nitramine stretch in the higher wavenumber range.[2-3, 6] The peaks at 1530, 1525 and 1540 cm^{-1} in ZIF-8, ZIF-90 and ZIF-71 respectively can be attributed to nitro- groups and those at 1560-1570 cm^{-1} to nitramines. Peaks corresponding to the symmetric stretch of NO_2 in the nitro- group should be present in the range 1330-1370 cm^{-1} as are observed in ZIF-8 and ZIF-71, but are masked in ZIF-90 by the strong reduction in intensity observed at 1315 cm^{-1}. While the aromatic C-N stretch for a nitro- group can be present within a large range (865-1180 cm^{-1}), I can assign the peaks at 1031, 1010 and 1020 cm^{-1} to the C-N stretch of the nitro- group based on the C-N stretch assignment for imidazoles such as tinidazole and metronidazole containing aromatic nitro- groups.[4, 12] Peaks around 930 cm^{-1} observed in ZIF-8 and ZIF-90 may rise from additional C-N stretches due to aliphatic nitro- group formation.[6] The absence of peaks in this region in ZIF-71, which lacks aliphatic C-H groups, further supports this assignment. The N-N stretch of nitramines can be assigned to the peak around 960-980 cm^{-1} in all the three ZIFs,

in accordance with literature reports.[6, 8] FTIR peaks in the range of 1360-1400 cm^{-1} can be unambiguously assigned to inorganic nitrate groups bonded to the metal center of the ZIFs.[6, 10-11] I have therefore assigned the common peak at ~1380 cm^{-1} present in all 3 ZIFs to the inorganic nitrate group in accordance with the FTIR spectra of zinc nitrate.[13-15] The route to inorganic nitrate formation may involve initial formation of inorganic nitrites whose main peak in the 1230-1280 cm^{-1} range is difficult to uniquely identify because of overlaps with other functional groups. Various peaks are present in the 1230-1300 cm^{-1} region in all 3 ZIFs on dry NO_2 exposure, which point to the formation of multiple species, including nitramines, organic nitrates and inorganic nitrites.[2-3, 5-8] In addition, a fundamental stretch of adsorbed N_2O_4 dimer is present at 1260 cm^{-1} complicating peak assignments in this region[16-17] Organic nitrates and nitrites contain strong stretches in the 1600-1680 cm^{-1} region and the peaks around ~1620 and ~1670 cm^{-1} have been assigned to nitrates and nitrites respectively in all 3 ZIFs.[6] However the peak observed around ~1620 cm^{-1} may also be attributed to the bending vibrations of water which could be produced on dry NO_2 exposures of hydrocarbons.[18-20] Adsorbed NO_2 species may also give a stretch around 1620 cm^{-1}.[10, 17] The C-O stretches for organic nitrates or nitrites could be present within a wide range and we have assigned peaks around ~1100 cm^{-1} for the same, from the C-O stretches of ethers and esters.[6] Different NO_2 deformation vibrations and N-O stretches of multiple species lie within the 650-850 cm^{-1} range and these peaks have been tentatively assigned in **Table C.3**. Peaks observed at ~1450-1500 cm^{-1} result from the formation of nitrosamines with the aromatic C-N stretch of nitramines/nitrosamines around 1160 cm^{-1}.[6, 9] Broad OH stretches characteristic of hydrogen bonding are observed in all 3 ZIFs around 3300 cm^{-1}.

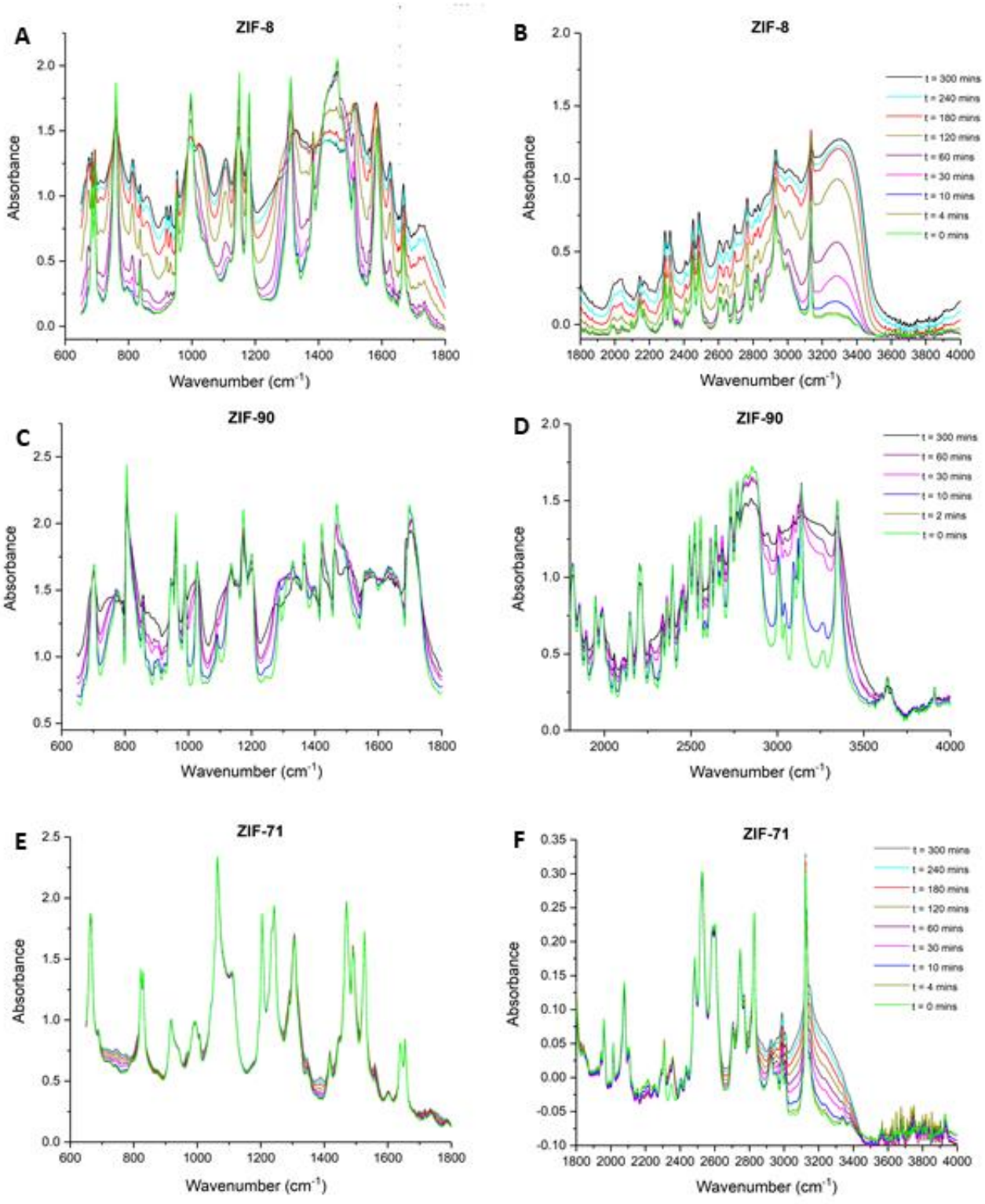

Figure C.3. Raw *in situ* FTIR spectra of ZIFs exposed to 1000 ppm dry NO_2 over 5 hours.

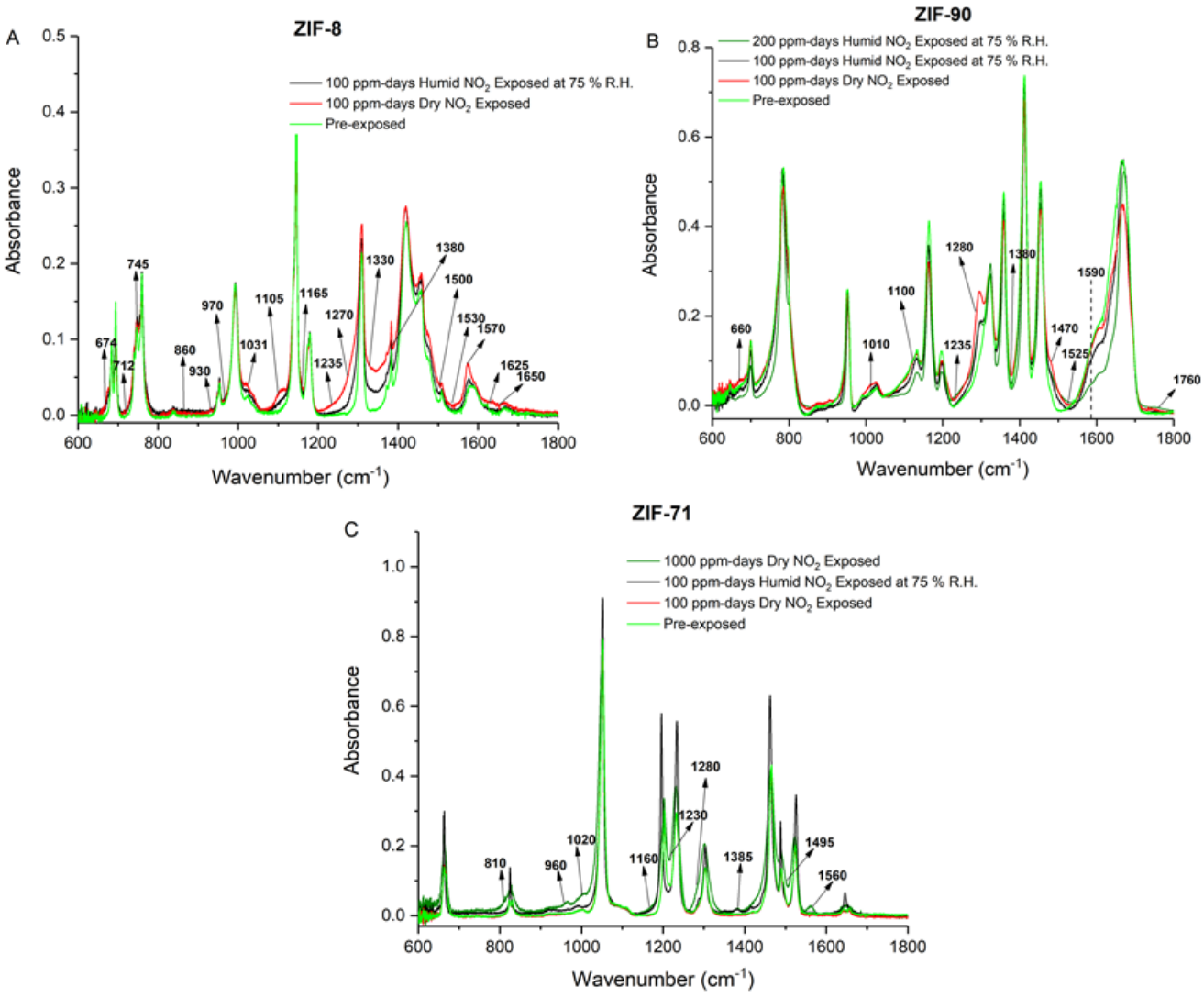

Figure C.4. *Ex situ* FTIR spectra of ZIFs with identical NO_2 dosage under dry and humid (75% RH) conditions. Important peaks discussed in the manuscript are marked in the figure.

The pre-exposed ZIF-8 spectrum in **Figure C.4** consists of peaks below 800 cm^{-1} (out-of-plane bending of the ring), 900-1350 cm^{-1} (in-plane bending of the imidazole ring), and between 1350 and 1500 cm^{-1} (vibration of the imidazole ring) respectively. [21-22] Similar

assignments for these regions can be made in ZIF-71 and ZIF-90, where these imidazole ring bending vibrations dominate the fingerprint region of the spectra and are difficult to uniquely identify. Specifically in ZIF-8, peaks at 1146 cm^{-1} and 1581 cm^{-1} may be assigned to =C-H bending and C=N stretching respectively.[21-23] The symmetric and asymmetric methyl group C-H stretch in ZIF-8 can be observed at 2930 cm^{-1} and 2980 cm^{-1} respectively while the aromatic ring C-H stretch, observed at 3135 cm^{-1}, is consistent with literature reports.[22-23] In ZIF-71, peaks observed at 665 cm^{-1} can be attributed to C-Cl vibrations,[24-27] while the characteristic C=O stretch of ZIF-90 is observed at 1680 cm^{-1} consistent with literature reports.[28-30]

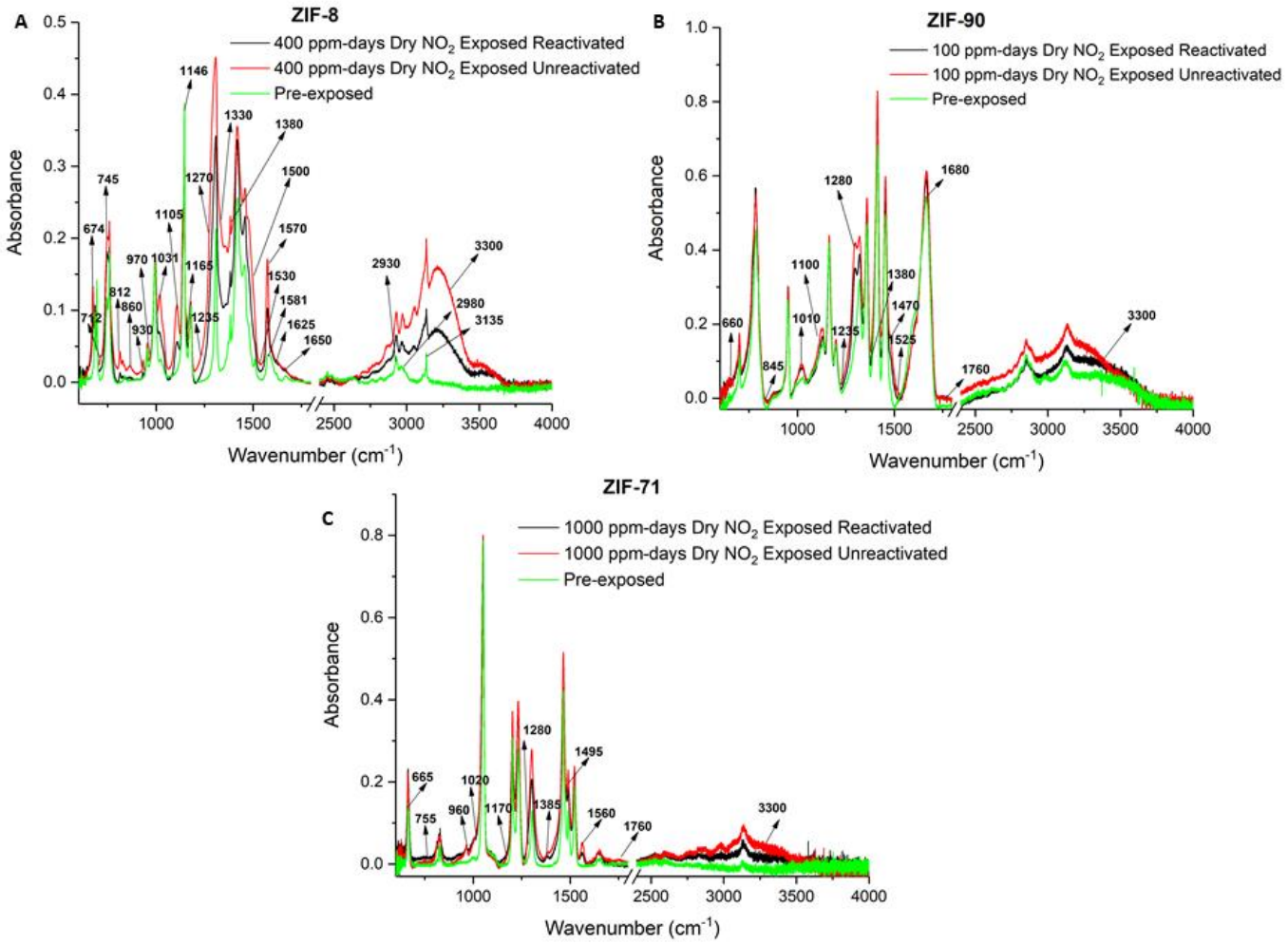

Figure C.5. *Ex situ* FTIR spectra of ZIFs exposed to dry NO_2 for different exposure times.

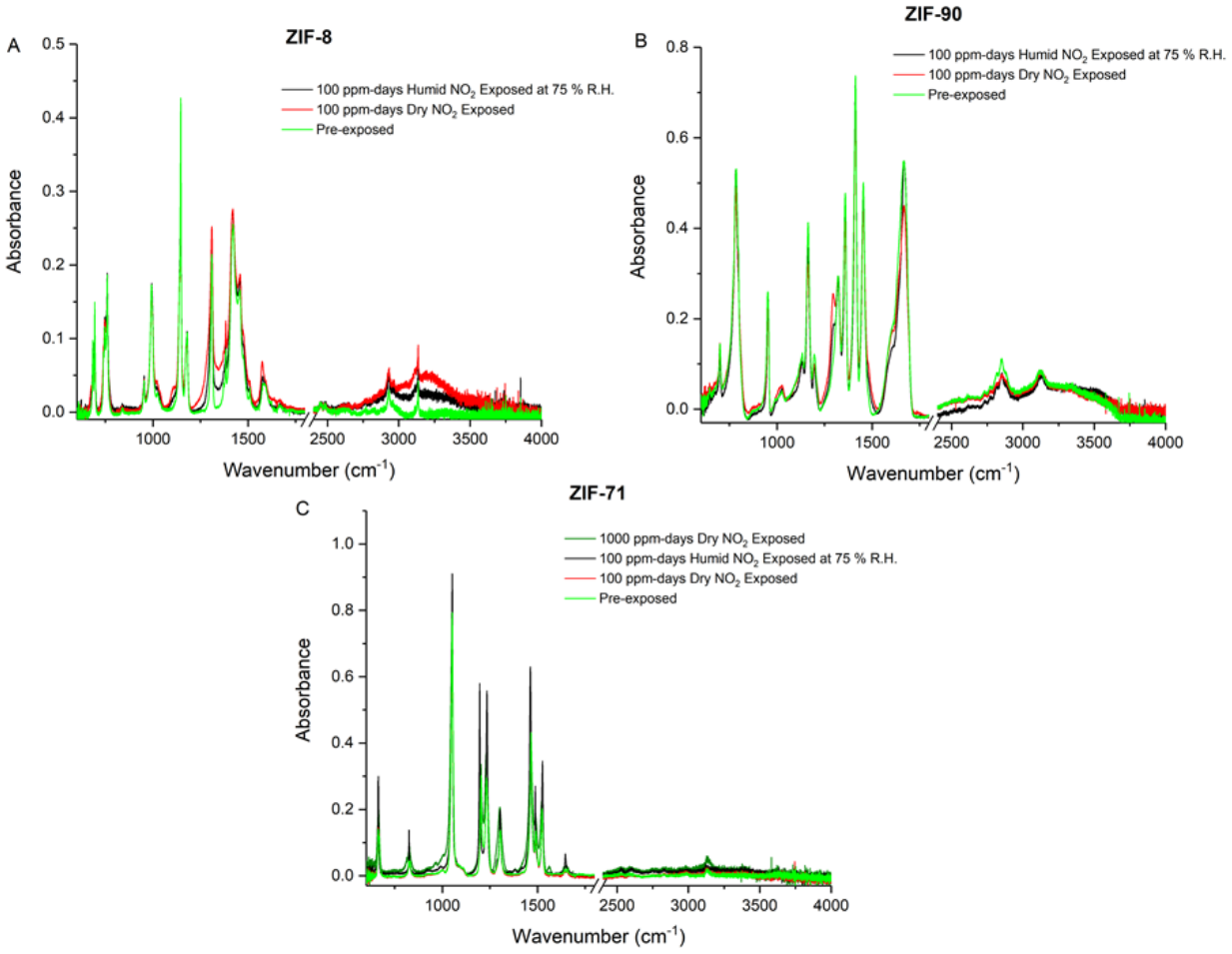

Figure C.6. *Ex situ* FTIR spectra of reactivated ZIFs after exposure to dry and humid NO_2.

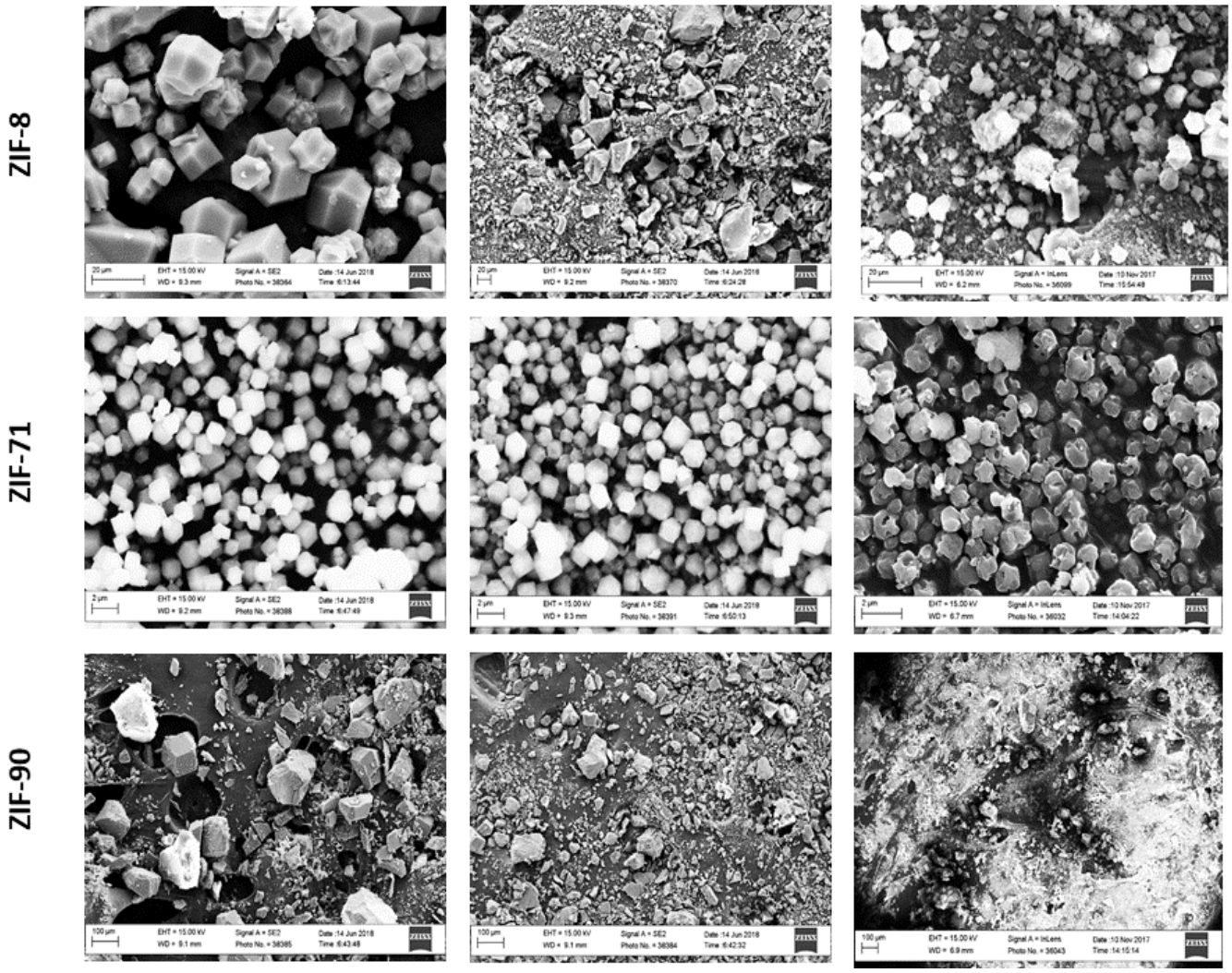

Figure C.7. SEM images of **(L)** pre-exposed, **(M)** dry NO_2 exposed and (**R**) 100 ppm-days humid NO_2 exposed and reactivated ZIFs. The samples in this figure are exposed to dry NO_2 for 400 ppm-days (ZIF-8), 1000 ppm-days (ZIF-71) and 100 ppm-days (ZIF-90) respectively.

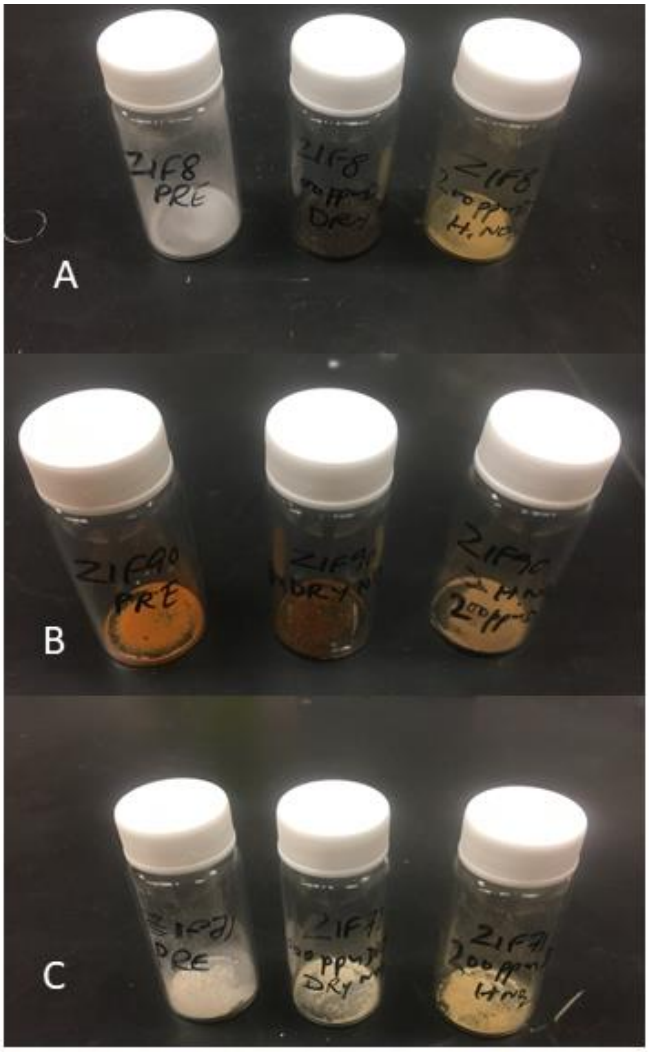

Figure C.8. Color changes of powder samples on NO_2 exposure in ZIF-8 (A), ZIF-90 (B) and ZIF-71 (C). From **left to right**: pre-exposed, dry NO_2 exposed, and humid NO_2 exposed materials.

Table C.4. Defect formation energies (eV) of reactions involving ZIF-8 computed using DFT.

Serial Number	Reaction Scheme	Defect Energy (eV)
1	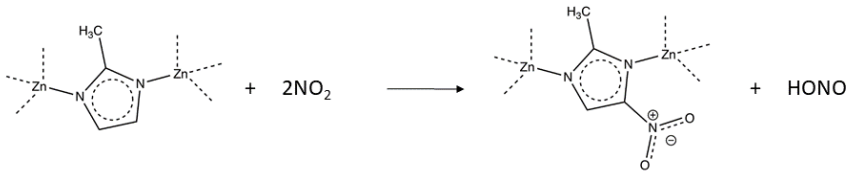	-1.95
2	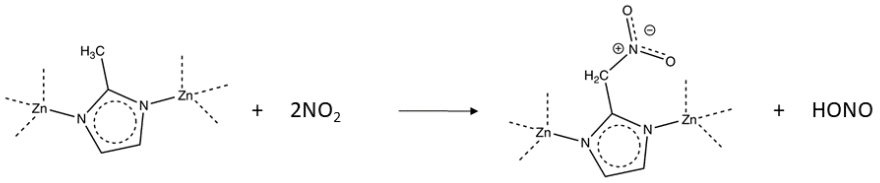	-1.73
3	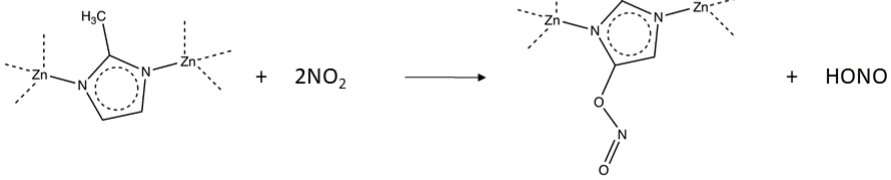	-1.69
4	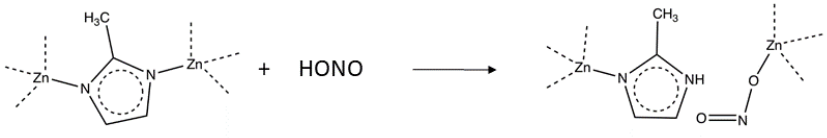	-0.1

5	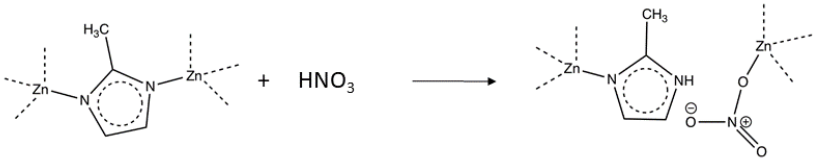	-0.29
6	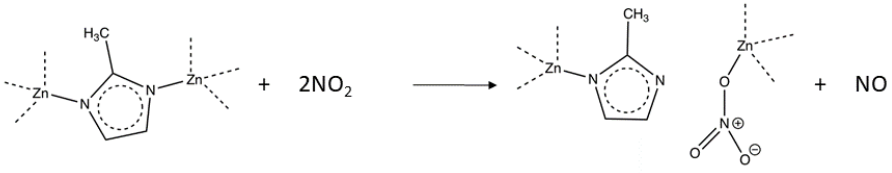	1.07

REFERENCES

1. Bhattacharyya, S.; Han, R.; Kim, W.-G.; Chiang, Y.; Jayachandrababu, K. C.; Hungerford, J. T.; Dutzer, M. R.; Ma, C.; Walton, K. S.; Sholl, D. S.; Nair, S., Acid Gas Stability of Zeolitic Imidazolate Frameworks: Generalized Kinetic and Thermodynamic Characteristics. *Chem. Mater.* **2018,** *30* (12), 4089-4101.

2. Akhter, M. S.; Chughtai, A. R.; Smith, D. M., Reaction of hexane soot with nitrogen dioxide/nitrogen oxide (N_2O_4). *J. Phys. Chem.* **1984,** *88* (22), 5334-5342.

3. Al-Abadleh, H. A.; Grassian, V. H., Heterogeneous reaction of NO_2 on hexane soot: A Knudsen cell and FT-IR study. *J. Phys. Chem. A* **2000,** *104* (51), 11926-11933.

4. Azambre, B.; Collura, S.; Trichard, J. M.; Weber, J. V., Nature and thermal stability of adsorbed intermediates formed during the reaction of diesel soot with nitrogen dioxide. *Appl. Surf. Sci.* **2006,** *253* (4), 2296-2303.

5. Kirchner, U.; Scheer, V.; Vogt, R., FTIR spectroscopic investigation of the mechanism and kinetics of the heterogeneous reactions of NO_2 and HNO_3 with soot. *J. Phys. Chem. A* **2000,** *104* (39), 8908-8915.

6. Socrates, G., *Infrared and Raman Characteristic Group Frequencies*. John Wiley & Sons, Ltd.: 2001.

7. Zawadzki, J.; Wisniewski, M.; Skowronska, K., Heterogeneous reactions of NO_2 and NO-O_2 on the surface of carbons. *Carbon* **2003,** *41* (2), 235-246.

8. Piskorz, M.; Urbanski, T., Ultraviolet and infrared spectra of some nitramines *Bull. Acad. Pol. Sci., Ser. Sci. Chim.* **1963,** *11* (11), 615-624.

9. Piskorz, M.; Urbanski, T., Ultraviolet and infrared spectra of some nitrosamines *Bull. Acad. Pol. Sci., Ser. Sci. Chim.* **1963,** *11* (11), 607-&.

10. W.L.Ross. The Infrared Absorption Spectra of Nitrogen Dioxide. The University of British Columbia, U.S.A., 1950.

11. Brooker, M. H., Raman and i.r. spectra of zinc, cadmium and calcium nitrate: A study of the low temperature phase transitions in calcium nitrate. *Spectroc. Acta Pt. A-Molec. Spectr.* **1976,** *32* (2), 369-377.

12. Mahendra, K. T.; Shrikant, P.; Harish, S.; Khemraj, B.; Snehasis, J., Spectroscopic Characterization of Biofield Treated Metronidazole and Tinidazole. *Med. Chem.* **2015,** *5* (7).

13. Li, P.; Xu, Z. P.; Hampton, M. A.; Vu, D. T.; Huang, L.; Rudolph, V.; Nguyen, A. V., Control Preparation of Zinc Hydroxide Nitrate Nanocrystals and Examination of the Chemical and Structural Stability. *J. Phys. Chem. C* **2012,** *116* (18), 10325-10332.

14. Wahab, R.; Ansari, S. G.; Seo, H.-K.; Kim, Y. S.; Suh, E.-K.; Shin, H.-S., Low temperature synthesis and characterization of rosette-like nanostructures of ZnO using solution process. *Solid State Sci.* **2009,** *11* (2), 439-443.

15. Wahab, R.; Kim, Y.-S.; Shin, H.-S., Synthesis, Characterization and Effect of pH Variation on Zinc Oxide Nanostructures. *Mater. Trans.* **2009,** *50* (8), 2092-2097.

16. Bibart, C. H.; Ewing, G. E., Vibrational-spectrum, torsional potential, and binding of gaseous N_2O_4. *J.Chem.Phys.* **1974,** *61* (4), 1284-1292.

17. Harris, L.; King, G. W., The Infrared Absorption Spectra of Nitrogen Dioxide and Tetroxide. *J.Chem.Phys.* **1934,** *2* (2).

18. Ashokkumar, M.; Muthukumaran, S., Microstructure, optical and FTIR studies of Ni, Cu co-doped ZnO nanoparticles by co-precipitation method. *Opt. Mater.* **2014,** *37*, 671-678.

19. Raja, K.; Ramesh, P. S.; Geetha, D., Synthesis, structural and optical properties of ZnO and Ni-doped ZnO hexagonal nanorods by Co-precipitation method. *Spectroc. Acta Pt. A-Molec. Biomolec. Spectr.* **2014,** *120*, 19-24.

20. Gray, P.; Yoffe, A. D., The Reactivity And Structure Of Nitrogen Dioxide. *Chem. Rev.* **1955,** *55* (6), 1069-1154.

21. Barbosa, P.; Rosero-Navarro, N. C.; Shi, F.-N.; Figueiredo, F. M. L., Protonic Conductivity of Nanocrystalline Zeolitic Imidazolate Framework 8. *Electrochim. Acta* **2015,** *153*, 19-27.

22. Hu, Y.; Kazemian, H.; Rohani, S.; Huang, Y.; Song, Y., In situ high pressure study of ZIF-8 by FTIR spectroscopy. *Chem. Commun.* **2011,** *47* (47), 12694-12696.

23. Cheng, P.; Hu, Y. H., H_2O-Functionalized Zeolitic Zn(2-methylimidazole)2 Framework (ZIF-8) for H_2 Storage. *J. Phys. Chem. C* **2014,** *118* (38), 21866-21872.

24. Lu, P.; Wu, Y.; Kang, H.; Wei, H.; Liu, H.; Fang, M., What can pKa and NBO charges of the ligands tell us about the water and thermal stability of metal organic frameworks? *J. Mater. Chem. A* **2014,** *2* (38), 16250-16267.

25. Liu, S.; Liu, G.; Zhao, X.; Jin, W., Hydrophobic-ZIF-71 filled PEBA mixed matrix membranes for recovery of biobutanol via pervaporation. *J. Membr. Sci.* **2013,** *446* (Supplement C), 181-188.

26. Springer, S.; Satalov, A.; Lippke, J.; Wiebcke, M., Nanocrystals and nanomaterials of isoreticular zeolitic imidazolate frameworks. *Microporous Mesoporous Mater.* **2015,** *216* (Supplement C), 161-170.

27. Japip, S.; Wang, H.; Xiao, Y.; Shung Chung, T., Highly permeable zeolitic imidazolate framework (ZIF)-71 nano-particles enhanced polyimide membranes for gas separation. *J. Membr. Sci.* **2014,** *467* (Supplement C), 162-174.

28. Liu, C.; Liu, Q.; Huang, A., A superhydrophobic zeolitic imidazolate framework (ZIF-90) with high steam stability for efficient recovery of bioalcohols. *Chem. Commun.* **2016,** *52* (16), 3400-3402.

29. Morris, W.; Doonan, C. J.; Furukawa, H.; Banerjee, R.; Yaghi, O. M., Crystals as molecules: Postsynthesis covalent functionalization of zeolitic imidazolate frameworks. *J.Am.Chem.Soc.* **2008,** *130* (38), 12626-12627.

30. Yang, T.; Chung, T.-S., Room-temperature synthesis of ZIF-90 nanocrystals and the derived nano-composite membranes for hydrogen separation. *J. Mater. Chem. A* **2013,** *1* (19), 6081-6090.